Falsification of the mathematical models of methane reforming process using generalized least squares method

Anna SCIAZKO

2015

A dissertation submitted in partial fulfilment of the requirements for the degree of Doctor of Philosophy

Division of Regional Environment Systems,
Graduate School of Engineering and Science,
Shibaura Institute of Technology

Supervisors:
Professor Shinji KIMIJIMA
Professor Janusz S. SZMYD

Acknowledgements

It is my great pleasure to express my sincere appreciation to all the people who supported me through the preparation of this dissertation in both the Shibaura Institute of Technology in Japan and AGH University of Science and Technology in Poland

I would like to convey my deepest appreciation to Professor Shinji Kimijima for accepting me in his laboratory, for his invaluable guidance, patience, sincere enthusiasm and advice in the field of experimental and numerical studies.

I would like to express my sincere gratitude to Professor Janusz S. Szmyd for his inestimable advices and supervision, encouragement to broaden knowledge and discover new areas in the fields of energy engineering and numerical modelling.

It is my pleasure to acknowledge Dr. Yosuke Komatsu and show my highest gratitude for his efforts and dedication during all stages of the preparation of this dissertation. His enthusiasm, motivation and patience for research and kind support during my exchange study in Japan can not be underestimated.

I appreciate the important contribution of Dr. Grzegorz Brus, for introducing me to the area of material issues in Solid Oxide Fuel Cells and all his ideas and support during the methane/steam reforming process studies. I would like to acknowledge the kind advice of Professor Zygmunt Kolenda in the subject of theoretical aspects of Generalized Least Squares Method, which improved the quality of this dissertation. Thanks are expressed here also to the members of the Professor Kimijima laboratory, especially to Mr. Nobuyuki Washio and Mr. Masayuki Ota, and to Mr. Marcin Mozdzierz and Mr. Marcin Zakrzewski for their research collaboration.

The research presented in this dissertation was conducted under the Joint Doctoral Diploma Program between Shibaura Institute of Technology in Japan and AGH University of Science and Technology in Poland. Therefore I would like to acknowledge Professor Akito Takasaki,

former Director of the Center for International Programs and current Dean of Graduate School of Engineering and Science at SIT for giving me the unique opportunity to broaden my knowledge during my research conducted at SIT. I would like also to express my sincere gratitude to Ms. Midori Yabe, Ms. Yuko Nishishita, Ms. Yumi Okada and Ms. Misa Nakamura from the International Section of Shibaura Institute of Technology for organizing my research internships and for the great amount of help and support I received during all of my stays in Japan.

Finally I would like to express my heartfelt acknowledgement for my family who supported me through the preparation of this thesis, for their understanding, motivation and constant encouragement,

The work was supported by the Polish National Centre for Research and Development (Project HTRPL, Contract No. SP/J/1/166183/12), the Precise Measurement Technology Promotion Foundation of Japan and JSPS-PAN Project.

Contents

Abstract

The presented research for methane/steam reforming process attempted to provide the comprehensive description of the methane/steam reforming process dedicated for Solid Oxide Fuel Cell (SOFC). Despite the fact that methane/steam reforming is currently one of the most popular industrial methods for hydrogen production, the kinetic of the reaction have not been fully described and the derived empirical models of the process are significantly divergent among themselves. In the classical approach to the mathematical modelling, the quality of the model of the physical phenomena is decreased because of the uncertainties derived from the model simplifications and uncertainties of the experimental measurements. The conducted research proposes the experimental and numerical analyses of the methane/steam reforming process using the Generalized Orthogonal Least Squares (GLS) method. The GLS algorithm is applicable for finding the most probable approximation of the unknown parameters, which define the reliability of the derived reforming reaction rate and provides a criteria for the objective quantifications of the mathematical models describing the physical process.

In the scope of thesis the following topics were concerned and discussed: the theoretical basis of the methane/steam reforming process, mathematical deliberation of the GLS method and the potential benefits of its incorporation into the determination of the kinetic of the highly nonlinear chemical process and the classical methods of deriving methane/steam reforming kinetic. The experimental studies, conducted as part of this dissertation were used as a basis for the a novel approach to evaluate the reaction kinetics of the methane/steam reforming process by adopting an Orthogonal Least Squares method. The GLS method was applied to the calculation of the empirical parameters defining kinetic of reaction on a Ni/YSZ SOFC anode cermet catalyst. A critical comparison of the obtained results with the literature data and discussion on the possible reasons for the essential discrepancies between various studies are presented. The GLS method has the potential to provide objective criteria for the formal evaluation and falsification of different mathematical models of the methane/steam reforming process. These studies particularly focused on the importance of the mathematical expressions of the physical phenomena occurring in the chemical reforming system. The analysis was conducted in the light of improving the precise quantification of uncertainties found in the evaluation of the chemical reaction process and providing a reliable reaction rate equation.

Nomenclature

For mathematical expression deriving reaction kinetics

A	Pre-exponential factor, mol g^{-1} s^{-1} $Pa^{-(a+b)}$
a	Reaction order coefficient on the partial pressure of CH_4, -
b	Reaction order coefficient on the partial pressure of H_2O, -
E	Activation energy, J mol^{-1}
e^-	Electron
F_i	Molar flow rate of the chemical i-th component, mol s^{-1}
F_{i_v}	Volumetric flow rate of the chemical i-th component, m^3 s^{-1}
f_A	Fractional conversion of substance A, -
$GHSV$	Gas Hourly Space Velocity, h^{-1}
ΔG	Change in Gibbs free energy, J mol^{-1}
ΔH^0	Standard enthalpy of reaction, J mol^{-1}
$K_{reaction}$	Equilibrium constant for chemical reaction, -
$K^+_{reaction}$	Forward rate constant for chemical reaction, -
$K^-_{reaction}$	Backward rate constant for chemical reaction, -
k	Reaction constant, mol g^{-1} s^{-1} $Pa^{-(a+b)}$
m_i	Molar fraction of chemical component i, -
NC	Nitrogen-to-Carbon ratio, -
n	Number of measurement points, -
P	Pressure, Pa
ΔP	Difference in pressure between inlet and outlet, Pa
p_i	Partial pressure of the chemical component i, Pa
R	Universal gas constant, 8.3144621 J mol^{-1} K^{-1}
R_{st}	Reaction rate, mol s^{-1}
r	Reaction rate, mol s^{-1} g^{-1}
SC	Steam-to-Carbon ratio, -
T	Temperature, ^oC or K

$\dot{V}_{gas}$	Gas velocity, $mm^3\ h^{-1}$
V_{cat}	Volume of the catalyst layer, mm^3
w_{cat}	Catalyst weight, g
x	Conversion rate of Methane Steam Reforming Reaction, -
y	Conversion rate of Water Gas Shift Reaction, -
α_{line}	Arrhenius line coefficient, -
β_{line}	Arrhenius line coefficient, -

Superscripts

i	Inlet
o	Outlet
*	Active site of the catalyst

Subscripts

ad	Adsorption reaction
CH_4	Methane
CO	Carbon Oxide
CO_2	Carbon Dioxide
H_2	Hydrogen
H_2O	Water
sh	Shift reaction
st	Steam reforming reaction

For mathematical derivation of LS and GLS Methods

$\mathbf{A}$	J×K Jacobi's matrixes of measurements
$\mathbf{A_B}$	J×(K+N) Jacobi's matrixes of variables
$\mathbf{B}$	J×N Jacobi's matrixes of unknowns
$\mathbf{C_B}$	*A-priori* covariance matrix for all variables; rank (K+N)×(K+N)
$\mathbf{C_S}$	*A-priori* covariance matrix with the variances of measurements

	σ_k^2 on the diagonal and 0 on the other positions; rank K×K
$\mathbf{C_{SX}}$	*A-priori* covariance matrix with the variances of unknowns σ_n^2 on the diagonal and 0 on the other positions; rank N×N
$\mathbf{C_U}$	*A-posteriori* covariance matrix for measurements rank K×K
$\mathbf{C_X}$	*A-posteriori* covariance matrix for unknowns rank N×N
$\mathbf{C_{VB}}$	*A-posteriori* covariance matrix for variables rank (K+N)×(K+N)
F	Auxiliary variable
G	Auxiliary variable
f_j	*j*-th equation in the constraint equation set
I	Unit matrix
J	Number of constraint equations
k	J-elements vector of Lagrange multipliers vector
K	Number of measurements
L	Lagrange function
N	Number of unknowns
S	Auxiliary variable
s_k, s_n	Error characterizing *k*-th measurement and *n*-th unknown
u	K-elements vector of measurements
u_k	*k*-th measurement
$\mathbf{u}^*$	K-elements vector of real values of the quantities to be measured
u_k^*	*k*-th quantity to be measured
w	J-elements vector of residuals of equations
w_i	Residual of *j*-th constraint equation
V_{K+N}	Volume of the covariance hyperellipsoid
$\mathbf{V_B}$	(K+N)-elements vector of measurements
v	K-elements vector of correction for measurement **u**
v_k,	Correction to *k*-th measurement u_k
x	N-elements vector of approximations of unknowns
x_n	Approximation of *n*-th unknown
$\mathbf{x}^*$	N-elements vector of unknowns (quantities to be solved by numerical computation)

x_n^*	n-th unknown (quantity to be solved by numerical computation)
$\mathbf{y}$	N-elements vector of correction for unknowns $\mathbf{x}$
y_n	Correction to n-th unknown x_n
Γ	Euler's gamma function
σ_k^2, σ_n^2	Variance of k-th measurement and n-th unknown
ϕ	Function to be minimized in the co-ordination algorithm

Superscripts

T	Transposed matrix

Figure Captions

Table Captions

1 Introduction

1.1 Introduction to syngas production

In the twentieth century fossil fuels played extremely significant role, being the driving force for the development and stimulation global economies. Oil, of which the first commercial extraction is dated to 1859, rapidly dominated the transportation energy market and the chemical industry, becoming the supplier of raw material for the majority of the organic chemicals produced. The rapid development of the world economy with the leading growth in the Asian markets increased the global demand for accessible and cheap energy sources. This trend is especially immediate in the context of the depletion of extractable oil reserves. Moreover, the fact that the geographical location of 40% of the world's oil reserves lies in politically unstable regions of the Middle East is of concern for assuring the security of fuel supply. The big “oil shocks” caused by the Suez Crisis (1956), the OPEC oil embargo related to the Arab-Israeli war (1973), the Iranian Revolution and overthrow of the Shah (1979), the Gulf War (1991) and the oil price spike (2008) arise questions about the future of oil in the energy market.

Therefore, the significance of alternate fuels and emerging technologies providing novel solutions for increasing energy demand is one of the most urgent issues of modern society. One of the proposed fuels supplementary to oil is natural gas, with world wide reserves estimated at 187.1 trillion m^3 (2014) [1]. Therefore, to promote and economize its applications, proper pathways to enable transportation and fluent incorporation to energy systems are necessary.

1.1.1 Syngas production methodology

The chemical conversion of methane and higher hydrocarbons, which are most primal components in natural gas, to synthesis gas containing H_2, CO and CO_2 are: steam reforming, dry reforming and partial oxidation. The general ideas, assumptions and applications of those

processes will be introduced in the present section. There is also syngas productions considered from the gasification of biomass and coal lately. However, it will not be explained in this thesis, because it is not the major concern.

1.1.1.1 Steam reforming reaction

The steam reforming process used for hydrocarbon fuel is the most popular process adopted for syngas production. It is widely used in the industrial applications and is considered to be the largest source of produced hydrogen and synthesis gas (syngas) [2]. The steam reforming process can dedicate to other productions process of ammonia and methanol [3]. It is the gas-phase conversion of energy carrier, of which the predominant chemical composition is described by $C_xH_yO_z$ according to the formula provided in the following [4]:

$$C_xH_yO_z + (x-z)H_2O \rightarrow xCO + \left(x - z + \frac{y}{2}\right)H_2 \tag{1.1}$$

The mixture of the product from the reaction is known as reformate. The reaction is endothermic and requires a supply of heat for maintaining the reforming process [4].

This methodology is used for the syngas production from various type of fuel, for example, methane [5], heavy hydrocarbon fuels such as ethane [6–10], propane [7,8,11–13] and butane [6,8,14,15] and etc. The syngas production from hydrocarbon is essentially important since the syngas is subsequently devoted to the basis of numerous chemical products and their industrial values are extensively remarkable [8]. The steam reforming of heavy hydrocarbon fuels in the production does not exist by itself and it can co-exist with numerous reaction mechanisms, dry reforming, oxidative reforming mechanisms. This is due to complex reaction steps. Thus, the development of an active catalyst to assist the reaction path and thus the process is primarily essential issue due to the occurrence of reaction hazards and catalytic deactivation due to sulphur poisoning, coking and etc.

The implementation of the steam reforming process has also been considered for the reforming of biogas [16,17]. The steam reforming of CO_2-rich gas such as biogas involves other reaction mechanisms, the so-called dry reforming ones, because CO_2 is a congenital

reforming agent. The involvement of other reaction kinetics makes the syngas production process complicated. This will be introduced and explained later.

There are also attempts of the syngas production by means of steam reforming carried out on other types of fuel and those attempts are summarized in the following articles: phenol [18], methanol [19–22], ethanol [23,24], bio-ethanol [25], diesel [26], biodiesel by-product glycerol [27,28] and bio-oil [29] and etc. Dealing with this type of fuel in the steam reforming process easily invites a coking problem.

Most commonly, the steam reforming process is thus used for synthesis gas production from natural gas, in which a concentration of methane is predominant. The steam reforming reaction of methane and simultaneously occurring water-gas-shift reaction are indicated in the following formula:

Steam reforming of methane: $CH_4+H_2O \rightarrow 3H_2+CO$, $\Delta H^0 = 206.2$ kJ mol^{-1} (1.2)

Water-gas-shift reaction: $CO+H_2O \rightarrow H_2+CO_2$, $\Delta H^0 = -41.2$ kJ mol^{-1} (1.3)

By the summary, total reaction process can be expressed as:

$$CH_4+2H_2O \rightarrow 4H_2+CO_2 \quad (1.4)$$

The steam reforming reaction of methane is endothermic and the water-gas-shift reaction is mildly exothermic.

The steam reforming of methane also risks the reaction hazards as mentioned earlier; sulphur poisoning and carbon formation on the catalyst surface for active reaction sites. These issues will be explained in Section 1.1.1.2. The efforts are undertaken to develop the catalytic materials that preclude the operation failure of reactor connected with those drawbacks. The investigation of the reaction kinetics of the methane/steam reforming involves also research on finding an appropriate catalyst for this reaction. This is partially focus of this thesis, which will be addressed later. There are also attempts to reduce the operating temperature of the methane/steam reforming process as summarized by Angeli et al. [30].

The kinetics of the steam reforming reaction has been widely and heavily studied over the years. Among such studies, Ni catalyst is the most attention-paid material due to the economical competitiveness and activity to promote the reaction [31], and numerous studies have been carried out to reveal the reaction mechanism [32] and develop reactor designs [33–35]. Since investigations on the reaction kinetics of the steam reforming reaction on Ni catalyst have became a major interest, it is generally believed that the reaction process is dominated by the rate-determining steps. It is agreed that the reaction involves initial adsorption and decomposition of methane to "CH_x ($0<x<4$)" species. This can be promoted by a reaction with the gas phase of H_2O or adsorbed oxygen species, though disagreement can be found over the specifics of the reaction mechanism and the nature of the rate-determining steps by methane chemisorption, surface reactions, gas phase reactions and/or the desorption of the product [3]. The first detailed study of this reaction mechanism can be found in the work of Bodrov et al [36]. Xu and Froment have developed Langmuir-Hinshelwood's model, which is known as the classic mechanism of the steam reforming reaction [37]. They proposed that the rate-determining step is a reaction of absorbed carbon and oxygen species, and therefore reaction rate depends on partial pressures of water, methane and hydrogen. Recent works have mentioned that the rate-determining step of the process is dissociative adsorption of methane [32,38]. However, this modelling assumption is valid and constrained when the empirical expression is derived on the basis of assumed elementary steps. The detailed atomic mechanism of the steam reforming of methane is still not revealed to compensate to the perfection of Langmuir-Hinshelwood model. This means that the agreement of experimental data is not a definite proof of identifying the reaction mechanism [39]. Further work must be devoted to reveal the mechanism of the steam reforming reaction. Nowadays, the reaction rate of the methane/steam reforming reaction derived from the simplified Hinshelwood model or power law expression derived from data fitting are popularly used. More details are found in Section 3.1.

.

1.1.1.2 Dry reforming reaction

Dry reforming is an alternative methodology for syngas production instead of the steam reforming process. The following is the exemplary of drying reforming of methane indicated:

Dry reforming of methane: $CH_4+CO_2 \rightarrow 2H_2+2CO$, $\Delta H^0 = 247$ kJ mol^{-1} (1.5)

As a product of the reaction, hydrogen is produced with CO in the presence of CO_2. This further involves a water-gas-shift reaction and may cause a steam reforming reaction of methane as well.

Reaction (1.5) can occur in the presence of carbon dioxide with hydrocarbon fuel in the reaction site. The reaction is a highly endothermic and rate-determining step as the steam reforming reaction is. The heat and mass transfer limitation that can be involved in the reaction process can be treated equivalently in the same manner as the steam reforming is [3]. Several attempts can be found for the investigation of the reaction over metal and novel metal catalysts [40–50]. Ni catalyst seems to be effective catalytic components for this reaction in chemical activation [50–52], though the carbon deposition seems to be more influential on their chemical activation than that noble metals possess [40]. The reaction kinetics of the drying reforming process is studied [53–56] though the number of reported investigations is very limited compared to that of the steam reforming process [3].

The first detailed study concerning the kinetic of the methane/steam reforming on a Ni foil-shaped catalyst was prepared by the group of Bodrov, Apel'baum and Temkin [36]. It was basically a study of the methane/steam reforming process. A dry reforming reaction, however, can occur in a methane/steam reforming process via water-gas-shift reaction. Later Bodrov and Apel'baum found that the conversion rate fitted to the expression [57]. Wei and Iglesia have studied the mechanism of dry reforming of methane over various types of catalysts [32]. They stated that the reaction mechanism of the dry reforming process is essentially based on the decomposition mechanism of methane and it is equivalent to those of the steam reforming reaction and carbon decomposition. Either of the reactions can primarily occur following the equilibrium condition in the reaction site where the reaction can occur. Nishino and Szmyd carried out the modelling of biogas reforming followed this statement [58]. They have implicitly expressed the dry reforming of methane with the compensation of the steam reforming and reverse water-gas-shift reaction. Brus et al. took this statement and brought it to the analytical investigation of dry reforming using model biogas, in which the chemical composition of methane and carbon dioxide was varied [59]. They developed a simplified reaction kinetic model for biogas reforming and found good agreement with their experimental results.

This reforming process is often considered for the syngas production from biogas, mostly consisted of methane and carbon dioxide depending on the raw material used and the production conditions. Inexpensive catalytic material of Ni is often used for the dry reforming of biogas. It should be noted that there are two significant negative factors in using Ni catalyst that degrades the production efficiency of syngas and the deterioration of catalytic material; carbon deposition and the sulphur poisoning on metal and noble metal catalysts are the problems to be solved in addition to addressing the key role of dry reforming. Carbon deposition occurs over the surface of the catalyst on which the active reaction sites is kept. It is often observed in the experimentation that Ni apparently cause the deposition of carbon over the reaction site. Brus et al mentioned that the operating condition for the reactor must be carefully chosen to have a carbon free regime that can ensure the prevention of carbon deposition over the catalytic material from the thermodynamic point of view. In this way, the proposed solution is the addition of water to the reactor, which promotes steam reforming of methane in biogas together with the dry reforming [60]. There are also attempts of material development of the catalyst to avoid the carbon formation. Valenti et al suggested to add a small portion of vanadium to a Ni/Al_2O_3 catalyst to avoid the formation of the aluminate spinel phase [61].

For biogas reforming over a Ni catalyst in the presence of H_2S, often highly composed in biogas, the active catalytic reaction site on the Ni catalyst is blocked by the sulphur sorption [62]. This deactivates the catalyst and is known as the most important root cause of sulphur poisoning. This chemisorption of sulphur on the Ni catalyst is considered as reversible process [63]. However, sulphur poisoning increases exponentially over the time with the reforming agents and this influences the catalytic activity of the material, of which the active surface is covered with the sulphur sorption [62]. Though its convergence at the saturated condition depends on the operating temperature, type of catalyst and partial pressure of the reactants. Catalysts with lower metal loading lose activity at a faster rate compared to catalysts with higher metal loading [64]. There is researches that report attempts on avoiding the sulphur poison problems. Quincoces et al investigated the dry reforming of methane over Ni/Al_2O_3 with the addition of small amount of Molybdenum (Mo). They found that the addition of Mo increased the resistance of the material to both carbon deposition and sulphur poisoning slightly [51]. For developing the Ni-based catalyst that can ensure catalytic activity in biogas reforming, the selection of appropriate promoter is one way solving the sulphur

poisoning issues. Adopting a bimetallic catalyst configuration such as Ni-Co is also considered for solving the problem connected with the sulphur poisoning [27].

As was mentioned earlier, that the dry reforming process may involve a reverse water-gas shift reaction and further the steam reforming reaction. The entire process becomes also more complicated. To properly address the problem of the fuel reforming process and optimize the operating condition are significant issues from the viewpoint of thermal engineering. For this purpose, the reaction kinetics of both steam and dry reforming reactions must be well studied.

1.1.1.3 Partial oxidation reaction

Partial oxidation is another way for syngas production. Partial oxidation reaction of methane occurs in the presence of oxygen. The reaction is slightly exothermic. The partial oxidation proceeds at high temperature (over 1100 ^{o}C), it is a so called thermal partial oxidation reaction. Uneconomical operating conditions, at a high temperature, makes this methodology difficult to be commercialised, thus, instead, catalytically promoting the reaction process was considered, the so-called Catalytic Partial Oxidation (CPOX) reaction.

Investigations on partial oxidation reaction mechanisms have started in the middle of the XX century. However the problems connected the carbon formation in the reaction process, the difficultly of choosing operating conditions, restrictions in gas phase reaction mechanism and other hazards abandoned the development of partial oxidation technology, though it potentially could exhibit advantageous characteristics that steam reforming does not own hereditary [3], [65] . Several decades ago, activity related this topic gradually came back to the development due to the development of catalytic stabilities towards the temperature degradation and inhabitation to the carbon formation problem at a lower temperature [66–68]. However, Enger stated that the day of syngas production by means of partial oxidation mechanism is still far to be commercialized, though the catalyst development came to pre-commercialization phase [66].

Among metal and noble metal catalytic material, Ni and Co is often used as a catalyst for catalytic partial oxidation reactions among cooper and ferrite metals and iridium, palladium, platinum, rhodium and ruthenium noble metals [66]. Ni based catalysts seem to be the most

popularly used catalysts, since it is believed that this enables the reaction reach to equilibrium conditions. Cobalt is the one that can exhibit active catalytic performance, yielding syngas production close to equilibrium conditions, considering the partial oxidation of methane at lower temperature, since high temperature operation causes large deactivation compared to nickel based catalysts [69].

The addition of promoters are considered a practical solution for increasing syngas production efficiency and bimetalic catalyst configuration is as well considered; All of those attempts reduce the risk of carbon formation in the active reaction site and to decrease operating temperatures.

The partial oxidation is mildly exothermic and very fast reaction. This enables the CPOX system to be more practical and beneficial in the light of building reactor plants, which are energy-efficient and wide range in scale. The partial oxidation reaction is denoted in the following formula:

$$CH_4 + \frac{1}{2}O_2 \rightarrow CO + 2H_2, \ \Delta H^0 = -36 \text{ kJ mol}^{-1} \tag{1.6}$$

The reaction occurs at the condition in which the amount of oxygen is insufficient to decompose the entire amount of methane supplied. Prettre et al found that an over-supply of oxygen to methane results in the complete oxidation of methane [70]:

$$CH_4 + 2O_2 \rightarrow CO_2 + 2H_2O, \ \Delta H^0 = -803 \text{ kJ mol}^{-1} \tag{1.7}$$

York et al. categorized the reaction kinetics of catalytic partial oxidation into two groups: Combustion and Reforming Reaction (CRR) Mechanism and Direct Partial Oxidation (DPO) Mechanism [3]. The CRR mechanism is a macroscopic distinction of the processes involving the total oxidation reaction found in the observation first done by Prettre et al; the initial stage of the syngas production process is dominated by fast and exothermic total oxidation reaction and later on the product of the reaction reacts with the leftover of methane to produce the syngas via the steam and dry reforming reaction. The steam and dry reforming reactions take place in the downstream of the process with the occurrence of the water-gas-shift reaction.

The yields of syngas, however, can not be predicted precisely from this observation. The DPO mechanism was found throughout the investigation done by Hickman and co-workers [71–75]. This mechanism is based on microscopic observation in the process; surface reactions that can occur on the reaction site of the catalyst, which heavily depending on the used metals or noble metals, is well taken into consideration [3].

The CPOX process can be affected by the carbon formation over the active surface area of a used catalyst. The unfavourable ratio of hydrogen-to-carbon monoxide can result in this particular problem. Increasing selectivity of hydrogen on the reaction site (carbon monoxide dominates hydrogen among the products of the process) is likely keen for preventing the carbon formation.

Devotion in the catalyst development can be noticeably found on this research topic. Investigating the reaction kinetics on those catalysts is also important, however, this process is faster and the conditioning of the operating setup seems to be more significant once the development reaches the commercialisation phase.

1.1.2 Application to the power generation sector

Syngas production from fossil fuel is usually applied in two different fields of industry: the chemical and the power generation sectors. As was mentioned earlier, syngas is an important source for numerous chemical productions. On the other hand, the syngas production becomes more significant today in light of power generation applications.

Nowadays, fossil fuel is the most privileged source of energy to provide the electricity. In the current situation, the largest amount of electricity is generated from the large-scale power sectors, in which natural gas, coal and oil are directly used for power generation driving steam turbines and gas turbines. With the increase of power demand and increased requirements on minimization of the environmental impacts, the efficient way to use the fossil fuel has been realized with combined thermal cycles. A most commonly known combined cycle is Gas Turbine Combined Cycle (GTCC) with a steam turbine, which records over 50% of thermal efficiency (based on the lower heating value: LHV). In the development of social infrastructure and the diversification of power demands, independently from the large power

system, attention on the development of distributed power generation systems is being paid to increase energy security and to answer the complex demands of network. The advantage of a distributed network system is that it can use the already-existing infrastructure such as city-gas pipelines and etc. They can also use the potential benefits of fuel cells (FC), which are considered as the most expected and highly efficient power source.

Fuel cells are electrochemical devices that can convert the chemical potential of fuel directly into electricity. Direct conversion of fuel to electricity thus possesses higher energy conversion efficiency than ordinary thermal cycles can achieve. Fuel cells are configured with electrolyte, anode electrode (fuel side electrode) and cathode electrode (air side electrode). They can generate electrical power in the principle of exchanging ions throughout the electrolyte, which usually is sandwiched by two different electrodes. Fuel cells are generally categorized into; polymer electrode fuel cells (PEFCs) (also known as polymer electrode membrane fuel cells: PEMFCs), molten carbonate fuel cells (MCFCs) and solid oxide fuel cells (SOFCs), depending on the type of material used to transport ion from one side to the other. PEFCs exchange proton throughout the polymer membrane from the anodic side to the cathode side. Nafion is the most often adopted polymer material performing proton conductivity at lower temperature (80-100 ^{o}C), though Nafion has a limitation in increasing its operating temperature due to its volatilization. It is usually difficult to ionize hydrogen and oxygen in this temperature at the reaction site over the electrodes. An expensive noble metal catalyst is thus used. Thus, syngas technically cannot be used to avoid carbon monoxide poisoning on the catalyst. Use of syngas for the PEFCs requires the separation of carbon monoxide. The PEFCs are often adopted for mobile purposes such as automobiles. The MCFCs and SOFCs on the other hand, have a different principle of transporting ions compared to the electrochemical principle of PEFCs. The MCFCs generate electricity in the exchange of negative carbonate ions from cathode to anode through lithium potassium carbonate salt as an electrolyte. For performing ion conductivity at the electrolyte, the MCFC requires a high operating temperature (around 650 ^{o}C). In the case of SOFCs, they allows for the transfer of oxygen ions from the cathode side to the anode side throughout the solid oxide electrolyte. This requires high operating temperature (700-1000 ^{o}C) to perform the ion conductivity of solid oxide electrolytes. An advantage of the MCFCs and SOFCs is related to this electrochemical principle that allows for the use of carbon monoxide as fuel, the so-called fuel flexibility. With this fuel flexibility, the MCFCs are SOFCs can readily incorporate the syngas for power generation at a high-energy conversion rate.

Hydrogen and syngas production by means of the steam reforming process can greatly incorporate fuel cells for their installations in the distributed grid network, and is literally a key solution for introducing the commercialization phase of fuel cell technologies.

1.2 Solid Oxide Fuel Cells

The Solid Oxide Fuel Cells (SOFCs) systems, with their high operating temperature, fuel flexibility [76] and simplicity of connection with city-gas infrastructures, advertise their potential and promote themselves to have numerous application possibilities in different sectors of industries. As the devices, which directly convert the chemical energy of fuel into electricity, they have the potential to be economically competitive technology that can provide higher electrical efficiency in comparison to the commonly used solutions. The high efficiency is related with the principle of direct energy conversion with small losses and is supported by the high operating temperature of SOFCs. Exemplary applications include large scale projects such as cogeneration power plants [77], as well as smaller units applied to refrigerated tracks, hybrid ships or remote power generators [78].

The original idea of SOFC, the basic principle and materials were proposed by Nernst and his colleagues at the end of 19^{th} century and the first application is dated from the beginning of the 1960s, when NASA used SOFC on board of the Apollo space shuttle.

The principle of operation of Fuel Cells is similar to batteries with the combination of electrochemical reactions in order to generate electricity without the direct combustion of fuel as an intermediate step. Contrary to batteries, the power production in the fuel cells is continued as long as the supply of fuel and oxidant is provided.

Fuel cells in general consist of two porous ceramic electrodes (a cathode and an anode), which are separated by a solid ceramic electrolyte layer. An electrolyte layer, oxygen-ion conductor, is typically solid oxide such as Yttria-Stabilized Zirconia (YSZ) [79]. An outline and working principle of a Solid Oxide Fuel Cell in tubular configuration are shown in Fig. 1.1.

The general electrochemical process dominant in SOFC is the oxidation of hydrogen via two half-cell reactions [80]:

Anode reaction: $H_2+O^{2-} \rightarrow H_2O+2e^-$ (1.8)

Cathode reaction: $\frac{1}{2}O_2+2e^- \rightarrow O^{2-}$ (1.9)

The overall reaction in the cell is summarized as:

Overall cell reaction: $H_2+\frac{1}{2}O_2 \rightarrow H_2O$ (1.10)

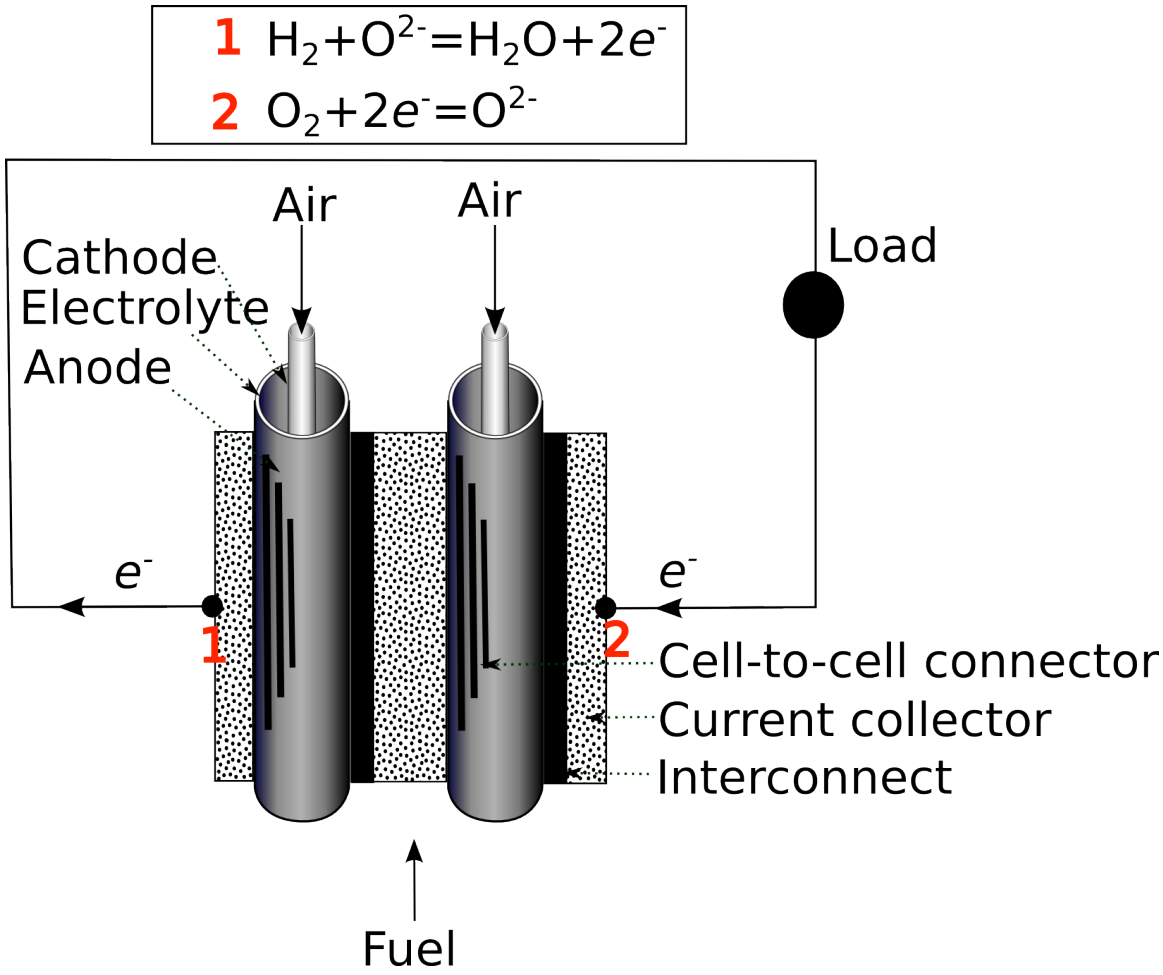

Figure 1.1 Schematic configuration of a Solid Oxide Fuel Cell in the tubular configuration and its working principle

SOFC provides only water and heat as by-products of the electrochemical reactions, makes it clean and environmentally friendly power source. However, if the cell is supplied by the fuel consisting carbon oxide and hydrocarbons (exemplary methane), the additional reactions occurs on anode side:

$$CO + O^{2-} \rightarrow CO_2 + 2e^- \tag{1.11}$$

$$\frac{1}{2}CH_4 + 2O^{2-} \rightarrow H_2O + \frac{1}{2}CO_2 + 4e^- \tag{1.12}$$

The maximum voltage provided by the preceding reactions is limited and with increasing current it significantly decreases [81]. In order to increase the voltage for the industrial application of SOFC, singular cells are connected into a cell stack by an interconnect.

The development of SOFC Systems is gradually shifting to the phase of initial commercialization (in the case of small-scale systems such as for residential use). Though there are still issues to overcome for commercialization of the larger-scale systems, which will take an important role in grid network. Current research on the topic is being carried out by both the industrial and academic sectors. Concerning commercial research and development projects, exemplary are the SOFC tubular cells for high efficiency hybrid power generation systems by Mitsubishi Hitachi Power Systems [82], SOFC for auxiliary units in automobiles and tractor-trailers developed by Delphi Automotive Systems [83,84].

Generally, SOFC systems research is focused on improving the properties of materials [85] and reducing start-up time particular for mobile applications [86]. The works are coried out also in the topic of the lower-temperature systems (at temperature 600 ^{o}C). The high operating temperatures of SOFC causes the material engineering issues, which have to be properly solved in order to provide stable operation. Lowering temperatures, lowers also the cost of materials and the start-up time [87,88]. The further investigated issue is improving the fuel flexibility of SOFCs to enhance their competitiveness. Although systems can be operated on the various hydrocarbons, the SOFC stacks usually relay on the external fuel processing in the present implementations.

1.3 Fuel Processing for Solid Oxide Fuel Cell

Low-temperature, proton-exchange membrane (PEM) fuel cells have very high requirements concerning the quality and purity of the supplied hydrogen. Therefore, in order to fuel them by hydrocarbons, a complex external reforming system, consisting of a fuel reformer, a shift reactor and clean-up devices, is necessary prior to the fuel cell [89].

On the other hand, the high operating temperature of the SOFC cell eliminates the necessity of the external heat source (in Fig. 1.2A) for the strongly endothermic reforming reaction. The high-temperature heat, which is a buy-product of SOFC (except for electrical power), is resulted from their elevated operating temperature and can be used directly to maintain reforming reactions. Regarding this advantage, coupling of the reforming process with SOFCs is a beneficial solution for hydrogen production in fuel cell technology and high exergy efficiency. Internal reforming of the fuel can be achieved by the indirect method using a separated reforming system installed within SOFC stack (in Fig. 1.2C) or by the internal direct reforming process which is conducted directly on the anode (in Fig. 1.2B). Internal reforming can be also constituted from both direct and indirect configuration, when part of the hydrocarbons is converted to synthesis gas by the separate module within the fuel cell with the balance of the fuel reforming occurring directly on the anode.

The internal reforming system is beneficial compared with the external configuration because of the great increase of the overall efficiency of the system compared with low-temperature fuel cells. An additional advantage is reducing the complexity of the system and hence reducing the initial and operational cost [78]. Moreover, the excess heat, not used in the reforming system, can be further applied for the gas turbine and finally in the combined heat and power (CHP) system. The maximum utilization of the heat induces further increases of system efficiency. Figure 1.3. shows a exemplary heat flow in the advanced internally reforming SOFC system with adsorption of heat by reforming. Regarding all of preceding points, many recent studies are focused on fuel reforming issues, which is a topic vital for the development of SOFC and their industrial applications.

The great fuel flexibility of SOFC and bigger impurities flexibility than other types of fuel cells [89], gives the possibility to use fuels as natural gas, biogas, vegetable matter and landfill gas or gasified coal. The large variety of possible fuel choices with the modular nature

of SOFC, makes them suited for both small-scale applications, stand-alone systems in remote areas and larger CHP and hybrid gas turbine systems.

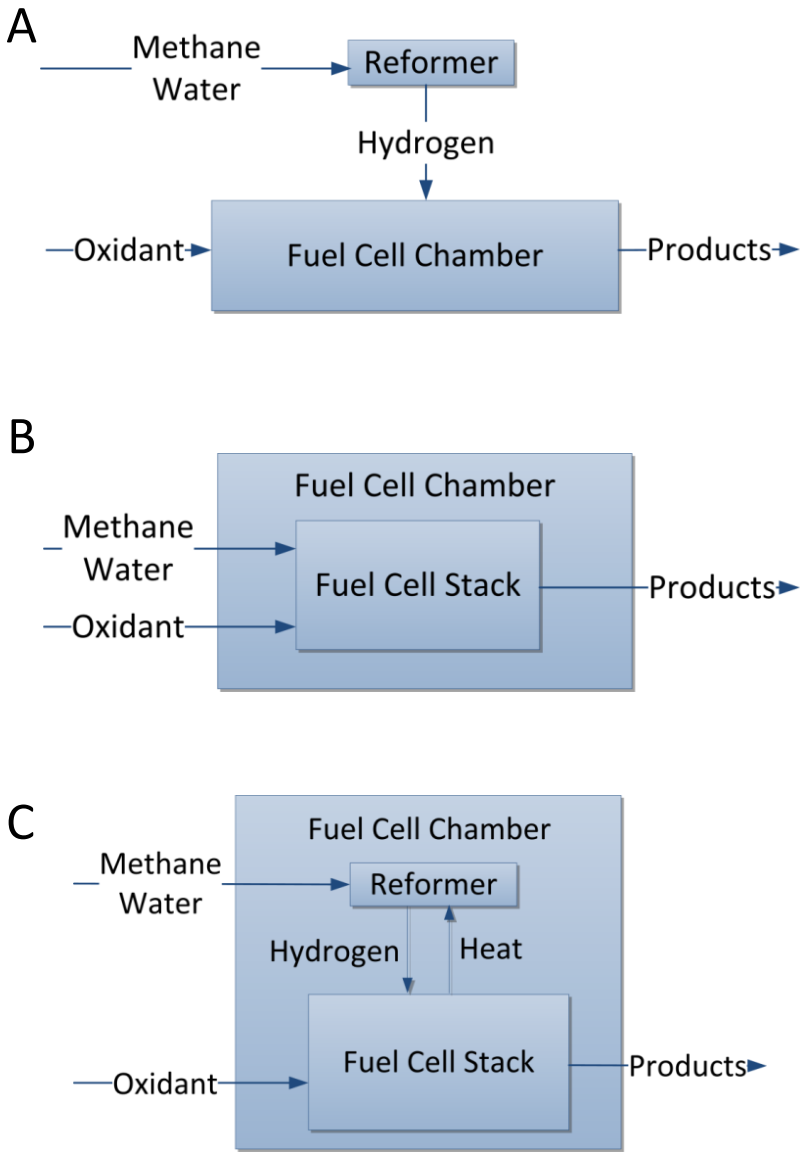

Figure 1.2 Fuel processing for Fuel Cell: A) External Reforming System, B) Direct Internal Reforming System, and C) Indirect Internal Reforming System

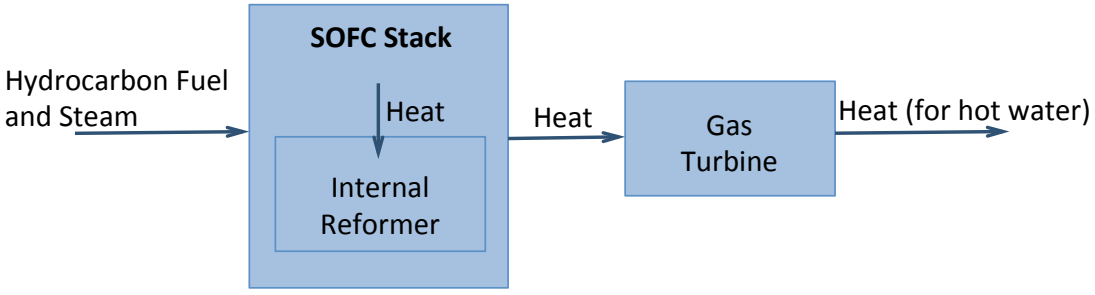

Figure 1.3 Heat flow in advanced system of SOFC with internal reforming and by-product heat utilization

Despite many advantages several issues have to be solved in order to couple of fuel reforming module and SOFC. A poorly designed system can suffer from the problems of deactivation and loss in cell performance, material failures and reduced cell durability. In the case of the internal reforming, hydrocarbon pyrolysis can occur and, as a result, the carbon deposition can affect the catalytic material. Methane and higher hydrocarbon steam reforming is a fast, highly endothermic reaction and when it is coupled with slow, exothermic fuel cell reactions, there can be potential instability. Additionally, during the start-up condition the reforming reactions can not be thermally self-maintained, because of the heat from stack is not sufficient to supply the fuel reforming requirements [89].

The direct internal reforming system can potentially assure the highest possible efficiency of the overall system by reducing the necessary energy transmission steps and the complexity of design [90]. However, the material requirements and thermodynamic management of the anode reaction are crucial issues. The anode composite has to fulfil the following points: it must to have catalytic properties for the reforming reaction, it has to be electrocatalyst, supporting the electrochemical oxidation of hydrogen and carbon monoxide to water and carbon dioxide and has to have proper electrical conduciveness. One of the major issues in this system configuration is the rapid cooling effect appearing in the inlet of the cell, which generates the step temperature gradient. The inhomogeneous temperature distribution along the cell is difficult to control and can cause the cracking of anode and electrolyte. In developing the internal direct reforming system the major challenge currently is the development and investigation focused on the material issues.

The indirect internal reforming system on the other hand, where the hydrogen production is conducted outside the cell, is integrated within the SOFC stack upstream of the anode. This configuration, despite smaller efficiency and bigger complexity than direct reforming, has a number of advantages. The system is easy to be thermodynamically controlled from both sides of the SOFC anode and the reformer at the point of the temperature gradient. The catalyst used in the reformer can be more dispersed compared to the SOFC anode, what is beneficial from the point of view of carbon deposition [89]. In this configuration it is also possible to use other than nickel catalyst on the fuel reforming side, which do not fulfil the SOFC anode requirements for electrical conductivity.

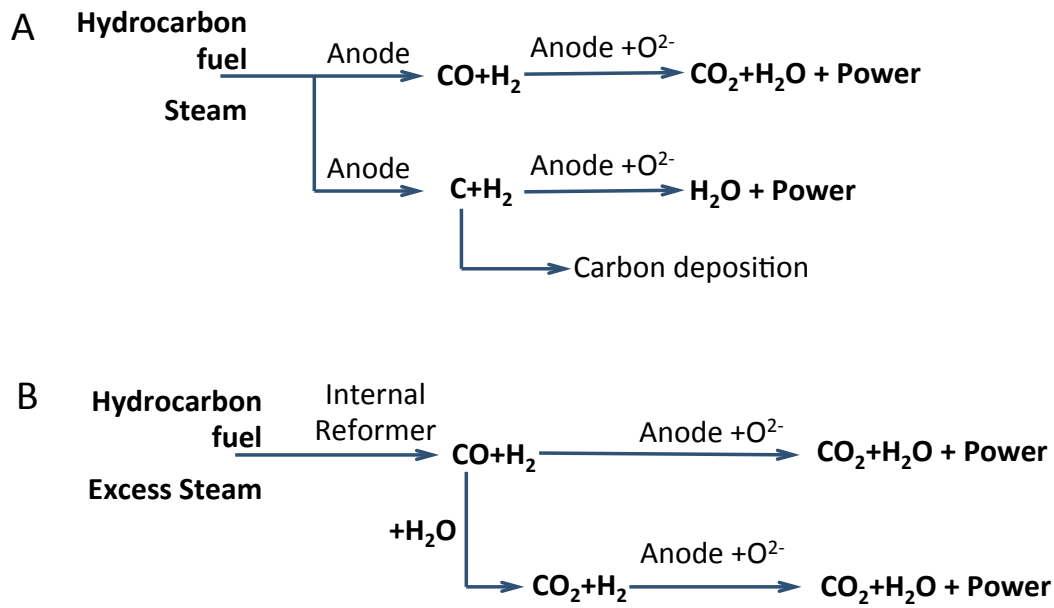

Figure 1.4 Possible reaction pathways in A) SOFC with direct internal reforming system B) indirect reforming system coupled with SOFC

The potential reaction pathways deriving the effects observed in the internal direct and indirect reforming systems are presented in Fig. 1.4. Generally, when the hydrocarbons are used to directly fuel the SOFC stack, pre-reforming of the fuel to the form when only methane is remaining is necessary. Fuelling SOFC with higher hydrocarbons would cause the carbon deposition in the stack because of the susceptibility of the anode to the pyrolysis of higher hydrocarbons. The build-up of carbon on the anode leads to the deactivation of the cell [91–93]. The probability of the carbon deposition is especially high in the low stem-to-carbon ratio [94], on the other hand, when the steam partial pressure is high, sintering of nickel anode particles can occur. This later causes a loss in the cell performance because of the decrease of the catalytic activity of the anode [95]. Therefore, in the case of SOFC development the biggest impact is on the methane/steam reforming kinetic and this process will be discussed within the scope of this thesis.

1.4 Models of SOFC coupled with reforming of fuel

The models of SOFC are widely used for the various purposes. Generally numerical models, as in many others fields of science, provides an inexpensive and fast method for testing new engineering designs and configurations of a stack [96–100] and for the quantification of power systems incorporating a SOFC stack as one of the compounds [101–109]. The models

are often used for the interpretation of experimental results [110] and determining the interest area for conducting future research [111]. In the case of a SOFC system it is difficult to measure the specific conditions for the temperature and distribution of the chemical species along the cells; the modelling techniques are indispensable tool to research those issues and predict the occurrence of hotspots [112–114] and the determination of optimal operation conditions and control strategies [115,116].

The modelling of all phenomena, which are influential for the behaviour of the SOFC stack, is very complex and numerical models are robust and require high computational power. Therefore, the usually proposed models focus on one or several issues and can be divided by their main interest into three general categories: micro models, cell/stack models and system models [39]. Properties of every approach with the exemplary studies are summarized in Table1.1.

The large number of SOFC modelling studies includes internal steam reforming in the cell model or external reformer in the configuration of the system. Reforming reaction is often the determining factor influencing the local and overall performance of the SOFC system, especially when the fuel contains a noteworthy amount of methane. Especially in the case of modelling the internal reforming configuration, the occurring reforming significantly changes the local temperature gradient and composition of the flow. Therefore, the kinetic of the methane reforming process should be accurately addressed in order to provide the compatibility between numerical simulation and experimental observations. The modelling approaches presented in various studies are summarized in Table 1.2. Many incompatibilities and divergences between assumed reaction rates have been reported. Several studies presented the simplified approach to deliberate the reforming process: equilibrium conditions were assumed [117–120] or artificial models were imposed. The example of artificial model proposed for describing reforming in SOFC was the one based on the assumption that in every consecutive finite element used for numerical modelling, the 75% of the remaining methane was reformed [121]. However, any of those approaches does not reflect the real kinetic of the process and should be used only as an approximation in the initial calculations. Some of the system models use the thermodynamic description and equilibrium conditions for internal reforming instead of the kinetic equations [120,122]. Although several models assume a simplified approach of thermodynamic equilibrium, more detailed and correct approaches are based on the kinetic expressions. However, among the models incorporating

the kinetic equation of methane/steam reforming a variety of assumed reaction kinetics can be observed. The most typical used kinetic equations are those derived by Achenbach and Riensche [123] and Lehnert et al. [110,124]. Unfortunately both of them are subjected to considerable inadequacies. Achenbach and Riensche kinetic equation was derived for the catalyst characterized by the relatively small, in the context of SOFC materials, 20% nickel content weight percentage (on ZrO_2) and experimentation was conducted on the thick anode that did not fulfil the electrochemical requirements for the SOFCs. This approach assumes first order dependency on methane partial pressure and no influence of partial pressure of steam for the reaction rate. It is consistent with the values of the reaction orders derived by Achenbach and Riensche: one for the reaction order with respect to the partial pressure of the methane and zero for the reaction order with respect to steam partial pressure [123]. Compared with other models, it gives a slightly higher than average results for the reaction rate [39]. Lehnert et al. expression on the other hand, assumes first order dependencies for both methane and water, what is rarely visible in other experimental studies and derived reaction kinetics [39].

Nadal et al. [100], who studied charge, mass and heat transfer interactions in solid oxide fuel cells operated with different fuel gases proposed a sensitivity analysis conducted for various reforming kinetic expressions implemented in the SOFC model. They investigated the influence of the reforming equation defined by the equilibrium equation, Achenbach kinetic model [123], Ahmed and Foger kinetic model [125], Leinfelder kinetic model [126] and Drescher kinetic model [127] for various operating parameters of SOFC. The results they obtained are presented in Fig. 1.5. Noticeable differences and the considerable influence for current density and Nernst voltage distribution, methane, hydrogen and carbon monoxide distribution, temperature distribution of IEA 2 gas and temperature difference between the predicted temperature difference for IEA1 and IEA2 gases are observed in all cases. IEA1 and IEA2 gases were defined by the International Energy Agency respectively for an explicit investigation of the impact of varying model constants on the electrochemical performance and for the determination of the coherences when also internal reforming reactions take place. Among the general conclusions it can be noted, that the faster methane/steam reforming kinetic results in a stronger cooling effect. This reaction is counteracted by higher temperatures in the latter parts of the cell caused by the higher current density values at the cell inlet.

Among the studies focused on the microstructure model of fuel cell, some incorporate reforming kinetic models based on the complete set of all 42 elementary reactions consisting on the process [128]. Every reaction is described by a separate kinetic expression. This method depends on the accuracy of the modelling of anode microstructure and gas diffusion [39]. The disadvantage of this methodology is the fact that kinetic data sets are taken from a variety of sources and have to be modified by optimizing procedures to assure thermodynamic consistency. In the case of complicated optimization problems and modelling of the system with an SOFC unit this approach is difficult to introduce because of its high computer power demand.

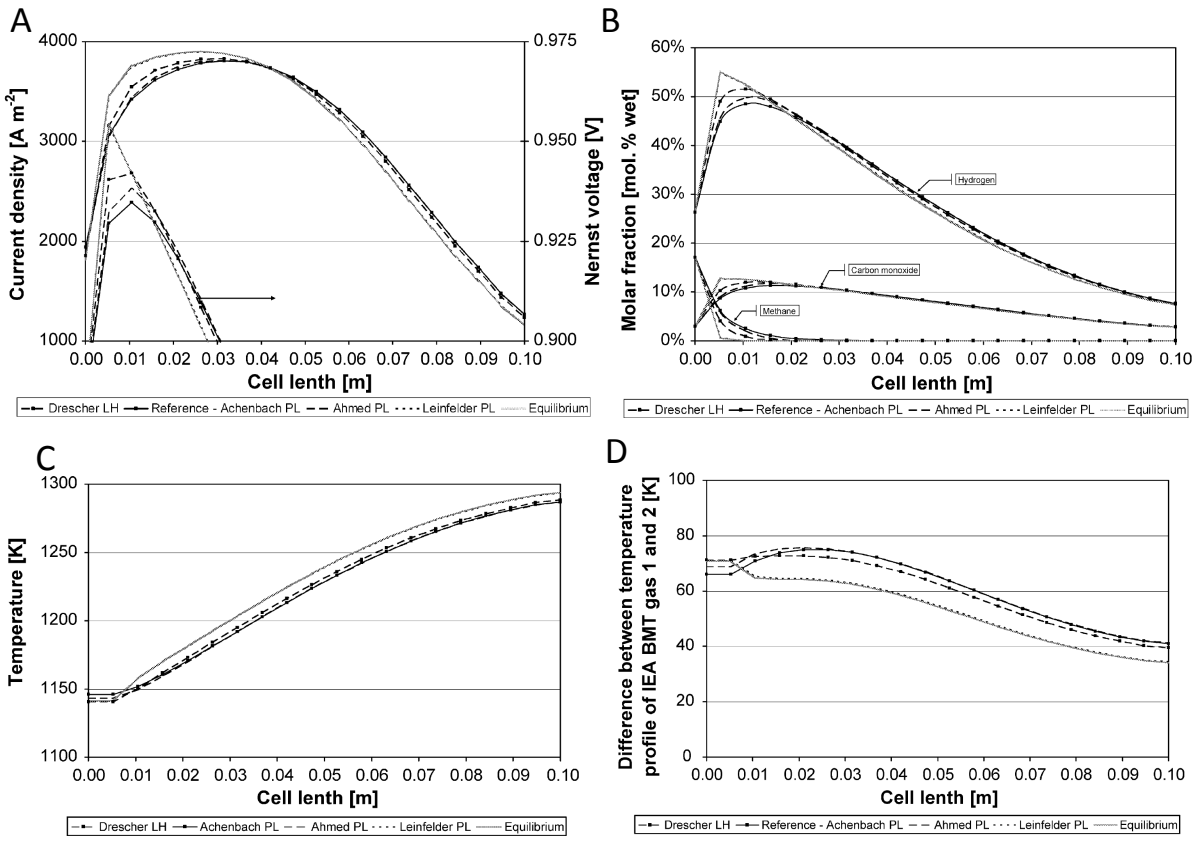

Figure 1.5 Influence of the assumed reaction kinetic model for A) current density and Nernst voltage distribution, B) methane, hydrogen and carbon monoxide distribution, C) temperature distribution of IEA 2 gas D) temperature difference between the predicted temperature difference for IEA1 and IEA2 gases (reproduced from [100])

Table 1.1 Comparison of numerical models for SOFC

	Micro model	Cell/stack model	System model
Principle	Detailed analysis of physicochemical phenomena	General model of single cell or stack of cells	Analysis of performance in the complex system
Application	Material research, Microstructure optimization	Concentration and temperature profiles, Identify hotspots and potential carbon deposition	Design and optimization of the systems including SOFC
Complexity of the model	One dimension; detailed description including mass and heat transfer in porous electrodes and electrical conduction	Two or Three dimension; simplified description of electrodes and electrolyte; sometimes include microstructure	Zero or One dimension; high simplification, focus on interaction with surrounding
Examples	• Experimental and modelling investigation on methane reforming kinetics within Ni-YSZ SOFC anode support, Hecht (2005) [128] • Prediction of tortuosity of SOFC anode from mass transport model and saturation currents, Brus (2014) [129] • Review of simulation of composite electrodes for SOFC with example of calculation of methane reforming for Ni/YSZ cermet, Sunde (2000) [111] • Effect of microstructure and thickness on performance of SOFC, Li (2014) [130] • Macro/micro structure parameters influence for methane fuelled single SOFC cell stack, Hosseini (2013) [99]	• 2D model of internal indirect reforming tubular SOFC, Nishino (2006) [131] • Sensitivity analysis for SOFC with internal direct reforming fed by various fuels, Nagel (2008) [100] • 3D model of planar SOFC with internal direct methane reforming for analysis of carbon formation and thermal stress, Nikooyeh (2007) [114] • CFD 2D elliptic model of SOFC with direct internal reforming, Janardhanan (2006) [132] • Comparison of Planar SOFC Models, Campanari (2005) [133] • 3D model model of APU SOFC stack under transient operation, Al-Masri (2014) [134] • 3D model for industrial-size SOFC fueled by diesel reformat, Schluckner (2014) [135]	• SOFC model for system simulation, Bove (2005) [136,137] • 0D planar SOFC model with internal direct reforming, Petersen (2006) [138] • Energy analysis of SOFC system fed by syngas, De Lorenzo (2015) [139] • Influence of reformer fault for SOFC system, Greco (2014) [140] • SOFC triple combined cycle for natural gas with photovoltaic, Obara (2015) [101] • SOFC-GT system fed by liquid fuels (internal and external reformer), Santin (2010) [102] • SOFC-micro GC system performance (internal indirect reformer), Komatsu (2010) [103]

Table 1.2 Investigations on the modelling of Solid Oxide Fuel Cells coupled with methane steam reforming systems with the approach to the reforming modelling

Study	Focus of the study	Approach to methane reforming modelling
	Simplified approach	
Costamagna (1996) [117]	Experimental and modelling on partial oxidation of CH_4 in SOFC	Chemical equilibrium of the reforming reactions into the gaseous anodic stream evaluated at solid temperature
Pfafferodt (2005) [118]	Prediction of suitable operating range of SOFC for an Auxiliary Power Unit	Chemical equilibrium of the gas phase reaction; finite reaction kinetic fulfilling the thermodynamic equilibrium condition
Sidwell (2005) [119]	Limitation of electrical efficiency in hydrocarbon fuelled SOFCs	Molar flow into volume reaches equilibrium immediately, rate at which every species is created is difference between entering and equilibrium mixture flows; Gibbs minimization
Apfel (2006) [121]	Thermal start-up and management of SOFC	75% of the remaining methane fraction is reformed in each of the 20 finite elements of stack
Chan (2003) [120]	Model of SOFC- gas turbine hybrid system	Equilibrium conditions applied for the process
Demin (1992) [122]	Thermodynamic analysis of SOFC system fed by methane	Equilibrium conditions coupled with thermodynamic analysis
Petersen (2006) [138]	Zero dimensional model of planar SOFC with internal direct reforming of methane	Chemical equilibrium conditions
	Kinetic rate expression	
Sucipta (2007) [141]	SOFC-MGT hybrid system fuelled by gasified biomass	Achenbach model [116,123]
Komatsu (2010) [103]	Analysis of system with SOFC and micro-gas turbine in part load operation	Achenbach model [116,123]
Komatsu (2013) [115]	Dynamic behaviour of SOFC with power output control scheme and load following operation	Achenbach model [116,123]

Study	Focus of the study	Approach to methane reforming modelling
	Kinetic rate expression	
Nagel (2008) [100]	Sensitivity analysis for SOFC fuelled by various fuels	Various calculation models: • Equilibrium equation • Achenbach model [116,123] • Ahmed and Foger model [125] • Leinfelder model [126] • Drescher model [127]
Nikooyeh (2007) [114]	Analysis of carbon formation and thermal stress in planar SOFC with internal direct methane reforming	Achenbach model [116,123]
Sunde (2000) [111]	Simulation of electrodes in Fuel Cell	Achenbach model [123]
Campanari (2005) [133]	Comparison of models for simulating planar cell geometry	Achenbach model [116,123]
Klein (2007) [96]	Modelling SOFC fuelled by methane	Lehnert model [110,124]
Klein (2008) [142]	Gradual internal reforming without coking in SOFC fuelled by methane	Lehnert model [110,124]
Haberman (2004) [98]	Chemically reacting gas flow in the porous structure of SOFC	Lehnert model [110,124]
Gemmen (2006) [143]	Coal syngas transport in anode of SOFC	Lehnert model [110,124]
Ni (2008) [144]	Comparison of proton and ion conducting electrolytes for SOFC	Lehnert model [110,124]
Ni (2008) [145]	Pressure gradient in SOFC modelling	Lehnert model [110,124]
Hosseini (2013) [99]	Combined effects of macro/micro structure on methane fuelled SOFC	Ahmed and Foger model [125]
Nagata (2001) [146]	Output characteristics of tubular SOFC with internal reformer	Odegard model [147]
Nishino (2006) [131]	Numerical modelling of indirect internal reforming tubular SOFC	Odegard model [147]
Nishino (2010) [58]	Numerical simulation of cell-based indirect internal reforming tubular SOFC operated with biogas	Odegard model [147]

Study	Focus of the study	Approach to methane reforming modelling
Kinetic expression measured for the specific cell		
Yakabe (2001) [113]	3-D model of planar SOFC	Power-law kinetic expression measured for Ni/YSZ cermet
Lehnert (2000) [110]	Gas transport phenomena in SOFC anodes	Volumetric reaction rate on Ni/8YSZ cermet anode; described in [124]
Achenbach (1994) [116]	3D time-dependent simulation of SOFC	The unity reaction order of CH_4 and no influence of vapour partial pressure; results form experimentation on nickel cermet
Brus (2012) [148]	Chemically reacting gas flow in the porous structure of internal reformer of SOFC system	Power-law kinetic expression measured on Ni/YSZ catalyst material by AGC Seimi Chemical CO
Kinetic model for complete set of 42 elementary reactions		
Hecht (2005) [128]	Methane reforming kinetic within anode support	Kinetic data set taken from variety of sources modified by optimizing procedure to assure thermodynamic consistency
Janardhanan (2006) [132]	CFD analysis of SOFC with internal direct reforming – interactions of transport, heterogeneous catalysis and electrochemical processes	Chemical reaction mechanisms, in particular for heterogeneous (gas/solid) catalytic systems, developed by the research group of Olaf Deutschmann [149]

1.5 Methane/Steam Reforming kinetics investigations

1.5.1 Nickel catalyst and SOFC applications

The kinetic of the methane/steam reforming has been widely studied in the literature for industrial catalytic reactors. The reforming reaction can be conducted on the various catalytic materials, however, the most common are nickel based catalysts. This dominance is mostly caused by high activity and relatively low cost. Also, As it was presented in Section1.2 nickel (especially in the form of Ni/YSZ cermet) is also one of the most significant materials used in the production of SOFC anodes. However, when the reforming dedicated for both of those applications is considered, significant differences has to be addressed. Typical support material for industrial nickel catalysts is alumina magnesium spinel, and for the SOFC

application on the other hand, the most common support is YSZ. The Ni content is varied from around 5% in the industrial catalyst and around 40%vol in the SOFC anodes. Industrial high scale application usually uses the Ni particle size in the range 5-10 nm, while in the case of SOFC typical size of fine grains is about 1 μm [81]. All of those properties induce the differences in the performance and methane/steam reaction rate for both types of catalyst. Therefore, wide research [39] focused on the industrial catalysts, which were performed in the condition and material far from the SOFC typical standards, can not be directly transferred for the applications in the SOFC systems with internal fuel reforming [81]. Further, only a limited amount of research was focused on SOFC dedicated materials in the context of methane/steam reforming.

1.5.2 Necessity of the reliable reforming kinetic description

Widespread disagreements between kinetic of the reforming proceeded on the typical industrial catalysts in spite of the extensive research in the field and lack of suitable kinetic on real SOFC anode materials, induce the necessity for reliable data dedicated to SOFC design. It is crucial in the context of the great influence of the implemented reforming kinetic model for the properties and performance of the overall SOFC modelling [100].

The mathematical forms of expression describing the highly non-linear kinetics of the reforming process are not consistent among themselves. The kinetic description is addressed by the various numerical models, which can be divided into three basic concepts: [32,37,39,148]:

- General Langmuir-Hinshelwood kinetics [37],
- first order reaction with respect to methane [32,123,150]
- power law expressions derived from data fitting [113,125,147,148,151–153].

Even among one numerical approach, the derived empirical parameters describing the process are divergent among themselves. For instance, Table 1.3 shows one of the empirical parameters, the so-called reaction orders in respect to the partial pressures of methane (reaction order *a*) and steam (reaction order *b*) found in the literature [81,94,113,123,125,147,150–154]. All of the studies presented in Table 1.3 were focused on

the Nickel based catalysts. Very significant differences can be found, although, the empirical parameters *a* and *b* should be independent from the specific property of the investigated sample, as far as the same type of catalyst is used [151]. Moreover, uncertainties of the obtained result, which may have influenced the derived reaction kinetics, were not substantially discussed in the published investigations.

Table 1.3 Comparison of the reaction kinetics parameter, reaction orders *a* and *b*, found in literatures for Ni/YSZ cermet [81,94,113,123,125,147,150–154]

Reference	*a*	*b*
Lee et al. (1990) [153]	1	-1.25
Achenbach (1994) [116]	1	0
Odegard et al. (1995) [147]	1.2	0
Ahmed and Foger (2000) [125]	0.85	-0.35
Yakabe et al. (2001) [113]	1.3	-1.2
Wei and Iglesia (2004) [32]	1	0
Timmermann et al. (2006) [152]	1.19	0
King et al. (2008) [150]	1	0
Brus (2011) [59]	0.98	-0.09
Mogensen (2011) [81]	0.7	0
Iwai et al (2012) [151]	0.82	0.14

To properly address and implement the reforming application due to the technological development of SOFCs, the implementation of an internal reforming system, modelling and numerical analyses of the phenomena occurring inside the SOFC systems are important subjects. The reason relies on the fact that the fuel reforming process, in particular the designing and optimizing of an indirect internal reformer and a cell with direct reforming for an SOFC application, involve problems connected with heat transfer phenomena in porous media. To conduct numerical modelling, proper kinetics of the reaction is also needed to improve the reliability of numerical modelling. Thus, the treatment of reaction kinetics and physical phenomena in a system are very important subjects to be accomplished.

1.6 Goal of the Thesis

On the basis of the preceding observations the necessity for a precise description of the methane/steam reforming process arises. Moreover, in the light of the lack of a uniform empirical kinetic for the reforming reaction and a deficiency in consistent calculation methodology, the proposition of thorough and reliable experimental and computation strategies is indispensable.

The primeval goal of the thesis is to provide comprehensive description of the methane/steam reforming process dedicated for Solid Oxide Fuel Cell with respect to the uncertainty of the postulated empirical process equations and to propose objective mathematical strategies for evaluating the quality of the imposed numerical models.

It is postulated that the Generalized Least Squares Method fulfils the above-mentioned criteria and can be applied to analyse, improve and quantity the mathematical modelling of the methane/steam reforming process.

Among the detailed objectives and hypothesis of the study the following can be pointed:

1. Conducting the analysis of the methane reforming process and the determination of empirical parameters describing the phenomenon. Proposing experimental and calculation strategies for methane/steam reforming, which enable the study of the process conducted on various catalyst materials.

2. Defining of a novel framework for incorporating the Generalized (Orthogonal) Least Squares Method for the analysis of the kinetic of chemical processes conducted in non-equilibrium conditions. The objective will be realized in several steps:
    - Preparation and implementation of a numerical algorithm which enables the application of the GLS method. The library of the GLS method operators provides the high portability and easy application for the various problems.
    – Preparing a mathematical model of the process;
    – Definition of constraints equations (model equations) describing the examined phenomenon;

3. Conduction an analysis of the methane steam reforming by the GLS algorithm and including additional data, which are commonly used for validation purposes, in the mathematical model as the supplementary variables. Presenting an improvement in quality of the obtained solution, a decrease in the uncertainty of the final result and increased security of the directly measured variables.

4. Falsification of the various sets of constraints equations describing the methane reforming process. Proposing the objective and quantitative method for validation of the proposed mathematical models.

2 Outline of the Generalized Least Squares method

The Least Squares (LS) method and the Generalized Least Squares Method (GLS) are methods for the approximate solutions of overdetermined problems. Overdetermined sets of equations are characterized by larger numbers of equations than numbers of unknowns. Another approach to approximate solutions of overdetermined problems, for example median regression, has bigger computational complexity and is less often used.

The general method objective is that various mathematical expressions for determining the behavior of a system are solved as a set of simultaneous equations. On the other hand, the measurements with the experimental errors are considered for the implementation of the model and those experimental observations are adjusted to fulfil the principle of the balancing the equation set. The adjusting (co-ordination) process is done judiciously so that the measurements more prone to be burdened with errors are also the subject of receiving a larger percentage adjustment. The second principle of the method is that total adjustment is limited to the necessary minimum [155].

The most popular and simplest application of the least squares method provides the possibility to find a most probable value of a real variable, which was measured in a series of a measurements with experimental uncertainties. Generally, this method is a very important technique of statistical and applied mathematics, used for curve fitting, statistical estimations and the adjustment of observations [156]. However, the method of least squares can be also used for much more complicated problems with larger numbers of variables that are functions dependent on the values of the measured variables. The generalized least squares method with the assumption of normal distribution of errors provides a way of finding values of unknown variables and increasing the reliability of the results of direct measurements. Moreover its unique feature is possibility of finding the error of an obtained solution (the approximation of a theoretical standard deviation) after co-ordination of the variables.

2.1 Approaches to mathematical modelling

The conventional methods of modelling multi-physical phenomena involving (heat and mass) transport problems usually describe an analysed system with a finite set of equations, which are uniquely defined in the mathematical sense. In general, the problem with N unknowns and K measured variables can be solved unambiguously when there are N equations in the mathematical model. This type of theoretical approach yields unique solutions from the peculiarly specified constraint set of equation for a system. Besides, they assume that each variable or model parameter is precisely defined and their uncertainties are negligible (Fig. 2.1A). However, in the case of the methane/steam reforming process, in which model parameters include properties from a general thermodynamic table, the assumption of accuracy of all of those factors can lead to the simplification of the model. Model simplification can also be inducted by an applied mathematical approach in both the defining phase and during the model solving stage. Moreover, one of the most significant factors in identifying the inaccuracies of the model solutions is connected with the uncertainties of the directly measured variables (observations) incorporated in the problem description (Fig. 2.1B). The model defined in this manner results in a unique description of the phenomena, although the numerical results can differ from the actual state of the system behaviour and the degree of accuracy of the model that is usually difficult to estimate. The present study will analyse the concept of most probable value of a theoretical solution and a measure of its inaccuracy. The proposed methodology allows for including additional data directly in the mathematical model of the process as the new (supplementary) variables. A model, which includes supplementary data, contains more equations than unknowns, and because the uncertainties of the directly measured variables (observations) can be internally contradicted. Choosing different subsets of constraint equations allows for the calculation of unknowns in many, theoretically correct ways and a problem, which arises, is how to determine the most probable result. The LS and GLS procedures are proposed as a method of correcting the measured data (co-ordination), securing its higher accuracy and obtaining the most probable value for the parameters to be determined by numerical computation (Fig. 2.1C). One of the most important features of those methods is the possibility of calculating the *a posteriori* errors characterizing the newly found values of the measurements and unknowns after co-ordination. Additionally, it can be noted that the GLS method provides an objective criteria for the formal evaluation and falsification of different mathematical models of investigated phenomena.

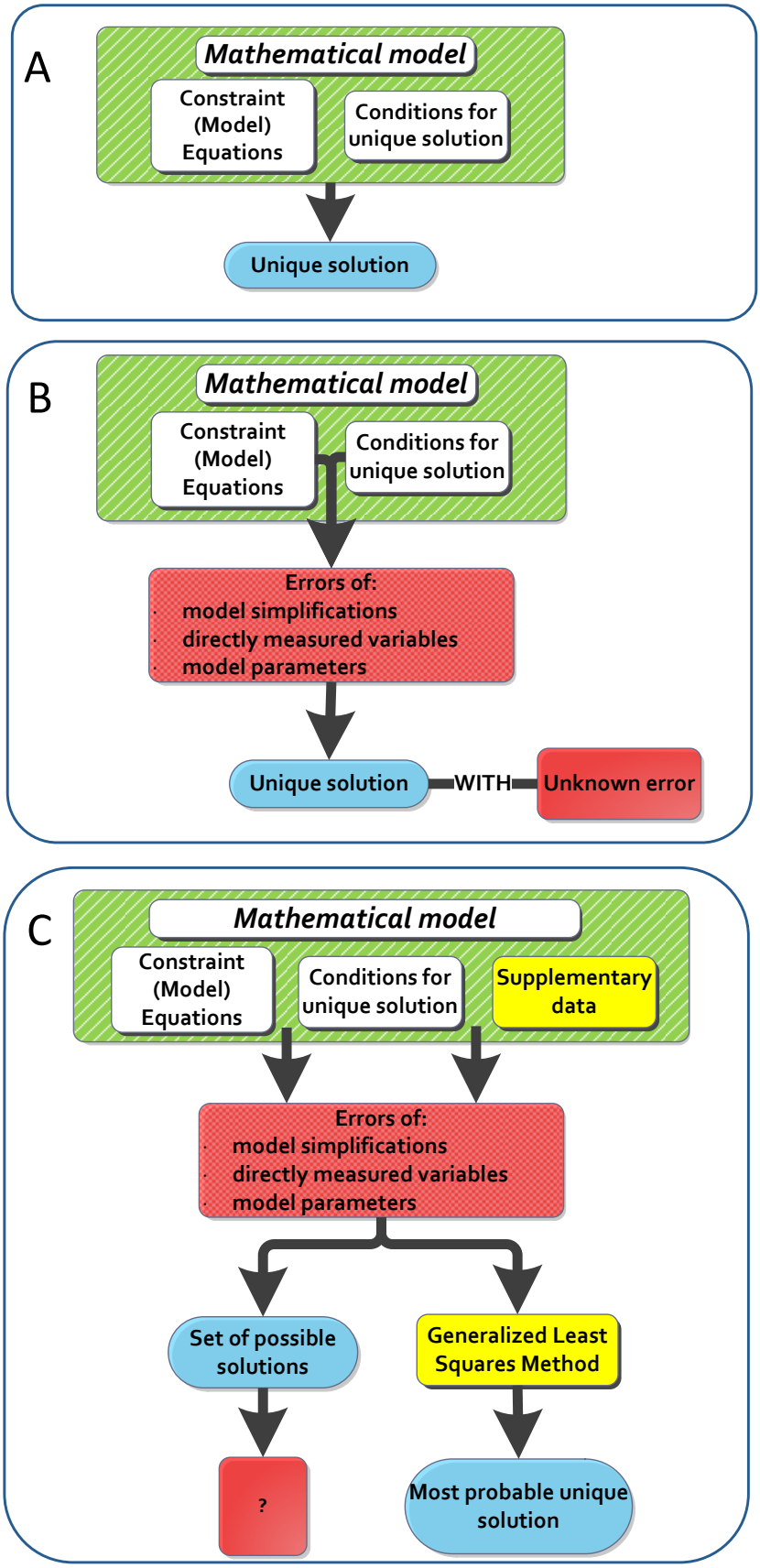

Figure 2.1 Approaches to mathematical modelling: A) classical problem definition, B) errors of mathematical models and C) models with supplementary data

The formal condition of the applicability of the Least Squares Method can be summed up by correlating the number of measurement values in system K, the number of unknowns N and the number of the constraint equations. When the number of the independent equation in the constraint set is equal to the number of the unknowns J=N, then the system can be solved but the co-ordination procedure cannot be applied. There is no supplementary information included and the problem is defined uniquely. In other words, the control of the correctness of the results of the measurements cannot be carried out. On the other hand, when the number of equations exceeds the number of the unknowns in the model, the control of the measured values is possible on the basis of the relations existing between variables. Therefore, the following inequality should be preserved:

$$N < J \tag{2.1}$$

The additional condition is that the number of the mutual independent equations in the constraint set should be smaller than the number of all the variables in the system:

$$J < K + N \tag{2.2}$$

This condition provides the possibility of using the supplementary measurements in the problem definition effectively.

2.2 Applications of Least Squares Method

The first comprehensive formulation of the least squares method can be found in Adrien Marie Legendre's Nouvelles méthodes pour la détermination des orbites des comètes (1805; "New Methods for the Determination of Comet Orbits") [157]. On the other hand, the most famous priority dispute in the history of statistics is between Gauss and Legendre and it is claimed that priority to the method introduction should be shared with Legendre's German rival. Simultaneously to Legendre, an American mathematician Robert Adrain published the method in late 1808 [158] and Carl Friedrich Gauss published it in 1809 [159]. Although the scientific norm usually determines priority on the basis of first publication, Gauss claimed that he used the least squares method from 1795. It is believed that the least squares method was used by him to adjust the data of measurement of a meridian arc on Earth, published in 1799 in his letter to the Journal "Allgemeine Geographische Ephemeriden" which alludes to

"meine Methode" [160]. The data was analyzed by Stigler [161], however, later work by Celmins does not support this theory and concludes that we have to take Gauss's word about his early discovery [162].

Initially, the least squares method was used mainly in surveying problems and geodetic calculations and then was applied to astronomy and scientific problems. Moreover, the least squares method is the basis of the modern errors theory and it is called the automobile of modern statistical analysis [161].

One of the most interesting examples of the application of this mathematical theory is the discovery of binary pulsar and the development of relativistic gravity theory, presented by Hulse and Taylor [163,164]. Those discoveries were awarded the Nobel Prize in Physics in 1993.The Orthogonal Least Squares Method was used as the basis of all of the calculations in the project. During the data processing, all of the directly measured pulse times of the arrival (TOAs) at the telescope, had to be transformed to a corresponding proper time of emission in the pulsar frame. This is a complex problem, as this relation depends on many factors. The telescope's location is calculated from the numerically-integrated solar system model and includes the Earth's unpredictable rotational variations. Among others, the equations require positions, velocities, masses of all the significant solar-system bodies, including the propagation effects and the description of the orbital motion of the pulsar. The model requires also the introduction of many *a priori* unknowns. The model parameters were extracted from an analysis conducted by the Least Squares Method on the long time-series of the measured TOAs. As it was stated: "*In addition to providing a list of fitted parameter values and their estimated uncertainties, the least-squares solution produces a set of post-fit residuals, or differences between measured TOAs and those predicted by the model*" [164]. By the application of the Least Squares method, Hulse and Taylor proposed a systematic approach to use the over-determined system of the equation and they have turned it into a calibrated laboratory for testing relativistic gravity.

The first application of the Least Squares Method in chemical engineering is attributed to Kuehn and Davidson [155], who proposed a solution of a simple problem, when all of the flows in a system are measured [165]. Applications of the data reconciliation in the industrial process was reported by Reilly and Carpani [166]. Extensive analysis and development of the mathematical formulation of the method was presented by Sweneker [167] who applied it to

the adjustment of mass balances in a gas pipeline. Sweneker proposed a solution in matrix form for linear constraints and the process description included both unmeasured flows and products of measured flows and measured concentrations. The comprehensive study of the method and its applications in energy engineering problems were presented by Szargut, in particular for mass and energy balances in chemical and energy technologies [168].

Applications to energy science and the theoretical aspects of the LS method were developed [169–178].

The research involved problems relevant to a theory of coordination of material and energy balance [169–171], heat transfer by convection and radiation, the prediction of temperature distribution [172,173] and solving inverse boundary heat conduction problems [177,178]. Other concerned issues were investigations related to carbon dioxide emissivity [174], the solidification of binary alloys [175], and the modelling of autocatalytic reactions [176]. The heat transfer problems were investigated by Szmyd, who previously considered the applicability of the Least Squares method to the steady-state conduction problem, and its goal was optimal planning of experimental measurements [179]. However, the model was represented as a fixed analysis example with a set number of calculation points and defined boundary conditions type I. The later studies generalize the consideration and introduce possibilities for incorporating the GLS method into different types of heat transfer problems in steady-state heat conduction [180].

The Least Squares Method and its generalized formulation is the tool used in many branches of science and its practical implementation and modification are currently under development. Bendig et al. applied the Least Squares methodology in the enhanced data reconciliation to the analysis of a heat exchanger including time intervals [181]. Singhmaneeskulchai investigated the applicability of dynamic data reconciliation in a hot-oil heat exchanger for validating energy consumption [182]. The published applications of the GLS method to the energy engineering problems include also the analyses of the methane/steam reforming process, which are partially presented in this dissertation [183–185]

2.3 Least squares method – Legendre formulation

The least squares method is based on the Legendre's postulation. The results of K consecutive measurements u_k: can be presented as the sum of an unknown variable u^* and experimental error v_k:

$$u_k = u^* + v_k \tag{2.3}$$

The goal of the least squares method is to find such values of the experimental errors $v_{k,}$, that the total value of their squares will be minimized:

$$\sum_{k=1}^{\mathrm{K}} v_k^2 = \sum_{k=1}^{\mathrm{K}} \left(u^* - u_k\right)^2 \rightarrow \min \tag{2.4}$$

Additional restriction given for the experimental error distribution is the assumption about fulfilling the normal distribution with mean value equals zero and variance σ_k^2: $v_k \sim N(0, \sigma_k^2)$. The normal distribution ensure the supply of the following properties:

$$E\left(v_k\right) = 0 \tag{2.5}$$

$$E\left(v_k^2\right) = \sigma_k^2 \tag{2.6}$$

$$\text{for } k = 1,2,...,\mathrm{K} \tag{2.7}$$

where $E(\,)$ is expected value, and σ_k^2 - variance of the K measurement. A consequence of the Legendre's formulation is the conclusion that the best estimate of a series of equally accurate measurements is their arithmetic average:

$$u^* = \overline{u_k} = \frac{1}{K}\sum_{k=1}^{\mathrm{K}} u_k \tag{2.8}$$

The variance of the result is equal to

$$\sigma^2\left(u^*\right) = \frac{\sigma^2}{K} \tag{2.9}$$

Analogically, it can be proved that for measurements with different accuracy σ_j the best approximation of real value is weighted average with weights inversely proportional to the value of the measurement errors:

$$u^* = \frac{\sum_{k=1}^{K} \frac{u_k}{\sigma_k^2}}{\sum_{k=1}^{K} \frac{1}{\sigma_k^2}} \tag{2.10}$$

with the following estimation of variance:

$$\sigma^2\left(u^*\right) = \frac{1}{\sum_{k=1}^{K} \frac{1}{\sigma_k^2}} \tag{2.11}$$

2.4 Least Squares Method

The Least Squares Method can be applied to complex problems of co-ordination and data adjustment. The basic formulation of the Least Squares Method provides a methodology for solving the modelling problem defined by the nonlinear equation sets consisting of algebraic functions and differential equations describing the governing equations of the problem. First, assume that the considered problem is described by a set of J algebraic equations:

$$f_j\left(\mathbf{u}^*, \mathbf{x}^*\right) = 0,\ \left(j = 1,2,\cdots,\mathrm{J}\right),\ \mathbf{u}^* = \begin{pmatrix} u_1^* \\ u_2^* \\ \vdots \\ u_{\mathrm{K}}^* \end{pmatrix} \quad \text{and} \quad \mathbf{x}^* = \begin{pmatrix} x_1^* \\ x_2^* \\ \vdots \\ x_{\mathrm{N}}^* \end{pmatrix} \tag{2.12}$$

where $\mathbf{u}^*$ is the K-elements vector of the quantities to be measured and $\mathbf{x}^*$ is the N-elements vector of the quantities to be solved by numerical computation [173]. Although for the measured values **u** and the approximations of the unknowns **x** the equation set is not precisely fulfilled:

$$f_j\left(\mathbf{u},\mathbf{x}\right)=-w_j,\ \left(j=1,2,\cdots,\mathrm{J}\right),\ \mathbf{u}=\begin{pmatrix}u_1\\u_2\\\vdots\\u_{\mathrm{K}}\end{pmatrix}\quad\text{and}\quad\mathbf{x}=\begin{pmatrix}x_1\\x_2\\\vdots\\x_{\mathrm{N}}\end{pmatrix}\tag{2.13}$$

where w_j designates the residual of the j-th equation [173]. Real values $\mathbf{u}^*$ and $\mathbf{x}^*$ are the sum of the measurements and approximations of unknowns ($\mathbf{u}$ and $\mathbf{x}$) and corrections ($\mathbf{v}$ and $\mathbf{y}$): $\mathbf{u}^*=\mathbf{u}+\mathbf{v}$ and $\mathbf{x}^*=\mathbf{x}+\mathbf{y}$. Therefore, it can be written as the formula in Eq. (2.14) [173]:

$$f_j\left(\mathbf{u}+\mathbf{v},\mathbf{x}+\mathbf{y}\right)=0,\ \left(j=1,2,\cdots,\mathrm{J}\right),\ \mathbf{v}=\begin{pmatrix}v_1\\v_2\\\vdots\\v_{\mathrm{K}}\end{pmatrix}\quad\text{and}\quad\mathbf{y}=\begin{pmatrix}y_1\\y_2\\\vdots\\y_{\mathrm{N}}\end{pmatrix}\tag{2.14}$$

Moreover, it is assumed that the experimental errors s_k of measurements satisfies the normal distribution with the mean value equals zero and variance $\sigma_k^{\,2}$: $s_k\sim N\left(0,\sigma_k^{\,2}\right)$.

According to the assumptions, $f_j\left(\mathbf{u},\mathbf{x}\right)$ is the unrestricted algebraic function. The first step in the application of the classical theory of Least Squares is linearization of the constraint equation. If the f_j functions are differentiable, they can be presented in the form of a Taylor series in the neighbourhood of point P(**u,x**). The linearization of function f_j is the first order term of its Taylor expansion around the point of interest. Then, the method developed for linear constraints is extended to nonlinearly constrained problems [186]. After linearization, the constraint equations can be written in matrix form:

$$\mathbf{Av}+\mathbf{By}=\mathbf{w}\tag{2.15}$$

where $\mathbf{A}=\dfrac{\partial f_j}{\partial u_k}$ is $\mathrm{J}\times\mathrm{K}$ Jacobi's matrix and $\mathbf{B}=\dfrac{\partial f_j}{\partial x_n}$ is $\mathrm{J}\times\mathrm{N}$ Jacobi's matrix [176]. The LS method assumes the minimization of the following function [179]:

$$\Phi(\mathbf{v}) = \mathbf{v}^{\mathrm{T}}\mathbf{C}_{\mathrm{S}}^{-1}\mathbf{v} = \sum_{k=1}^{\mathrm{K}}\left(\frac{v_k}{\sigma_k}\right)^2 \rightarrow \min \tag{2.16}$$

where $\mathbf{C_S}$ is the covariance matrix with the measurement variances σ_k^2 on the diagonal and 0 on the other positions (due to the independence of the variables):

$$\mathbf{C}_{\mathrm{S}} = \begin{bmatrix} \sigma_1^{\,2} & & & 0 \\ & \sigma_2^{\,2} & & \\ & & \ddots & \\ 0 & & & \sigma_{\mathrm{K}}^{\,2} \end{bmatrix} \tag{2.17}$$

The method of Lagrange multipliers is applied in order to achieve the extreme and find corrections; the Lagrange function is defined as:

$$L = \mathbf{v}^{\mathrm{T}}\mathbf{C}_{\mathbf{S}}^{\,-1}\mathbf{v} - 2\mathbf{k}^{\mathrm{T}}\left(\mathbf{A}\mathbf{v} + \mathbf{B}\mathbf{y} - \mathbf{w}\right) \tag{2.18}$$

where $\mathbf{k}$ is the Lagrange multipliers vector rank J. The function $\Phi(\mathbf{v})$ achieves the minimum with the simultaneous fulfilling of the equation set (2.15), when the derivative of the Lagrange function L is equal to zero:

$$d\mathbf{L} = \frac{\partial \mathbf{L}}{\partial \mathbf{v}}d\mathbf{v} + \frac{\partial \mathbf{L}}{\partial \mathbf{y}}d\mathbf{y} = 0 \tag{2.19}$$

Equation (2.19) provides the following equation set:

$$\begin{cases} \mathbf{C}_{\mathbf{S}}^{\,-1}\mathbf{v} - \mathbf{A}^{\mathrm{T}}\mathbf{k} = 0 \\ \mathbf{B}^{\mathrm{T}}\mathbf{k} = 0 \end{cases} \tag{2.20}$$

After solving the equation set and performing an appropriate mathematical conversion, the final formulas defining the correction vector for measurements $\mathbf{y}$ and unknowns $\mathbf{v}$ are derived [173]:

$$\begin{aligned}\mathbf{y} &= \mathbf{G}^{-1}\mathbf{B}^{\mathrm{T}}\mathbf{F}^{-1}\mathbf{w} \\ \mathbf{v} &= \mathbf{C}_{\mathrm{s}}\mathbf{A}^{\mathrm{T}}\mathbf{F}^{-1}\left(\mathbf{w}-\mathbf{B}\mathbf{y}\right)\end{aligned} \tag{2.21}$$

where **F** and **G** are auxiliary variables:

$$\mathbf{F} = \mathbf{A}\mathbf{C}_{\mathrm{S}}\mathbf{A}^{\mathrm{T}} \tag{2.22}$$

$$\mathbf{G} = \mathbf{B}^{\mathrm{T}}\mathbf{F}^{-1}\mathbf{B}\,. \tag{2.23}$$

2.5 Generalized Least Squares Method

The Generalized Least Squares (GLS) method (Unified Least Squares method) was introduced by Mikhail and Ackermann in 1976 [187]. The classical definition of the least squares method assumes that the rank of matrix **A** is equal to the amount of model equations J. However, in many practical problems the least squares method cannot be conveniently applied, because of the computational problem connected with the formulation of the constraint equations set. When the number of equations f_j is different than the amount of measured values u_k the primary assumption of the LS method is not fulfilled [188]. Thus, Eq. (2.21) proposed in that classical method cannot be used because matrix $\mathbf{F}^{-1}$ does not exist and $\det\left(\mathbf{F}\right) = \det\left(\mathbf{A}\mathbf{C}_{\mathrm{S}}\mathbf{A}^{\mathrm{T}}\right) = 0$ [188]. Therefore the modified approach has to be used

The most important assumption of the GLS method is that all model variables (measured values **u** and unknowns **x**) are observations and are treated numerically in the same manner [175]. The only difference between them is the assumption that the errors of the unknowns are much bigger than the errors of the measured values ($s_k >> s_n$) [176].

After the linearization of the model equations the constraints can be written:

$$\mathbf{A}_{\mathrm{B}}\mathbf{V}_{\mathrm{B}} = \mathbf{w} \tag{2.24}$$

where $\mathbf{A_B} = [\mathbf{A}\,\mathbf{B}]$ and $\mathbf{V_B} = [\ \mathbf{v}^T \quad \mathbf{y}^T\ ]^T$ and then the covariance matrix has the following form:

$$\mathbf{C_B} = \begin{bmatrix} \mathbf{C_S} & 0 \\ 0 & \mathbf{C_{SX}} \end{bmatrix} \tag{2.25}$$

where $\mathbf{C_S}$ and $\mathbf{C_{SX}}$ are the covariance matrices with diagonals consisting of variances of measurements σ_k^2 and unknowns σ_n^2, respectively [176]. To solve the GLS problem and minimize the function $\Phi(\mathbf{v},\mathbf{y})$, which has the following form:

$$\Phi(\mathbf{v},\mathbf{y}) = \sum_{k=1}^{K}\left(\frac{v_k}{s_k}\right)^2 + \sum_{n=1}^{N}\left(\frac{y_n}{s_n}\right)^2 \rightarrow \min \tag{2.26}$$

the Lagrange multiplier method is used and it gives the following solution [179]:

$$\mathbf{V_B} = \mathbf{C_B}\mathbf{A_B^T}\mathbf{F_B^{-1}}\mathbf{W_B}, \text{where } \mathbf{F_B} = \mathbf{A_B}\mathbf{C_B}\mathbf{A_B^T} \tag{2.27}$$

2.6 Covariance Matrix and errors of the solution

The proposed methods of Least Squares and Generalized Least Squares are superior to other numerical approaches because they define a unique formal strategy to evaluate the uncertainties characterizing the results after the co-ordination process. The uncertainty characterizing the obtained results is expressed in the form of *a posteriori* covariance matrix calculated on the basis of corrected variables. This matrix gives the new error bounds for corrected measured data ($\mathbf{u}$, $\mathbf{C_U}$) and the theoretically solved variables ($\mathbf{x}$, $\mathbf{C_X}$).

To yield new error bounds for the corrected measured data ($\mathbf{u}$, $\mathbf{C_U}$) and the theoretically solved variables ($\mathbf{x}$, $\mathbf{C_X}$), the law of error propagation can be applied. The new covariance matrices for the classical LS method can be written:

$$\begin{aligned} \mathbf{C_U} &= \mathbf{C_S} - \mathbf{SAC_S} \\ \mathbf{C_X} &= \left(\mathbf{B^T T^{-1} B}\right)^{-1} \end{aligned} \tag{2.28}$$

where $\mathbf{S}=\mathbf{C}_{\mathbf{S}}\mathbf{A}^{\mathrm{T}}\mathbf{F}^{-1}\left(\mathbf{I}-\mathbf{B}\mathbf{G}^{-1}\mathbf{B}^{\mathrm{T}}\mathbf{F}^{-1}\right)$ and $\mathbf{I}$ is the unit matrix [173].

On the other hand, in the case of the generalized approach, the calculated covariance matrix of the improved observations has the following form [179]:

$$\mathbf{C}_{\mathbf{VB}}=\mathbf{C}_{\mathbf{B}}-\mathbf{C}_{\mathbf{B}}\mathbf{A}_{\mathbf{B}}^{\mathrm{T}}\mathbf{F}_{\mathbf{B}}^{-1}\mathbf{A}_{\mathbf{B}}\mathbf{C}_{\mathbf{B}}=\begin{bmatrix}\mathbf{C}_{\mathbf{U}} & \mathbf{C}_{\mathbf{UX}}\\ \mathbf{C}_{\mathbf{UX}}^{\mathrm{T}} & \mathbf{C}_{\mathbf{X}}\end{bmatrix} \tag{2.29}$$

The covariance matrix $\mathbf{C}_{\mathbf{VB}}$ defined by the Eq. (2.29) represents the hyperellipsoid of the (K+N)-dimensional normal distribution. The exemplary two-dimensional covariance ellipse is presented in Fig. 2.2. The covariance ellipsoid is the hypersurface in the (K+N)-dimensional space and is always inside the (K+N)-dimensional cuboid defined by the central point P'($\mathbf{u}^{*}$,$\mathbf{x}^{*}$) and the square roots of the diagonal elements of $\mathbf{C}_{\mathbf{VB}}$ which represent the lengths of the cuboid edges. The covariance hyperellipsoid touches the cubicoid at 2(K+N) points and its volume can be calculated using the formula:

$$V_{\mathrm{K+N}}=\frac{\sqrt{\left(\mathrm{K+N+2}\right)\pi^{\left(\mathrm{K+N+2}\right)}\left|\mathbf{C}_{\mathbf{VB}}\right|}}{\Gamma\left(\frac{1}{2}\left(\mathrm{K+N}\right)+1\right)} \tag{2.30}$$

where Γ is the Euler's gamma function [179].

Generally, it can be noted that the lines of constant probability are ellipsoids similar to the covariance ellipsoid. Those ellipsoids are situated inside (outside) of it for larger (smaller) probability. For the largest probability, the ellipsoid collapses to the central point [189]. Thus, it can be pointed out that conditions for achieving the global minimum can be presented equivalently as the minimization of the hyperellipsoid's volume and the minimization of the covariance matrix's determinant [179]:

$$\min\left(V_{\mathrm{K+N}}\right)\rightarrow\min\left(\left|\mathbf{C}_{\mathbf{VB}}\right|\right)\text{or}\min\left[\frac{1}{\mathrm{K+N}}\left(\sum_{k=1}^{\mathrm{K}}\sigma_k^2+\sum_{n=1}^{\mathrm{N}}\sigma_n^2\right)\right] \tag{2.31}$$

The presented formula can be used for the falsification of different mathematical models describing the examined physical phenomena.

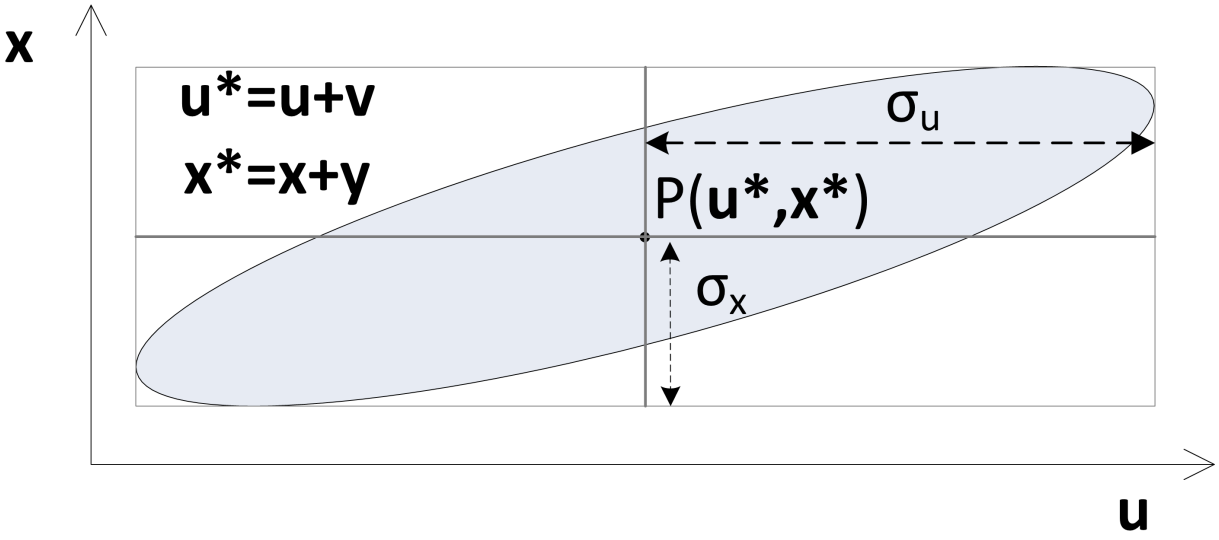

Figure 2.2 Hyperelipsoid of the bivariate normal distribution

2.7 Formation principles of constraint equations

The critical step in the application of the Least Squares and Generalized Least Squares algorithms is the definition of the constraint equation set, which describes the physical laws governing the observed phenomena. The general approach to the formulation of the condition equation in the theory of the co-ordination of the material and energy balances assumes that all of the balance equations are determined for the space limited with the balance cover [190]. The investigated system can be further divided for the subsystems limited by the separated balance covers if it is necessary. Commonly, the number of balance covers should be equal to the number of the parts under investigation and the balance covers should cover the whole system [190].

The generally used types of the equation in the field related to energy engineering are the material and energy balances. The constraint equation set includes the balances of the principal elements, the sum of the substantial fractions of the materials, the relations concerning the mineralogical composition of the materials and the energy balances defined for the separate balance covers.

The substantial balances of the principal elements are defined for each of the balance covers. The constraints create a system of non-linear equations and their number is equal to the product of the defined balance covers and the principal elements in the system [190]. The amount of the substances is defined in mol or as the molar flow rates in mol s^{-1} and the general form of the equation is:

$$F_j^{\mathrm{i}} = F_j^{\mathrm{o}} + \Delta F_j \tag{2.32}$$

where F_j^{i} [mol s^{-1}] is the molar flow rate of the *j*-th principal element carried in with substrates, F_j^{o} [mol s^{-1}] is the molar flow rate of the *j*-th principal element carried out with the product and ΔF_j [mol s^{-1}] is the increase of the amount of the substance of the *j*-th principal element in the system.

In the case of an investigation of the system in stationary or periodically quasi-stationary states the simplified approach is applied. The assumption is that there is no increase in the amount of the substances in the system, so the substantial balances are simplified to the form:

$$F_j^{\mathrm{i}} = F_j^{\mathrm{o}} \tag{2.33}$$

The second group of the constraint equations are the sums of the substantial fractions of components of substrates and products, which are linear functions.

The next group includes the mineralogical composition of some materials. A definition of those linear equation is usable in the systems where some of the detected elements existed in the form of more complex substances. The complete bounding of the chemical groups detected in the analysis can be achieved, as exemplary bounding CO_2 and SO_3 which are natural components of limestone and dolomites.

The equations of energy balances are created in the analogical way as the substantial balances, separately for the different balance covers. The general form of the equations is:

$$E^{\mathrm{i}} = E^{\mathrm{o}} + \Delta E \tag{2.34}$$

where E^{i} [J] is the energy supplied to the system, E^{o} [J] is the energy led out of the system and ΔE [J] is the increment of the energy of the system.

In order to simplify the considerations, the system is often assumed to be in the steady state, when the increment of the energy of the system is not observed $\Delta E=0$. The energy balances form the set of the non-linear equations, which number is equal to the number of balance covers in the system [190].

The set of the constraint equations must be always adjusted to the analysed problem. Essentially the model equations should include all of the fundamental psychical laws governing the observed psychical phenomenon. On the other hand, the benefit of applying the Least Squares and Generalized Least Squares, is the possibility of applying a black-box approach, where no artificial assumptions are necessary. This approach results in higher veracity and easier scalability of the proposed analysis.

3 Mathematical methodologies of deriving the methane reforming kinetic

The mathematical baseline of the methodology and numerical algorithms incorporated into the calculations of the reaction kinetic of the methane/steam reforming are presented. All of the presented algorithms, particularly, all of the codes for the preliminary calculations of the kinetic parameter according to the modified method and Arrhenius plot calculations, as well as the simulation algorithm, are implemented in C language.

3.1 Mathematical description of the methane/steam reforming process

Methane/steam reforming is the conventional method for hydrogen production. The chemical reactions governing the process are following [147]:

Methane/steam reforming reaction: $CH_4+H_2O \rightarrow 3H_2+CO$ (3.1)

Water-gas-shift (WGS) reaction: $CO+H_2O \leftrightarrow H_2+CO_2$ (3.2)

The Methane/Steam Reforming reaction (MSR) described by Eq. (3.1) is slow and highly endothermic, whereas the accompanying water-gas-shift reaction (WGS) presented by Eq. (3.2) is slightly exothermic and a quick process. The reaction enthalpies are 206.2 kJ mol^{-1} and -41.2 kJ mol^{-1} at 25 ^oC respectively for the MSR and SR reactions. Therefore, the overall process is highly endothermic and a substantial supply of thermal energy is required to maintain the reaction temperature. The water-gas-shift reaction is considerably faster than the Methane/Steam Reforming reaction and can be assumed to be in equilibrium at the reforming temperature [123,153,191], so the overall rate of the process is determined by the MSR reaction kinetic. Moreover, the conversion of methane along the reformer depends not only on the local temperature distribution, but also on the partial pressures of the particular chemical

species. The other influential factor deciding the reaction rate is the catalyst active area derived from the catalyst density and microstructure of the material in the case of reforming conducted directly on SOFC anode [151,192].

In the literature [32,37,39,148], many approaches to modelling and describing methane/steam reforming can be found. The reforming process on the Nickel catalyst is the heterogeneous catalysis, where the phases of the catalyst and reactants differ. The kinetics of the reforming process can be described by one of three concepts:

- General Langmuir-Hinshelwood kinetics, which includes detailed steps of the heterogeneous catalysis processes [37]

and the more generalized approaches, especially important in numerical modelling of the complex energy systems:

- first order reaction with respect to methane [32,123,150]
- power law expressions derived from data fitting [113,125,147,148,151–153].

Langmuir-Hinshelwood kinetics approach is based on the description of surface species reactions. The classical derivation of the mechanistic scheme was presented by Xu and Froment [37], who proposed that the rate determining step is a reaction of absorbed carbon and oxygen species, therefore the reaction rate depends on partial pressures of water, methane and hydrogen:

1. $$CHO^* + {}^* \rightleftarrows CO^* + H^* \tag{3.3}$$
2. $$CO^* + O^* \rightleftarrows CO_2{}^* \tag{3.4}$$
3. $$CHO^* + O^* \rightleftarrows CO_2{}^* + H^* \tag{3.5}$$

The second approach dominant in recent research is based on the assumption, that the rate-determining step of the process is dissociative adsorption of methane. The derived elementary reactions model has the following forms [32,128]:

I. $$CH_4 + 2^* \rightleftarrows CH_3{}^* + H^* \tag{3.6}$$

II. $$CH_3^* + {}^* \rightleftarrows CH_2^* + H^* \quad (3.7)$$

III. $$CH_2^* + {}^* \rightleftarrows CH^* + H^* \quad (3.8)$$

IV. $$CH^* + {}^* \rightleftarrows C^* + H^* \quad (3.9)$$

V. $$H_2O + 2^* \rightleftarrows HO^* + H^* \quad (3.10)$$

VI. $$C^* + O^* \rightleftarrows CO^* + {}^* \quad (3.11)$$

VII. $$C^* + O^* \rightleftarrows CO^* + {}^* \quad (3.12)$$

VIII. $$C^* + HO^* \rightleftarrows CHO^* + {}^* \quad (3.13)$$

IX. $$CHO^* + {}^* \rightleftarrows CO^* + H^* \quad (3.14)$$

X. $$CO^* \rightleftarrows CO + {}^* \quad (3.15)$$

XI. $$2H^* \rightleftarrows H_2 + 2^* \quad (3.16)$$

where * denotes an active site of the catalyst. General agreement is on the dominating role of reaction I. However there is disagreement if reactions V and VII should also be considered as the rate determining steps [39]. The different studies incorporating the Langmuir-Hinshelwood approach for deriving kinetics proposes various final equations [39]. The exemplary reforming reaction kinetics derived from the Langmuir-Hinshelwood approach were presented by Peters [38], who followed the classical reaction set composed of reactions 1-3 (Eqs. (3.3), (3.4) and (3.5)):

$$r = k \frac{K_{ad,CH_4} K_{ad,H_2O} p_{CH_4} p_{H_2O}}{\left(1 + K_{ad,CH_4} p_{CH_4} + K_{ad,H_2O} p_{H_2O} + K_{ad,CO} p_{CO}\right)^2} \quad (3.17)$$

and by Bebelis [193], who assumed reactions I and VII as a rate determining step:

$$r = k_{ad,CH_4} p_{CH_4} \left(1 - \frac{k_{ad,CH_4}}{k_{VII} K_{ad,H_2O}} \frac{p_{H_2} p_{CH_4}}{p_{H_2O}}\right) \quad (3.18)$$

One of the possible explanations of the variation in the proposed reaction equations is that reactions I and VII are both dominating the overall process, but in the different temperature ranges. It is postulated that dissociative adsorption of methane (reaction I) is kinetically

controlling at high temperatures, while carbon oxide formation (reaction VII) is dominant in lower ones [194,195]. Moreover, many different expressions with different constants and acceptable fit to the experimental data can be derived from the Langmuir-Hinshelwood scheme. It is especially influential when the dominant reaction, and therefore the reaction kinetics of the process, can be potentially varied with changes in temperature.

The investigation by Wei and Iglesia uses the method of isotopic tracing the elementary steps of the steam reforming and water-gas-shift reaction [32]. They concluded that they are in quasi-equilibrium and the rate-determining step is reaction I. Therefore, the overall expression for the methane/steam reforming reaction with water-gas-shift reaction and hydrogen formation is first order dependence in relation to methane partial pressure. The results of investigations are summarize in Fig. 3.1.

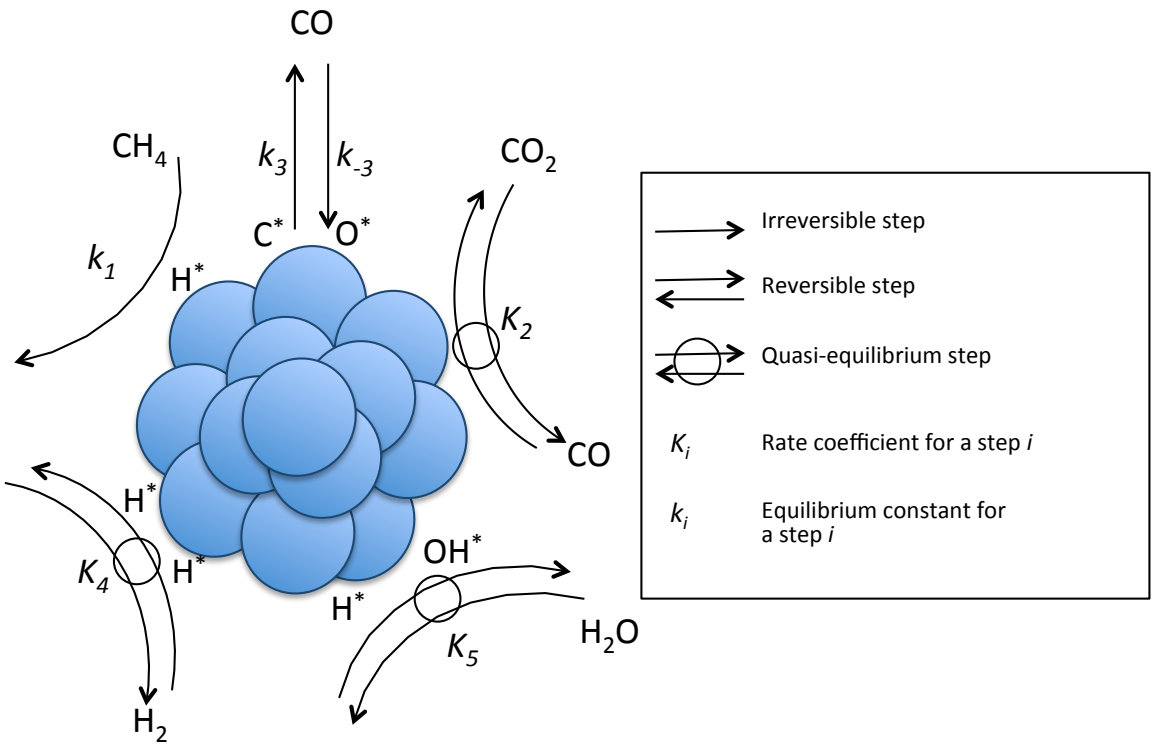

Figure 3.1 Sequence of the elementary steps for the methane steam reforming on the Ni catalyst according to Wei and Iglesia [32]

Wei and Iglesia conducted also wide research on the kinetic of the reforming process on various catalysts by the packed bed method [32,154,196,197]. The result were fitted for the general expression in approach to equilibrium, where net CH_4 conversion is determined as:

$$r_n = r_f\left(1 - \frac{Q_{sr}}{K_{sr}}\right) \tag{3.19}$$

where r_f denotes the forward reaction rate, K_{sr} stands for the equilibrium constant for steam reforming and Q is expressed by the following formula:

$$Q_{sr} = \frac{\prod p_{products}}{\prod p_{reactants}} \tag{3.20}$$

It was found that the forward reaction is dependent only on the partial pressure of methane, with no correlation to partial pressures of other species, including that of a reforming agent. The kinetic was summarized in the form of a simple equation for all of the examined catalysts:

$$r_f = kp_{CH_4} \tag{3.21}$$

A similar approach was presented by the classical work of Achenbach and Riensche [123] who studied methane/steam reforming kinetic dedicated for SOFC application. The proposed methodology was analogical to the study done by Wei and Iglesia, and the final result stated the first order dependency on methane.

It can be noted that the first order kinetic with respect to the partial pressure of methane is equivalent to the Langmuir-Hinshelwood approach with the additional assumptions:

- there is only one rate-determining step and the rate-determining step is dissociative adsorption of methane (reaction I)
- the surface is not covered with other adsorbents

The second assumption is valid in the high temperature and low pressure conditions and those conditions are applicable for standard kinetic derivations.

All of the presented approaches, especially the Langmuir-Hinshelwood methodology, are built on a supplementary assumptions according to the system description, as the quasi-

equilibrium state, one dominating species on the surface of the catalyst or the single rate-determining step. The alternative description of the methane/steam reforming reaction kinetics is expressed in the form of power law expression, which is a most general equation formula, not giving additional conditions and not tracking the elementary steps of chemical reactions. The general form of the kinetic equation is formulated as:

$$r_{CH_4} = k p_{CH_4}^{a} p_{H_2O}^{b} p_{H_2}^{c} p_{CO_2}^{d} p_{CO}^{e} \tag{3.22}$$

In the power law expression approach, general agreement was achieved that the reaction orders of hydrogen, carbon dioxide and carbon oxide, *c*, *d* and *e* respectively, are equal or close to zero. However, the reaction orders of methane and steam, *a* and *b* respectively, as well as reaction constant *k* differs significantly in various studies.

In the present study, the primarily assumed form of the equation describing the methane/steam reforming reaction kinetic is derived by the power law expression with respect to the partial pressures of methane and steam. This approach provides the most general derivation without additional assumptions and simplifications [39] and is superior to the second modelling concept - first order reaction with respect to methane. The power law expression could be reduced to the first order reaction equation if the measured kinetic would be independent of the influence of the steam partial pressure. Moreover, for the modelling of complex SOFC systems, determining the overall reaction rate with the power law equation seems to be the most appropriate approach from the numerical point of view. The time effectiveness of the model requires a fast convergence algorithm providing the correct prediction of the anode behaviour – to achieve those objectives usually the power law form of the equation is adopted [113,115,116,131,198].

3.2 Power law expression adopted for the evaluation of the reaction kinetics

In the power law expression with respect to the partial pressures of methane and steam, the reaction rate of the methane/steam reforming reaction can be presented in the form of the following equations:

$$r = k\left(p_{CH_4}\right)^a \left(p_{H_2O}\right)^b$$
$$k = A\exp\left(\frac{-E}{RT}\right) \tag{3.23}$$

where r is the reaction rate [mol s^{-1} g^{-1}], k is the reaction constant, p_{CH_4} and p_{H_2O} are the partial pressures of CH_4 and H_2O [Pa], a and b are the reaction order coefficients, A [-] is the pre-exponential factor [mol g^{-1} s^{-1} $Pa^{-(a+b)}$], E is the activation energy [J mol^{-1}], R is the universal gas constant (R = 8.314 J mol^{-1} K^{-1}) and T is the temperature [K]. On the other hand, the rate of water-gas-shift reaction r_{shift} [mol s^{-1} g^{-1}] is calculated as:

$$r_{shift} = K^+_{shift} p_{CO} p_{H_2O} - K^-_{shift} p_{H_2} p_{CO_2} \tag{3.24}$$

where p_{H_2}, p_{CO_2}, p_{CO} and p_{H_2O} are the partial pressures of H_2, CO_2, CO and H_2O [Pa]. K^+_{shift} and K^-_{shift} stands respectively for forward rate constant and backward rate constant [-].The water-gas-shift reaction is a fast process and reaches equilibrium instantaneously, therefore it is assumed that the partial pressures of the species satisfies the equilibrium equation and this chemical equilibrium is represented by the equilibrium constant K_{shift} [-]:

$$K_{shift} = \frac{K^+_{shift}}{K^-_{shift}} = \frac{p_{H_2} p_{CO_2}}{p_{CO} p_{H_2O}} \tag{3.25}$$

On the other hand, the equilibrium constant is the temperature function:

$$K_{shift} = \exp\ K_{shift} = \exp\left(\frac{-\Delta G^0_{shift}}{RT}\right) \tag{3.26}$$

where, ΔG^0_{shift} denotes the change in standard Gibbs free energy of water-gas-shift reaction [J mol^{-1}], R is the universal gas constant [J mol^{-1} K^{-1}], and T determines the reaction temperature [K].

It can be concluded that the reforming process is defined by the values of the empirical parameters describing the reaction: reaction order coefficients *a* and *b*, activation energy *E*, and a pre-exponential factor *A*. Therefore, in order to achieve the primeval goal, establishing the methodology for the evaluation of the reaction kinetics of the reforming process, two steps has to be accomplished; proposing the methodology of determining empirical constants *a*, *b*, *A* and *E* and then building a model to find the composition of the reformed gas.

3.3 Methane/steam reforming reaction in a Plug Flow Reactor

The assumed reactor model is a Plug Flow Reactor (PFR) used to describe the chemical process in continuous, flowing system of cylindrical geometry. The PFR systems are operated under steady-state conditions with no accumulation of mass in the volume – the flow is entering an open system and leaving its boundaries of reaction zone. For conducting the calculation with the model of ideal isothermal PFR, the small volume element (plug) is considered under succeeding assumptions:

1. Radial mixing is indefinitely rapid so that each plug of fluid is uniform in the distribution of temperature, pressure, composition and etc.
2. There is no longitudinal (axial) mixing between these plugs as they move through reactor
3. All volume elements move through reactor in the same amount of time [199].

The schematic idea of modelling Plug Flow Reactor is presented in Fig. 3.2. The limiting reactant A is subject of the mass balance in the differential volume element: the entering rate flow of A is equal to the sum of the exuding flow rate of reactant A decreased by the rate of the disappearance of A by the chemical reaction [199]:

$$F_{\mathrm{A}} = \left(F_{\mathrm{A}} + \mathrm{d}F_{\mathrm{A}}\right) + \left(-r_{\mathrm{A}}^{\mathrm{v}}\right)\mathrm{d}V_{\mathrm{r}} \tag{3.27}$$

where F_{A} is the molar flow rate of reactant A [mol s^{-1}], the volumetric reaction rate is described as $r_{\mathrm{A}}{}^{\mathrm{v}}$ [mol m^{-3} s^{-1}] and $\mathrm{d}V_{\mathrm{r}}$ is considered the differential volume element.

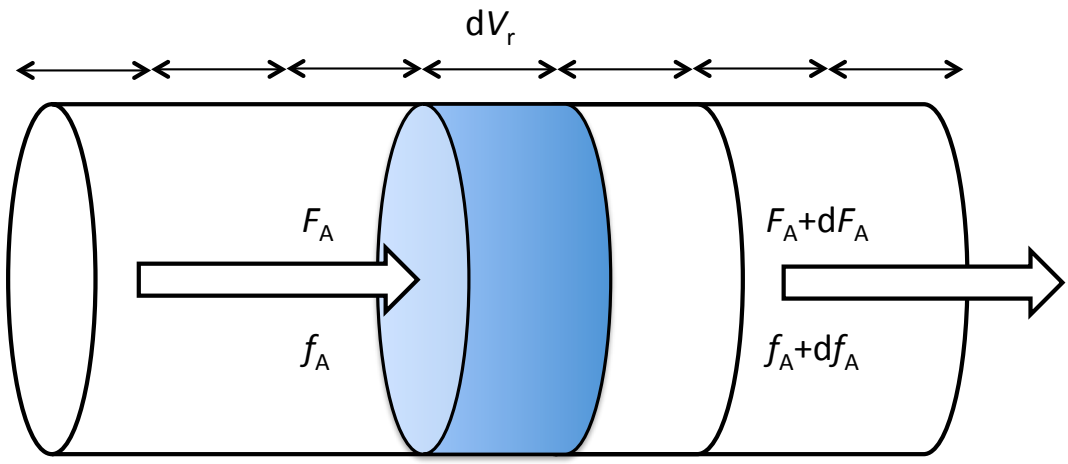

Figure 3.2 Schema of plug flow reactor: a differential volume element dV_r with flow rate F and fractional conversion f of the limiting reactant A [199]

The local molar flow rate of reactant A can be described as the function of local dimensionless fractional conversion f_A and the initial input flow rate of this reactant F_A^i [mol s^{-1}]:

$$F_A = F_A^i\left(1 - f_A\right) \tag{3.28}$$

and after operation of differentiation:

$$dF_A = -F_A^i df_A \tag{3.29}$$

Then, after rearranging equation in Eq. (3.29) and combining it with Eq. (3.28), it becomes:

$$\frac{dV_R}{F_A^i} = -\frac{df_A}{r_A^V} \tag{3.30}$$

which can be integrated over the entire reaction volume:

$$\frac{V_R}{F_A^i} = \int_{f_A^i}^{f_A^o} \frac{df_A}{-r_A^V} \tag{3.31}$$

In the fixed-bed reactor, in the laboratory applications, when the packing density is known, then Eq. (3.31) is modified to the dependence of the rate of reaction per unit mass of catalyst R_A [mol kg s^{-1}] and the mass of the catalyst in the reactor w_{cat}:

$$\frac{w_{cat}}{F_A^{\,i}} = \int_{f_A^{\,i}}^{f_A^{\,o}} \frac{df_A}{-r_A} \tag{3.32}$$

Generally, in laboratory experimentation, the weight of the catalyst and the input flow of the reactant are known. The initial fractional conversion $f_A^{\,i}$ is equals to 0 and the final outlet conversion $f_A^{\,o}$ is measured.

3.4 Conversion of methane and basic definitions

The stoichiometry of the fuel reforming reaction and water-gas-shift reaction (in Eqs. (3.1) and (3.2)) defines the changes in the chemical composition of the reactants resulting from those processes. The changes induced by both of them are presented in Table 3.1. As included in Table 3.1, nitrogen has flowed into the reactor, although it does not affect the reforming process itself. Nitrogen was used in the experimental studies in order to diversify and decrease the partial pressures of other species in the system. The process was conditioned by changing the flow rates of the methane, steam and nitrogen in the inlet gas; the abbreviation *SC* stands for steam-to-carbon ratio [-] and *NC* is nitrogen-to-carbon ratio [-]. The dimensionless methane and carbon oxide conversion rate were designated respectively as *x* and *y*.

On the basis of the stoichiometry of the Steam Reforming reaction and Water-Gas-Shift reaction presented in Table 3.1, the following formulas for determining partial pressures of all chemical species in the system, methane, hydrogen, water, carbon dioxide, carbon monoxide and nitrogen, can be presented:

$$p_{CH_4} = \frac{1-x}{1+SC+NC+2x} P \tag{3.33}$$

$$p_{H_2} = \frac{3x + y}{1 + SC + NC + 2x} P \tag{3.34}$$

$$p_{H_2O} = \frac{SC - x - y}{1 + SC + NC + 2x} P \tag{3.35}$$

$$p_{CO_2} = \frac{y}{1 + SC + NC + 2x} P \tag{3.36}$$

$$p_{CO} = \frac{x - y}{1 + SC + NC + 2x} P \tag{3.37}$$

$$p_{N_2} = \frac{NC}{1 + SC + NC + 2x} P \tag{3.38}$$

where P designates the total pressure. Note that the total pressure here should be the one at the reaction site, however, it is difficult to determine precisely. Instead of that, the present study uses the average pressure at the reaction site inlet and its outlet. This is a very important concern for both of the evaluation procedures of the reaction kinetics: classic or modified approaches (will be introduced in the next section).

Table 3.1 Changes of the chemical species during the steam reforming process derived on the basis of the stoichiometry of the chemical reactions governing the process

Gas	Input Flow	Steam Reforming Reaction	Water-Gas-Shift Reaction	Outlet Flow
CH_4	$F^i_{CH_4}$	$-x \cdot F^i_{CH_4}$	0	$(1-x) \cdot F^i_{CH_4}$
H_2O	$SC \cdot F^i_{CH_4}$	$-x \cdot F^i_{CH_4}$	$-y \cdot F^i_{CH_4}$	$(SC-x-y) \cdot F^i_{CH_4}$
H_2	0	$+3x \cdot F^i_{CH_4}$	$y \cdot F^i_{CH_4}$	$(3x+y) \cdot F^i_{CH_4}$
CO	0	$+x \cdot F^i_{CH_4}$	$-y \cdot F^i_{CH_4}$	$(x-y) \cdot F^i_{CH_4}$
CO_2	0	0	$y \cdot F^i_{CH_4}$	$y \cdot F^i_{CH_4}$
N_2	$NC \cdot F^i_{CH_4}$	0	0	$NC \cdot F^i_{CH_4}$
Total	$(1+SC+NC) \cdot F^i_{CH_4}$	$+2x \cdot F^i_{CH_4}$	0	$(1+SC+NC+2x) \cdot F^i_{CH_4}$

The conversion rate (fractional conversion) of methane can be calculated on the basis of the composition of the outlet gas as it was presented by Itoh et al. [184,200]:

$$x = \frac{m_{CO} + m_{CO_2}}{m_{CO} + m_{CO_2} + m_{CH_4}} \tag{3.39}$$

where m_{CO}, m_{CO_2} and m_{CH_4} are the output molar fraction of carbon oxide, carbon dioxide and methane. On the other hand, the conversion rate of the carbon oxide *y,* resulted from water-gas-shift reaction (Eq. (3.2)), is estimated on the basis of the equilibrium reaction (Eq. (3.25)), where the partial pressures of the chemical species are defined by formulas Eqs. (3.33), (3.34), (3.35), (3.36), (3.37) and (3.38):

$$K_{sh}\left(x-y\right)\left(SC-x-y\right) = y\left(3x+y\right) \tag{3.40}$$

After solving the above mentioned quadratic equation, the carbon monoxide conversion rate is determined as:

$$y = \frac{K_{sh}\cdot SC + 3x - \sqrt{\left(K_{sh}\cdot SC + 3x\right)^2 - 4K_{sh}\left(K_{sh}-1\right)\left(SC\cdot x - x^2\right)}}{2\left(K_{sh}-1\right)} \tag{3.41}$$

where K_{shift} is determined as the temperature function from Eq (3.26).

The theory of the Plug Flow Reactors mentioned in Section 3.3 can be in particular applied to the methane/steam reforming process conducted in the present experimentation. The dimensional fractional conversion of methane in the reforming process is defined with the dimensionless conversion rate of methane x :

$$F_{CH_4} = F_{CH_4}^{\,i}\left(1-x\right) \tag{3.42}$$

Figure 3.3 presents the correlation between weight of the catalyst in the Plug Flow Reactor and the flow rate of methane at the reactor outlet. Generally, a larger amount of catalytic material, increases the conversion of methane and finally decreases the flow rate of methane at the outlet. This observation is valid only for the case when the amount of catalyst is smaller than w_{eq}; in opposite, when the amount of catalyst is larger , the reaction is in the equilibrium state and no further changes in the amount of reformed methane can be observed. The kinetic of the reaction can be investigated only if the reaction is conducted in the conditions ensuring the non-equilibrium state of the process. In light of preceding restrictions and observations derived in Section 3.3, the correlation between the change in the flow rate of methane and the change in the amount of the catalyst can be expressed as the non-equilibrium reaction rate:

$$r = -\frac{dF_{\mathrm{CH_4}}}{dw_{\mathrm{cat}}} \tag{3.43}$$

where $F_{\mathrm{CH_4}}$ is defined by formula (3.42).

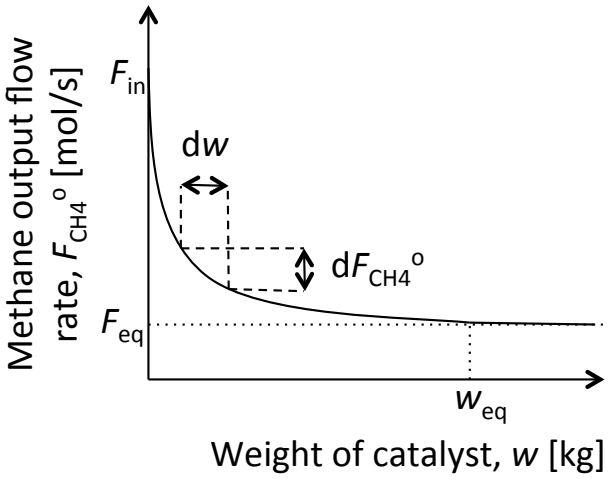

Figure 3.3 Methane flow rate in a function of catalyst weight [94]

Formula in Eq. (3.39), presented for the methane conversion rate, can be expressed in the form of the following differential equation:

$$\frac{w_{\text{cat}}}{F_{\text{CH}_4}^{\text{i}}} = \int_0^x \frac{dx}{-r} \tag{3.44}$$

and by combining it to Eq. (3.39) the final form of the equation defining the reaction constant k is derived (the partial pressures of the chemical components in the system are calculated by the formulas in Eqs. (3.33), (3.34), (3.35), (3.36), (3.37) and (3.38), and derived from the composition of the reactants and products and the stoichiometry of the reactions):

$$k = \frac{F_{\text{CH}_4}^{\text{i}}}{w_{\text{cat}}} \int_0^x \frac{\left(1+SC+NC+2x\right)^{a+b}}{\left(1-x\right)^a \left(SC-x-y\right)^b P^{a+b}} dx \tag{3.45}$$

where a and b are coefficients relevant to the reaction orders on the partial pressure of methane and steam, respectively.

3.5 A standard approach for the analysis of the reaction order coefficients

The first step for determining the methane/steam reforming reaction kinetics proposes an algorithm to estimate the values of reaction constant for various different sets of methane and water flow rates, respectively for determining reaction orders a and b. In the chemical kinetics, the reaction order coefficient is the order of reaction with respect to a given substance (here methane for reaction order a and steam for reaction order b). The reaction order is defined as the index or exponent, to which the concentration of this substance in the rate equation is raised. The reaction orders depend on the reaction mechanism and can be determined experimentally.

Two approaches are proposed to evaluate reaction orders in the methane/steam reforming process: classical and modified. In the classical approach for the estimation of the a and b parameters, their values are calculated separately and laborious experimental measurements, divided for two independent data sets, have to be conducted. The experiment is based on the

assumption, that constant partial pressure is preserved for one of the species: steam or methane.

The determination of the coefficient *a* is done on the basis of measurements conducted with the constant partial pressure of water and the varying partial pressure of methane. Those conditions are achieved by the manipulation of the flow rates of methane and nitrogen and maintaining the constant flow of water. The Steam-to-Carbon *SC* and Nitrogen-to-Carbon *NC* ratios are various for every measurement point.

It can be noticed that the reforming reaction constant *k* depends only on the temperature of reaction as it is described in the formula: $\left(k = A\exp\left(\frac{-E}{RT} \right) \right)$. Because the partial pressure of water is assumed to be constant, the new modified parameter *k'* can be defined:

$$k' = k\left(p_{\mathrm{H_2O}} \right)^{b} \tag{3.46}$$

It can be noticed that the value of this parameter depends only on the reaction temperature *k'=f(T),* it is also constant at a certain level of temperature:

$$T = const \rightarrow k' = const \tag{3.47}$$

Therefore, the reaction rate equation can be rewritten as:

$$r = k'\left(p_{\mathrm{CH_4}} \right)^{a} \tag{3.48}$$

After the transformation, the following linear equation can be obtained:

$$\ln\left(r \right) = \ln\left(k'\left(p_{\mathrm{CH_4}} \right)^{a} \right) = a\ln\left(p_{\mathrm{CH_4}} \right) + \ln\left(k' \right) \tag{3.49}$$

It is denoted that $\ln\left(k' \right)$ is a constant value in the case of a constant temperature. Hence, on the basis of the Eq. (3.49) and the linear approximation of the experimental results presented in a logarithmic graph, the parameter *a* can be found.

Reaction order coefficient *b* can be calculated in the same manner as the coefficient *a* was calculated. The measurements are conducted with the constant partial pressure of methane and the changing partial pressure of water. Those conditions are assured by keeping a constant flow rate of methane and a changing a flow rate of water and nitrogen, which results in the various *SC* and *NC* ratios. To approximate the value of *b* the new reaction constant *k''* is defined:

$$k'' = k\left(p_{\mathrm{CH_4}}\right)^{a} \tag{3.50}$$

This new parameter has constant value at a constant temperature.

$$T = const \rightarrow k'' = const \tag{3.51}$$

Therefore, the reaction rate equation can be rewritten as:

$$r = k''\left(p_{\mathrm{H_2O}}\right)^{b} \tag{3.52}$$

After the transformation, the following linear equation can be obtained:

$$\ln\left(r\right) = \ln\left(k''\left(p_{\mathrm{H_2O}}\right)^{b}\right) = b\ln\left(p_{\mathrm{H_2O}}\right) + \ln\left(k''\right) \tag{3.53}$$

As previously denoted, $\ln\left(k''\right)$ is a constant in the case of a set certain level of temperature. On the basis of the Eq. (3.53) and the linear approximation of the experimental results presented in a logarithmic graph, parameter *b* can be found.

In general, in order to determine the values of the parameters *a* and *b* in the classical approach, the several different experiments need to be performed in various temperature conditions with different values of *SC* and *NC* ratios. During all experimental investigations, it is assumed that the total molar flow rate of substances in the process is all the time constant to ensure the constant gas space hourly velocity (GHSV), and the molar flow rate of one of the species, water or methane, is kept at a constant. The parameters *a* and *b* are determined separately, on the basis of different measurement sets conducted at a certain level of temperature. The algorithm of the classical approach used to determine reaction orders is presented in Fig. 3.4.

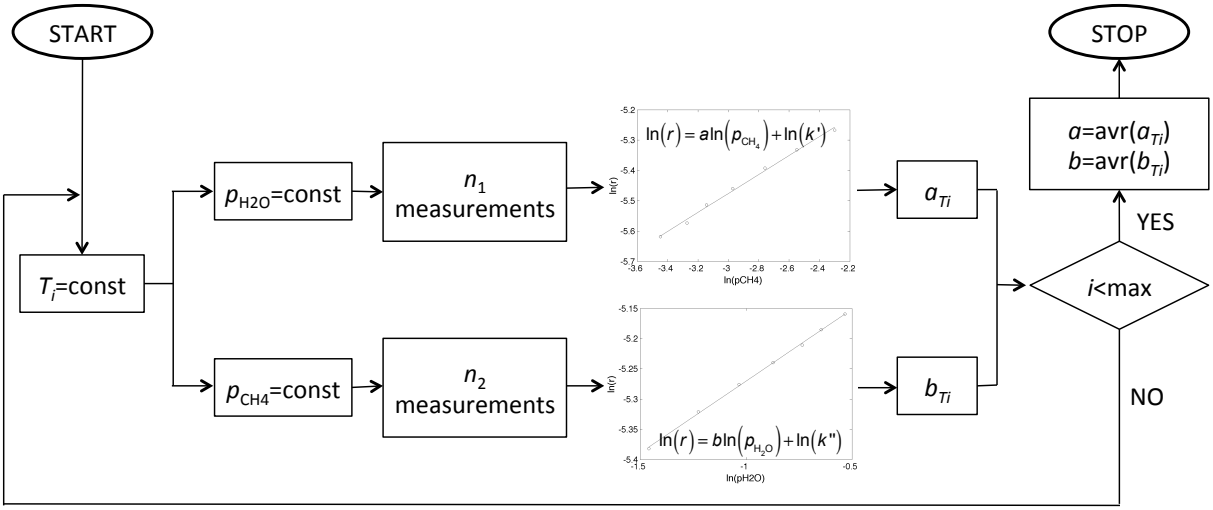

Figure 3.4 Algorithm of standard approach to evaluate reaction orders *a* and *b*

3.6 A modified approach for the analysis of reaction order coefficients

The modified approach for the calculation of the reaction order coefficients *a* and *b* is based on the combined experimental-numerical methodology proposed by Odegard [147] and modified by Brus et al. [59]. The modified method significantly decreases the number of necessary experimental measurements and provides the higher independency and reliability improved by the reduced experimental errors. As it does not impose the assumption of constant partial pressures of any of the species, the approach is more general. The experiment is conducted in various temperatures, however, the parameter *a* and *b* are considered to be calculated simultaneously on the basis of the same experimental measurements.

The modified approach is based on the observation, which was described in the previous Section 3.5, that the reaction constant is independent of the assumed *SC* and *NC* ratios in the constant temperature:

$$k = A\exp\left(\frac{-E}{RT}\right) \tag{3.54}$$

Despite this independency during the experimentation step, the *SC* and *NC* ratios characterizing the experimental conditions were widely and properly dispersed to minimize the influence of the possible measurement uncertainties and deviation found on their results.

The experimental conditions were set to keep the total inlet flow rate at a constant level. For various *SC* and *NC* ratios, the reaction constant should have the same value. Different combinations of the parameters *a* and *b* in the preliminary assumed intervals are tested and used to calculate the reaction constants. The values of the reaction constant were compared with the experimental results from the conditions, at which widely dispersed *SC* and *NC* ratios were applied. For each computation conducted for different temperature experimental conditions, the possible coefficients *a* and *b*, at which the results shows the smallest standard deviation found on the reaction constant *k*, were selected. The relative standard deviation RSD_k is expressed as follows:

$$RSD_k = \frac{\sqrt{\sum_{j=1}^{n}\left(k_i - k_{ave}\right)^2}}{n \cdot k_{ave}} \quad \left(i = 1,2,\cdots,n\right) \tag{3.55}$$

where, n and k_{ave} stand for the number of measurements and the average of the reaction constant k at each temperature condition, respectively. In this stage, the reaction constant k was derived by the following observation presented in Section 3.3: the non-equilibrium reaction for the plug flow reactor rate can be described as a ratio between the change in the flow rate of methane and the change in the amount of catalyst [199]. Therefore, for constant temperatures the reaction constant is the function of the reaction rate parameters:

$$k_i = k_i\left(a,b\right) = \frac{F_{\mathrm{CH_4}}^{\mathrm{i}}}{w_{\mathrm{cat}}} \int_0^x \frac{\left(1 + SC + NC + 2x\right)^{a+b}}{\left(1-x\right)^a \left(SC - x - y\right)^b P^{a+b}} dx \tag{3.56}$$

The modified algorithm provides a possibility to conduct two types of averaging the result in the different temperature conditions: separating calculations for every temperature and then using the arithmetical average to obtain final value of the reaction orders or including all of the temperatures in the parallel calculation of the summed relative standard deviation for all of the temperatures. The later version of the algorithm, assuming the modified averaging procedure, is presented in Fig. 3.5.

In this study, the range of tested parameters *a* and *b* was chosen in accordance with published data [59,147,150] as the intervals [0; 1.5] and [-0.5; 0.5] respectively for reaction orders *a* and *b*.

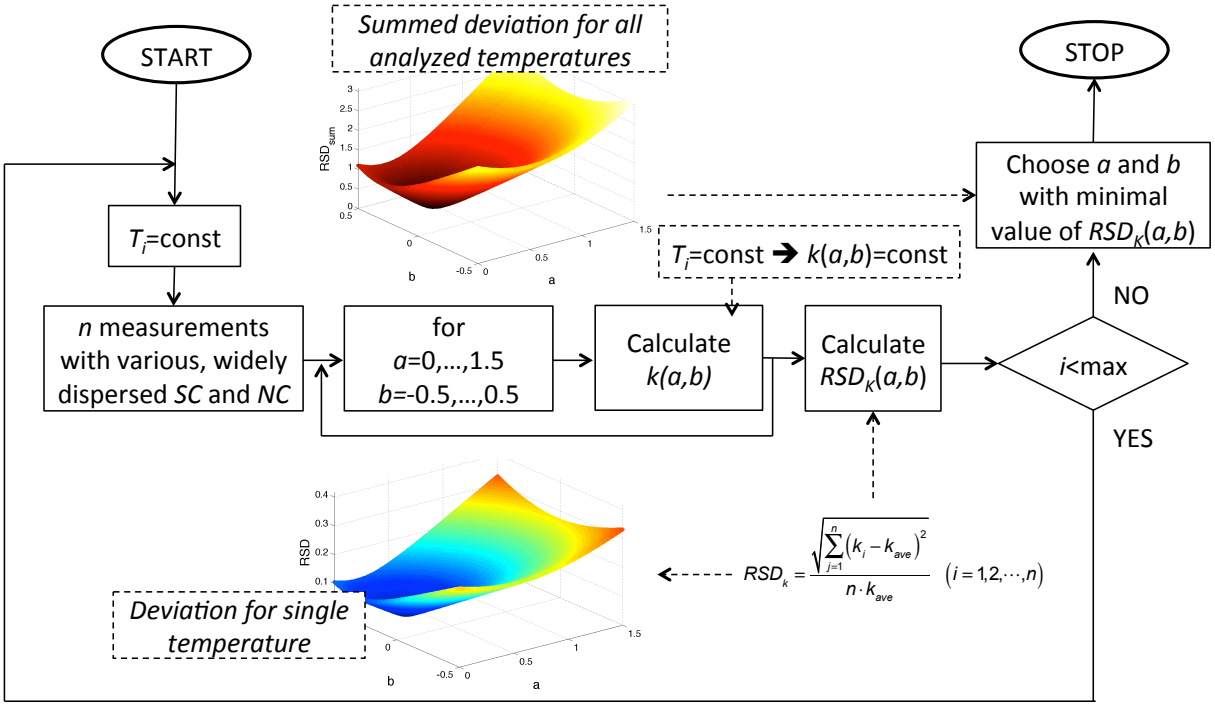

Figure 3.5 Algorithm of the modified approach to evaluate reaction orders *a* and *b*

3.7 The calculation of activation energy and Arrhenius constant

In order to develop a full kinetic model of methane/steam reforming reaction, the approximation of the activation energy and Arrhenius pre exponential factor is necessary. The applied method is derived from the formula for temperature dependence of the reaction rates proposed by Svante Arrhenius in 1889 [201]. Activation energy *E* is the minimum that energy molecules must possess in order to react.

The Arrhenius plot presents the correlation between logarithms of kinetic constant $\ln(k)$ on the ordinate axis displayed against the inverse temperature $\frac{1}{T}$ as abscissa and it can be used to find both the activation energy and the pre-exponential factor. The experimental data are plotted on the graph; the reaction constant is calculated from Eq. (3.45) with the values of the reaction rates estimated in the previous step of derivations by the standard or the modified method described respectively in the Section 3.5 and 3.6. Then, the experimental data are

fitted as a straight line by the ordinal method of least squares: The slope of the Arrhenius plot determines the value of the activation energy and by extrapolating the approximation line to the intercept point with the *y*-axis the pre-exponential factor is calculated. The general idea of the Arrhenius plot is presented in Fig. 3.6.

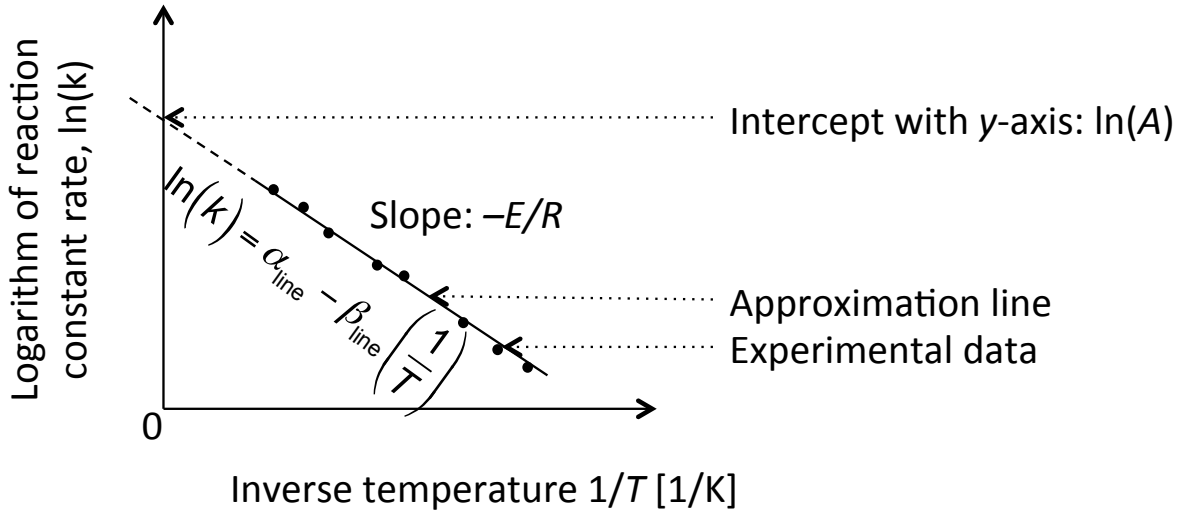

Figure 3.6 Arrhenius plot for calculation of activation energy and pre-exponential constant

The linear approximation of the data plotted on the Arrhenius graph has the form:

$$\ln\left(k\right)=\beta_{\text{line}}-\alpha_{\text{line}}\left(\frac{1}{T}\right) \tag{3.57}$$

On the other hand, the equation defining the correlation between the kinetic constant and the temperature (in Eq.(3.23)) can be presented in logarithmic form:

$$\ln\left(k\right)=\ln\left(A\right)-\frac{E}{R}\left(\frac{1}{T}\right) \tag{3.58}$$

By comparing formulas in Eqs. (3.57) and (3.58) the final values of the activation energy and the pre-exponential factor (known as Arrhenius constant) are calculated.

It can be noticed, that the Eq. (3.23) uses as the denominator of the exponential function factor containing the gas constant *R* and temperature *T*. This form of the Arrhenius equation is characteristic, when the formula is depended on the moles of the substance (unit of gas

constant R is J mol^{-1} K^{-1}). When the molecules of the substance are considered, the Boltzmann constant replaces the gas constant in the denominator.

3.8 An algorithm for the calculation of reaction kinetics

The outlet gas composition is calculated as the sum of the initial composition and change in the amount of every chemical species caused by the occurrence of the reactions. The proposition for the calculation algorithm is presented in Fig. 3.7. The inputs to the numerical procedure are the conditions of the process: temperature, pressure, amount of the catalyst, molar flow rate of methane and the *SC* and *NC* ratios. The initial partial pressures are used to calculate initial partial pressures of methane and water. Those values are later used to calculate the reaction rate and therefore the changes in the chemical composition and finally the gas composition at the outlet of reaction tube. Subsequently, the outlet partial pressure of methane and water are calculated from the new gas composition. The procedure is then repeated until good convergence is obtained and the partial pressures and gas composition in step j+1 are calculated from the composition and changes derived from the condition characterizing step j. The output of the numerical procedure is the composition of the reformed gas, molar fraction of the each chemical species in the dry gas composition and the reforming rate value.

The calculation formulas in the simulation model are derived directly from the mathematical description of the process presented in Sections 3.2-3.4. In particular, partial pressures of all of the chemical species are calculated on the basis of the conversion rates in the reactions of the fuel reforming of methane and water-gas-shift reaction described by formulas in Eqs. (3.33), (3.34), (3.35), (3.36), (3.37) and (3.38). The reaction rate R_{st} [mol min^{-1}] in the system is calculated from the assumed amount of catalyst and Eq. (3.23), which particularly has the following form:

$$R_{st} = w_{cat} r_{st} = w_{cat} A \exp\left(\frac{-E}{RT}\right)\left(p_{CH_4}\right)^a \left(p_{H_2O}\right)^b \tag{3.59}$$

The outlet flows of the species is defined as:

$$n_s^{\,o} = n_s^{\,i} + \Delta n_s, \text{ where } s,k \text{ are chemical species of } CH_4,\ H_2,\ CO,\ CO_2,\ H_2O,\ N_2 \qquad (3.60)$$

where the consumption or the production of each of the chemical substance is calculated as follows:

$$\begin{aligned}
\Delta n_{CH_4} &= -R_{st} \\
\Delta n_{H_2} &= 3R_{st} + R_{sh} \\
\Delta n_{CO} &= R_{st} - R_{sh} \\
\Delta n_{CO_2} &= R_{st} \\
\Delta n_{H_2O} &= -R_{st} - R_{sh} \\
\Delta n_{N_2} &= 0
\end{aligned} \qquad (3.61)$$

It is assumed that the dry outlet gas consists of methane, hydrogen, carbon monoxide and carbon dioxide. The nitrogen used in the experimentation does not influence the pathway of the reactions and its molar flow is not changed during the process. Therefore, the molar fraction of each species in the dry gas composition of the outlet gas are expressed as:

$$m_s = \frac{n_s^{\,o}}{\sum_k n_k^{\,o}}, \text{ where } s,k \text{ are chemical species of } CH_4,\ H_2,\ CO,\ CO_2 \qquad (3.62)$$

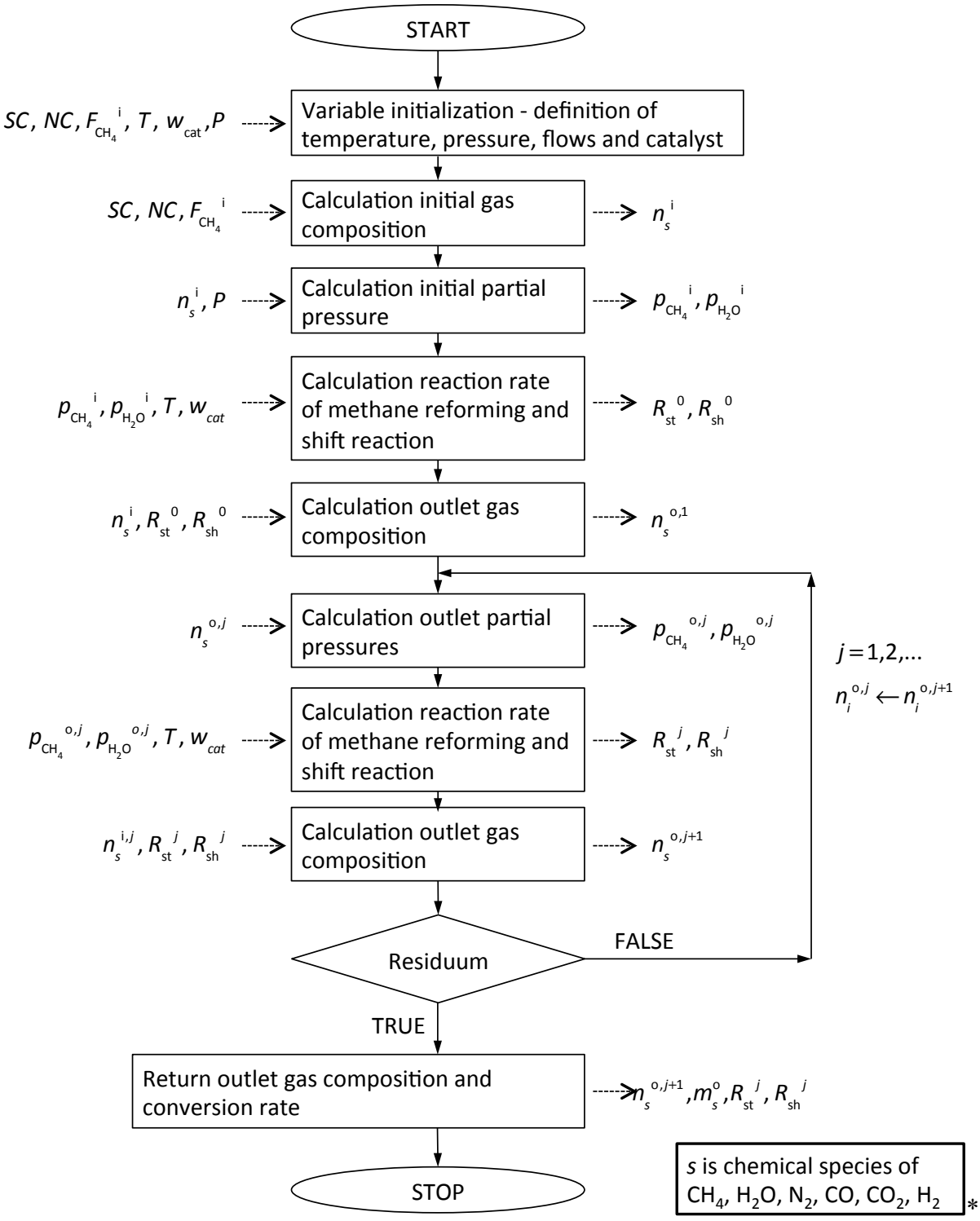

Figure 3.7 Schema of the numerical algorithm for calculation of reaction kinetic from the derived kinetic equation

4 Experimental studies

The experimental studies were conducted in order to evaluate the methane/steam reforming kinetic on various nickel-based catalyst materials. Experimentation was carried out in the plug-flow reactor with two main types of catalyst: commercial Ni/YSZ powder and catalyst prepared as crushed, sintered anodes. The anodes were prepared in an analogical process to the production of the SOFC electrode, sintered and crushed into fine powder. The investigations of the anode powders were carried out to validate the influence of the Ni/YSZ volumetric composition on the kinetic of the reaction. In the present chapter the experimental setup, measuring procedure and conditions, as well as the investigated catalysts will be introduced.

4.1 Experimental setup and methodology

Figure 4.1 shows the schema of the experimental setup with a plug-flow reactor for the measurement of the methane/steam reforming reaction kinetic. Three main parts of the system can be noted: the inlet part, where the substrate gases are prepared, the reaction part with the reformer tube placed in the furnace and the outlet part where the product of the reforming reaction is analysed.

The experiment was performed with high purity methane (CH_4) supplied from a gas cylinder via the mass flow controller and water (H_2O) fed by a pump. Additionally, nitrogen (N_2) was also supplied to the reactor to maintain the reforming conversion rate at a low level and to enable deriving the correct reforming kinetics equation, since the reaction has to occur in the entire volume of the catalyst. N_2 does not have a direct influence on the occurring reactions but changes the partial pressures of the components and finally decreases the methane conversion rate. Thus, the gas mixture of CH_4, N_2 and H_2O was supplied to the reaction zone. CH_4 was regulated 200 kPa and supplied with a mass flow controller, N_2 was and also treated in the same way. H_2O was pumped and supplied to the evaporator, which is used at the same time as the preheater for heating the gas mixture.

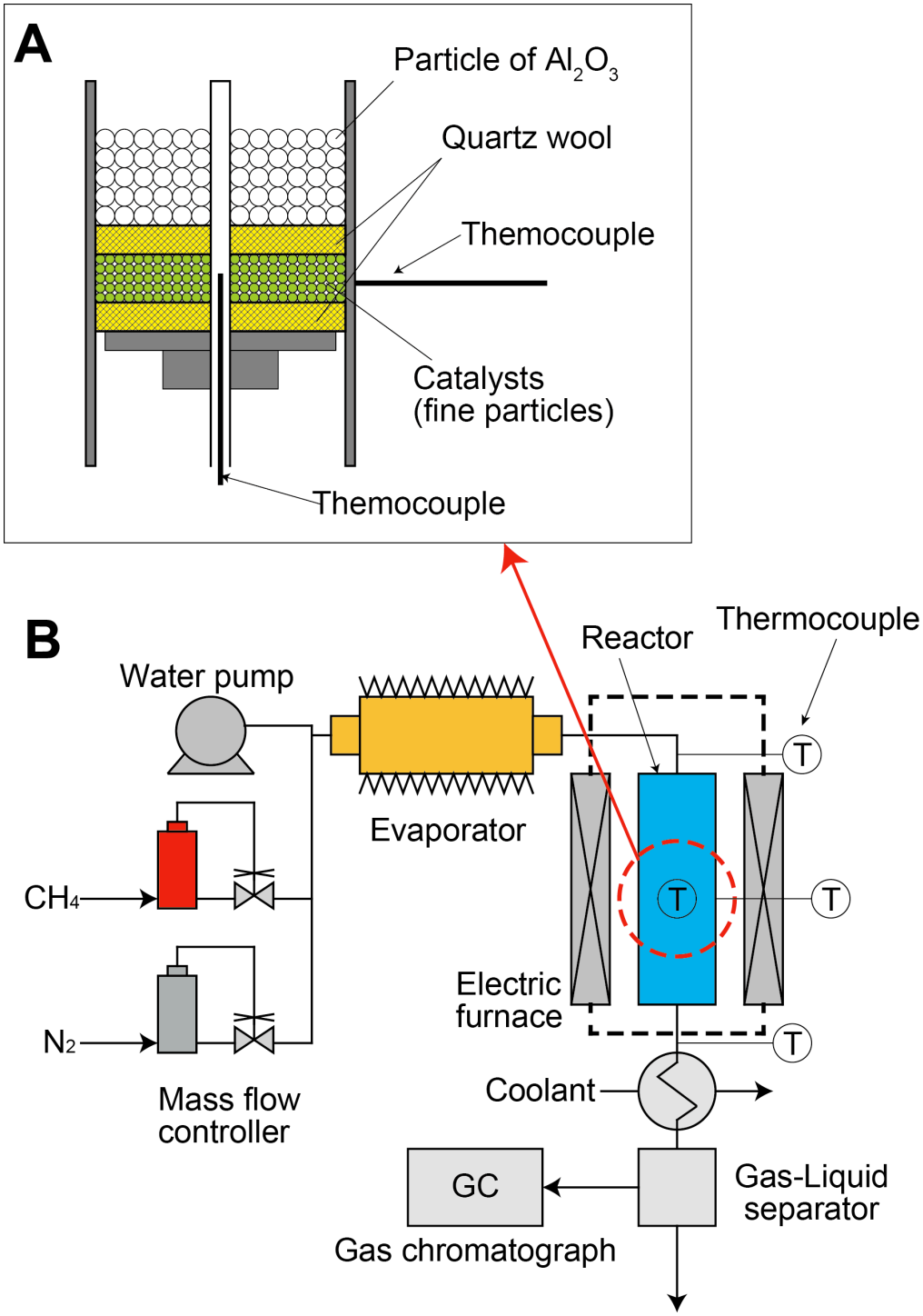

Figure 4.1 Schema of A) reactor and B) experimental setup

The main part of the system is the stainless steel reformer of which the schema is presented in Fig. 4.1A. The fine powder catalyst was dispersed to be a homogeneous distribution over the quartz wool-made bed located in the middle of the reactor. Then, the catalyst layer was covered with the quartz wool and then the half upper of the reactor was fulfilled with Al_2O_3 balls. The catalyst is preceded by Al_2O_3 balls used to prevent a cooling effect of the entering fluid and avoid a large temperature gradient in the reformer. The gas mixture reaches the

reaction zone with the catalyst after preheating by the electric furnace to the reaction temperature. A reformer tube is placed in the electrical furnace with a maximum temperature of 800 ^{o}C. The preheater and after-heater leads to the maximal temperature of 400 ^{o}C, however, the temperature was set at 200 ^{o}C for both of them during the experimental procedure. The temperature of the reactor and the temperature around it are controlled with the thermocouples located before and after the furnace as well as by the thermocouple in vicinity of the reformer (on the surface and inside of the reaction zone).

After the reforming reaction the exhaust gas was analysed by the gas chromatograph (GC390B by GL Sciences). The gas supplied to the gas chromatograph was dried by cooling down the gas mixture to 2 ^{o}C for the preliminary of the chromatography. Two methods of gas detection were used: TCD (Thermal Conductivity Detector) for the methane $m^{o}_{CH_4}$ and hydrogen $m^{o}_{H_2}$ and FID (Flame Ionization Detector) with a methanizer for the carbon monoxide m^{o}_{CO} and carbon dioxide $m^{o}_{CO_2}$ detection, where m stands for the molar fraction of the chemical species and superscript o denotes the measurements at the outlet.

Before conducting the measurements, the catalyst was treated at the evaluated temperature of 600 ^{o}C with a mixture flow of 150 ml min^{-1} nitrogen and 100 ml min^{-1} hydrogen due to the fact that reduction process of NiO. NiO/YSZ had been kept in the reduction process for 6 h for the unsintered catalyst and for 2 h for the sintered material. Additional tests were conducted to assure the stability of the achieved conversion versus the duration of the reduction process to assure that the assumed reduction time is sufficient to fully reduce the catalyst. The measurements were carried out with different conditions based on the various temperatures (in the range of 500-750 ^{o}C), Steam-to-Carbon (*SC*) ratio (in the range of 2.5 - 6) and Nitrogen-to-Carbon (*NC*) ratio (in the range of 0.5 - 6). The details of the experimental conditions will be introduced for every experimental case. *SC* and *NC* were manipulated to satisfy the constant total molar flow rate all of the time in any given condition, in order to keep the Gas Space Hourly Velocity (GSHV) constant. Furthermore, the *SC* and *NC* ratios characterizing the experimental conditions were widely and properly dispersed to minimize the influence of the possible measurement uncertainties in the analysed procedure.

Details of the experimental apparatus are presented in Appendix A.

4.2 Analysis of errors of the measuring devices

One of the goals of the present work is the quantitative evaluation of the effect of acceptable inaccuracies (caused by the specificity of the measurements) on the reforming performance in the form of the rate equation, which is dependent on the empirical parameters. The first step in achieving the goal is determining the uncertainty characteristic for every measurement device.

During the experimentation the following values were measured and later introduced into the the evaluation procedure of the reaction kinetic:

- Catalyst weight, w [g]
- Temperature of the reforming process T [^{o}C]
- Pressure change between inlet and outlet to the reformer tube (used for the estimation of the average pressure in the reaction zone) ΔP [MPa]
- Composition of the inlet gas, defined by: H_4 input flow $F_{CH_4\_v}^{\ i}$ [mL min^{-1}], H_2O input flow $F_{H_2O\_v}^{\ i}$ [mL min^{-1}], N_2 input flow $F_{N_2\_v}^{\ i}$ [mL min^{-1}]
- Composition of the outlet gas, defined by: CH_4 molar fraction in products $m_{CH_4}^{\ o}$ [-], H_2 molar fraction in products $m_{H_2}^{\ o}$ [-], CO_2 molar fraction in products $m_{CO_2}^{\ o}$ [-], CO molar fraction in products $m_{CO}^{\ o}$ [-]

The experimental error of the catalyst weight measurement was estimated on the basis of the measurement accuracy of the laboratory scale. The catalyst weight uncertainty was assumed as: $\sigma_w = \pm 0.0005$ g.

The process temperature was measured by the thermocouple K type by Ichimura Metals and the controller by YOKOKAWA UT150. The uncertainty of the measurement is consistent with the effect of the measurement device, the effect of electricity fluctuation in the grid and the influence of the ambient temperature. The temperature measurement error is determined as:

$$\sigma_T = \pm\left(2 + 0.0007 \cdot T\right) \tag{4.1}$$

The pressure difference between the inlet and outlet of the reformer was measured by the detector from NAGANO KEIKI. The measurement uncertainty of the gauge was assumed as:

$$\sigma_{\Delta P} = \pm 0.3\% \cdot \Delta P[\text{MPa}] \tag{4.2}$$

It can be noticed, that the measured value of the pressure difference has minimal influence on the final results. In the kinetic description the incorporated parameter is the average pressure in the reformer tube, which is in fact calculated from the following formula (it is assumed, that the outlet pressure is 1 atm.):

$$P = \frac{10000}{1013.2}\Delta P + 1[\text{atm}] \tag{4.3}$$

By the applying the fundamental error propagation law:

$$\sigma_y^2 = \sum_i \partial x_i^2 \left(\frac{\partial y}{\partial x_i}\right)^2 \tag{4.4}$$

the uncertainty of the average pressure P is calculated:

$$\sigma = 4.9\sigma_{\Delta P} \tag{4.5}$$

Table 4.1 Measurement uncertainty for the measured pressure difference and the averaged pressure

ΔP [MPa]	$\sigma_{\Delta P}$ [MPa]	P [atm]	σ_P [atm]	Relative error σ_P [%]
0.003	$\pm 9 \cdot 10^{-6}$	1.015	$\pm 4.41 \cdot 10^{-5}$	$\pm 0.0043\% P$
0.006	$\pm 1.8 \cdot 10^{-5}$	1.030	$\pm 8.82 \cdot 10^{-5}$	$\pm 0.0086\% P$
0.009	$\pm 2.7 \cdot 10^{-5}$	1.044	$\pm 1.32 \cdot 10^{-4}$	$\pm 0.013\% P$

The exemplary uncertainties characterizing presser difference 0.003, 0.006 and 0.009 MPa are presented in Table 4.1. The error of the pressure P was calculated and presented in the form of relative error, which for all of the investigated conditions is below $0.00013P$.

The uncertainty of the flow rates of the input gases, methane and nitrogen, and of water was estimated on the basis of the specification of the mass flow controllers and defined as:

$$\sigma_{F^{i}_{\mathrm{CH_4\_v}}} = \pm 0.002 \cdot F^{i}_{\mathrm{CH_4\_v}} \ [\mathrm{ml\ min^{-1}}] \tag{4.6}$$

$$\sigma_{F_{\mathrm{N_2\_v}}{}^{i}} = \pm 0.002 \cdot F_{\mathrm{N_2\_v}}{}^{i} \ [\mathrm{ml\ min^{-1}}] \tag{4.7}$$

for nitrogen and methane gauges. In the case of the flow of water the uncertainty of flow was estimated:

$$\sigma_{F_{\mathrm{H_2O\_v}}{}^{i}} = \pm 0.002 \cdot F_{\mathrm{H_2O\_v}}{}^{i} \ [\mathrm{ml\ min^{-1}}] \tag{4.8}$$

on the basis of the literature and previous research. The additional test was conducted to assure the range of uncertainty for water flow and pump.

After the separation of water from the reformate, the composition of the outlet gas was measured by the gas chromatography by the TCD detector to evaluate the ratios of methane and hydrogen and by the FID detector to calculate ratios of carbon dioxide and carbon monoxide. The errors of gas chromatography were estimated separately for those two detectors and they cannot be assumed only on the basis of the device specification, because gas chromatography accuracy is depended on many factors as for example the accuracy of the calibration curves. In parallel with the experimentation on the methane/steam reforming, supplementary measurements of the composition of the Standard Gas with defined molar composition were carried out. Those measurements were used to estimate the experimental error of gas chromatography by comparing the measured output with the defined composition. The presented analysis contains data from years 2009-2015; the Standard Gas tests were conducted in parallel with the measurement series of the reforming experiment. In the experimentation five cylinders of the Standard Gas with different mixtures of gas were used. The composition of the Standard Gases is listed in Table 4.2. A comparison of the real gas composition with the Gas Chromatography results is presented in Fig. 4.2. The total number of measurements is equal to 182.

Table 4.2 Composition of the standard gas used for the evaluation of the gas chromatography uncertainty

	CH_4	H_2	CO_2	CO
Cylinder 1	28.000	43.218	9.270	3.160
Cylinder 2	27.600	43.964	9.150	3.150
Cylinder 3	27.700	43.527	9.210	3.320
Cylinder 4	27.600	43.540	9.260	3.330
Cylinder 5	27.900	43.188	9.250	3.350

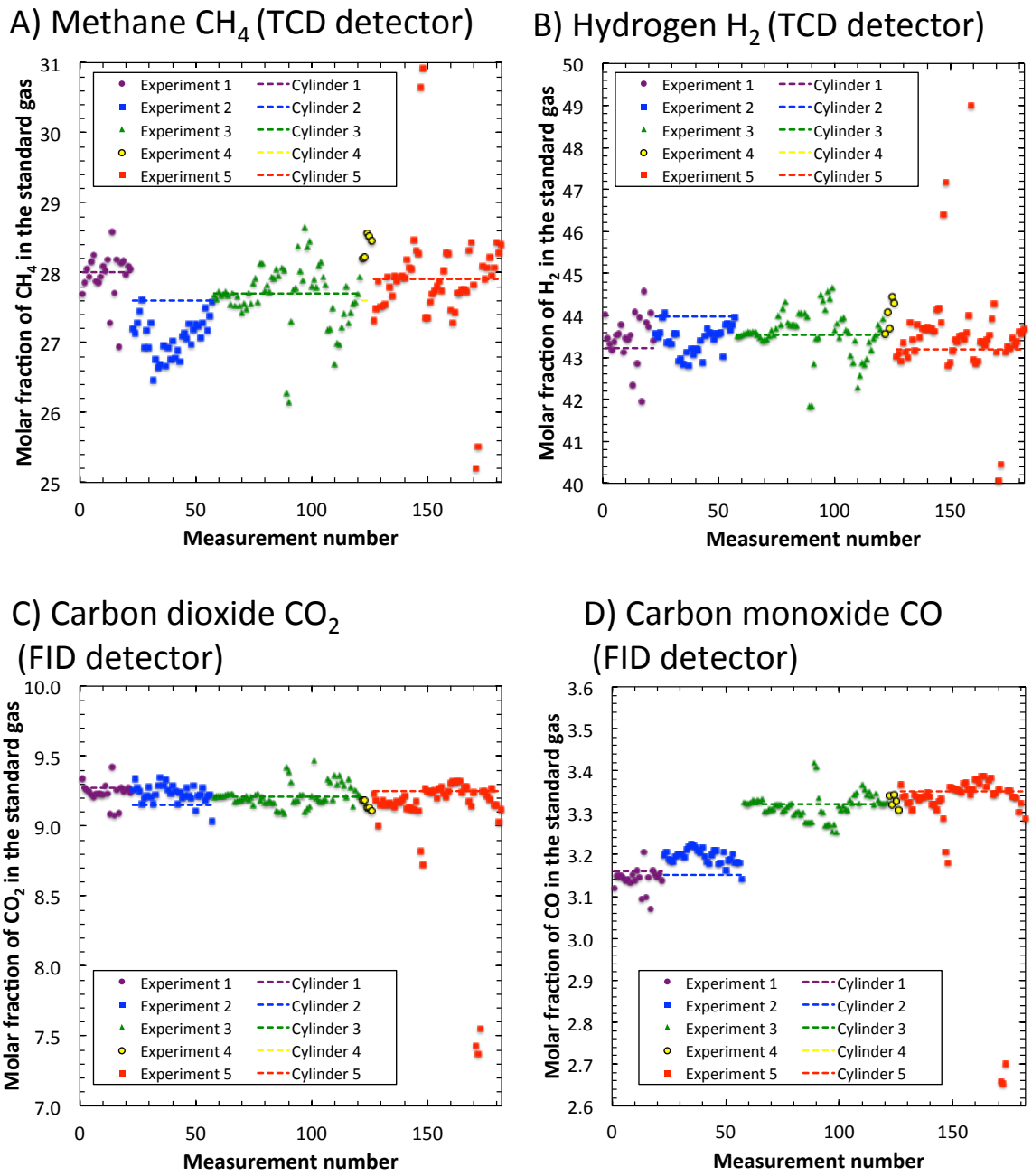

Figure 4.2 The measurements of standard gas composition and the expected value for A) methane, B) hydrogen, C) carbon dioxide and D) carbon monoxide

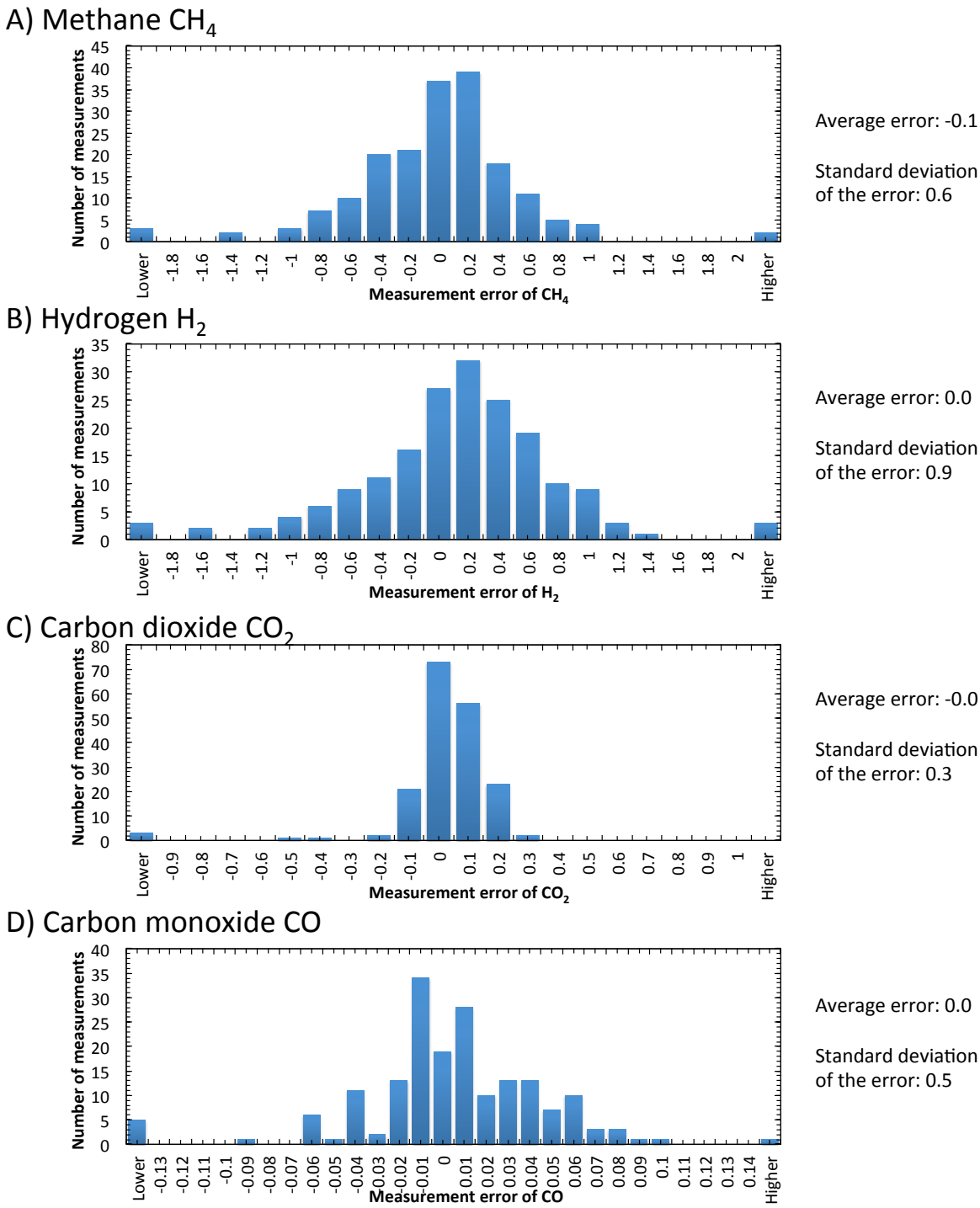

Figure 4.3 Histogram of error distribution for the measurement of the composition of A) methane, B) hydrogen, C) carbon dioxide and D) carbon monoxide in standard gas

Table 4.3 Average error and standard deviation for the measurement of the standard gas composition by gas chromatography

	CH_4	H_2	CO_2	CO
Average of errors	-0.1	0.0	0.0	0.0
Standard deviation of errors	0.64	0.89	0.25	0.45

The differences between real composition of the Standard Gas and measured ratios for all investigated species, which determines the measurement error, are presented in the form of histogram graphs in Fig. 4.3. It can be noticed that all of them have normal distribution with expected value 0 for H_2, CO_2 and CO and -0.1 for CH_4. The average of errors and the standard distributions are summarized in Table 4.3. In the case of the carbon oxide, though the majority of the errors are lower than 0.1, some of the results are much higher and considerably increase the value of the standard deviation.

The final errors of the measurement with the gas chromatograph were assumed as the error of the measurements by the TCD and FID detectors separately, so that the estimation of the uncertainties of methane and hydrogen concentration are the same, and analogically the uncertainty of carbon dioxide and carbon monoxide are assumed to have the same value. The nominal values of the uncertainties were taken as a higher standard deviation estimated during the analysis of the accuracy of Gas Chromatography detectors (TCD and FID) increased by 10%:

$$\sigma_{m_{CH_4}^{o}} = \pm 1 \text{ [-]} \tag{4.9}$$

$$\sigma_{m_{H_2}^{o}} = \pm 1 \text{ [-]} \tag{4.10}$$

$$\sigma_{m_{CO_2}^{o}} = \pm 0.5 \text{ [-]} \tag{4.11}$$

$$\sigma_{m_{CO}^{o}} = \pm 0.5 \text{ [-]} \tag{4.12}$$

4.3 Catalyst material

To investigate the influence of the catalyst properties several various materials were experimentally tested. The focus in the study is put on a Nickel/Yttria-Stabilized Zirconia catalyst material. The Ni/YSZ cermet is often chosen for the anode material of the SOFCs, because it satisfies the following criteria of the requirements: inexpensive fabrication cost, high electrical conductivity, high electrocatalytic activity, stability under reducing environment, thermal expansion and chemical compatibility with other materials composing the SOFC cell layers and it ensures sufficient Three Phase Boundary (TPB) for the electrochemical process [85,202–204]. Moreover, a lot of studies on the reaction kinetics of

the methane/steam reforming reaction over Ni/YSZ catalysts have been published earlier, and numerous inconstancies were found in them.

The investigated catalyst materials are divided into two groups: commercial NiO/YSZ powder and NiO/YSZ powders from sintered anode materials. The first one is industrial non-sintered material of NiO/YSZ (60:40vol.%), provided by AGC SEIMI CHEMICAL CO. LTD. [205]. The material was used to compare derived kinetic with the literatures.

In order to simulate the anode material to derive the kinetic equation applicable for modelling the internal direct reforming process, the cermet material was prepared and sintered at an elevated temperature. Applied preparation methodology followed the classical methods for the fabrication procedure of SOFC anode materials, the so-called solid-phase synthesis. Several methods of the cermet preparation were proposed and tested to design the optimal strategy, which will be useful to prepare an anode material suitable for electrochemical reactions as well as for the reforming process that is expected in the SOFCs. Additionally, the catalysts with various volumetric composition ratios of Ni to YSZ were prepared to understand the influence of the composition ratio for the reaction rate of the reforming process.

The anodes were prepared with YSZ powder and both Ni and NiO powders. The prepared samples can be divided into two groups: Ni/YSZ catalyst materials (prepared compositions were 30:70vol.%, 40:60vol.%, 50:50vol.%, 60:40vol.%, and 70:30vol.%) and a NiO/YSZ catalytic material (the prepared composition ratio after a reduction process gave the composition Ni/YSZ 60:40vol.%). A detailed specification of the prepared anodes is presented in Table 4.4. In the preparation process, the commercial 8mol% Yttria-Stabilized Zirconia (YSZ), fabricated by TOSOH CORPORATION, was used. NiO and Ni powders were acquired from KANTO CHEMICAL CO., INC. To ensure equal distribution of the particles, both powders were mixed together in the ball mill continuously for 24 h with ethanol or acetone dispersants. Afterwards, the ethanol (or acetone) was evaporated in a thermal treatment and the obtained material was mechanically crushed. To provide a proper condition for the viscosity of the slurry, which allows for pressing anode tablets, the methylcellulose (2% water solution) binder in the form of liquid was added to the NiO/YSZ (Ni/YSZ) powder mixture. Methylcellulose (4000cP) power, fabricated by the KANTO CHEMICAL CO., INC was used in the present experiment. The pressed anode pellets were

sintered firstly at a temperature of 400 ^{o}C for 1h to evaporate the binder and then at a temperature of 1400 ^{o}C for at least 5h. The heating rate during sintering the process was set at 10 ^{o}C/min. The schema of the sintering process is presented in Fig. 4.4. Figure 4.5 presents the anodes before and after the sintering process. The size of the NiO/YSZ pellets was constricted in the duration of the sintering process, because of the evaporation of the binding agent. After preparing the anodes, the pellets were crushed mechanically in the mortar for 48 h to obtain fine catalyst powder. The schema of the preparation process is presented in Fig. 4.6.

Table 4.4 Details of the prepared samples with NiO and YSZ powders

Ni [%v]	YSZ [%v]	Mixing type
Samples prepared with NiO and YSZ powders		
60	40	no dispersant
60	40	ethanol
60	40	acetone
Samples prepared with Ni and YSZ powders		
70	30	ethanol
60	40	ethanol
50	50	ethanol
70	30	acetone
60	40	acetone
50	50	acetone
40	60	acetone
30	70	acetone

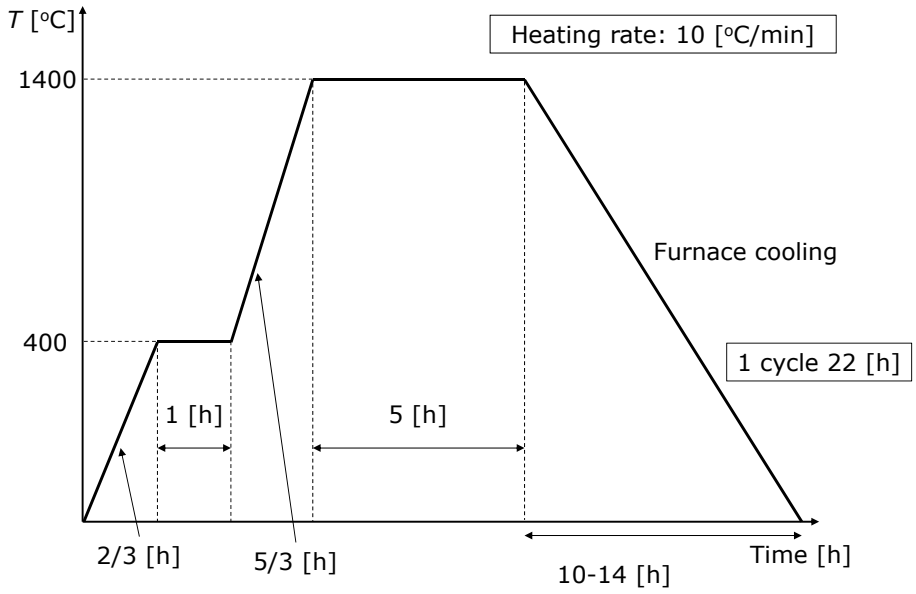

Figure 4.4 Sintering an anode samples

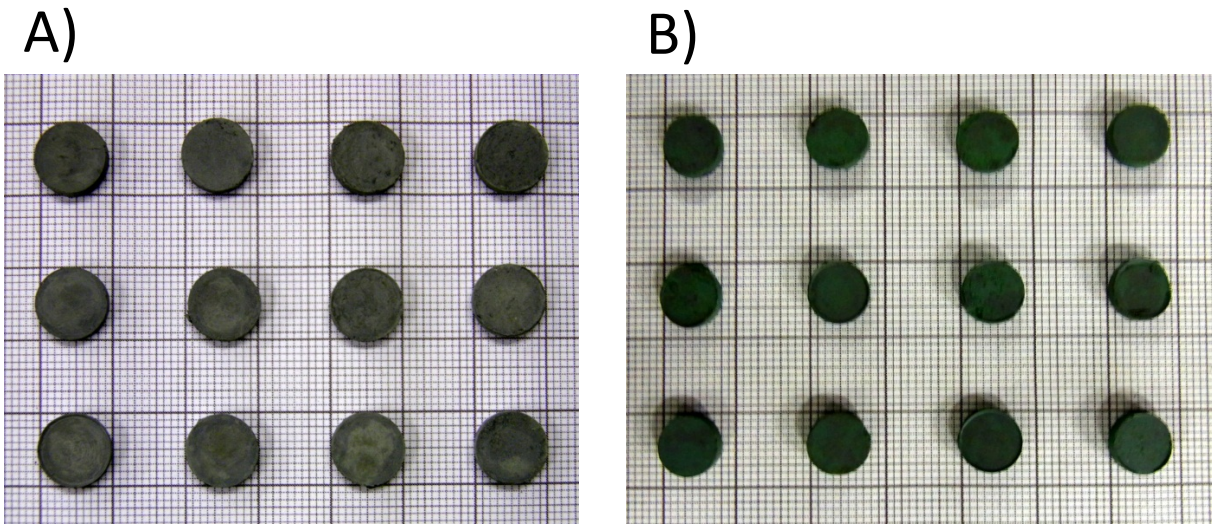

Figure 4.5.A) Anodes before sintering and B) Anodes after sintering

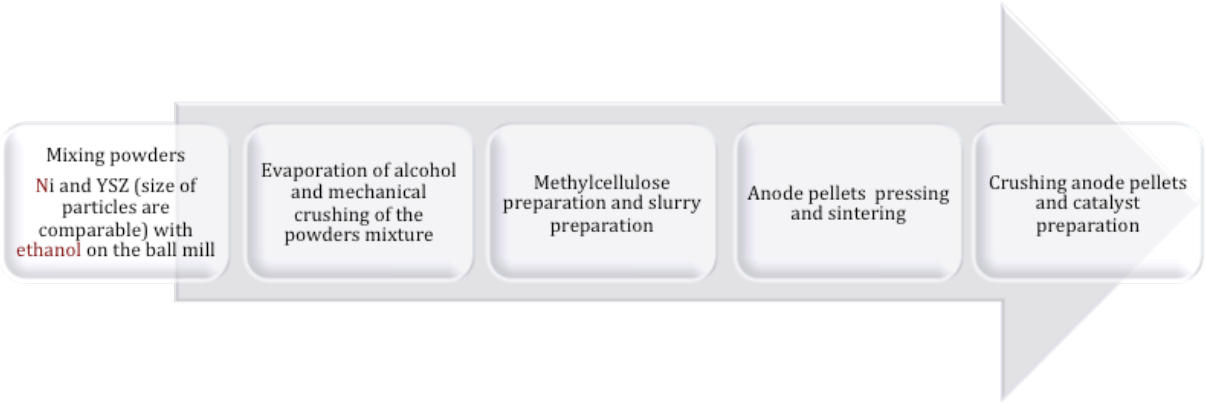

Figure 4.6 Catalyst preparation schema

4.4 Size of the catalyst particles

The microstructure of the applied catalyst highly influences the final conversion rate and therefore determine the various kinetic equations [151]. In the present study, in order to determine the kinetics of the catalysed methane/steam reforming reaction without the influence of the mass transport process, a fine powder catalyst was used [81]. It should be noted that it is possible to include concentration and temperature gradients in the system model, however, in order to obtain accurate overall results a proper reaction kinetic equation is necessary. On the other hand, the accurate kinetic equation can seldom, or even never, be calculated on the basis of the experimental data influenced by the heat and mass transfer limitations [199]. It is crucial to avoid the mass transfer limitations because they can lower the

activity of the catalyst, especially in the case of exponentially fast reactions [81,147,152,153]. All of the investigated catalysts were prepared to fulfil the preceding requirements. In commercial reactors for syngas production, the effects of mass and heat transfer often play significant roles.

Generally, to estimate the catalyst surface area that is actually used for the chemical reaction, the area and the effective thickness of the cermet for steam reforming are needed. However, the discussion about nominal value in the literature is not concluded yet, the Ni catalyst effective thickness used for the SOFC dedicated deliberation is 2 μm [151]. All of the catalysts used in this study were crushed to obtain fine particles with a radius not exceeding the previous value. Therefore, it is assumed that the reforming reaction occurs in the whole volume of the catalyst.

The first catalyst used in the experimentation was industrial, not-sintered NiO/YSZ 60:40vol%, was powder provided by AGC SEIMI CHEMICAL CO. LTD. The catalyst is spherical in shape and has a 0.85 μm diameter with a specific surface area 5.2 m^2 per 1 g of catalyst [205]. The provided raw catalyst samples and the samples after the reforming experiment were investigated by the Scanning Electron Microscopy (SEM). Figure 4.7 presents SEM images of the unsintered industrial catalyst sample before and after conducting the measurement. The spherical shape of the cermet particles can be observed in both of the pictures, however, the occurring deviation from the ideal shape, especially being noticeable for bigger particles, are caused by the rigidity of the sample affecting the crushing process. The change in the structure of the catalyst after the experiment is connected with the reduction of NiO resulting in higher shredding of the final material.

The SEM pictures were also prepared for samples of the experimentally prepared and sintered catalyst. The detailed pictures of the all SEM investigations are presented in Appendix B.1, particularly in Figure B.1 for for the industrial NiO/YSZ powders (60:40vol.% and NiO/SDC powder) by the AGC SEIMI CHEMICAL CO. LTD., and for the laboratory-scale prepared catalysts: Ni/YSZ made of NiO and YSZ powers to satisfy the composition of 60:40vol.% in Fig. B.2, various composition ratios of Ni/YSZ catalysts (70:30vol.%, 60:40vol.%, 50:50vol.%, 40:60vol.% and 30:70vol.%) in Fig. B.3.

A) NiO/YSZ 60:40%vol (AGC Semi Chemical) before experiment

B) NiO/YSZ 60:40%vol (AGC Semi Chemical) after experiment

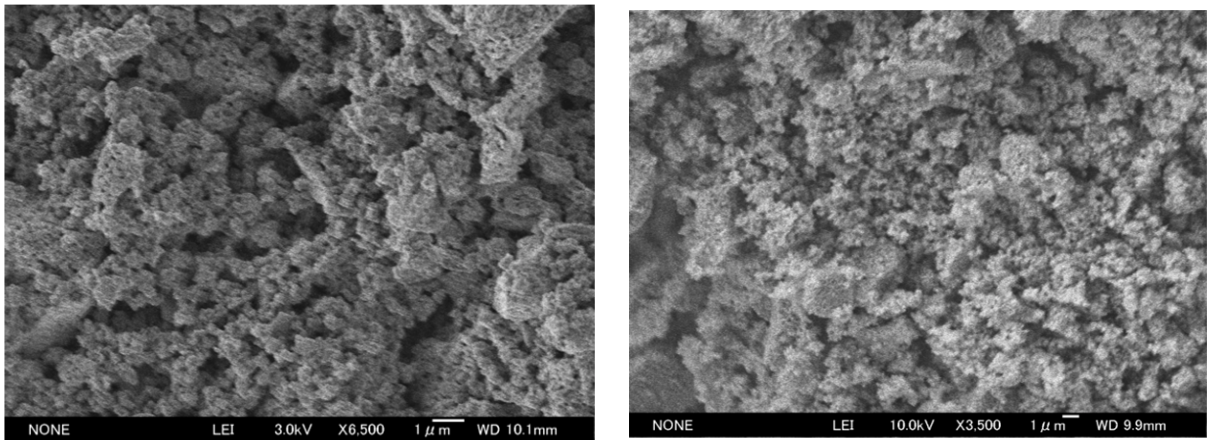

Figure 4.7 SEM measurement of the sample A) before and B) after the conducted experiment for industrial non-sintered catalyst

The SEM images of the unsintered (in Fig. 4.8A) and sintered anode (in Figs. 4.8B-C) are presented. The organized structure after the sintering process is created by the melted Ni/NiO and the powder of YSZ. Generally, the size of the created clusters in the catalyst, prepared with the Ni power, after the sintering process is bigger than the catalyst prepared with the NiO powder, because of the larger initial Ni particles in the unsintered anode.

Figure 4.9 presents the surface of an anode pellet, of which the diameter is around 10 mm. In order to investigate in plug-flow reactor, the anodes were crushed in several ways. The crushed powders are shown in Fig. 4.9 for the hand-crushed NiO/YSZ (60:40vol.%) catalyst prepared without a dispersant. A mechanically crushed fine powder NiO/YSZ (60:40vol.%) catalyst, being prepared with acetone and ethanol dispersants, is presented in Figs. 4.10A and 4.10B, respectively. The hand-crushed material (with a pestle in a mortar) does not have the appropriate size of particles - some of them have still a recognizable structure of sintering and are bigger than 10 μm (in Fig. 4.10). On the other hand, mechanical crushing of the sample into powder allows for obtaining fine spherical particles of the catalyst (in Fig. 4.10).

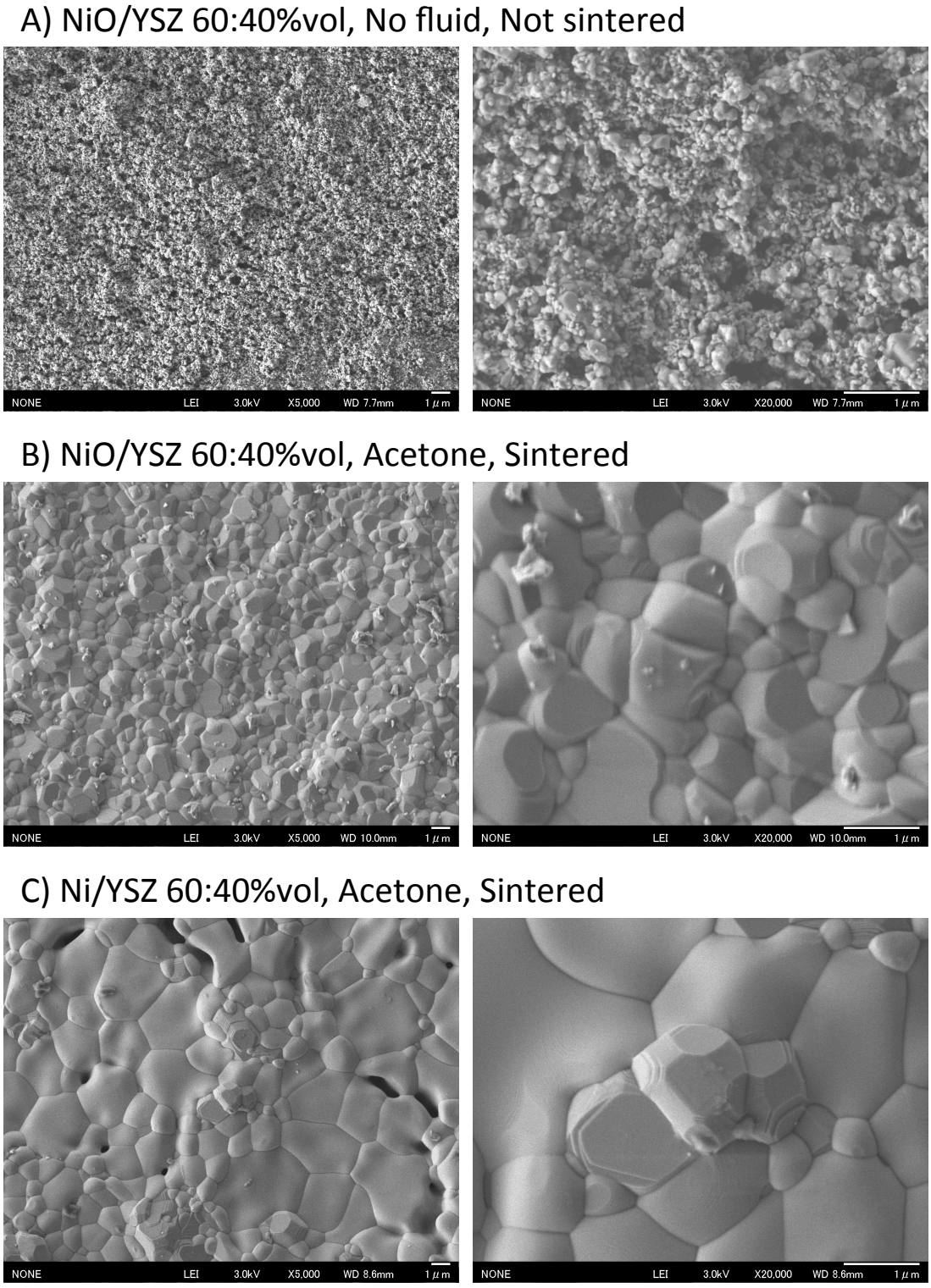

Figure 4.8 SEM images of anodes: A) a unsintered NiO/YSZ (60:40vol.%) catalyst, prepared without a liquid dispersant, B) a sintered NiO/YSZ (60:40vol.%) prepared with the acetone dispersant and C) a sintered Ni/YSZ (60:40vol.%) catalyst prepared with the acetone dispersant

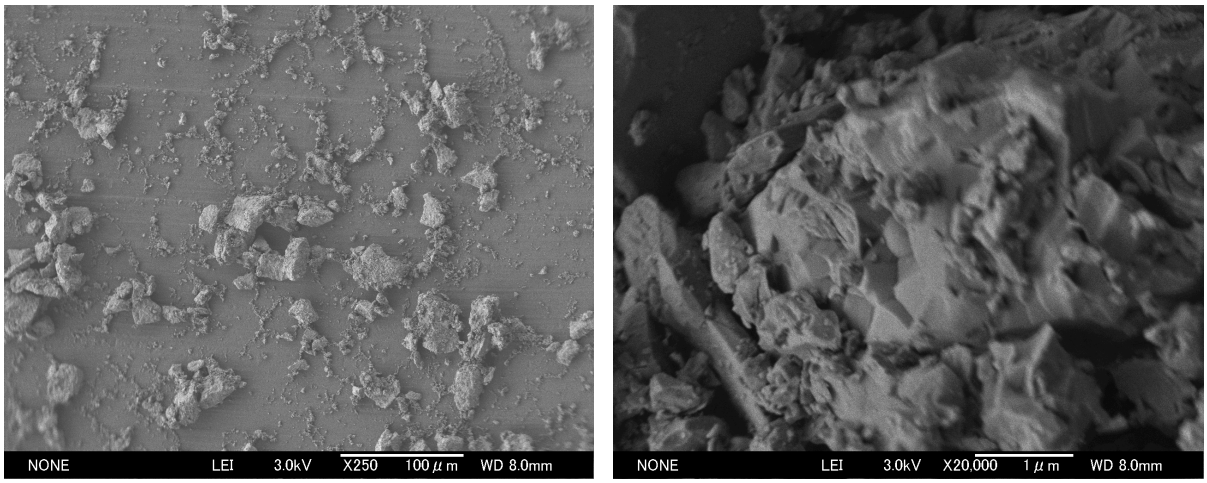

Figure 4.9 NiO/YSZ 60:40% catalyst prepared without the liquid dispersant and prepared by the hand crushing process

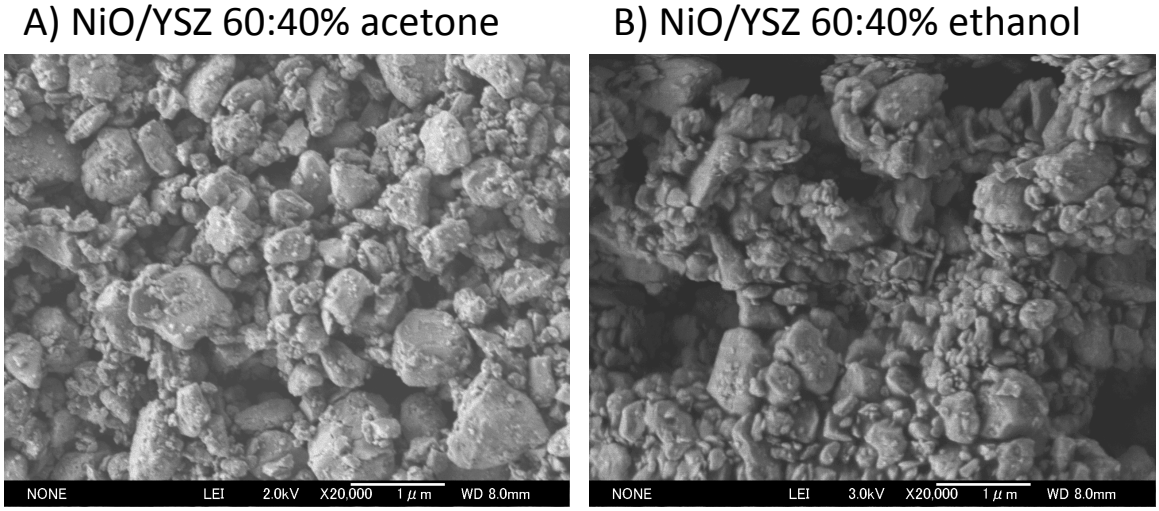

Figure 4.10 Mechanically crushed fine powder NiO/YSZ 60:40% catalyst prepared with liquid dispersants of A) acetone and B) ethanol

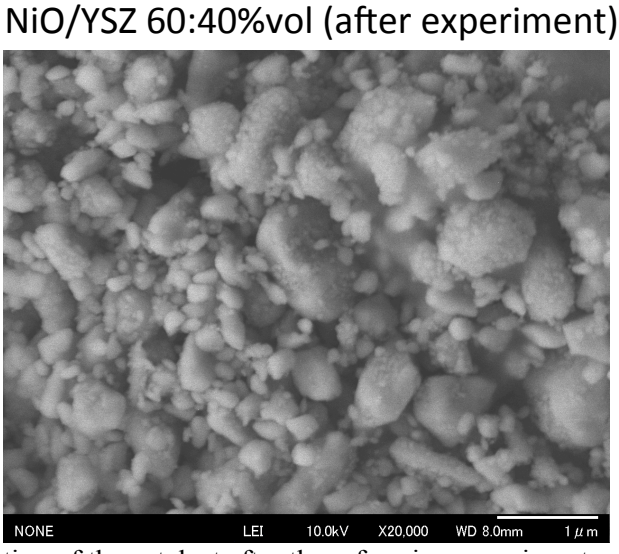

Figure 4.11 Observation of the catalyst after the reforming experiment using the SEM technique: NiO/YSZ (60:40vol.%) catalyst prepared with the acetone dispersant

Additional SEM photography of the NiO/YSZ (60:40vol.%) catalyst, prepared with the dispersant of the acetone, after the methane/steam reforming experiment was presented in Fig. 4.11. The analogical decrease in the size of the catalyst grains for the industrial catalyst by AGC SEIMI CHEMICAL CO. LTD. (in Fig. 4.11) can be observed. A more detailed observation of the catalyst after the reaction by SEM technique can be found in Appendix B.1 together with a discussion on the change in the particle size and appearance.

In order to confirm the quality of the powders, the mechanically crushed sample of catalysts were analysed by SHIMADZU SALD-DS3 (Free-Fall Type Dry Measurement). The exemplary results for catalyst NiO/YSZ (60:40vol.%) prepared without a dispersant are presented in Figures 4.12 and 4.13. Detailed measurements are shown in Appendix B.2 for the catalysts of NiO/YSZ (60:40%vol) and various compositions of the Ni/YSZ catalyst (70:30vol.%, 60:40vol.%, 50:50vol.%, 40:60vol.% and 30:70vol.%) A mode, median, average value and standard deviation of the particle diameter for each investigated catalyst material is summarized in Appendix B.2 and compared for all of the prepared catalyst materials.

In the exemplary case, the examined average size of the particles was given as 0.639 µm with a standard deviation of 0.243 µm for the NiO/YSZ (60:40vol.%) catalyst, which was prepared the without liquid dispersant. Figures 4.12 and 4.13 show the probability density function and cumulative probability distribution of the size of the particles, respectively. The results are characterized by the normal distribution of the grains size.

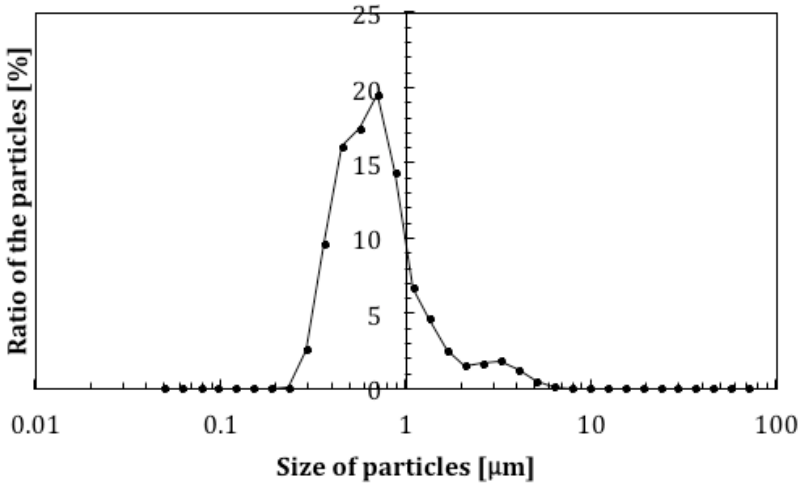

Figure 4.12 Size of the particles - probability density function

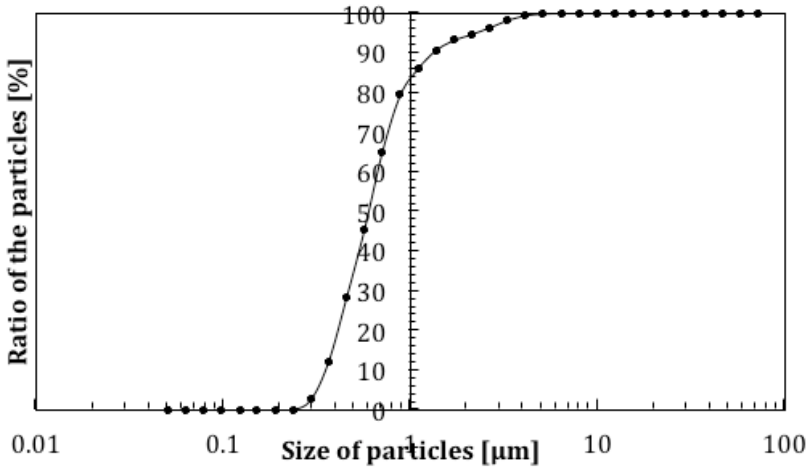

Figure 4.13 Size of the particles - cumulative probability distribution

4.5 Designed Experimental conditions

The proposed experimental conditions incorporated in the measurements are listed in Tables 4.5 and 4.6. The experimental conditions were set to keep the total molar flow rate at a reactor inlet to be at the constant level of $F^{i}_{\text{total}}=1.43\times10^{-2}$ mol min^{-1} in the case of a smaller total molar flow rate (see Table 4.5) and $F^{i}_{\text{total}}=4.29\times10^{-2}$ mol min^{-1} in the case of a higher total molar flow rate (see Table 4.6). The different levels of the flow rates were incorporated in order to assure proper conditions to derive the reaction kinetic for the reactivity of the various catalysts investigated. The experimental conditions are divided into three different measurements series. In Series 1, experimental conditions with the constant molar flow rate of methane and varied *SC* ratio in the range of 2.5-5.5 were provided. In Series 2, experimental conditions with the constant molar flow rate of steam were defined, however the *SC* ratio in the range of 2.5-5.5 was changed while the flow rate of methane is varied. Finally in Series 3, the consistent of measurements with widespread distribution of experimental conditions for the molar flow rates of water and methane (the *SC* ratio is in the range of 2.5-6). Different measurement series are defined to specify the requirements for the calculation methodologies proposed to derive the kinetic of methane/steam reforming.

The set temperatures were in the range of 500-750 ^{o}C, generally measurements were conducted at every constant interval of 25 ^{o}C. However, the precise range depends on the particular experimental case. All the experimental conditions kept the *SC* ratio above the level of 2.5, above which carbon deposition is not influential in the investigated temperatures.

The correlation between the methane molar flow rate and steam molar flow rate is presented in Fig 4.14. The data listed in Table 4.5 with the total molar flow rate of $F^{i}_{total}=1.43\times10^{-2}$ mol min^{-1} corresponds to Fig. 4.14A and data from Table 4.6 with the total molar flow rate of $F^{i}_{total}=4.29\times10^{-2}$ mol min^{-1} are shown in Fig. 4.14B. In both charts, data corresponding to Series 1 creates a vertical line, and the one corresponding to Series 2 has a horizontal position. On the other hand, the data plotting, made of the experimental conditions corresponding to Series 3 with the limited number of experimental points, covers the whole area better than any of the previous series.

Table 4.5 Details of the experimental conditions with a lower total molar flow rate $F^{i}_{total}=1.43\times10^{-2}$ [mol min^{-1}]

SC [-]	NC [-]	Volume flow rate [ml min^{-1}]			Total molar flow rate [mol min^{-1}]
		CH_4	N_2	H_2O	
Series 1: Experimental condition with constant molar flow rate of methane					
5.5	0.5	50	25	0.20	1.43×10^{-2}
5	1	50	50	0.18	1.43×10^{-2}
4.5	1.5	50	75	0.17	1.43×10^{-2}
4	2	50	100	0.15	1.43×10^{-2}
3.5	2.5	50	125	0.13	1.43×10^{-2}
3	3	50	150	0.11	1.43×10^{-2}
2.5	3.5	50	175	0.09	1.43×10^{-2}
Series 2: Experimental condition with constant molar flow rate of water					
2.5	2.3	60	140	0.11	1.43×10^{-2}
3	3	50	150	0.11	1.43×10^{-2}
3.5	3.7	43	157	0.11	1.43×10^{-2}
4	4.3	38	162	0.11	1.43×10^{-2}
4.5	5	33	167	0.11	1.43×10^{-2}
5	5.7	30	170	0.11	1.43×10^{-2}
5.5	6.3	27	173	0.11	1.43×10^{-2}
Series 3: Experimental condition with widespread distribution					
3	3	50	150	0.11	1.43×10^{-2}
5	4	35	140	0.13	1.43×10^{-2}
6	0.5	47	23	0.21	1.43×10^{-2}
4	2	50	100	0.15	1.43×10^{-2}
3	1	70	70	0.15	1.43×10^{-2}
2.5	6	37	221	0.07	1.43×10^{-2}

Table 4.6 Details of the experimental conditions with a higher total molar flow rate $F^{i}_{total}=4.29\times10^{-2}$ [mol min^{-1}]

SC [-]	NC [-]	Volume flow rate [ml min^{-1}]			Total molar flow rate [mol min^{-1}]
		CH_4	N_2	H_2O	
Series 1: Experimental condition with constant molar flow rate of methane					
5.5	7.5	75	562	0.30	4.29×10^{-2}
5	8	75	599	0.28	4.29×10^{-2}
4.5	8.5	75	637	0.25	4.29×10^{-2}
4	9	75	674	0.22	4.29×10^{-2}
3.5	9.5	75	712	0.19	4.29×10^{-2}
3	10	75	749	0.17	4.29×10^{-2}
2.5	10.5	75	787	0.14	4.29×10^{-2}
Series 2: Experimental condition with constant molar flow rate of water					
2.5	8.2	90	734	0.17	4.29×10^{-2}
3	10.0	75	749	0.17	4.29×10^{-2}
3.5	11.8	64	760	0.17	4.29×10^{-2}
4	13.7	56	768	0.17	4.29×10^{-2}
4.5	15.5	50	774	0.17	4.29×10^{-2}
5	17.3	45	779	0.17	4.29×10^{-2}
5.5	19.2	41	783	0.17	4.29×10^{-2}
Series 3: Experimental condition with widespread distribution					
3	10	75	749	0.17	4.29×10^{-2}
5	20	40	807	0.15	4.29×10^{-2}
6	11	58	641	0.26	4.29×10^{-2}
4	12	62	740	0.18	4.29×10^{-2}
3	8	88	699	0.19	4.29×10^{-2}
2.5	13	64	826	0.12	4.29×10^{-2}

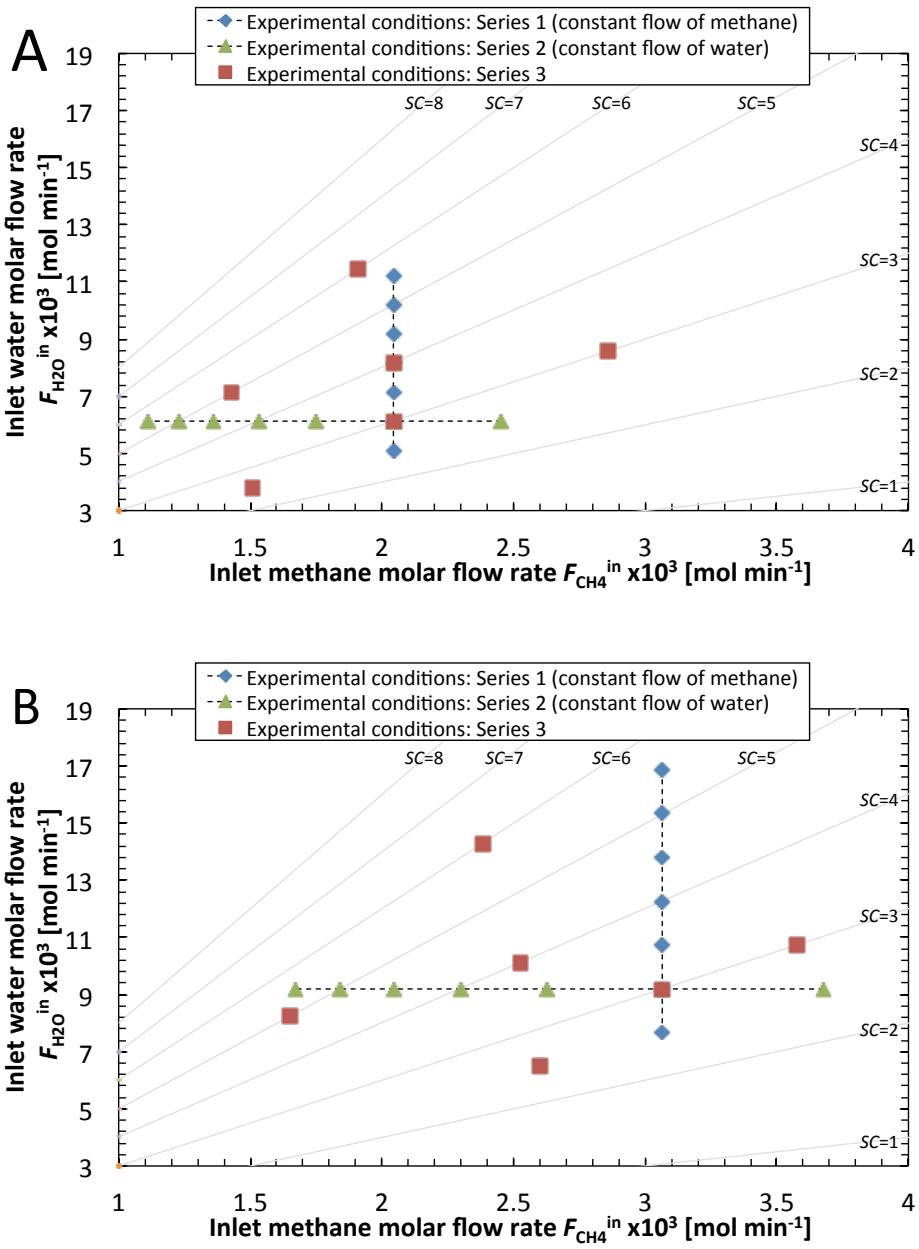

Figure 4.14 Distribution of experimental condition for A) lower total molar flow rate and B) higher total molar flow rate

4.6 The influence of Gas Hourly Space Velocity

Figure 4.15 shows the representative examples of the conversion rates obtained from the experiment on the unsintered NiO/YSZ (60/40vol.%) catalyst. One of the most important factors in deriving the proper non-equilibrium kinetic equation are the adequate experimental conditions which ensure the conversion rate and reaction rate does not follow the equilibrium reaction. This can be achieved by choosing the appropriate amount of catalyst and total flow rates of the reaction substances.

The quantity often used in chemical and reactor engineering is Gas Hourly Space Velocity (*GHSV*). The *GHSV* defines the quotient of the entering flow of the reactants divided by the reactor (or the catalyst bed) volume. The *GHSV* indicates how many reactor volumes of feed can be treated in the unit time. For analysed case the formal definition of the *GHSV* is described as a function of the mixture gas velocity [$mm^3\ h^{-1}$] $\dot{V}_{gas}$ and the volume [mm^3] of the catalyst layer V_{cat}:

$$GHSV = \frac{\dot{V}_{gas}}{V_{cat}} \tag{4.13}$$

Gas Hourly Space Velocity is very influential factor for the methane/steam reforming reaction rate and methane conversion rate. Figures 4.15B and 4.15C represent *GHSV* for both of those factors in the correlation with achieved conversion rates. Figure 4.15B is the case where the *SC* and *NC* ratios are fixed at 3 for each of them. In the meantime, Figure 4.14C is the case where the reaction temperature is fixed at 700 ^{o}C. It can be noted that for a certainly small *GHSV* value (a small amount of gas in a high amount of the catalyst), the achieved conversion rate is high, which means that the reaction is very close to the equilibrium and is not proper for delivering a kinetic equation. On the other hand, a definite large *GHSV* value means that the changes obtained from the conversion rates are very small and difficult to observe. For the consideration of the reaction kinetic, the best solution is to moderate values of the *GHSV*, which results in moderated conversion rates for different observed temperatures and *SC* and *NC* conditions.

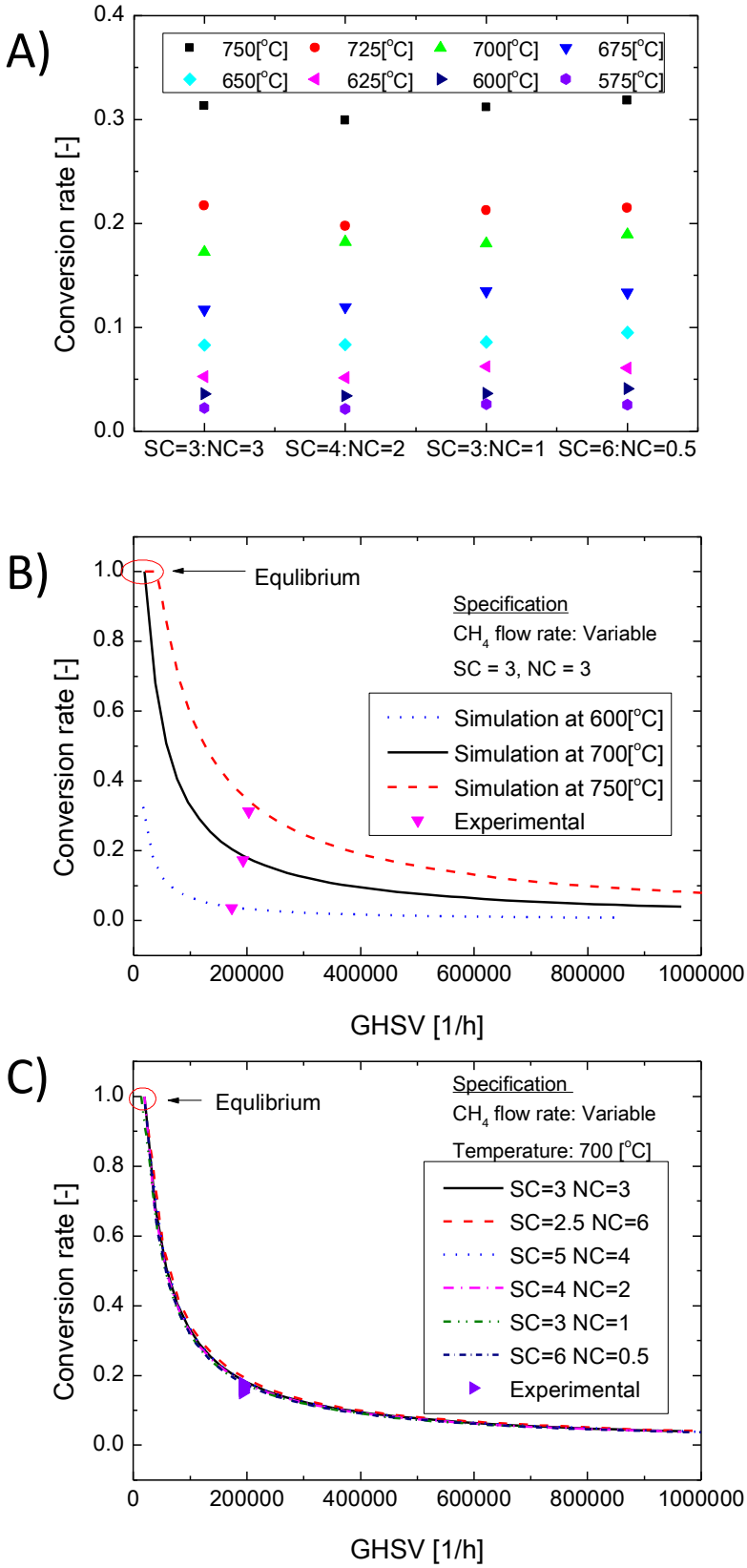

Figure 4.15 Conversion rate for the unsinterred NiO/YSZ (60:40vol.%) catalyst for A) representative examples obtained from the experiment, B) in the correlation with the Gas Hourly Space Velocity (*GHSV*) at the condition (*SC*=3 and *NC*=3), C) in the correlation with the *GHSV* at the condition of the reaction temperature at 700 °C

5 Derived mathematical kinetics using classical approaches

Chapter 3 introduced the classical approaches adopted for estimating the reaction kinetics of methane/steam reforming processes. The greatest emphasis concerns the power law expressions adopted for describing the reaction rate as the most popular and appropriate technique in the problems of modelling systems based on internal fuel reforming coupled Solid Oxide Fuel Cells.

Sections 5.1 – 5.4 presents an analysis conducted for the sintered catalyst of NiO/YSZ in the composition ratio of 60/40vol.% (sample weight: 0.3g). The last section in the present chapter presents the influence of molar composition of the catalysts used for deriving reaction kinetics.

5.1 Standard approach

The first estimation of the reaction rates defining the methane/steam reforming process for reaction order coefficients on the partial pressures of methane and water, parameters *a* and *b*, was conducted using the classical approach described in Section 3.5. The methodology requires suitable experimental conditions, providing constant partial pressure of methane and separately constant partial pressure of water. The incorporated experimental conditions are described in Table 4.5 as Series 1 and Series 2. The *SC* ratio was manipulated in the range 2.5 – 5.5 and the *NC* ratio was changed in the range 0.5 – 6.3. All conditions were designed to maintain a total molar flow rate at a constant level, which was equal to 1.43×10^{-2} mol min^{-1}. The measurements were conducted at a reaction temperatures of 500 ^{o}C, 550 ^{o}C, 575 ^{o}C, 650 ^{o}C and 700 ^{o}C for both Series 1 and 2 at a constant molar flow rate of methane and constant molar flow rate of water, respectively. The results of the measurements in the form of the achieved conversion rates over the measurement conditions are presented in Fig. 5.1 for all of the investigated temperatures separately.

The increase in the reaction temperature causes an increase in the conversion rate of methane. It can be observed that the conversion rate of methane is lowered in Series 1, where the measurements were carried out at a constant flow rate of methane 50 ml min^{-1} that means the decreasing flow rate of water (the decreased value of *SC* ratio). The measurement in Series 2, where the constant molar flow rate of water 0.11 ml min^{-1} was set (and therefore the flow rate of methane is varied in the range of 27 – 60 ml min^{-1}), are characterized by analogical tendency; the increased *SC* ratio increases the conversion rate of methane. Although the *SC* ratios are the same in Series 1 and Series 2, the obtained conversion rates are different, because of various partial pressures of the species in the system, which was caused by the different nominal flow rates of methane, water and nitrogen.

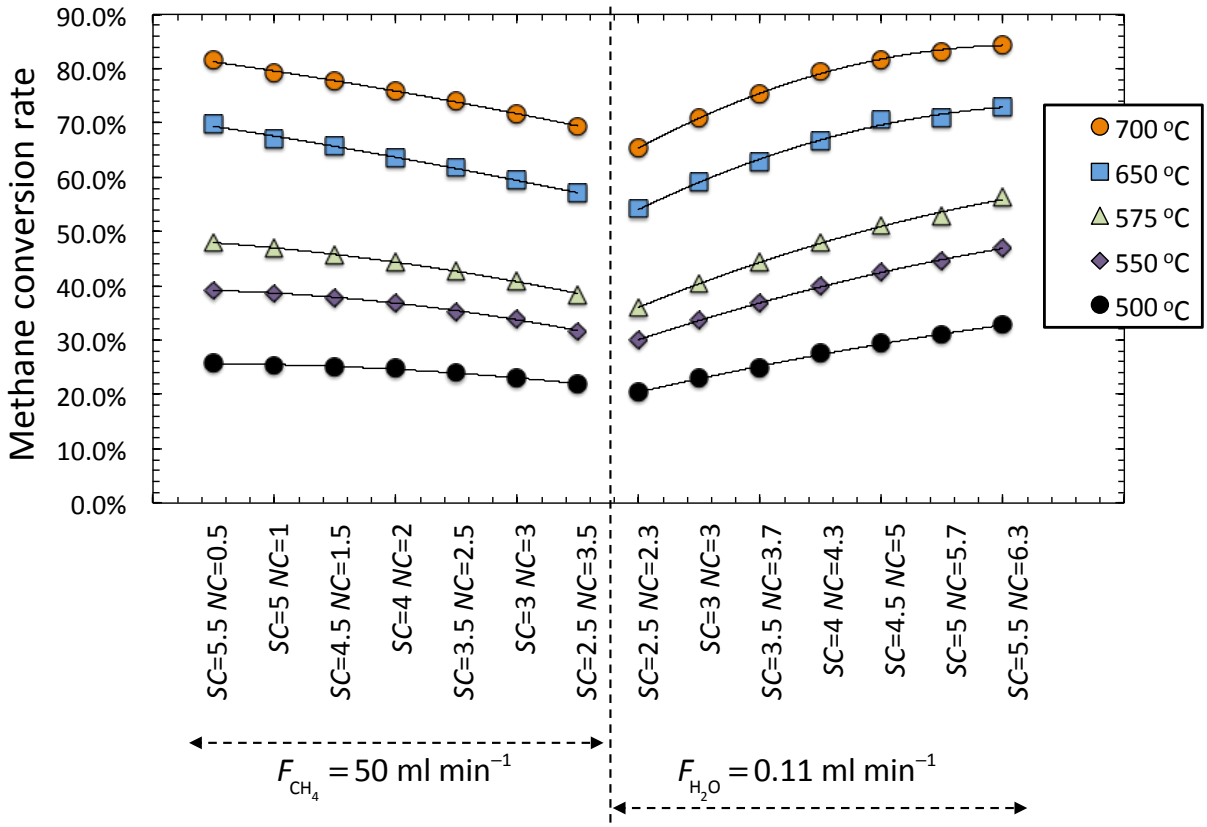

Figure 5.1 Experimentally obtained results of the conversion rate for the measurements with the constant flow rates of methane and of water (standard approach)

Figure 5.2 presents the results of the investigated reaction kinetic by the standard method, in which two different types of measurements were separately carried out at the constant flow rates of methane (Series 1) and of water (Series 2). The presented results include experimentation at a temperature of 500 °C. Additional results obtained at temperatures 550 °C, 575 °C, 650 °C and 700 °C are presented in Appendix C.1. The experimental results

obtained from tests with the constant flow of water were used to calculate the reaction order coefficient *a* (in Fig. 5.2A), and the experimental results obtained from tests which the constant flow of methane were used to calculate the reaction order coefficient *b* (in Fig. 5.2B). Figure 5.3 illustrates the correlation between the partial pressures of methane and water in the test temperature of 500 ^{o}C for measurements in Series 1 (in Fig. 5.3B) and in Series 2 (in Fig. 5.3A). The partial pressures of water and methane are constant, so that the standard calculation methodology can be applied as its assumptions are preserved. As the final result, the reaction orders are approximated to be *a*=0.34 [-] and *b*=0.18 [-].

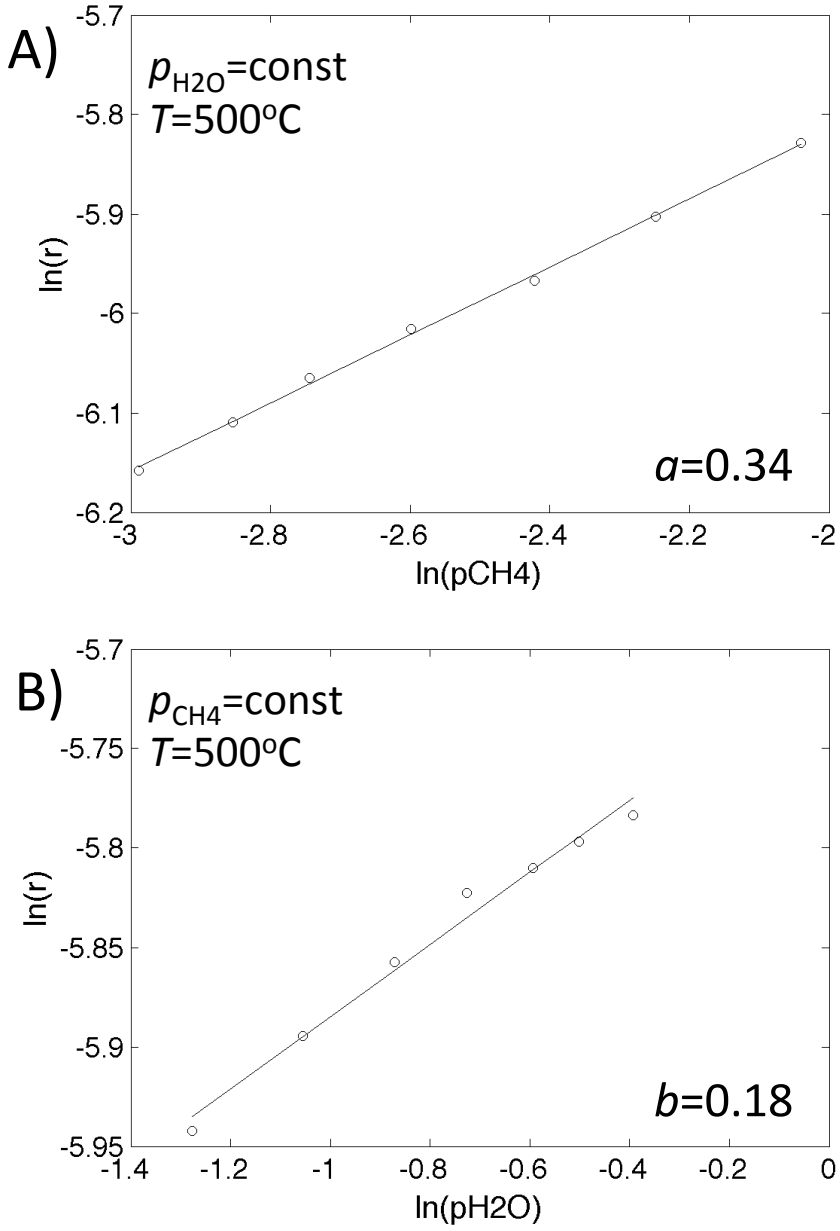

Figure 5.2 Experimental results obtained from the measurements conducted at 500^{o}C for the approximation of the reaction orders by the standard approach: correlations between the reaction rate and A) partial pressure of methane for the calculation of parameter *a* and B) partial pressure of water for the calculation of parameter *b*

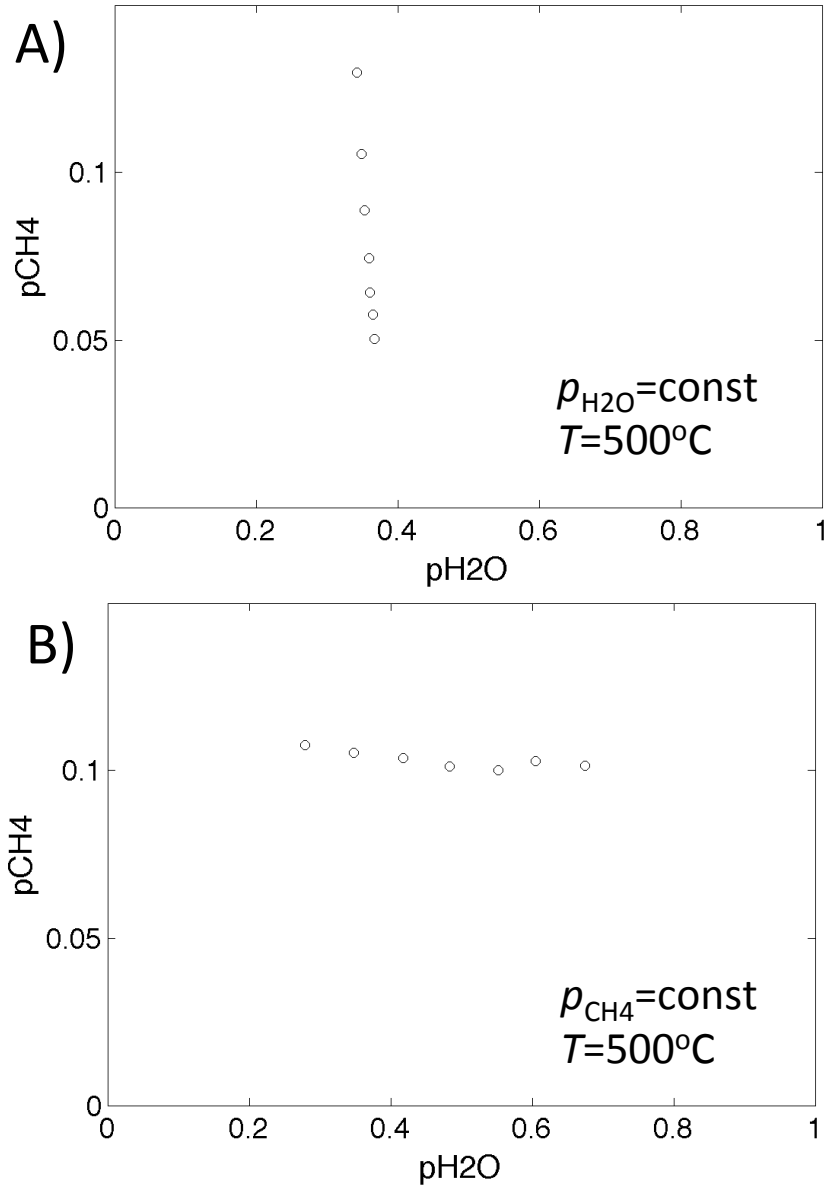

Figure 5.3 Correlation between partial pressures of methane and water at a test temperature of 500 °C for the measurements at A) the constant flow of water and B) the constant flow of methane

A summary of the results obtained for all considered temperatures is presented in Table 5.1. In the analysed results by the standard method, no significant differences were noticed on the calculated reaction order *a* at the different test temperatures. On the other hand, reaction order *b*=0.15, calculated from the results at a temperature of 700 °C, is considerably smaller than reaction orders *b* evaluated at lower temperatures. This difference can be explained by the deviation observed in Fig. C.1H (in Appendix C) for the partial pressure of methane. The input flow rate of methane was kept at a constant level as mentioned frequently, but because of a significantly high conversion rate of methane obtained from the condition of the high test temperature and a high *SC* ratio, the partial pressure of methane in the reaction rate equation (in Eq. (3.53)), to derive the reaction rate in Fig. 5.2, is not kept at a constant level. Although

the absolute error is smaller than in the corresponding case of the measurement carried out at the condition of the constant water flow rate and of the temperature at 700 ^{o}C (see Fig. C.1D), the percentage error is much more significant.

The final value of the reaction orders was taken as the average value determined in all temperatures: a=0.35 and b=0.2. The presented case did not show significant differences in the reaction orders calculated for different temperatures. In the other reported studies applying the standard method for the evaluation of reaction kinetics of the methane/steam reforming, the differences found on the reaction orders at different temperatures are much more influential. For example, the studies conducted by Mogensen [81] for the model anode material in the packed bed reactor resulted in the rate order a in the range 0.779-0.937 for test temperatures in the range of 600 – 800^{o}C and the final order was determined as the mean value for the sake of the power law expression.

Table 5.1 Results of the calculation reaction orders a and b for different test temperatures by the standard approach

Temperature	$a\left(p_{H_2O}=\text{const}\right)$	$b\left(p_{CH_4}=\text{const}\right)$
500^{o}C	0.34	0.18
550 ^{o}C	0.34	0.24
575 ^{o}C	0.31	0.24
650 ^{o}C	0.39	0.20
700 ^{o}C	0.35	0.15
Average value	0.35	0.20

5.2 The modified approach

The modified approach described in Section 3.6 does not require a specific experimental data set, as it does not impose any additional conditions for the derivation found on reaction orders. The only requirement is the widespread distribution of the experimental results, which increase the accuracy of the solution. Therefore, two types of analysis were conducted: one with the modified experimental data set defined in Table 4.5 as Series 3 and other one with the data designed for the standard approach and defined in Table 4.5 as Series 1 and Series 2. The latter data set was applied to the analysis presented in the previous Section 5.1.

The results of the carried-out measurements in the modified conditions are presented in Fig. 5.4 in the form of the methane conversion rate over the investigated conditions. The dashed lines in Fig. 5.4 show the trend of the methane conversion rate along different sets of the experimental condition at a constant temperature in the range of 700°C – 500 °C at intervals of every 25 °C. All the experiments were conducted in the one series starting from 700 °C and then the temperature was decreased. The results in one certain temperature condition follow the same pattern. The measured range of the conversion rates is wide: from 20% at the lowest temperature of 500 °C to almost 90% at the highest temperature of 700 °C.

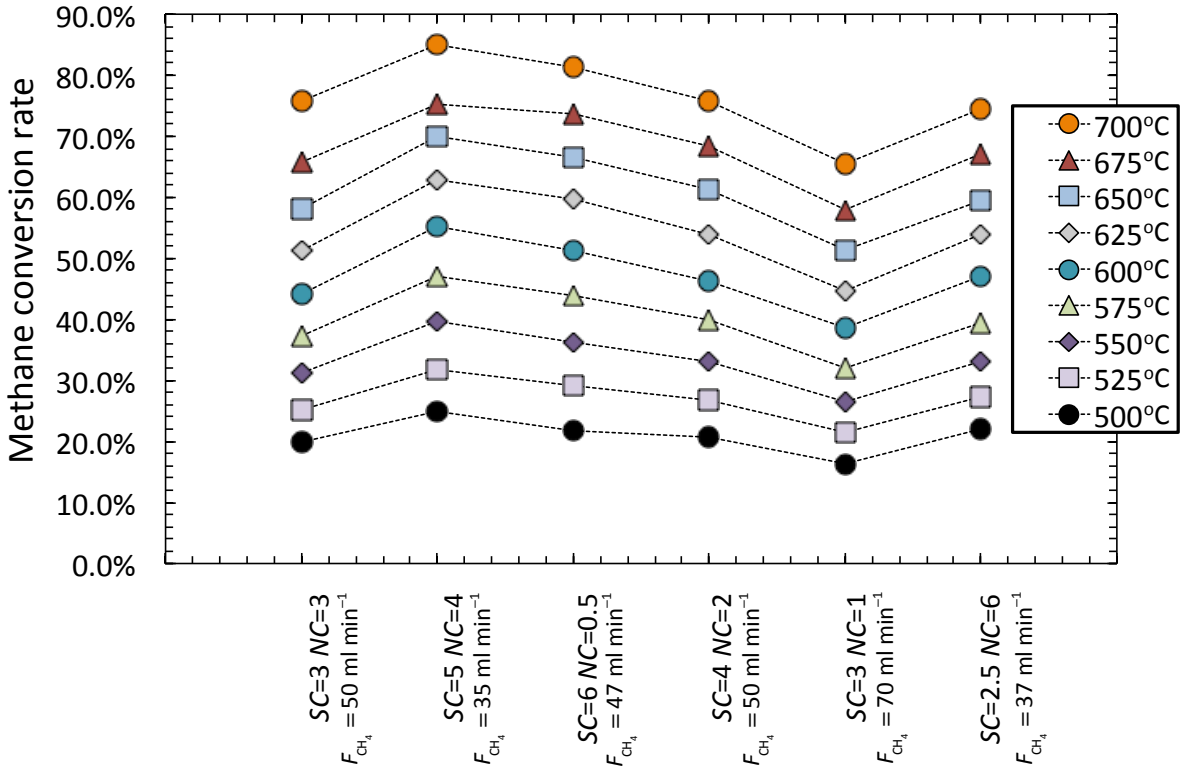

Figure 5.4 Experimental results of the methane conversion rate obtained at various flow rates of methane and water (modified approach)

The results of the calculations defined for the modified method with data obtained from the modified experimental conditions (Series 3) are present in Fig. 5.5 for the exemplary temperature of 600 °C (in Fig. 5.5A) and as the summed calculation for all of the temperature conditions (in Fig. 5.5B). Additionally, in Appendix C, the results obtained from all the test temperature conditions are presented in Fig. C.3. The difference of the reaction orders evaluated at higher temperatures comparing with the reaction orders calculated at lower ones can be explained by the high conversion rates at higher temperatures, which interfere with the calculations. The benefit of the modified methodology is the possibility of analysing all

experimental data simultaneously (Figure 5.5B) and applying a general approach to the studies. The values of the estimated reaction order coefficients are a=0.38 and b=0.21, which were characterized by the minimal summed standard deviation of the calculated reaction constant.

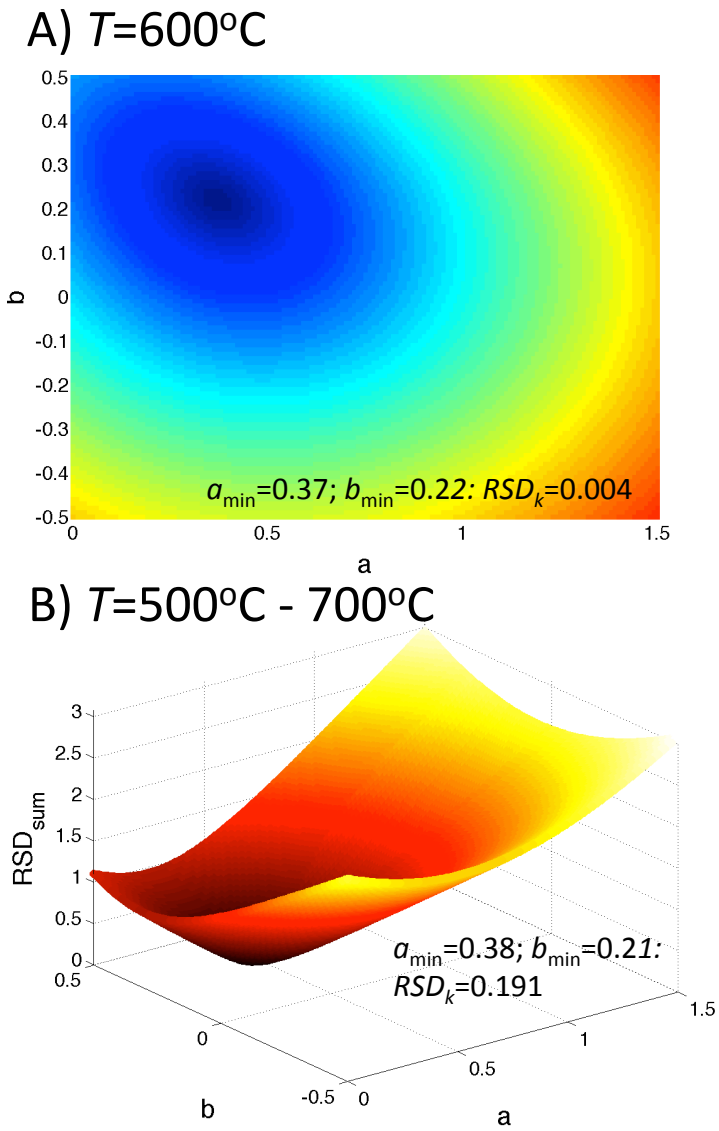

Figure 5.5 An approximation of reaction orders using the modified approach with modified experimental data: A) an exemplary result for the distribution of the relative standard deviation on reaction constant at a temperature of 600 °C and B) summed standard deviation for temperatures 500-700 °C

The modified calculation methodology does not impose additional conditions on the experimental data, so that the data sets prepared for the standard methodology (Series 1 and Series 2 presented in Figure 5.1) were applied to the modified calculation method. The results of the calculations are presented in Fig. 5.6 for the test temperatures in a range between 500°C

and 700°C. The analysis conducted for the remaining temperatures of 550 °C, 575 °C and 650°C are shown in Appendix C (see Fig. C.4).

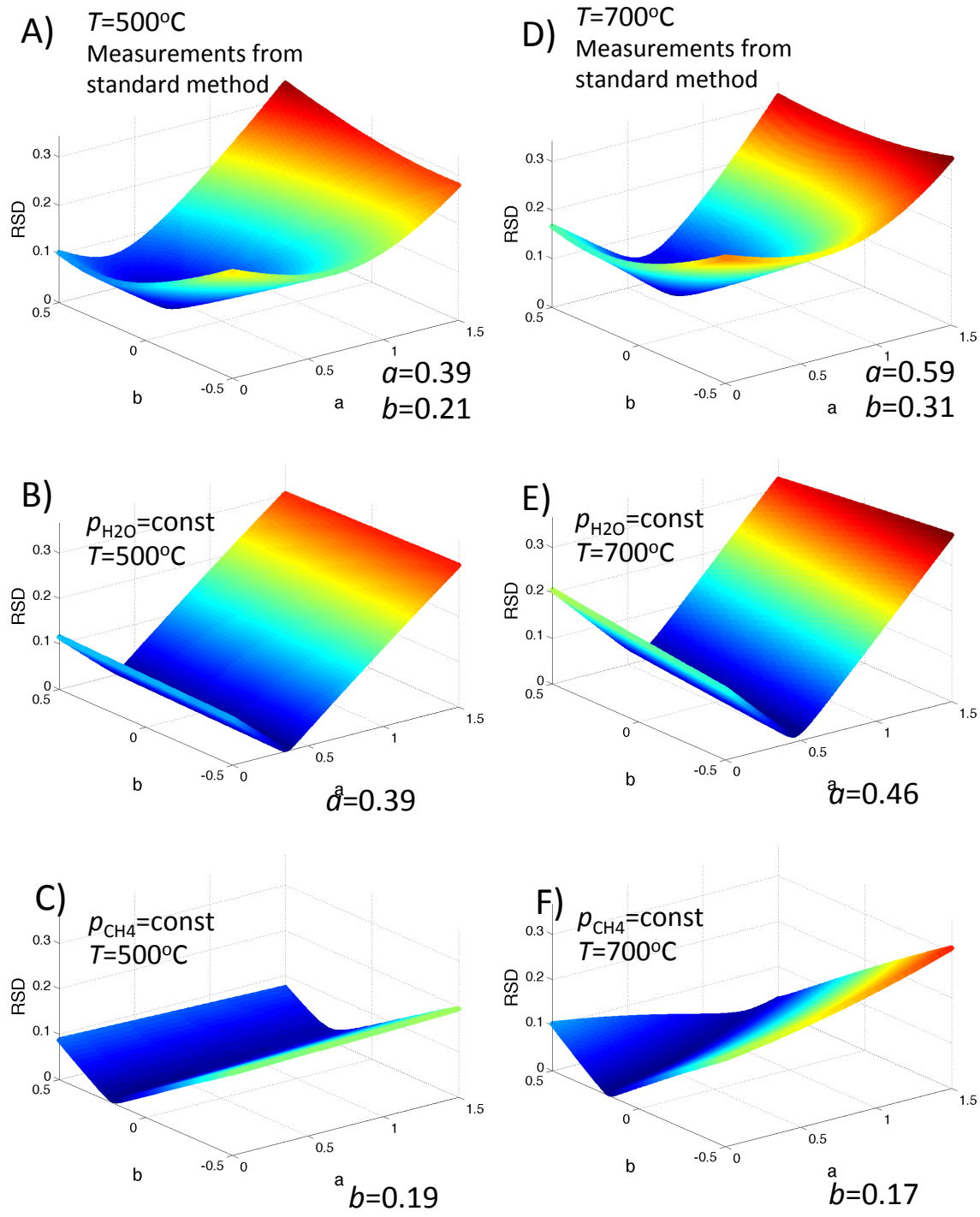

Figure 5.6 The distribution of the relative standard deviation of reaction constant calculated by the modified method using data from the measurement for the standard method (Series 1 and 2): all the experimental data (in A and D), data at the constant flow rate of water (in B and E), and one at the constant flow rate of methane (in C and F) at a temperature of 500 °C (in A-C) and of 700 °C (in D-F)

Two types of analyses were conducted. Firstly, all the data obtained from Series 1 and 2 were analysed simultaneously for each temperature (in Figs. 5.6A and 5.6D) to estimate the values of the reaction order coefficients *a* and *b* where the smallest relative standard deviation on the reaction constant was found. However, the results of this calculation are not comparable with the values calculated in the previous step (by the standard method presented in Section 5.1) and the difference is clearly visible at the higher temperature, both reaction orders were overestimated in this process. In the second analysis, both reaction order coefficients *a* and *b* were calculated individually with a separated set of results obtained from Series 1 and 2. The results of the calculations are shown in Figs. 5.6B and 5.6E for reaction order *a* at 500 ^{o}C and 700 ^{o}C, respectively (data obtained from experimental Series 2 at the constant flow rate of water). Figures 5.6C and 5.6F shows the calculation of reaction order *b* at 500 ^{o}C and 700 ^{o}C, respectively (data obtained from experimental Series 1 at a constant flow rate of methane). The difference in the calculation is visible, especially in the higher reaction temperature compared to the data obtained with the standard method (see Table 5.1). The value estimated at a temperature of 700 ^{o}C from the merged data is a=59 [-] and b=0.31 [-], while for separated data the values decreased to a=46 [-] and b=0.17 [-], which is consisted with the calculation presented earlier. The characteristic feature observed in Fig. 5.6 for the separated experimental conditions is lack of one significant extreme point, minimizing the value of the relative standard deviation calculated for the reaction constants. In all of the previous cases and the studies found in the literature [206], for the analysis of the reaction orders by the modified method, the isolines of the constant value of the relative standard deviation calculated for reaction constant *k* creates the concentric ellipsoids. In Figs. 5.6B, 5.6C, 5.6E and 5.6F, the minimum isoline is not degenerated to the point, but has a linear shape, parallel to the *b* axis in Figs. 5.6B and 5.6E and to axis *a* in Figs. 5.6C and 5.6F. This shape is resulted from the assumed experimental condition. In the case of experiments with the constant flow rate of water (in Figs. 5.6B and 5.6E), the influence of the change in methane flow rate is only investigated. Therefore, we can estimate its effect on the reaction rate, which is expressed in the form of reaction order coefficient for the partial pressure of methane - parameter *a.* The effect of the water flow rate, predominantly determining the partial pressure of steam, is neglected, so that the trustful value of parameter *b* cannot be estimated from this data series. The analogical situation is observed for the constant molar flow rate of methane with the varied flow rate of water (in Figs. 5.6C and 5.6F), which gives a correct estimation only for the influence of the flow rate of water (to predominantly the partial pressure of steam) expressed in parameter *b*.

The comparison presented in Fig. 5.7 explains the uncorrected results obtained for the analysis with merged Series 1 and Series 2. The value of reaction order coefficients *a* and *b* scoring the minimum value of RSD_k, in the case of merged data (in Fig. 5.7A), can be found in the intersection of the isoline of minimal RSD_k for separated measurements in Series 1 (in Fig. 5.7B) and Series 2 (in Fig. 5.7C). At the temperature of 500^{o}C, the results obtained by the merging-data approach (determining a=0.39 and [-], b=0.21 [-]) and the separately treating-data approach (determining a=0.39 [-] and b=0.19 [-]) are convergent. On the other hand, at the temperature of 700 ^{o}C, the differences between two approaches are clear. It is caused by the deviation in the final partial pressures, which are difficult to be defined as constant, even though the initial flow rates were the same. The high conversion rate changes the results significantly in each measuring conditions, therefore interfere with the expected results. This effect is also observed in the constant RSD_k isolines, which are not parallel to the axis in Figs. 5.7E and 5.7F. The analogical analysis for temperatures 550 ^{o}C, 575 ^{o}C and 650^{o}C are presented in Appendix C (in Fig. C.5), which are very consistent for the observation concluded in this section.

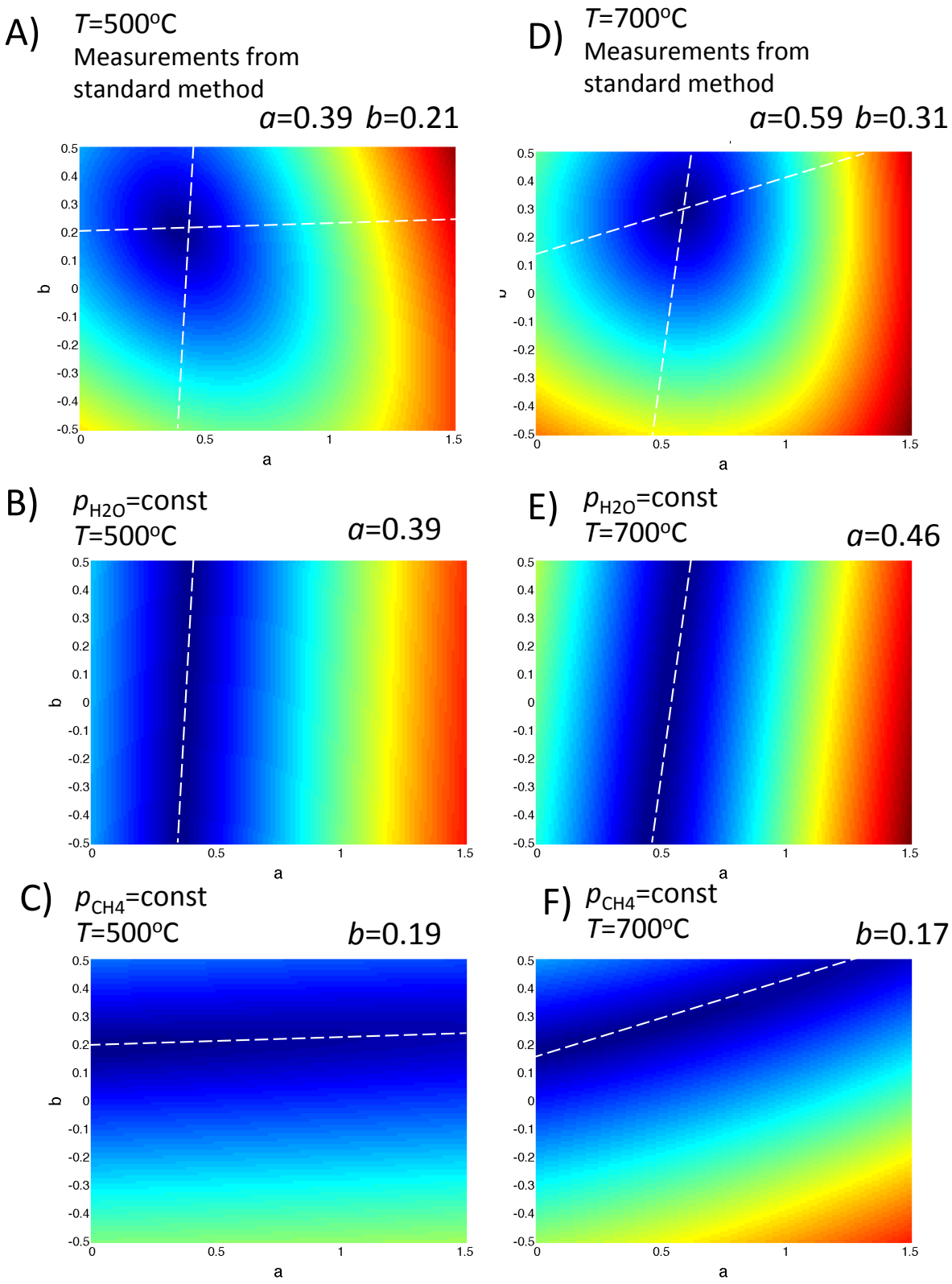

Figure 5.7 The influence of the unstable partial pressure of methane for the approximation of reaction orders by the modified approach with standard experimental data obtained at a temperature of 500 °C (in A-C) and 700 °C (in D-F)

5.3 Comparison of the methods

The three main types of analyses were conducted; the standard methodology calculated with the experimental data obtained from designated standard experimental conditions (separate measurements for the constant partial pressure of steam and methane), the modified methodology method calculated with the experimental data obtained from the designated modified experimental conditions (a limited number of measurements with various flow rates of methane and water) and, additionally, the experimental data obtained from the designated standard experimental conditions were applied to the calculation procedure of the modified methodology method , in order to verify the calculated output and its comparability with other computations. Detailed descriptions of the adopted analyzed methods and conditions are presented in Fig 5.8.

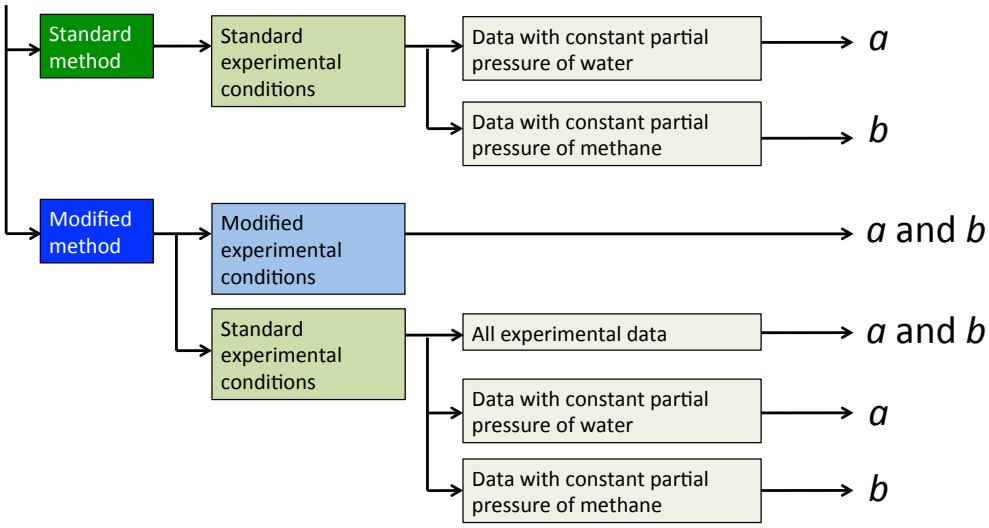

Figure 5.8 Conducted numerical analysis for standard and modified method with standard and modified experimental conditions

In Sections 5.1 and 5.2 and corresponding Appendices C.1 and C.2, a detailed analyses were presented for both the standard and modified methods. Good convergence between the standard method with standard experimental conditions and the modified method with modified experimental conditions were achieved. The values of the estimated parameters were $a_{standard}$=0.35 and $b_{standard}$=0.2 and $a_{modified}$=0.38 and $b_{modified}$=0.21 for both the standard and modified methods, respectively.

The comparison of experimental results obtained on the basis of the standard experimental conditions expressed in Series 1 and 2 are summarized in Table 5.2. The reaction orders

calculated with the application of merged experimental data, being obtained from the designated standard conditions (from both Series 1 and Series 2), to the modified method significantly overshot the values obtained in the other analysis, and it is most clearly visible in the case of parameter *a* (reaction order with respect to the partial pressure of methane) and higher experimental temperatures. The reasons of this deviation were explained in Section 5.2 and the solution is proposed by conducting an individual analysis for separated measurement conditions in Series 1 and Series 2.

Table 5.2 Comparison of the results of calculated reaction orders *a* and *b* by different approaches

Temperature	Standard method: Standard condition		Modified method: Standard conditions (merged)		Modified method: Standard conditions (separated)	
	a	*b*	*a*	*b*	*a*	*b*
500°C	0.34	0.18	0.39	0.21	0.39	0.19
550 °C	0.34	0.24	0.41	0.29	0.42	0.25
575 °C	0.31	0.24	0.41	0.31	0.35	0.26
650 °C	0.39	0.20	0.57	0.32	0.45	0.22
700 °C	0.35	0.15	0.59	0.31	0.46	0.17
Average	0.35	0.20	0.47	0.29	0.41	0.22

The general conclusion in comparing the standard and modified methods for estimating reaction order parameters is that the modified approach reduces significantly the number of experimental conditions necessary for the estimation of reliable reaction kinetics. Furthermore, it does not impose additional conditions, which has to be fulfilled in order to obtain credible data. Therefore, for the derivation of the reaction kinetics provided in the next sections, the modified method was chosen. The method was applied for the experimental measurement with the widespread distribution of initial flow rates of the species to assure full information about the process.

To derive a full reaction kinetic equation for the sintered catalyst of NiO/YSZ (60:40vol.%), initially prepared with a liquid dispersant of ethanol, the activation energy and pre-exponential factor have to be calculated. The reaction orders a=0.38 and b=0.21 were used in the preparation of Arrhenius plot (see Section 3.7). The Arrhenius plot is presented in Fig. 5.9

and the linear approximation of the logarithm of reaction constant in relation to temperature is:

$$\ln(k) = 2.45 - 5786\left(\frac{1}{T}\right) \tag{5.1}$$

and therefore calculated activation energy and pre-exponential factor are:

$$A = 11.6\ [\text{mol min}^{-1}\ \text{g}^{-1}\ \text{atm}^{-0.59}] \tag{5.2}$$

$$E = 48105\ [\text{J mol}^{-1}] \tag{5.3}$$

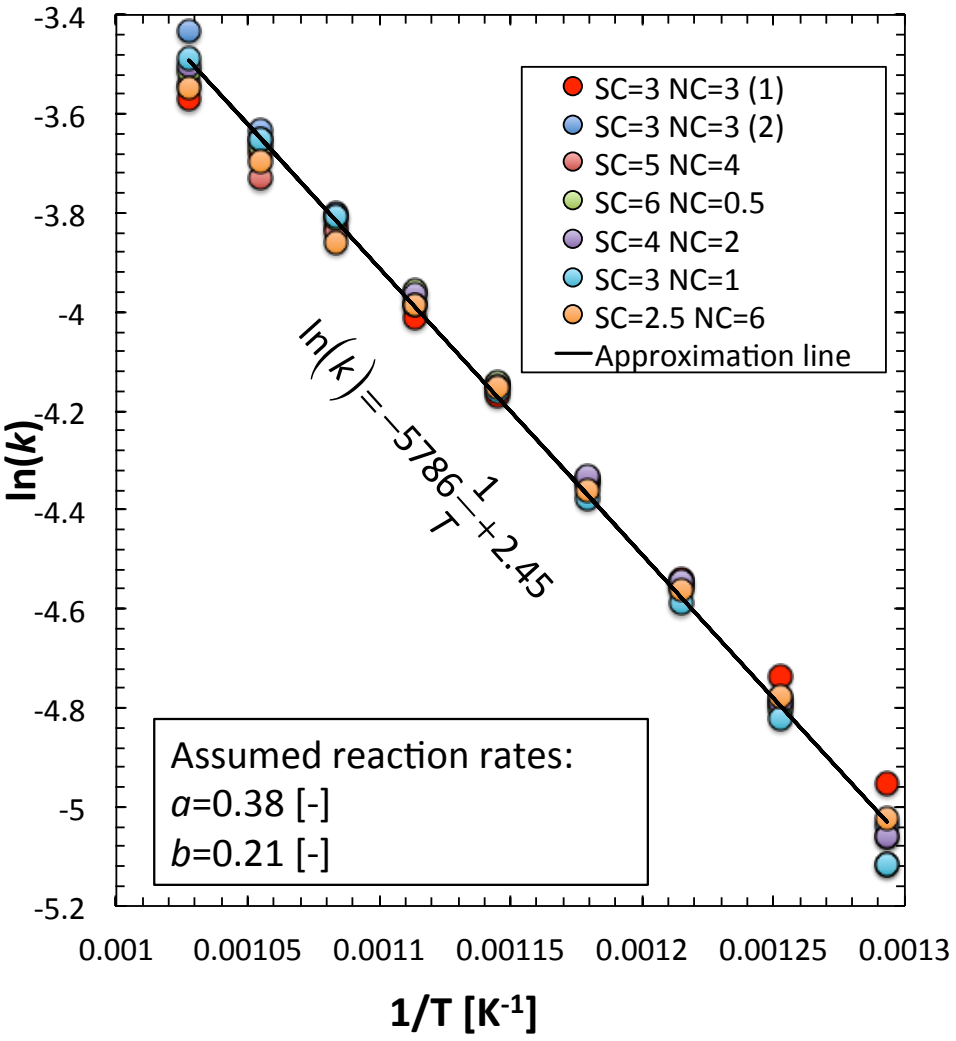

Figure 5.9 Arrhenius plot for the catalyst, of NiO/YSZ (60:40vol.%) prepared with ethanol dispersant, calculated with the reaction orders calculated in accordance with the modified method

Finally the full kinetic equation of the methane/steam reforming process over the sintered NiO/YSZ catalyst can be written as:

$$R_{st} = w_{cat} \cdot r = w_{cat} \cdot 11.6 \cdot \exp\left(\frac{-48105}{RT}\right)\left(p_{CH_4}\right)^{0.38}\left(p_{H_2O}\right)^{0.21} \tag{5.4}$$

5.4 Model of the methane/steam reforming process

Reaction rate equation Eq. (5.4) determined in Section 5.3 was used in order to simulate the gas composition at the reactor outlet from the defined initial conditions of a system with the methane/steam reforming process over the NiO/YSZ (60/40vol.%) catalyst (sample 0.3g). The numerical simulation was conducted by means of the algorithm proposed in Section 3.8. The experimental and simulation results are presented in Figs. 5.10 – 5.14.

The quality of the proposed numerical model is presented in Figure 5.10, where the experimentally obtained conversion rate of methane is plotted versus the methane conversion rate calculated by the simulation model with the empirical reaction kinetics in Section 5.3. The points located on the line presents a perfect fit of numerical and experimental results. It should be noted that Fig. 5.10 presents all of the experimental data collected during the investigations, including measuring Series 1 and Series 2 (described in Table 4.5), which were not used directly in the derivation of methane/steam kinetic expressions described by Eq. (5.4). These data sets can be treated as a validation set to evaluate the quality of modelling. Good agreement between experimental and numerical results is observed for the lower conversion rates in the range of 20-60%. As it was presented in Figs. 5.1 and 5.4 these conversion rates are reached in the experiments conducted below 650^{o}C. With increasing temperature, the conversion rate increases and the divergence between numerical and experimental methane conversion rates becomes more significant. This type of behaviour is explained by the deliberation in Section 4.6, where the influence of the Gas Hourly Space Velocity for the estimation of kinetic behaviour is discussed. The high conversion rates indicate that the reforming process was carried out at the condition close to the equilibrium state. Generally, the experimental conversion rate should be kept at a low level in order to estimate kinetic changes in the reaction rate. In the investigation on the sintered catalysts, characterized by the high catalytic activity, presented in next Section 5.5, the GHSV was increased by decreasing the weight of the catalyst sample from 0.3 g to 0.1 g and increasing

the total molar flow rate of gas mixture input from $F_{total}^{i} = 1.43 \cdot 10^{-2}$ mol min^{-1} to $F_{total}^{i} = 4.29 \cdot 10^{-2}$ mol min^{-1} (the experimental conditions introduced in Table 4.6). The increased GHSV provides the decreased conversion rates of methane, which locates the process in the non-equilibrium condition, are dominant and then will dedicate the determination of the proper kinetic equation.

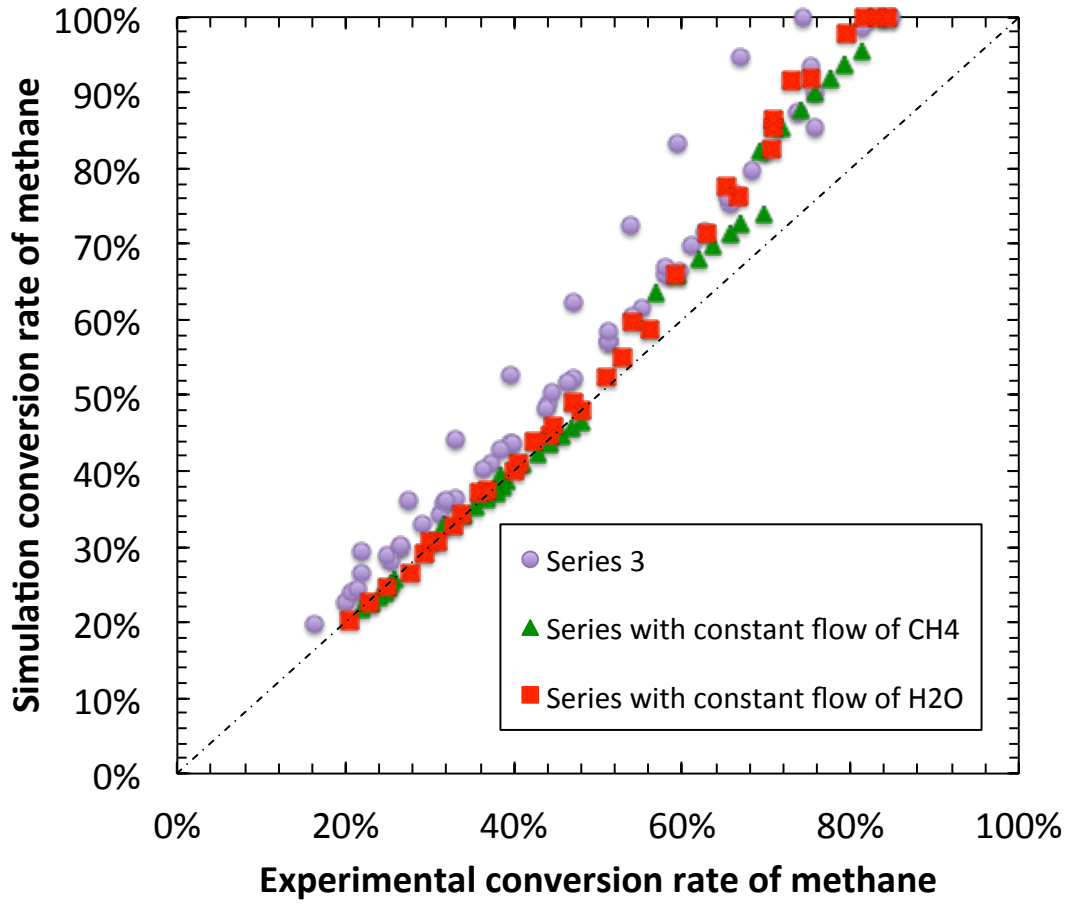

Figure 5.10 Comparison of conversion rates obtained experimentally and calculated by simulation for measurements in Series 1 – 3

The influence of the process temperature on the gas composition at the reformer outlet is presented in Fig. 5.11 for the case when the flow rate of the methane was F_{CH4}^{i}=50 ml min^{-1}, *SC*=3, *NC*=3 and the weight of the catalyst was equal to 0.3 g. The molar fraction of the methane at the reformer outlet decreased with the increase of the process temperature as was expected. Opposite behaviour is observed for the molar fraction of hydrogen – in the high temperature almost all the methane is reformed to hydrogen, to carbon monoxide and, by the means of water-gas-shift reaction, to carbon dioxide. Generally, with the increased temperature the amount of carbon oxide in the outlet gas composition is increased, however,

the amount of carbon monoxide increases more significantly. It is beneficial in the contexts of a high operating temperature SOFCs, because the carbon monoxide can be electrochemically converted as a fuel [123] and, in contrast to low operating temperature fuel cells, it does not poison them.

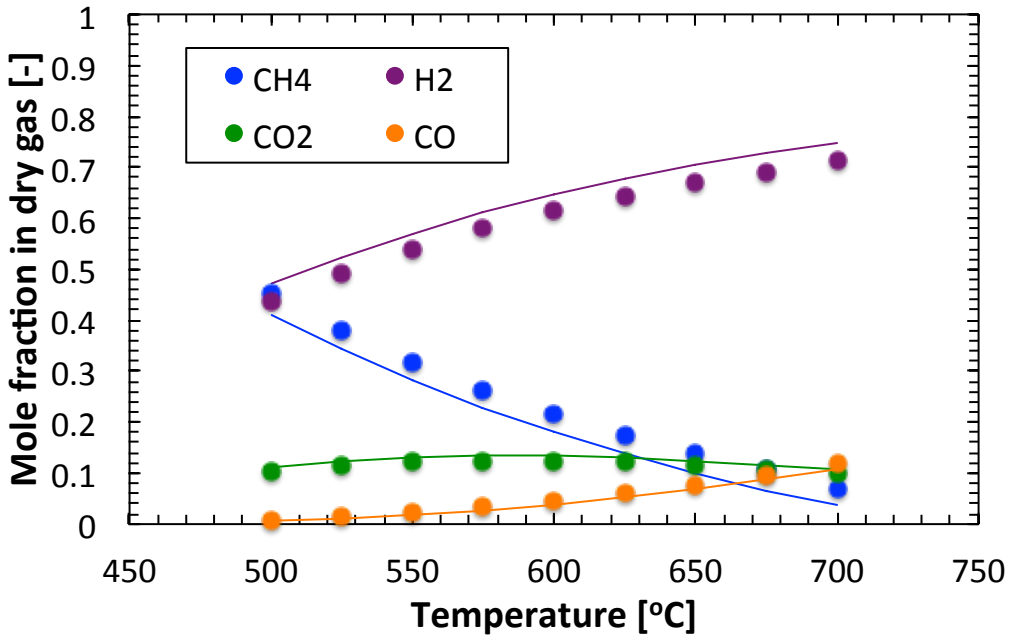

Figure 5.11 Comparison of experimental and numerical molar fraction of species (in condition of F_{CH4}^{i}=50 ml min^{-1}, *SC*=3, *NC*=3); lines represent the numerical simulation and dots present the experimental results

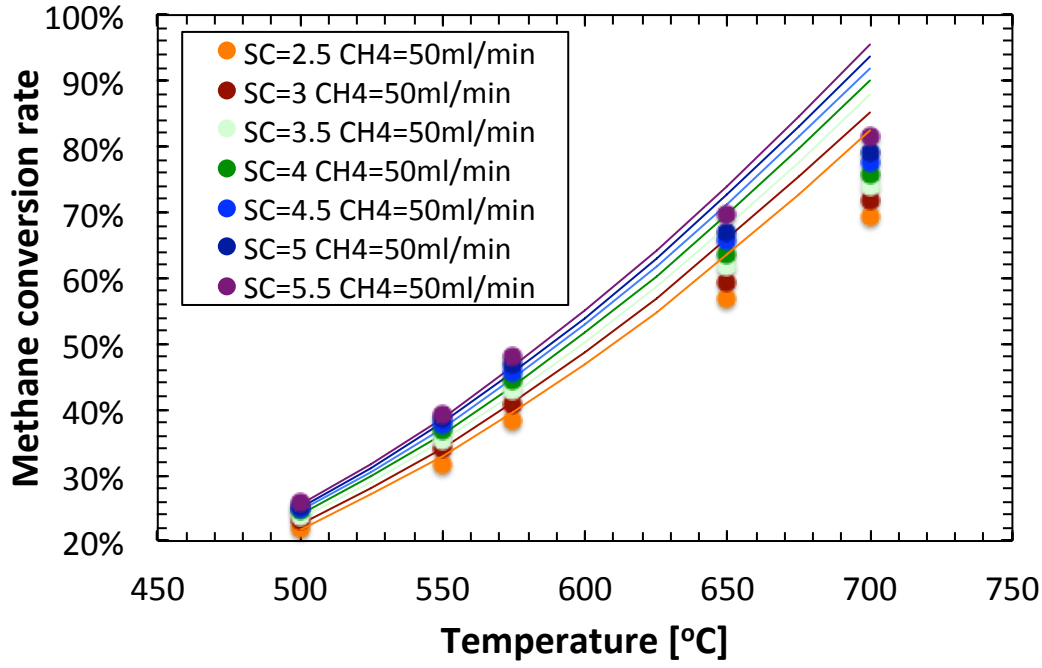

Figure 5.12 Influence of temperature and the *SC* ratio on the methane conversion rate – a comparison of experimental and numerical results (in conditions F_{CH4}^{i}=50 ml min^{-1}, Series 1); lines represent the numerical simulation and dots indicate the experimental results

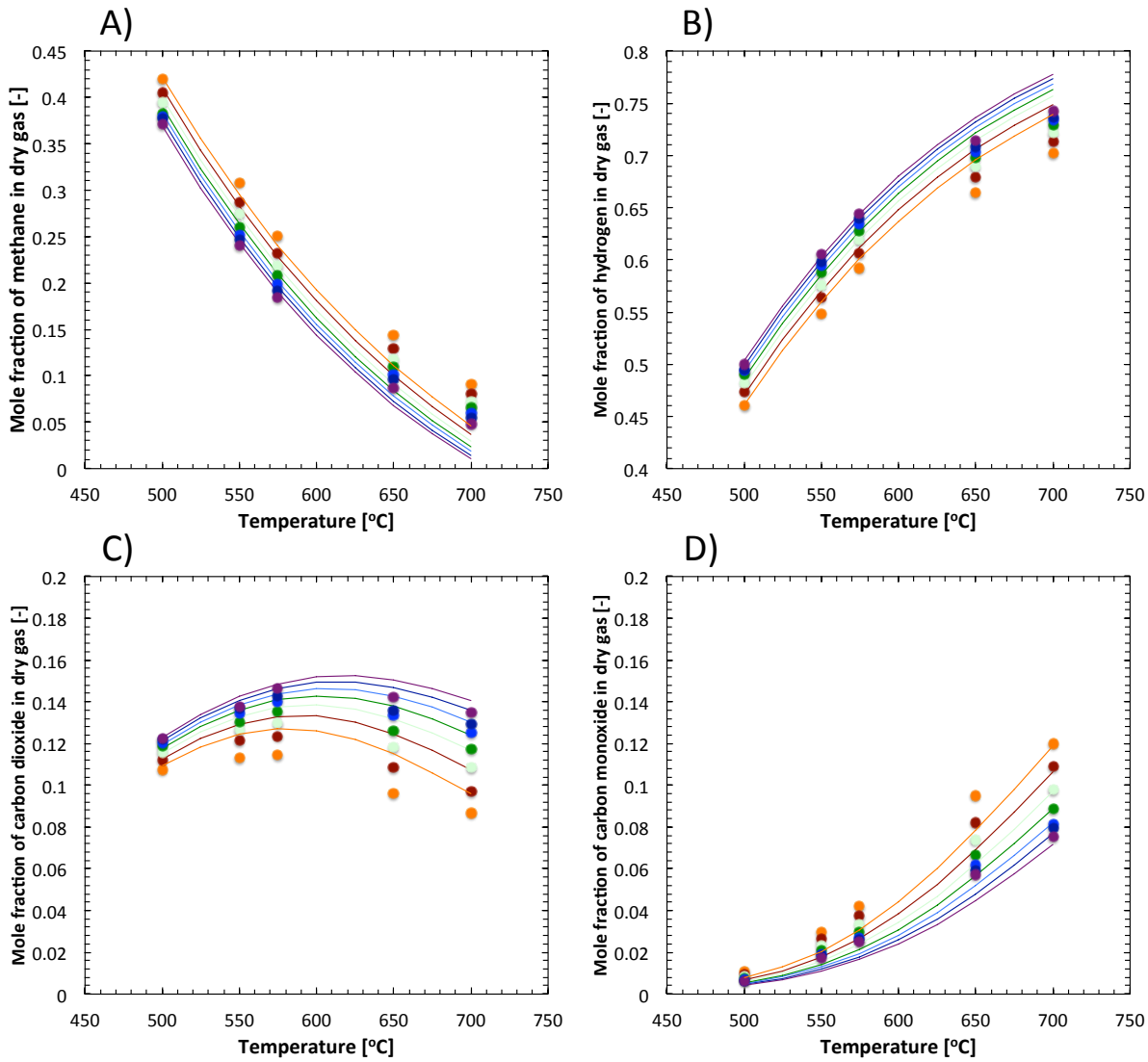

Figure 5.13 Influence of temperature and *SC* ratio for the chemical composition of outlet gas – a comparison of experimental and numerical results (in condition of F_{CH4}^{i}=50 ml min^{-1}, Series 1) for A) methane, B) hydrogen, C) carbon dioxide and C) carbon monoxide; lines represent numerical simulation and the dots indicate the experimental results

The investigation on the influence of *SC* ratio on the conversion rate and the gas composition at the reformer outlet are shown in Figs. 5.12 and 5.13, respectively. The results are given for the measurement series with the constant flow rate of methane F_{CH4}^{i}=50 ml min^{-1}, and *SC* ratio varied in the range of 2.5 – 5.5. The *SC* ratio is varied by manipulating the flow rate of water in the range of 0.09 to 0.2 ml min^{-1}. As was noted before, the numerical model well fits the experimental results at lower temperatures, but at higher ones the differences are noticeable for both the conversion rates and molar fractions of the chemical species in the outlet gas. It is observed that with the increased input flow rate of water resulting in an increased *SC* ratio, the conversion rate of methane increases, which is the result of the

decreased share of methane in the outlet gas composition and increased shares of hydrogen and carbon oxides. This correlation is valid throughout the whole temperature range.

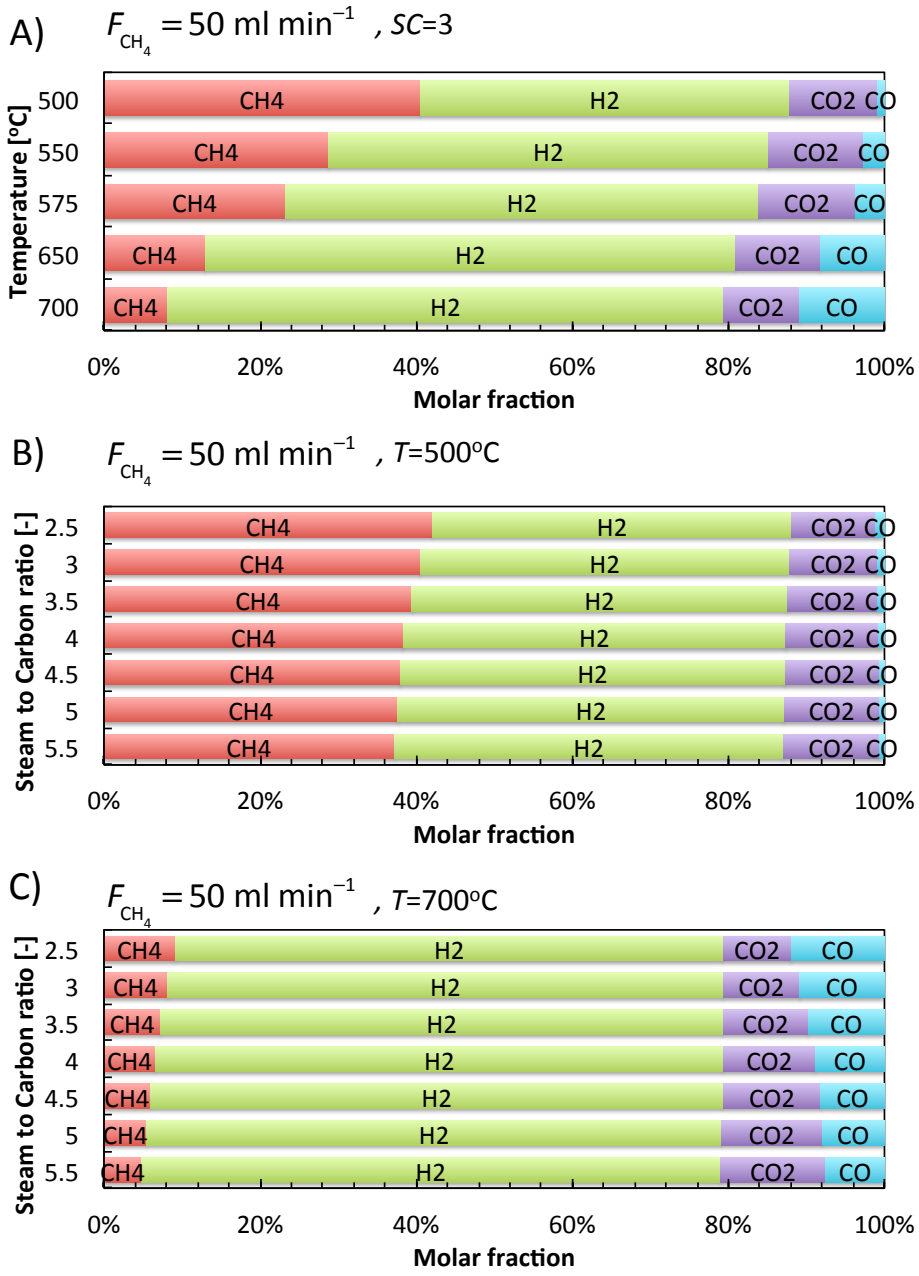

Figure 5.14 Experimentally obtained dry gas composition A) influence of temperature (F_{CH4}^{i}=50 ml min^{-1}, SC=3, NC=3), B) influence of SC rate (T=500°C, F_{CH4}^{i}=50 ml min^{-1}, Series 1) and C) influence of SC ratio (T=700°C, F_{CH4}^{i}=50 ml min^{-1}, Series 1)

The influence of the experimental condition for the gas composition at the reformer outlet is in the detail discussed in Fig. 5.14, where the shares of the chemical species in the dry gas are shown. The influence of the temperature is presented in Fig. 5.14.A, and the influence of the varied flow rate of water (namely varied SC ratio) on the outlet gas composition at the

temperature of 500 ^{o}C is presented in Fig. 5.14B and the one at a temperature of 700 ^{o}C is in Fig. 5.14C. The change in the proportion of carbon monoxide and carbon dioxide is observed with the change in temperature and *SC* ratio. Generally, the increase in temperature decreases the amount of CO_2 in comparison to CO. The CO_2 is produced as an effect of shift reaction from CO and H_2O. Potentially, a large amount of water is utilized in the methane reforming process at the higher temperature, which decreases the amount of converted carbon monoxide species. The total amount of carbon oxides with increase of *SC* ratio is slightly increased and the significant difference is visible at the ratio of CO_2 to CO. The increased flow rate of steam at the inlet increases the conversion rate of carbon oxide to carbon dioxide, which subsequently increases the amount of hydrogen produced in the system.

5.5 Influence of the catalyst for the derived kinetics

The adjusted experimental conditions described in the previous section (increased total molar flow rate and decreased weight of catalyst sample) were used in investigations of catalyst materials with different volumetric percentage of nickel. The details of the experimental conditions are given in Table 4.6. All of the investigated catalyst materials were prepared with acetone dispersant. The investigated samples were catalyst prepared with Ni and YSZ powders with volume ratios of Ni and YSZ in the cermet as (Ni:YSZ) = (30:70), (40:60), (50:50), (60:40), (70:30). The samples were named as Ni/YSZ 30:70vol.%, Ni/YSZ 40:60vol.%, Ni/YSZ 50:50vol.%, Ni/YSZ 60:40vol.% and Ni/YSZ 70:30vol.%. One additional cermet sample was prepared with NiO powder and the proportions of NiO and YSZ powders were chosen to have 60vol.% share of nickel in the sample after the reduction process. This sample is distinguished as NiO/YSZ 60:40vol.% catalyst, however, prior to reaction of methane/steam reforming, nickel oxide was firs reduced to nickel.

The analysis by the standard method (experimental data listed in Table 4.6 as Series 1 and 2) and by the modified method (experimental data listed in Table 4.6 as Series 3) was conducted for sample NiO/YSZ 60:40vol.%. The experimentations were carried out at temperatures 550 ^{o}C, 600 ^{o}C and 650 ^{o}C for all experimental conditions in Series 1-3.

The results of the modified method application are presented in Fig. 5.15. A summary of the application standard and modified method in all investigated conditions is given in Table 5.3

and 5.4, respectively. Good convergence between investigated conditions and method was found. /As the final values of reaction orders for catalyst sample NiO/YSZ 60:40vol.% values designated by the modified method were chosen: a=0.71 and b=-0.08.

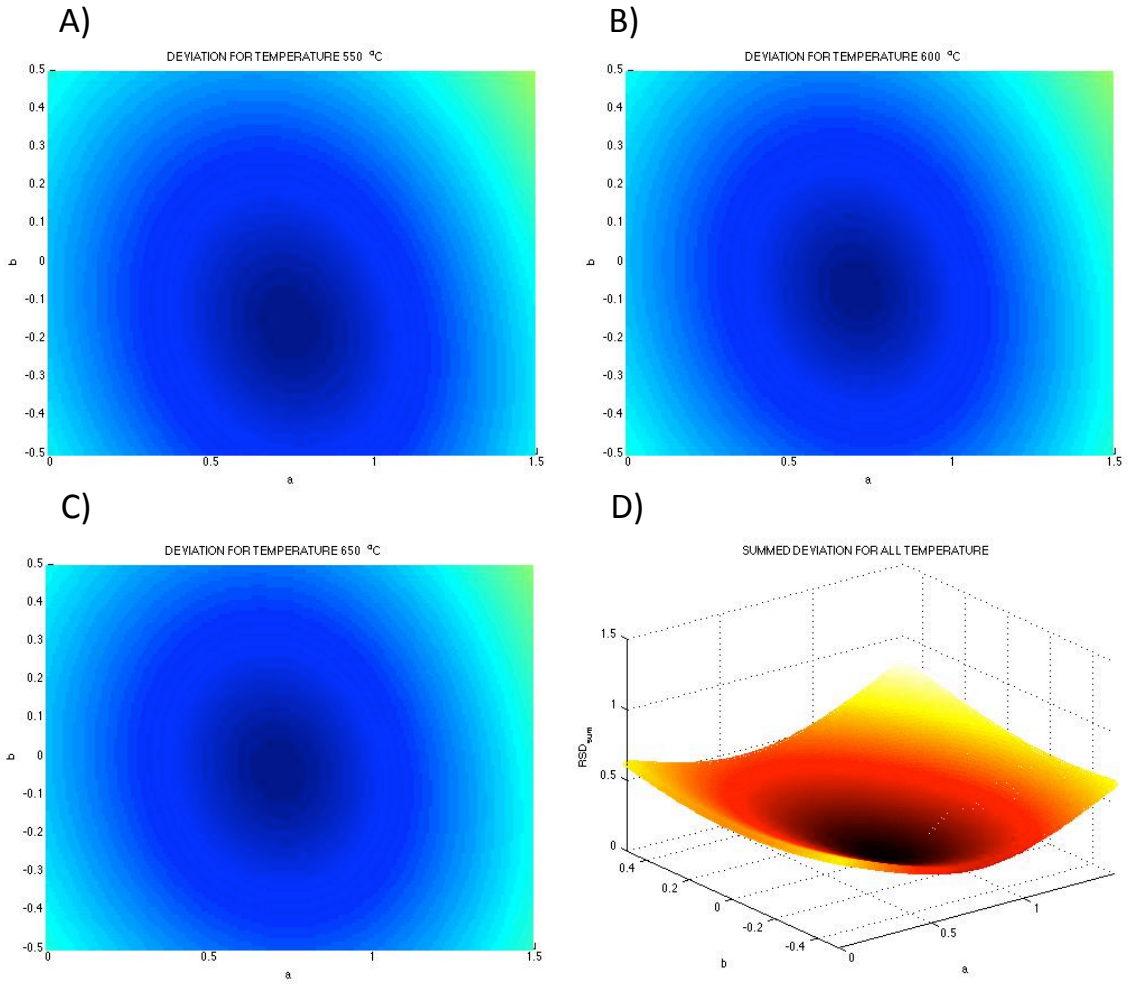

Figure 5.15 An approximation of reaction orders by the modified approach with modified experimental data: A) 550 °C, B) 600 °C, A) 650 °C and D) summed standard deviation for temperatures 550-650 °C

Table 5.3 Comparison of reaction orders parameters calculated by modified method

	550°C	600°C	650°C	Average	All temperatures
a	0.74	0.71	0.71	0.72	0.71
b	-0.16	-0.07	-0.04	-0.09	-0.08

Table 5.4 Comparison of reaction orders parameters calculated by standard method

	550°C	600°C	650°C	Average
a	0.82	0.71	0.75	0.76
b	-0.04	0.04	0.10	0.04

The modified method was chosen to investigate the influence of the volumetric composition of the nickel cermet for the reaction kinetic. The reaction orders were estimated by the analysis with modified method and modified experimental conditions presented in Table 4.6 as experimental Series 3 with total molar flow rate $F_{total}^{i} = 4.29 \cdot 10^{-2}$ [mol min^{-1}]. The *SC* ratio was varied between 2.5 and 6, and the *NC* ratio was changed in the range 8-20. The results of the calculated reaction orders with respect to methane and water are summarized in the Table 5.3

Table 5.5 Comparison of reaction orders parameters for various catalysts

	NiO/YSZ	Ni/YSZ				
	60:40vol.%	30:70vol.%	40:60 vol.%	50:50 vol.%	60:40 vol.%	70:30 vol.%
a	0.71	0.73	0.73	0.73	0.71	0.69
b	-0.08	-0.13	-0.03	-0.03	-0.07	-0.07

The obtained reaction orders are convergent for all of the tested materials and they are in the range *a*=0.71-0.73 [-] for the reaction order with respect to methane (in the case of Ni/YSZ 70:30vol.% catalyst the reaction order is slightly lower *a*=0.69 [-]) and in the range *b*=-0.13 - -0.03 for the reaction order with respect to water. The value of the reaction order concerning water is convergent with the literature data, which suggests a slight dependence of water partial pressure. On the other hand, the evaluated reaction orders with regard to methane seems to be lower than the results presented in the literature for the methane/steam reforming process over nickel catalyst (see Table 1.3). The literature suggests that methane/steam reforming is a first order reaction with respect to methane partial pressure. However, those studies were usually conducted using industrial catalysts and catalysts which were not sintered. The materials investigated in this study (Section 5.5) were prepared in the procedure analogical to the production of SOFC anodes, including sintering Ni/YSZ pellets at a temperature of 1400°C. The comparable studies are investigations conducted by Mogensen

[81] and Iwai [151] using SOFC anodes materials to evaluate the kinetic of the methane/steam reforming process.

Details of both studies (Mogensen and Iwai) are given in Chapter 7, in which an extensive comparison of the reaction kinetics in various studies is presented. Here the main focus is on estimated reaction orders with respect to methane. Mogensen investigated the anode materials and SOFC stack anodes samples, all of them composited of Ni/YSZ cermet, in the form of powders in packed bed measurements. The standard method of calculation reaction orders was used in this study and the results for the reaction order with regard to methane are summarized in Table 5.4. Iwai proposed an analysis of the disk shaped cermet materials sintered in 1400^{o}C for catalysts: Ni/YSZ 100:0vol.% (designated as Ni100), Ni/YSZ 75:25vol.% (Ni75), Ni/YSZ 50:50vol.% (Ni50), Ni/YSZ 25:75vol.% (Ni25) and Ni/YSZ 50:50vol.% catalyst sintered in 1450^{o}C (designated as Ni50*). The modified calculation method was used for finding values of the reaction orders concerning methane and water. The results of the calculation for the reaction order with respect to methane are listed in Table 5.5.

In the studies presented by Mogensen and Iwai the evaluated reaction orders concerning methane are significantly lower than one: Mogensen averaged the results of the standard analysis method, and the results are in the range 0.74 – 0.813 for the investigated materials. In Iwai's research, it was shown that the composition of cermet did not influence the reaction orders with regard to methane significantly: the effect of inlet gas composition is similar regardless of the Ni/YSZ volume ratio in the cermet. The calculated reaction range with respect to methane is 0.82 for catalysts sintered at temperature 1400 ^{o}C and 0.84 for the catalyst sintered at temperature 1450 ^{o}C.

Table 5.6 Reaction orders with respect to methane *a* calculated by Mogensen [81]

Temperature	Model anode	Industrial anode	Old stack anode sample	New stack anode sample
600°C	0.779			0.702
625 °C	0.839	0.751		
650 °C	0.906	0.721	0.89	0.77
675 °C	0.906	0.684		
700 °C	0.871	0.666	0.858	0.789
725 °C	0.937	0.803		
750 °C	0.378	0.805	0.763	0.765
775 °C	0.797	0.802		
800 °C	0.797		0.739	0.712
Average	0.801	0.747	0.813	0.748

Table 5.7 Reaction orders with respect to methane *a* calculated by Iwai et all [151]

	Ni100	Ni75	Ni50	Ni25	Ni50*
a	0.82	0.82	0.82	0.82	0.84

6 An application of the GLS Method

The Generalized Least Squares method can be applied for methane/steam reforming in order to secure the most probable description of the kinetic of analysed process in the context of the non-equilibrium state of the reaction. In Chapter 6 the possibility and technical aspect of the implementation are presented with the focus on the analysis of the reforming process on the NiO/YSZ (60:40vol.%) un-sintered catalyst material provided by the AGC SEIMI CHEMICAL CO. LTD. The description of all the steps from the definition of the mathematical model, calculation of the initial approximation of unknowns with the standard method, application of the GLS algorithm and the discussion of their results is provided.

The numerical implementation of the GLS algorithm to methane/steam reforming analysis was prepared in the MATLAB package. Additionally, the general library of the classes responsible for GLS operators was prepared in the C# language for the possible easy extensions and applications to the various research problems in the field of energy science. Among others, the library was used in the analysis of the heat transfer problems [180].

6.1 An application of the GLS method to the methane/steam reforming process – a general approach

The mathematical bases of the GLS method were introduced in Section 2.5 and 2.6. The application of mathematical theory to the analysis of kinetic of chemical reactions requires the preparation of a numerical algorithm, which will include the consecutive steps of the theoretical method. General requirements and the schematic idea are introduced in Fig. 6.1. The input information required for the application of the GLS algorithm includes the implementation of the mathematical equations describing the process and the definition of input data for the values of both the measured and unknown variables. The GLS algorithm is a universal method, which allows for the flexible definition and changes in the number of defined equations in the mathematical model. Adding new constraint formula to the system does not influence the already existing set, as all of them are defined independently. The

model equations are based on the system variables, which can be divided for two groups: measured and unknown variables. The definition of both of them, measured and unknown variables is congruent and demands specifying the numerical values of the variables and characterizing them uncertainty. The values of the measurements are the direct experimental results. The values of the unknowns are taken as random values or are estimated on the basis of preliminary calculations to assure the convergence of the final solution in the case of highly nonlinear and complex constraint sets. In the case of the analysis of methane/steam reforming process, the numerical model consisted of the nonlinear equations defining the kinetic of the process – therefore, in the practical implementation of the method, the initial values of unknowns were estimated by the methods described in Sections 3.6 and 3.7. The results of the application of the statistical and numerical operators of the GLS algorithm to the analysis of engineering problem are the full descriptions of the most probable state of the system with the values of unknowns and corrected in the assumed uncertainty range value of measurements. Additionally, one of the outputs is *a posterior* covariance matrix, which contains the standard deviations of all of the variables after reconciliation process. The newly calculated error bounds provide an objective criteria for a verification of the quality of a mathematical model by comparison of the volume of the hyperellipsoide of the distribution for various models as it was introduced in Section 2.6. This property together with the simplicity of the definition constraint equations and combining them with the GLS algorithm constitutes an excellent tool for the verification and evaluation numerical models, even for problems in complex systems.

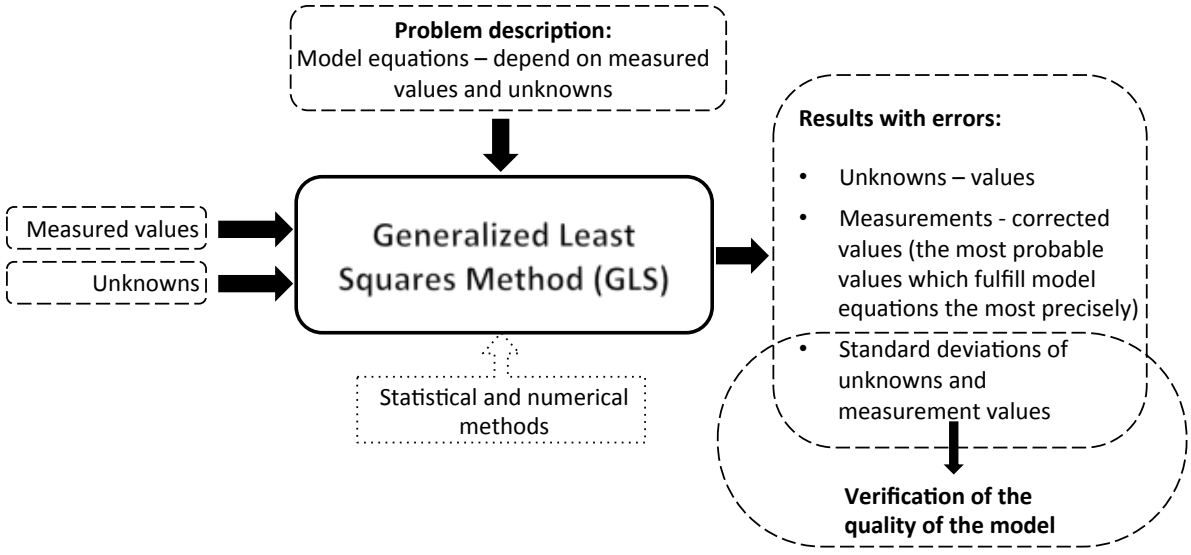

Figure 6.1 Application schema of the Generalized Least Squares Method

The consecutive steps of the GLS algorithm are presented on the schema in Fig. 6.2. The analysis starts from the selection and a precise definition of mathematical equations describing a physical process, which states the constraints set of the problem. Then, the structure of the vector containing the measurements and unknowns has to be defined. As all system variables are treated in the same way from a mathematical point of view, vector **x** contains the values of all measurements in the front part, and subsequently there are unknown values located. The difference between the measured and unknown variables is an assumed value of uncertainties connected with those two types of variables. The uncertainty values were then used in the initialization of the *a priori* covariance matrix $\mathbf{C_B}$ built in the same manner as vector **x** – diagonal variances of direct measurements are followed by variances of the unknowns. All of the non-diagonal elements of the matrix $\mathbf{C_B}$ are equal to 0 since all of the variables are independent measured variables.

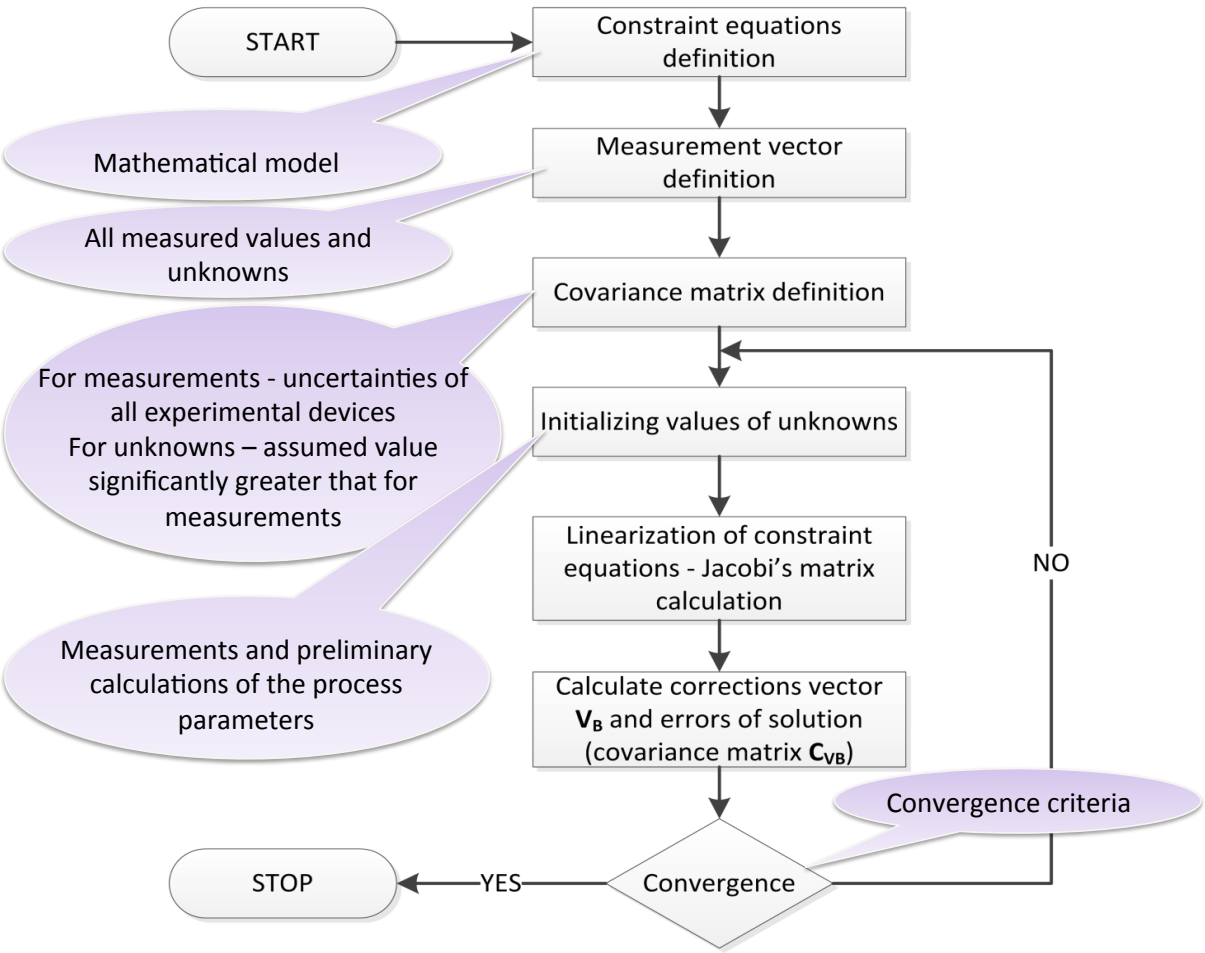

Figure 6.2 Schema of the GLS algorithm applied to the reaction kinetic calculations

After the definition of all of the model elements, the main part of the GLS algorithm was performed. The nonlinear adjustment problems need to be solved numerically by the linearization procedure using the Taylor's expansion [175]. In the iterative algorithm the values of the Jacobi's matrix were calculated by using the values from the previous iteration, and then the Lagrange multipliers method allows for the calculation of the correction vector $\mathbf{V_B}$ and finding the corrected values of the direct measurements and unknowns. In addition, the new error bounds for both of them were estimated. The last step of the iterative algorithm is to verify the convergence of the obtained solution and this is stipulated with the criteria of convergence or the recalculation on the basis of the unknown values determined in the previous step.

6.2 The definition of the Equations

The main equations used in the description of the methane/steam reforming process were introduced in Chapter 3. Usually, the methodologies for the calculation of the reforming reaction kinetic parameters are based on assumptions in accordance with the stoichiometry of the chemical reactions included in the process model [81,94]. It was shown by Mogensen, that measuring only a partial composition of the outlet, ratios of carbon monoxide and carbon dioxide among all outlet gases, is enough to determine the reforming rate [81]. However, this type of analysis can lead to simplifications, which can affect the final conclusions, increases the uncertainty of the obtained results and possibly explain the great disagreements between the different presented studies. Excluding the stoichiometric assumptions from the model and including supplementary data (as methane and hydrogen composition in the outlet gases) can give additional information about the problem and improve the reliability of the obtained solution.

It is known that experimental results should fulfil some equations, which are genuine for the behaviour of any physical system, specifically for a system with a catalytic chemical reaction. Among those physics' laws we can particularly distinguish the basic balances of all chemical elements, which are contained in the products of the reaction. On the other hand, the catalytic chemical reaction should follow the Eq. (3.23), which actually contains the most important unknown parameters in terms of the presented analysis (reaction orders a and b, activation energy E and Arrhenius coefficient A). Moreover, it should be pointed out that each general

constraint equation should be fulfilled by each measurement (measurement point), therefore the total number of mathematical equations in the problem description is equal to the number of measurement points multiplied with the amount of the general equations.

The constraint equations used in the GLS algorithm to describe the process of steam reforming of methane can be divided into four basic categories; in all of the presented examples the basic definition of the problem is supplemented by the additional equations describing the fundamental laws governing the chemical reaction which can be divided /for the following groups:

reaction rate equation:

$$\frac{F_{\mathrm{CH_4}}^{\mathrm{i}(j)} - F_{\mathrm{CH_4}}^{\mathrm{o}(j)}}{w^{(j)}} - A \cdot \exp\left(\frac{-E \cdot 10^3}{RT^{(j)}}\right)\left(p_{\mathrm{CH_4}}{}^{(j)}\right)^a \left(p_{\mathrm{H_2O}}{}^{(j)}\right)^b = 0, \tag{6.1}$$

linear Arrhenius correlation:

$$\ln\left[A \cdot \exp\left(\frac{-E \cdot 10^3}{RT^{(j)}}\right)\right] - \left(-\alpha_{\mathrm{line}} \cdot \frac{1}{T^{(j)}} + \beta_{\mathrm{line}}\right) = 0, \tag{6.2}$$

water-gas-shift reaction equation:

$$\frac{p_{\mathrm{H_2}}{}^{(j)} p_{\mathrm{CO_2}}{}^{(j)}}{p_{\mathrm{CO}}{}^{(j)} p_{\mathrm{H_2O}}{}^{(j)}} - \exp\left(\frac{-\Delta G}{RT^{(j)}}\right) = 0, \tag{6.3}$$

balances of the elements in the reactants and products

$$F_{\mathrm{CH_4}}^{\mathrm{i}(j)} - \left(F_{\mathrm{CH_4}}^{\mathrm{o}(j)} + F_{\mathrm{CO_2}}^{\mathrm{o}(j)} + F_{\mathrm{CO}}^{\mathrm{o}(j)}\right) = 0, \tag{6.4}$$

$$4F_{\mathrm{CH_4}}^{\mathrm{i}(j)} + 2F_{\mathrm{H_2O}}^{\mathrm{i}(j)} - \left(4F_{\mathrm{CH_4}}^{\mathrm{o}(j)} + 2F_{\mathrm{H_2O}}^{\mathrm{o}(j)} + 2F_{\mathrm{H_2}}^{\mathrm{o}(j)}\right) = 0, \tag{6.5}$$

$$F_{\mathrm{H_2O}}^{\mathrm{i}(j)} - \left(F_{\mathrm{CO}}^{\mathrm{o}(j)} + F_{\mathrm{CO_2}}^{\mathrm{o}(j)} + 2F_{\mathrm{H_2O}}^{\mathrm{o}(j)}\right) = 0, \tag{6.6}$$

$$F_{\mathrm{N_2}}^{\mathrm{i}(j)} - F_{\mathrm{N_2}}^{\mathrm{o}(j)} = 0, \tag{6.7}$$

where F designates molar flow [mol s^{-1}], superscripts i and o are input and output flow respectively and subscripts describe the respective chemical species. The additional variables m_{line} and n_{line} are the Arrhenius line coefficients [-]. All of the above equations were used for every measurement point – index j designates the j-th measurement point.

6.3 The definition of the Variables

Application of the GLS algorithm demands a definition of both constraint equations in the mathematical model and the variables used in the system along with their uncertainties presented in the form of the covariance matrix. Among all variables they can be distinguished into two groups: directly measured and unknown variables. The unknown parameters are dependent on the model definition; some of them are artificial and are introduced only to make the mathematical model transparent. Therefore, firstly the constraint set will be presented and then the necessary additional variables will be specified.

All of the measured variables with the specification of the experimental error characteristic for all of them are summarized in Table 6.1. Uncertainties of the measured values were determined on the basis of the technical documentation of the instruments or error analysis conducted for the respective measuring devices. The molar fraction of the chemical components in the outlet gas produced by the reforming process were investigated by the gas chromatograph (GL Sciences, GC390B) equipped in the Thermal Conductivity Detector and Flame Ionization Detector. Then uncertainty of both detectors was estimated on the basis of the additional measurements of the standard gas conducted in parallel with the measurements for the methane/steam reforming process.

The unknown parameters defined in the process description are divided into major and supplementary variables. All unknowns and the uncertainty correlated with them are presented in Table 6.2. The values of the errors of the unknowns and the uncertainty of the measurements presented in Table 6.1 are used for the initial definition of the covariance matrix $\mathbf{C}_{\mathbf{VB}}$.

Table 6.1 Experimental variables and correlated uncertainties

Variable	Symbol	Unit	Detector	Experimental uncertainty
Temperature	T	^{o}C	Thermocouple	$\pm\left(2+0.007\cdot T\right)$
Catalyst weight	w	g	Electronic balance	±0.0005
Pressure difference (inlet and outlet)	ΔP	MPa	Pressure meter	$\pm 0.003\cdot\Delta P$
CH_4 input flow	$F_{CH_4\_v}^{\ i}$	mL min^{-1}	Flow meter	$\pm 0.002\cdot F_{CH_4\_v}^{\ i}$
H_2O input flow	$F_{H_2O\_v}^{\ i}$	mL min^{-1}	Flow meter	$\pm 0.04\cdot F_{H_2O\_v}^{\ i}$
N_2 input flow	$F_{N_2\_v}^{\ i}$	mL min^{-1}	Flow meter	$\pm 0.002\cdot F_{N_2\_v}^{\ i}$
CH_4 molar fraction in products	$m_{CH_4}^{\ o}$	-	Gas Chromatograph, GL Sciences, GC390B, TCD detector	±1
H_2 molar fraction in products	$m_{H_2}^{\ o}$	-	Gas Chromatograph, GL Sciences, GC390B, TCD detector	±1
CO_2 molar fraction in products	$m_{CO_2}^{\ o}$	-	Gas Chromatograph, GL Sciences, GC390B, FID detector	±0.5
CO molar fraction in products	$m_{CO}^{\ o}$	-	Gas Chromatograph, GL Sciences, GC390B, FID detector	±0.5

Table 6.2 Defined unknown variables for the GLS algorithm

Unknown		**Unit**	**Error**	**Unknown**		**Unit**	**Error**
Major variables				**Supplementary variables**			
Reaction order	a	-	100% a	Line coefficients	α_{line}	-	100% m_{line}
				Line coefficients	β_{line}	-	100% n_{line}
Reaction order	b	-	100% b	**Supplementary variables (for each measurement)**			
Pre-exponential factor	A	mol g^{-1} s^{-1} atm$^{-(a+b)}$	100% A	H_2O output flow	$F_{H_2O}^{\ o(j)}$	mol min^{-1}	100%$F_{H_2O}^{\ o(j)}$
				N_2 output flow	$F_{N_2}^{\ o(j)}$	mol min^{-1}	100%$F_{N_2}^{\ o(j)}$
Activation energy	E	J mol^{-1}	100% E	Total output flow	$F_{ALL}^{\ o(j)}$	mol min^{-1}	100%$F_{ALL}^{\ o(j)}$

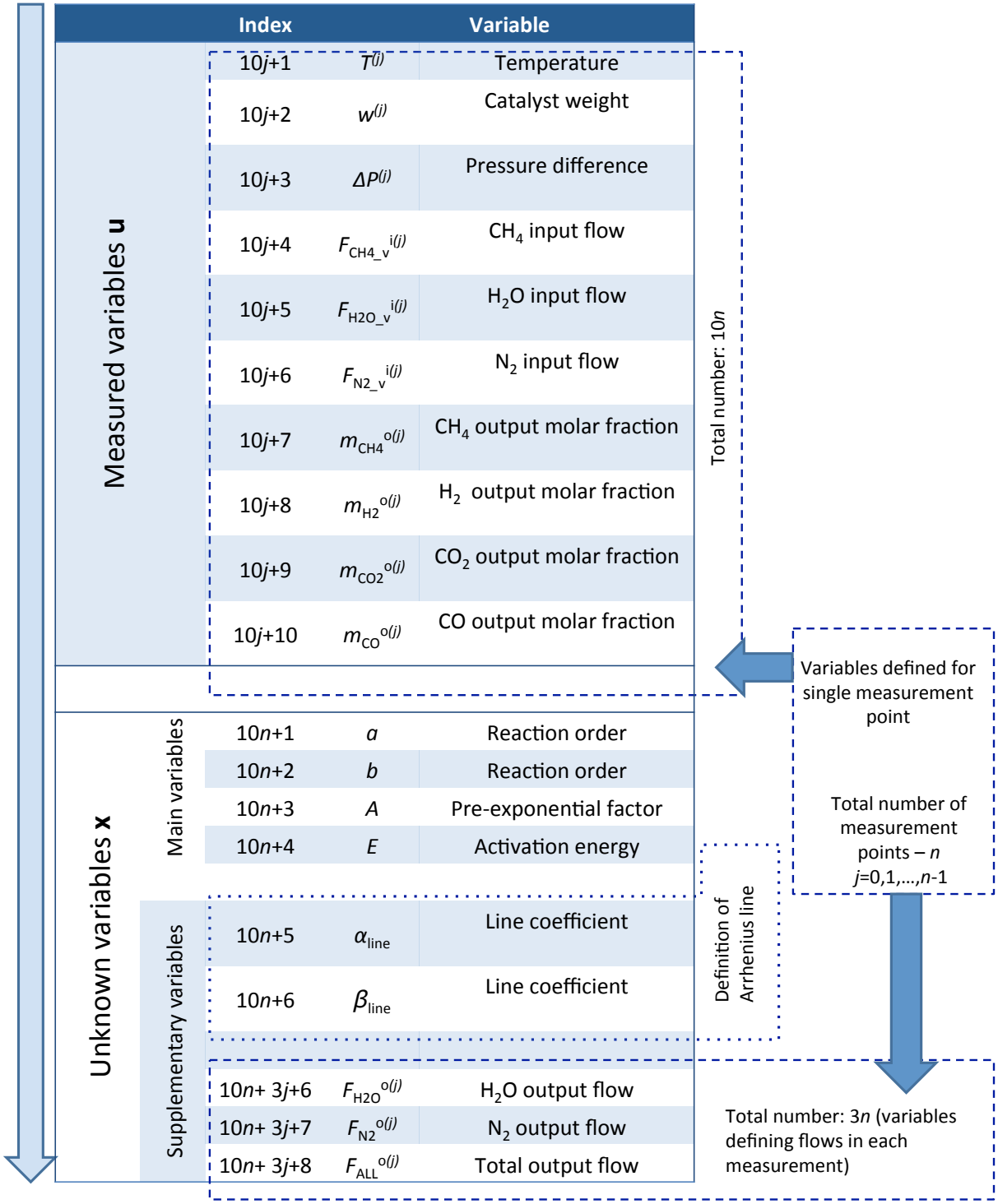

Figure 6.3 Structure of the variables vector with measurements **u** described in the front part and unknowns **x** in the back part

The overall structure of the variables vector containing measured and unknown variables is introduced in Fig. 6.3. The beginning part of Table 6.1 contains measured values (10 variables for each measurement point, in total $n \cdot 10$ variables, where n is the total number of measured

points) and then the unknowns. The most important unknowns are the empirical parameters that describe the process: a, b, E and A. Among the supplementary variables there were defined the line coefficient for the linear Arrhenius correlation and the variables describing the outlet flows of water, nitrogen and total output molar flow rate $F_{\mathrm{H_2O}}{}^{o(j)}$, $F_{\mathrm{N_2}}{}^{o(j)}$ and $F_{ALL}{}^{o(j)}$. Those parameters are necessary for defining the elemental balances. Moreover, the introduction of additional variables allows for avoiding the assumptions of stoichiometry of reactions and allows for analysis of the process from the most objective point of view. Including all supplementary variables, the total number of unknowns equals to $n \cdot 10 + 6$. Tables 6.1 and 6.2 present the assumed errors for all the variables, which defines the covariance matrix (squared matrix, rank $n \cdot 10 + n \cdot 3 + 6$). In the case of the unknowns, the *a priori* error was assumed as 100% of the initiatory value, which are determined in the preliminary calculations.

It should be pointed that only the main variables defining kinetic parameters and additional variables for the Arrhenius correlation are constant for all of the measurement conditions. All other variables are unique for specific experimental conditions and therefore are defined separately for every measurement point.

6.4 The definition of the Model

The model described in Sections 6.1 – 6.3 is general and can be applied to an analysis with a different number of measurement points and various equation sets. In particular, the numerical code implementing the algorithm allows for a definition of the various combinations of the equation and applied experimental data. This feature, is applicable for the example in an theoretical approach, for the determination of the influence of the model constraints for the quality of the final solution or when the part of the acquired data is used as a validation set to determine the accuracy of the proposed solution.

However, in the application described in the current chapter, the applied configuration of the model is fixed. A constraints model consists of all of the proposed mathematical equations describing system: the kinetic reforming equation in Eq. (6.1), the linear Arrhenius equation in Eq. (6.2), the water-gas-shift reaction equation in Eq. (6.3) and the balances of the basic chemical elements (carbon, hydrogen, oxygen and nitrogen Equations in Eqs. (6.4)-(6.7)).

The total number of the equation types equals seven. As all the equations presented above are applied for the calculation of each experimental point and the total number of measurement points used in the analysis is n=52, the total number of equations in the mathematical model is equal to 364.

The model equations depend on the measured and unknown variables defined in vector **x.** The part of vector **x** containing measurements consists of 520 variables (10 measured values for every measurement point) and 162 variables in the unknowns' part (4 main variables and 158 supplementary variables).

6.5 The calculation of the values of the initial approximation of the unknowns

The highly nonlinear model of the reaction kinetic requires a proper initialization of unknown parameters. This subsection presents the computations leading to the estimation of the initial approximations of unknowns in the model.

Unknowns in the methane/steam reforming reaction kinetic model are divided into main and supplementary variables. The main variables defining the reforming process are the values of the empirical parameters describing the reaction order coefficients a and b, activation energy E, and pre-exponential factor A. The initial values of those parameters were estimated by the modified method described in the Section 3.6 and 3.7. The experimental conditions incorporated in the measurements are the conditions defined in Table 4.5. as Series 3: an experimental condition with widespread distribution. The total molar flow rate in the experiment was $F_{total}^{i} = 1.43 \cdot 10^{-2}$ [mol min^{-1}]. The smaller value of the total molar flow rate was used, because the unsintered NiO/YSZ catalyst is characterized by lower conversion rates than the sintered one, which were presented in Chapter 4. Figure 6.4 shows the representative examples of the measured fractional conversion of CH_4 over the unsintered NiO/YSZ (60:40vol.%) catalyst material provided by the AGC SEIMI CHEMICAL CO. LTD. The fractional conversion (conversion rate) of CH_4 was calculated from the correlation with the molar ratios in the dry gas of CH_4, CO and CO_2 measured by the gas chromatography [200]:

$$x_{CH_4} = \frac{m^o_{CO} + m^o_{CO_2}}{m^o_{CH_4} + m^o_{CO} + m^o_{CO_2}} \tag{6.8}$$

The fractional conversions in all of the analysed condition are in the range, which provides the proper evaluation of the reaction kinetic, as it was introduced in Section 4.6.

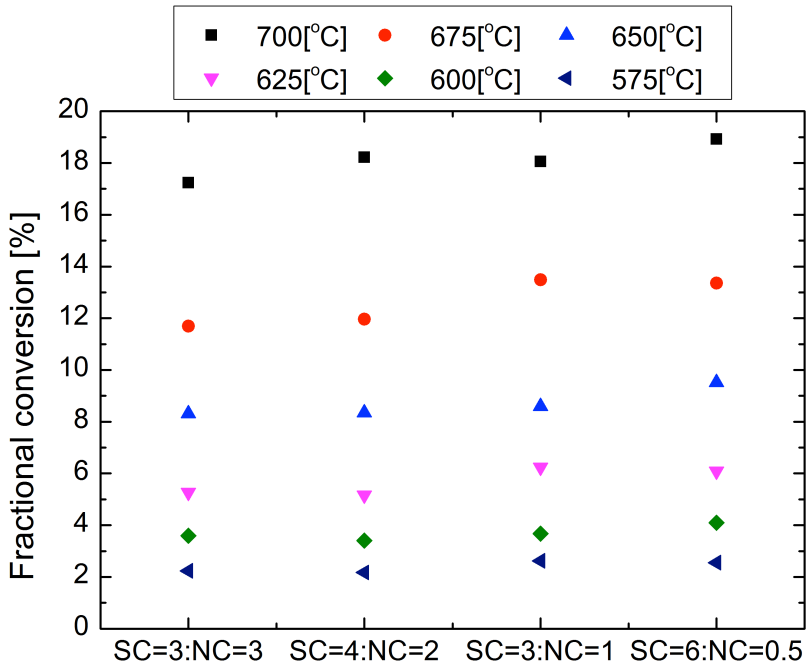

Figure 6.4 Fractional conversion measured experimentally over NiO/YSZ 60:40%vol unsintered catalyst

The first step of the calculation of the initial approximations of unknowns was based on the observation that the value of the reaction constant does not depend on the *SC* and *NC* ratios. Different combinations of the parameters *a* (range 0 – 1.5) and *b* (range -0.5 – 0.5) were tested and the calculated reaction constants were compared with the experimental results. The values *a*=0.97 and *b*=-0.08 were characterized by the smallest summed standard deviation and chosen as the best description of the process (see Fig. 6.5).

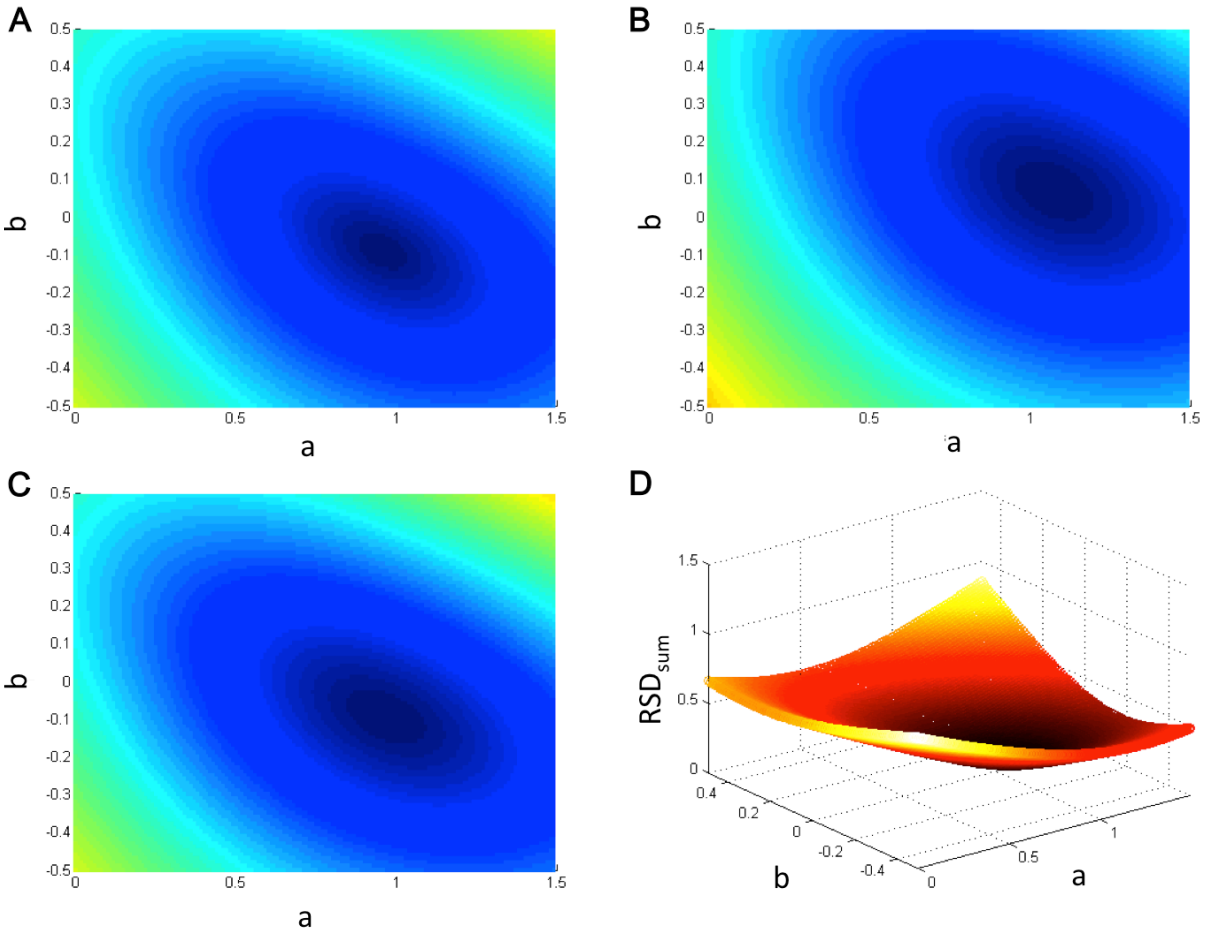

Figure 6.5 Preliminary calculations of the process parameters by the modified method: analysis of standard deviation of the reaction constant at the temperature of A) 700 °C, B) 725 °C and C) 750 °C and D) the sum of the Relative Standard Deviation (RSD_{sum}) with different values of parameters of reaction orders *a* and *b* for the unsintered NiO/YSZ (60:40vol.%) catalyst

The next stage was the preparation of the Arrhenius plot based on the data obtained from experiments carried out at different temperatures (550 °C – 750 °C). The approximation line (see Fig. 6.5):

$$\ln k = \ln A - \frac{E}{R} \cdot \frac{1}{T} \tag{6.9}$$

was used to find the values of the activation energy $E = 117.219 \times 10^3$ J mol^{-1} and the pre-exponential factor $A = 1.554 \times 10^{-3}$ mol g^{-1} s^{-1} Pa$^{-0.89}$. Thus, the first approximation of the kinetic equation of the methane/steam reforming reaction can be consequently written as:

$$R_{st} = w_{cat} \cdot r = w_{cat} \cdot 1.554 \times 10^{-3} \cdot \exp\left(\frac{-117 \times 10^{3}}{RT}\right)\left(p_{CH_4}\right)^{0.97}\left(p_{H_2O}\right)^{-0.08} \qquad (6.10)$$

where, w_{cat} stands for the weight of a catalyst [g], p indicates the partial pressure [Pa] and the subscript *st* denotes the methane/steam reforming reaction.

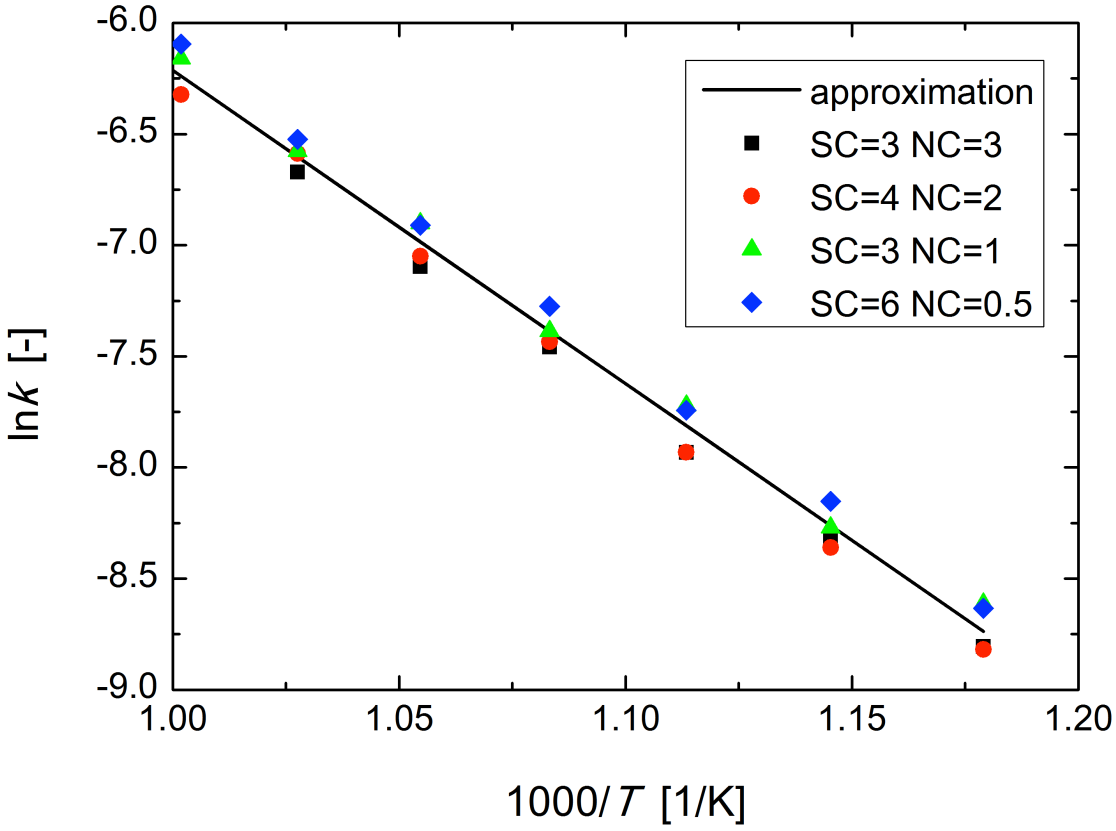

Figure 6.6 Arrhenius plot for catalyst NiO/YSZ 60:40%vol unsintered

The calculation of the initial approximation of additional unknowns (output flow rates of water, nitrogen and total output flow rate) were conducted in an analogical way as the calculation of the main unknowns, and was based on the additional assumption of the stoichiometry of the reactions. However, the stoichiometry of the process incorporates only in the preliminary computation and the equations in the main model do not contain those assumptions.

The variables determining the coefficient of the Arrhenius line are estimated from the general form of the Arrhenius equation described in Eq. (3.57). The values of the activation energy and the pre-exponential constant were calculated in the previous step on the basis of

experimental results. The values of output flow rates of water, nitrogen and all components, ${F_{H_2O}}^{o(j)}$, ${F_{N_2}}^{o(j)}$ and ${F_{ALL}}^{o(j)}$ are calculated on the basis of stoichiometric correlations described in Table 3.1 as:

$${F_{H_2O}}^{o(j)} = \left(SC - x - y\right) \cdot {F_{CH_4}}^{i(j)} \tag{6.11}$$

$${F_{N_2}}^{o(j)} = NC \cdot {F_{CH_4}}^{i(j)} \tag{6.12}$$

$${F_{ALL}}^{o(j)} = \left(1 + SC + NC + 2x\right) \cdot {F_{CH_4}}^{i(j)} \tag{6.13}$$

where x and y are defined in Eqs. (3.39) and (3.41) respectively.

6.6 Criteria of applicability of the system of condition equations for co-ordination purposes

Before the application of the GLS algorithm, the validity of the proposed mathematical model should be checked in terms of the appropriateness for the Least Squares approach. Validity checking is conducted for both: decreasing and the systematization of the constraint equations, as well as the verification of the formal criteria concerning the independence of the equations and the determinability of unknowns

6.6.1 Possibility of the reduction of the constraint equation set

The first step in the applicability checking of the mathematical model is the determination of the necessity for the introduction of all of the mathematical equations in the model. Generally, the equations contain only one unknown, which does not appear in other equations, can be excluded from the model dedicated to the co-ordination purposes. As there is only one way to calculate this particular unknown, there is no possibility to correct its final value. Then, the application of the GLS algorithm will not increase the security of the model for this variable.

Additionally the number of the imposed constraint equations can be decreased by eliminating some of the unknowns. However, this strategy should be applied with caution. The elimination of the unknowns leads generally to more complicated constraint equations, which

are more difficult to apply to the linearization procedure. The exception is the case of the substantial fractions, which usually appears in the linear equations. Therefore, their elimination can simplify calculations [190]

The equation set proposed in Section 6.2 follows the above-mentioned rules. The number of the additional unknowns was chosen as the set providing for easy scalability of the model. On the other hand, the number of additional variables was limited in order to decrease the number of unnecessary linear correlations among the constraint equations.

6.6.2 Determination of the validity of the constraint equation set for application of the GLS algorithm

In order to apply the GLS method two formal requirements have to be fulfilled [190]:

- mutual independence of the equations
- determinability of the unknowns

The first criteria to be fulfilled is the correlation between the number of unknowns, the total number of variables in the model and the number of constraint equations. General inequality should be maintained:

$$N < J < K + N \tag{6.14}$$

where N is the number of unknowns, J is number of the constraint equation and K+N determines the number of all variables in the mathematical model. When this condition is fulfilled it is possible to carry out the co-ordination algorithm. As it was in introduces in Section 6.4, N=162, J=364 and K=520 and the condition in Eq. (6.14) is fulfilled for the proposed application of the GLS algorithm to the methane/steam reforming process.

The mutual indecency of the equations can be checked by the application of the method from the theory of the implicit functions. It is necessary because in the case of investigating the physical processes the relations between the measured values can potentially lead to the mutually related equations. As they were introduced in Chapter 2, constraint equation form a system of functions:

$$f_j = f_j\left(u_1, u_2, ..., u_K, x_1, x_2, ..., x_N\right), \quad j = 1,2,...,J \tag{6.15}$$

where u_k determines the measured values and x_n describes the unknowns in the system. To determine the independency of the unknown, the Jacobi matrix formed from the partial derivatives has to investigated:

$$\mathbf{A_B} = \begin{bmatrix} \frac{\partial f_1}{\partial u_1} & \cdots & \frac{\partial f_1}{\partial u_K} & \frac{\partial f_1}{\partial x_1} & \cdots & \frac{\partial f_1}{\partial x_N} \\ \vdots & \ddots & \vdots & \vdots & \ddots & \vdots \\ \frac{\partial f_J}{\partial u_1} & \cdots & \frac{\partial f_J}{\partial u_K} & \frac{\partial f_J}{\partial x_1} & \cdots & \frac{\partial f_J}{\partial x_N} \end{bmatrix} \tag{6.16}$$

If the rank of the matrix rank($\mathbf{A_B}$) is equal to the number of the constraint equations J, then the functions in the equation set are independent from each other. The rank of the matrix fulfils the condition if there is at least one determinant of the rank J made from the matrix column which has a value different from zero. The determination of the matrix rank can be simplified by the introduction of the numerical values of the measured variables and the approximate values of unknowns into the partial derivatives. It is not necessary to calculate the rank of the matrix on the general symbols.

The rank of matrix $\mathbf{A_B}$ was checked for the proposed application of the GLS algorithm. The definition of the constraint equation and variables vector with the initial approximation of the unknowns and the values of the experimental measurements were taken as introduced in Sections 6.2-6.5. The calculated result is rank($\mathbf{A_B}$)=364, what is equal to the number of equation in the system J=364. It was proven that the equations in the constraints set are mutually independent.

The problem of determinability of the unknowns can appear in the case when the number of measured quantities is not sufficient and the definition of the constraint equations result in the creation of the independent aggregates of unknowns. If the number of the independent aggregates is smaller than the number of unknowns itself, the unknowns are indeterminable. The number of indeterminable unknowns is equal to the difference between the number of

unknowns and the number of aggregates of unknowns. In order to evaluate the determinability of the unknowns in the system, the following Jacobi matrix should be investigated:

$$\mathbf{B} = \begin{bmatrix} \frac{\partial f_1}{\partial x_1} & \cdots & \frac{\partial f_1}{\partial x_N} \\ \vdots & \ddots & \vdots \\ \frac{\partial f_J}{\partial x_1} & \cdots & \frac{\partial f_J}{\partial x_N} \end{bmatrix} \tag{6.17}$$

Matrix **B** is formed from the partial derivatives of the constraint functions f_j for unknowns x_n. Unknowns are determinable when the rank(**B**) is equal to the number of unknowns in the system. According to the inequality in Eq. (6.14), the number of rows in the matrix **B** is greater than the number of columns. The rank of matrix **B** equals to N, if there is at least one determinant of the rank N made from the matrix rows which has a value different from zero. Similar to the foregoing case, the calculations are simplified by the introduction of the numerical values of the measured values and the unknowns into the matrix.

As previously, the rank of matrix **B** was checked for the proposed definition of the modelling problem for methane/steam reforming. The obtained result is rank(**B**)=162 what is equal to the number of unknowns in the system N=162. Therefore, all of the unknowns are determinable and the system definition fulfils all of the formal criteria.

6.7 Results of the investigation

After all of the elements of the mathematical model were defined and the validity of the proposed mathematical model was checked, it was possible to apply the GLS algorithm: to linearize the constraint equations, determine the Jacobi's matrix and compute the correction vectors $\mathbf{V_B}$ and new error bounds for the corrected data (covariance matrix $\mathbf{C_{VB}}$). Coupling the least-squares adjustment of the measurement results with the mathematical model leads to the most probable model solution and estimates of the kinetic parameters of the process. The values of the corrected unknowns and its errors, as well as the initially assumed values of the parameters, are presented in Table 6.3, and the corrected kinetic equation is:

$$R_{st} = w_{cat} \cdot 1.354 \times 10^{-3} \cdot \exp\left(\frac{-123 \times 10^3}{RT}\right)\left(p_{CH_4}\right)^{0.89}\left(p_{H_2O}\right)^{0.05} \tag{6.18}$$

Table 6.3 Analyzed results: unknown variables and variables for one of the measurement point (initial and corrected values).

Unknown	Initial value	± *A priori* error	Correction	Corrected value	±Corrected error
a [-]	0.97	±0.97	0.076	0.89	±0.055
b [-]	-0.08	±0.08	-0.13	0.05	±0.038
A [mol g^{-1} s^{-1} Pa$^{-(a+b)}$]	1.554×10^{-3}	$\pm1.554\times10^{-3}$	-0.2×10^{-3}	1.354×10^{-3}	$\pm3.5\times10^{-4}$
E [J mol^{-1}]	117.22×10^{3}	$\pm117.22\times10^{3}$	-5.3×10^{3}	122.5×10^{3}	$\pm2.6\times10^{3}$

Table 6.4 Analysed results: variables for one of the measurement point (initial and corrected values and their uncertainties)

Unknown	Initial value	± *A priori* error	Correction	Corrected value	±Corrected error
T	700	±2.5	-0.30	700.30	±0.36
w	1.887	$\pm5.0\times10^{-4}$	1×10^{-7}	1.887	$\pm4.99\times10^{-4}$
ΔP	5.0×10^{-3}	$\pm1.5\times10^{-5}$	1×10^{-9}	5.0×10^{-3}	$\pm1.5\times10^{-5}$
$F_{CH_4\_v}^{i}$	37	$\pm7.4\times10^{-2}$	-2.4×10^{-4}	37.00	$\pm7.4\times10^{-2}$
$F_{H_2O\_v}^{i}$	0.07	$\pm2.8\times10^{-3}$	9×10^{-5}	0.07	$\pm2.78\times10^{-3}$
$F_{N_2\_v}^{i}$	221	±0.44	0.00	221.00	±0.44
$m_{CH_4}^{o}$	13.8	±1	0.2	13.63	±0.59
$m_{H_2}^{o}$	11.4	±1	-0.04	11.43	±0.79
$m_{CO_2}^{o}$	2.32	±0.5	-0.24	2.56	±0.15
m_{CO}^{o}	0.68	±0.5	0.29	0.396	±0.074

Table 6.4 presents the results obtained for one of the measurement points and similar results can be observed in all the cases. It can be noted that the corrected data has a smaller uncertainty than the initially assumed one. It is an effect of applying the constraint equations, which provides additional information about the analysed system. The most significant improvement can be seen in the case of temperature measurement as well as in the results obtained from the gas chromatography – output flow rates of CH_4, H_2, CO_2 and CO.

The residuum of the main equation of Eq. (6.1) can be understood as the inaccuracy of the calculated and measured reaction rate. Before the application of the GLS algorithm the residuals were calculated for all measurement points with the measured values and initially estimated parameters of reaction order coefficients *a* and *b*, pre-exponential factor *A* and activation energy *E* presented in Eq. (6.10). The sum of all the residuum, which is the total inaccuracy of the applied model, was equal to 1.43×10^{-2}. After the GLS data adjustment the model (see Eq. (6.18)) was drastically upgraded. For new, corrected data and newly estimated values of the process parameters, the improvement of the model was proven by the recalculation of the residual values, of which the sum becomes almost 10 times smaller than the initial one and was equal to 1.5×10^{-3}.

6.8 Comparison of the result by the GLS and standard approach method

After the preceded GLS method was applied, the simulation of the outlet gas composition and the fractional conversion were calculated on the basis of the reaction input, and it was done by the numerical algorithm proposed by Brus [94] and described in Section 3.8. The algorithm inputs are the reaction kinetic equation (parameters *a*, *b*, *A* and *E*) and the initial gas composition. The calculated results are presented in Figs. 6.7-6.9. Figure 6.7 presents the experimental outlet gas composition compiled with the one calculated on the basis of Eqs. (6.10) and (6.18). The presented results describe the reaction which occurred at the conditions of $m_{CH_4}^{\ i}$ = 50 mL min^{-1}, *SC*=3 and *NC*=3 performed at temperature ranges between 575 ^{o}C and 700 ^{o}C. The simulation results present the improvement obtained by the application of the GLS algorithm – the solid lines, representing the reaction kinetic calculated after application of the GLS method, matches the experimental results more precisely than the dashed lines representing the initial kinetics equation.

Figure 6.8 presents the fractional conversion calculated from the experimental results (Eq.(6.8)) coupled with the one estimated on the basis of the kinetic expression with the initial and corrected process parameters. The average difference between the experimental fractional conversion and the calculated one is 1.65% for the initial equation and 1.26% for the corrected equation. Not only a decrease in the mean error after GLS adjustment can be observed – the more important fact is, the corrected model is better fitted to the experimental

data in the whole temperature range. The initial one is adjusted to the experimental data good only for the small fractional conversions (specifically at lower temperatures). It is illustrated by the linear approximation lines in Fig. 6.8. Similar dependence can be observed also in Fig. 6.9 which presents the correlation between the temperature and the fractional conversion of the reforming reaction conducted in the temperature range between 575 ^{o}C and 700 ^{o}C ($m_{CH_4}{}^{i}$=50 mL min^{-1}, *SC*=3 and *NC*=3). The fractional conversions were calculated in three different ways: on the basis of the experimental data, with the initial kinetic equation and with the corrected kinetic expression. The graph shows that in the lower temperatures both models behave similarly and well fit to the data, but with increasing temperature the initial model deviates from the data more significantly. On the contrary, the model with the corrected kinetic equation works properly in the whole temperature range.

The presented considerations are especially important in the light of the inconsistency found in the reaction kinetics on the methane/steam reforming process in the various works [4,8,11–20,36,40–45]. The results shown in the discussion convince the necessity of evaluating the uncertainties and unknowns measured in the experiment and securing an approach to derive the reaction kinetics of the methane/steam reforming process.

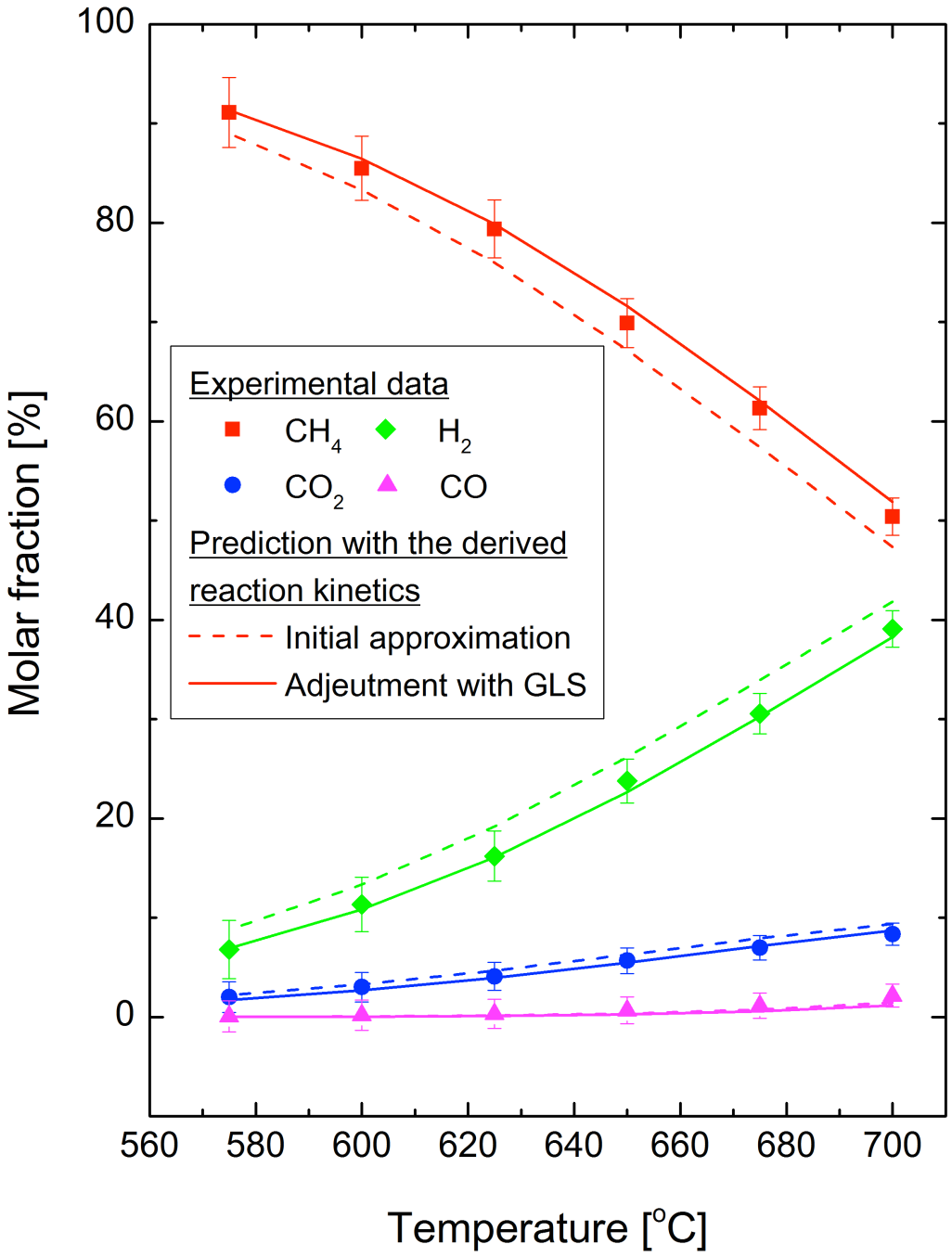

Figure 6.7 The outlet composition of the reformed gas over Ni/YSZ catalyst. Experimental condition: $SC = 3$, $NC = 3$, $m_{CH_4}{}^{i}$=50 mL min^{-1}, w_{cat} = 1.887 g

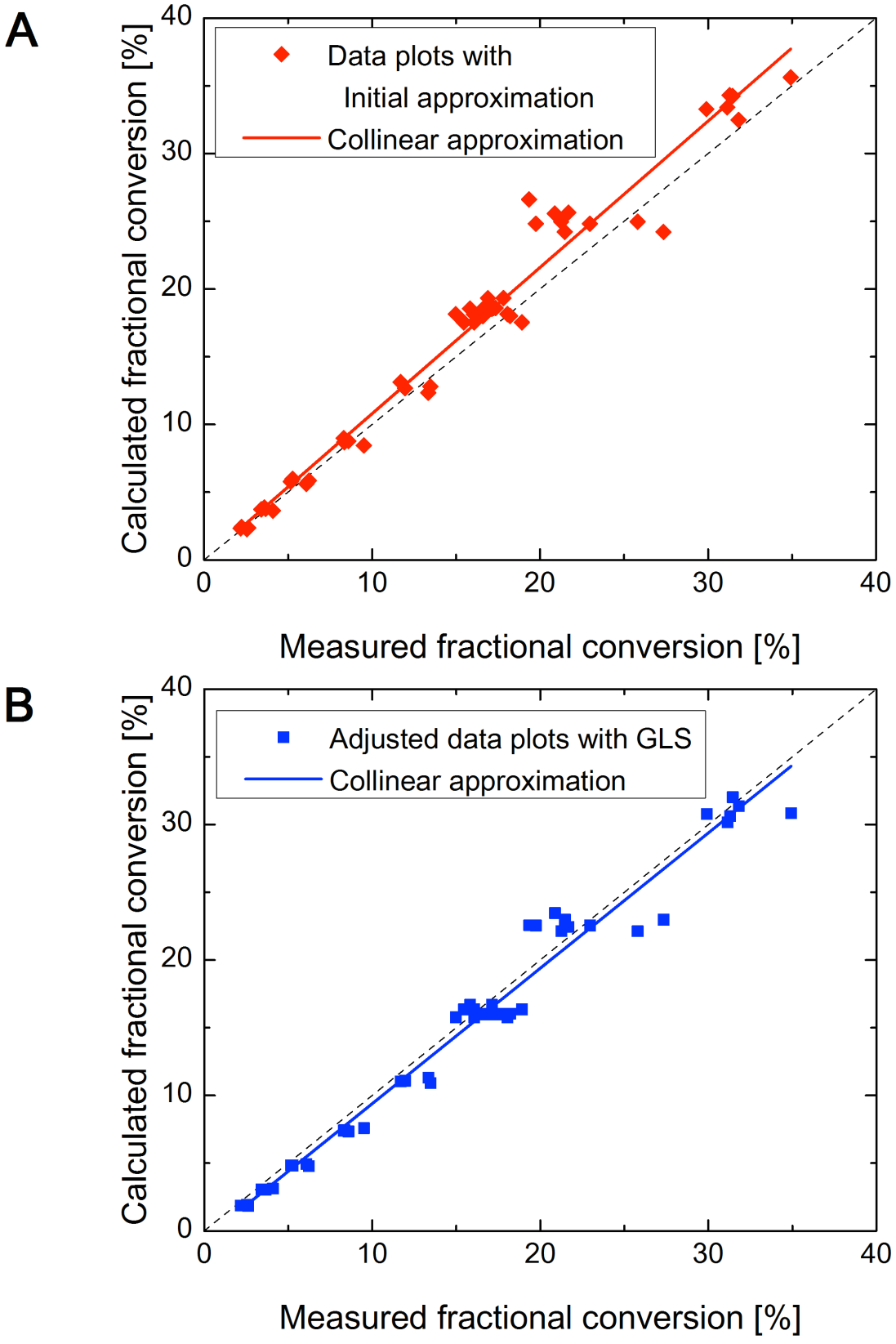

Figure 6.8 Correlation plots of the measured against the calculated fractional conversions, A) before the GLS method applied and B) after the GLS method applied

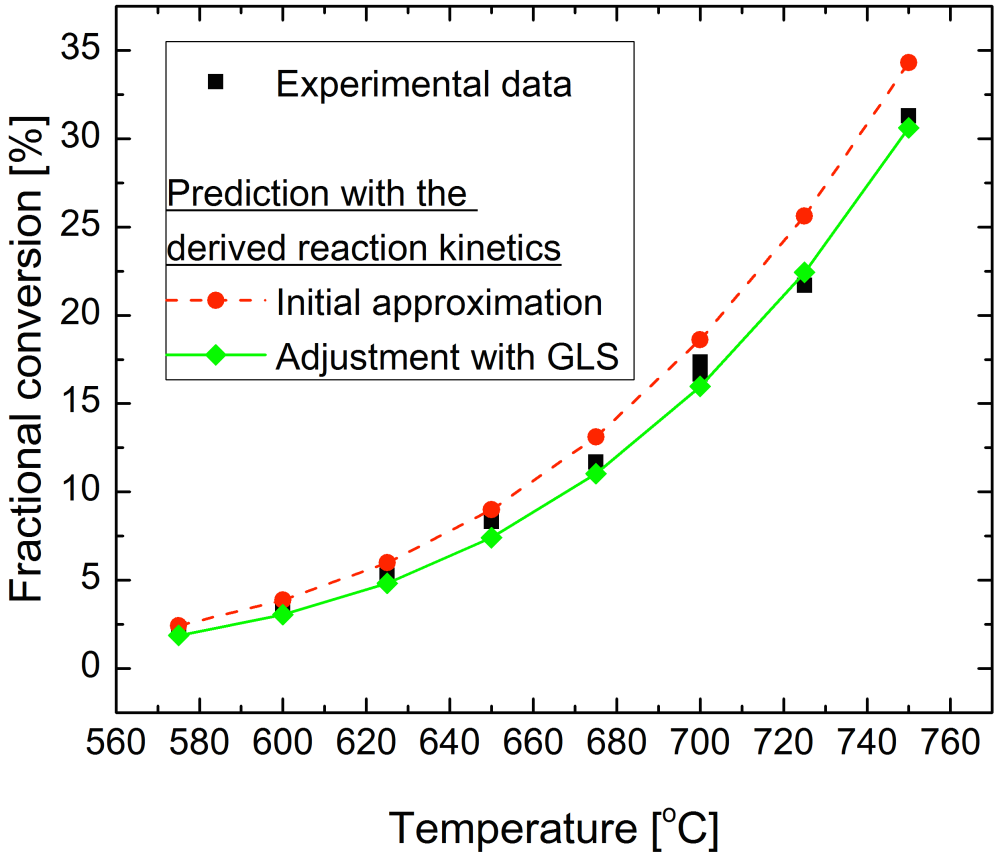

Figure 6.9 Fractional conversion of CH_4 along the reaction temperature

7 Comparison of the reaction kinetics

The reaction kinetics of methane/steam reforming has been studied for many years. Particularly, for SOFCs dedicated applications, the reaction kinetics was studied on the Ni-based anode cermet material supported with solid oxides. The reaction kinetics of methane/steam reforming was derived as can be seen in many papers [32,37,39,113,123,125,147,148,150–153]. As mentioned previously, the formulas can be classified primarily into three basic concepts [32,37,39,148]:

- General Langmuir-Hinshelwood kinetics [37],
- first order reaction with respect to methane [32,116,123,150], which is also known as simplified Langmuir-Hinshelwood kinetics
- power law expressions derived from data fitting [113,125,147,148,151–153].

Those derived reaction kinetics are listed in Table 7.1 with additional literatures [38,81,123,193,207–210]. The derived reaction kinetics were obtained from the measurements conducted either on a shaped SOFC anode or on a packed catalysts in the form of powder. The reported activation energy of in particular Ni/YSZ supported catalysts lies in the range of 58 kJ mol^{-1} and 191 kJ mol^{-1}. The reported range of the obtained activation energies is broad and the obtained activation energy is in the middle of the broad range. However, the majority of the values found on the cited literatures seems to be less than 100 kJ mol^{-1} [39].

In the case of the power law expression, the estimated reaction orders are between 0.8 and 1.3 and between -1.25 and 0.12, respectively for *a* and *b*. The derived reaction orders in the present study are in the ranges of reported reaction kinetics.

A pre-exponential factor heavily depends on the physical properties of an used catalyst. The form and structure of the catalyst, fine powder or fabricated SOFC anode support, and prepared size of the Ni in the catalyst attribute to the microstructure and contact area, which is influential to the reaction rate. Table 7.2 shows the formula and the reaction kinetics which

Mogenesen found on a variety of samples [81]. The reported activation energies of the material from Ni/YSZ anodes used in the short- and long-term tests is in the range between 164-185 kJ mol^{-1} and they are close. However, the reported pre-exponential factor is in the range from 1.7×10^{-3} mol s^{-1} g^{-1} $Pa^{-0.6}$ to 139 mol s^{-1} g^{-1} $Pa^{-0.9}$. The materials used after long term and short-term tests differ remarkably, though the activation energies do not differ sufficiently. The large size of the nickel particles in the anode, giving a smaller surface area for the same nickel content and thus less active sites, will influence the reaction rate of the steam reforming [39]. In fact, the agglomeration of Ni toward to larger size has been observed in an Ar-H_2(4%)-H_2O(3%) atmosphere at 1000 °C with increasing exposure time, thus the change in the microstructure has been reported [95], which is coarsening Ni-supported solid oxide anode and is recognized as a major degradation phenomenon on the Ni/YSZ supported SOFC anodes [211].

Iwai et al. have conducted a derivation of the reaction kinetics on the various compositions of Ni/YSZ cermet samples, of which the Ni contents are 75 vol.%, 50 vol.% and 25 vol.% [151]. The investigated cermet material had a disk shape with a thickness of 30 μm, 6 mm and 13 mm of inner and outer diameter respectively. The high-temperature sintering process of the catalyst materials resulted in the various microstructure of test samples. Table 7.3 shows the detailed information about the composition and microstructure of the prepared samples and the determined steam reforming process kinetics [151]. The reaction orders and activation energies they found are very similar for various compositions of the catalysts, however, the values of the pre-exponential factors derived on the basis of the apparent surface area are inconsistent among the various compositions. On the other hand, the values of the modified pre-exponential factors based on the Ni-pore contact area becomes close to each other. It seems that the composition of Ni and YSZ does not affect the pre-exponential factor, nevertheless, the microstructure created by the different compositions gives significance on determining the pre-exponential factor [151].

A comparison of the derived reaction kinetics with the results obtained in this study is shown in Figs. 7.1 and 7.2 For the comparison, models from two concepts, ii) first order reaction [32,116] and iii) power-law expression [81,147,148,153], were used. In demonstrating the comparison, formula and the values of reaction orders *a* and *b*, and the activation energy *E* are directly based on the literature data. Additionally, the following assumptions were made:

- The measurement is conducted on the packed catalyst bed.
- The used catalyst is prepared in the form of fine powder of at least 0.85 μm to avoid the effect of mass transport phenomena on the reaction kinetics.
- The properties of the used catalyst, density, porosity and active area, are the same as the one used in the present study. Properties such as density, porosity, support material and general microstructure influence the catalytic behaviour of the catalytic material and finally define its active area and are included in the value of the pre-exponential factor.
- Thus, the microstructure of the used catalyst is assumed to be the same as the one used in the present study.

Based on those assumptions, the pre-exponential factor is recalculated for all the reaction models to be adjusted to the experimental conditions incorporated in this study – the value of pre-experimental factor A is determined so that the standard deviation of A based on the experimental results becomes minimal. All of the reported studies for deriving the reaction kinetics did not use the exact same methodology to describe measurements, and moreover did not follow the appropriate conditions to avoid the possible effects of mass transport [39]. Thus, the reported kinetics may be specific to the setup of their systems, and will probably fail to describe and represent other systems [39]. By postulating the above mentioned assumption and applying the preceded approach, all the models are now modified and constrained to certain specification that have been applied in the present measurement and the comparison of the proposed models can be considered as practical and meaningful.

Figures 7.1 and 7.2 present the results obtained in two exemplary experimental conditions with the theoretical fractional conversion of methane based on the literature data and the present study. The results show that the kinetic model proposed in this study is the most accurate for the various operational conditions. Some of the competitive kinetic equations presented in the literature approximate the experimental results well in the limited temperature range (Mogensen equation) or for specified SC conditions (Lee equation). However, the overall accuracy of the model derived in this study exceeds the other models in the case of the analysed cases.

Table 7.1 The used formula for the steam/methane reaction and derived reaction kinetics found in the literatures [4,8,11-15,17-20,22,36,40-45]

Reference	Material	Ni content	Reaction rate formula	Pre-exponential factor A	Activation energy E [kJ mol^{-1}]
(*i*) *General Langmuir-Hinshelwood kinetics*					
Xu and Froment [37]	$Ni/MgAl_2O_4$		$r = k/p_{CH_4}^{2.5}\left(p_{CH_4}p_{H_2O} - p_{CO}p_{H_2}^3/K\right)/\alpha^2 + k'/p_{CH_4}^{2.5}\left(p_{CH_4}p_{H_2O} - p_{CO}p_{H_2}^3/K'\right)/\alpha^2$ $\alpha = 1 + K_{CO}p_{CO} + K_{H_2}p_{H_2} + K_{CH_4}p_{CH_4} + \frac{K_{H_2O}p_{H_2O}}{p_{H_2}}$		
Bebelis et al.[193]	Ni/YSZ	70 wt.%	$r = k_{ad}p_{CH_4}\left(1 - \frac{k_{ad}}{k_r K_{H_2O}}\frac{p_{H_2}p_{CH_4}}{p_{H_2O}}\right)$		
Nakagawa et al. [210]	Ni/YSZ/CeO		$r = \frac{kK_{CH_4}p_{CH_4}K_{H_2O}p_{H_2O}}{\left(1 + K_{CH_4}p_{CH_4} + K_{H_2O}p_{H_2O}\right)^2}$		
Peters et al. [38]	Ni/YSZ	50 wt.%	$r = \frac{kK_{CH_4}p_{CH_4}K_{H_2O}p_{H_2O}}{\left(1 + K_{CH_4}p_{CH_4} + K_{H_2O}p_{H_2O} + K_{CO_2}p_{CO_2}\right)^2}$		
Dicks et al. [212]	Ni/ZrO_2		$r = \frac{kp_{CH_4}}{\left(1 + K_{H_2}p_{H_2}^{1/2} + K_S p_{H_2O}p_{H_2}\right)^n}$		

Table 7.1 The used formula for the steam/methane reaction and derived reaction kinetics found in the literatures [4,8,11-15,17-20,22,36,40-45] – continuation

Reference	Material	Ni content	Reaction rate formula	Pre-exponential factor A	Activation energy E [kJ mol^{-1}]
(*ii*) *Expression with first order kinetics respect to methane*					
Akers and Camp [209]	Ni-based material		$r = kp_{CH_4}$		
King et al. [150]	Ni/YSZ	50 wt.%	$r = kp_{CH_4}$		113~124
Achenbach [116]			$r = kp_{CH_4}$	4.274×10^{-2}[mol s^{-1} m^{-2} Pa^{-1}]	82
Belyaev et al. [207]	Ni/ZrO_2/CeO_2		$r = kp_{CH_4}$	2.57×10^{-2} [mol s^{-1} g^{-1} Pa^{-1}]	82
Achenbach and Riensche [123]	Ni/ZrO_2	20 wt.%	$r = kp_{CH_4}\left(1-\frac{p_{CO}p_{H_2}^3}{p_{CH_4}p_{H_2O}K_p}\right)$	4.274×10^{-2}[mol s^{-1} m^{-2} Pa^{-1}]	82
Wei and Iglesia [32]	Ni/MgO	7 wt.%	$r = kp_{CH_4}\left(1-\frac{p_{CO}p_{H_2}^3}{p_{CH_4}p_{H_2O}K_{eq}}\right)$	2.5×10^{2} [s^{-1} Pa^{-1}]	102

Table 7.1 The used formula for the steam/methane reaction and derived reaction kinetics found in the literatures [4,8,11-15,17-20,22,36,40-45] – continuation

Reference	Material	Ni content	Reaction rate formula	Pre-exponential factor A	Activation energy E [kJ mol^{-1}]
(*iii*) *Power-law expressions derived from data fitting*					
Yakabe et al. [113]	Ni/YSZ		$r = k\left(p_{CH_4}\right)^{1.3}\left(p_{H_2O}\right)^{-1.2}$		191
Ahmed and Foger [125]	Ni/YSZ		$r = k\left(p_{CH_4}\right)^{0.85}\left(p_{H_2O}\right)^{-0.35}$	27.012[mol s^{-1} m^{-2} Pa$^{-0.5}$]	95
Iwai et al.[151]	Ni/YSZ	75 vol.%	$r = k\left(p_{CH_4}\right)^{0.82}\left(p_{H_2O}\right)^{0.12}$	0.1324[mol s^{-1} m^{-2} Pa$^{-0.96}$]	89.7
		50 vol.%		0.103[mol s^{-1} m^{-2} Pa$^{-0.96}$]	87.0
		25 vol.%		0.07[mol s^{-1} m^{-2} Pa$^{-0.96}$]	89.3
Lee et al. [153]	Ni/ZrO_2	60 vol.%	$r = k\left(p_{CH_4}\right)^{1.0}\left(p_{H_2O}\right)^{-1.25}$	4.3~42[mol s^{-1} g^{-1} Pa$^{0.25}$]	74~98
Odegard et al. [147]	Ni/YSZ	60 vol.%	$r = kp_{CH_4}^{1.2}$	1.73×10^{-6}[mol s^{-1} g^{-1} Pa$^{-1.2}$]	58
Timmermann et al. [152]	Ni/CGO		$r = kp_{CH_4}^{1.19}$	4.05×10^{-5}[mol s^{-1} m^{-2} Pa$^{-0.9}$]	26
Brus [148]	Ni/YSZ	60 vol.%	$r = k\left(p_{CH_4}\right)^{0.98}\left(p_{H_2O}\right)^{-0.09}$	1.55×10^{-3}[mol s^{-1} g^{-1} Pa$^{-0.89}$]	117
Mogensen [81]	Ni/YSZ		$r = k\left(p_{CH_4}\right)^{0.8}\left(p_{H_2O}\right)^{-0.2}$	1.7×10^{-3}[mol s^{-1} m^{-2} Pa$^{-0.9}$]	183

Table 7.2 The reaction kinetics of the methane steam reforming on various catalysts derived by power-law expression by Mogensen [81]

Description	Reaction rate formula	Pre-exponential factor *A*	Activation energy *E* [kJ/mol]
Model anode material Ni composition: 42 wt.%, size of the particles: approx. 0.3mm	$r = k\left(p_{CH_4}\right)^{0.9}\left(p_{H_2O}\right)^{-0.2}\left(p_{CO_2}\right)^{0.2}$	139 [mol s^{-1} g^{-1} $Pa^{-0.9}$]	185
Industrial anode material	$r = k\left(p_{CH_4}\right)^{0.8}\left(p_{H_2O}\right)^{-0.2}\left(p_{CO_2}\right)^{0.2}$	23 [mol s^{-1} g^{-1} $Pa^{-0.8}$]	166
Industrial stack anode material after short term test (Material of anode crushed with electrolyte)	$r = k\left(p_{CH_4}\right)^{0.8}\left(p_{H_2O}\right)^{-0.2}$	1.7×10^{-3} [mol s^{-1} g^{-1} $Pa^{-0.6}$]	183
Industrial anode from stack after long term test (Material of anode crushed with electrolyte)	$r = k\left(p_{CH_4}\right)^{0.8}$	15.3 [mol s^{-1} g^{-1} $Pa^{-0.8}$]	164

Table 7.3 Comparison of reaction kinetic parameters for various materials derived with respect to their microstructure by Iwai et al. [151]

		Sample A	Sample B	Sample C	Sample D
Composition of the catalyst	Ni [vol.%]	32	34.6	10.3	37.1
	YSZ [vol.%]	9.8	31	29.8	39.4
	Pore [vol.%]	58.2	34.4	59.9	39.4
Contact area density between Ni and pore [μm^2 μm^{-3}]		0.740	0.785	0.388	0.283
Reaction kinetic parameters	*a* [-]	0.82	0.82	0.82	0.84
	b [-]	0.14	0.14	0.14	0.11
	E [kJ mol^{-1}]	89.7	87.0	89.3	86.3
	A based on apparent surface area	0.132	0.103	0.07	0.036
	A based on Ni-pore contact area	0.126	0.111	0.116	0.108

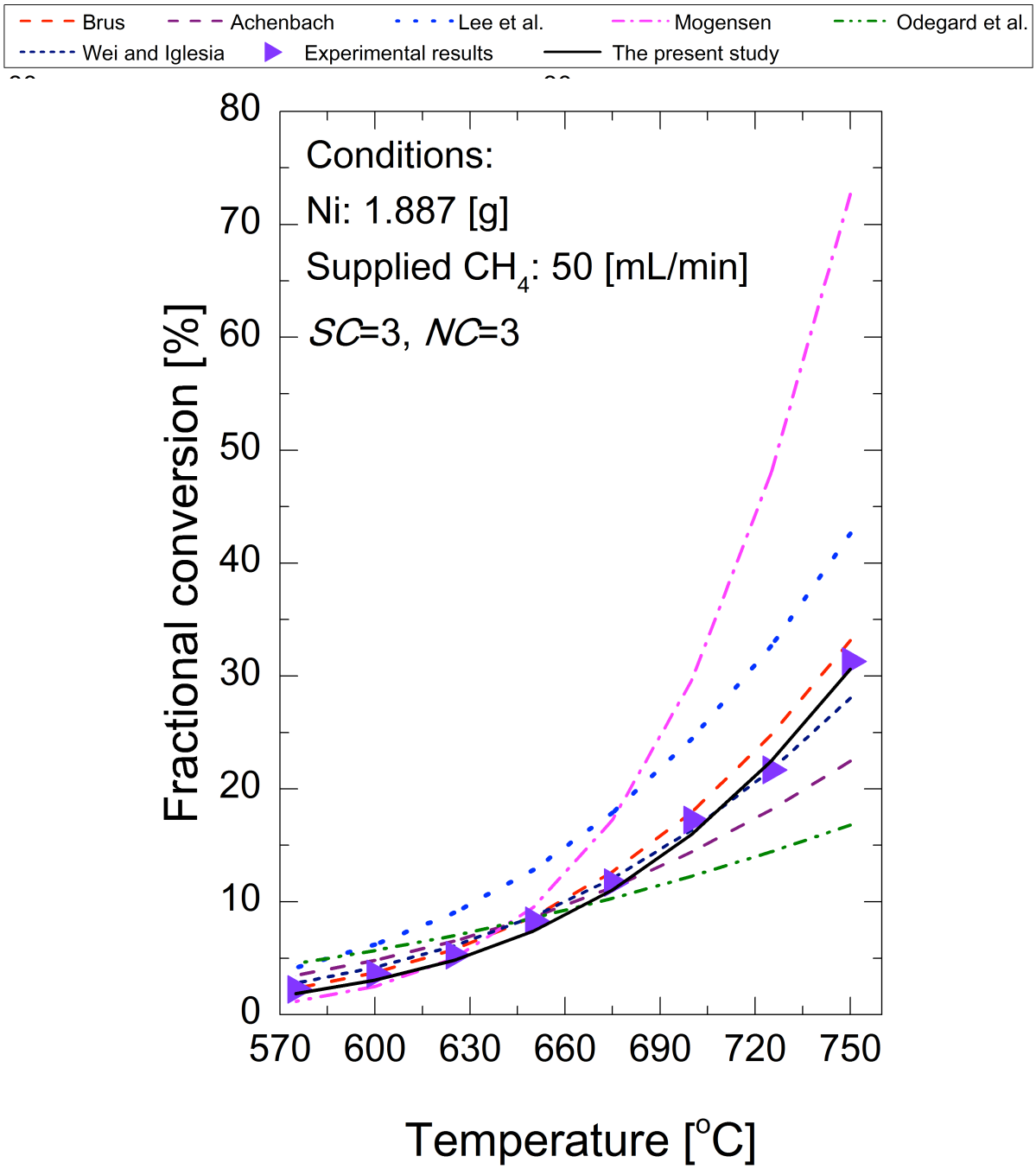

Figure 7.1 The comparison of the obtained fractional conversion with ones obtained from the proposed reaction kinetics in the published literature [32,81,116,147,148,153] in the conditions of *SC* = 3, *NC* = 3

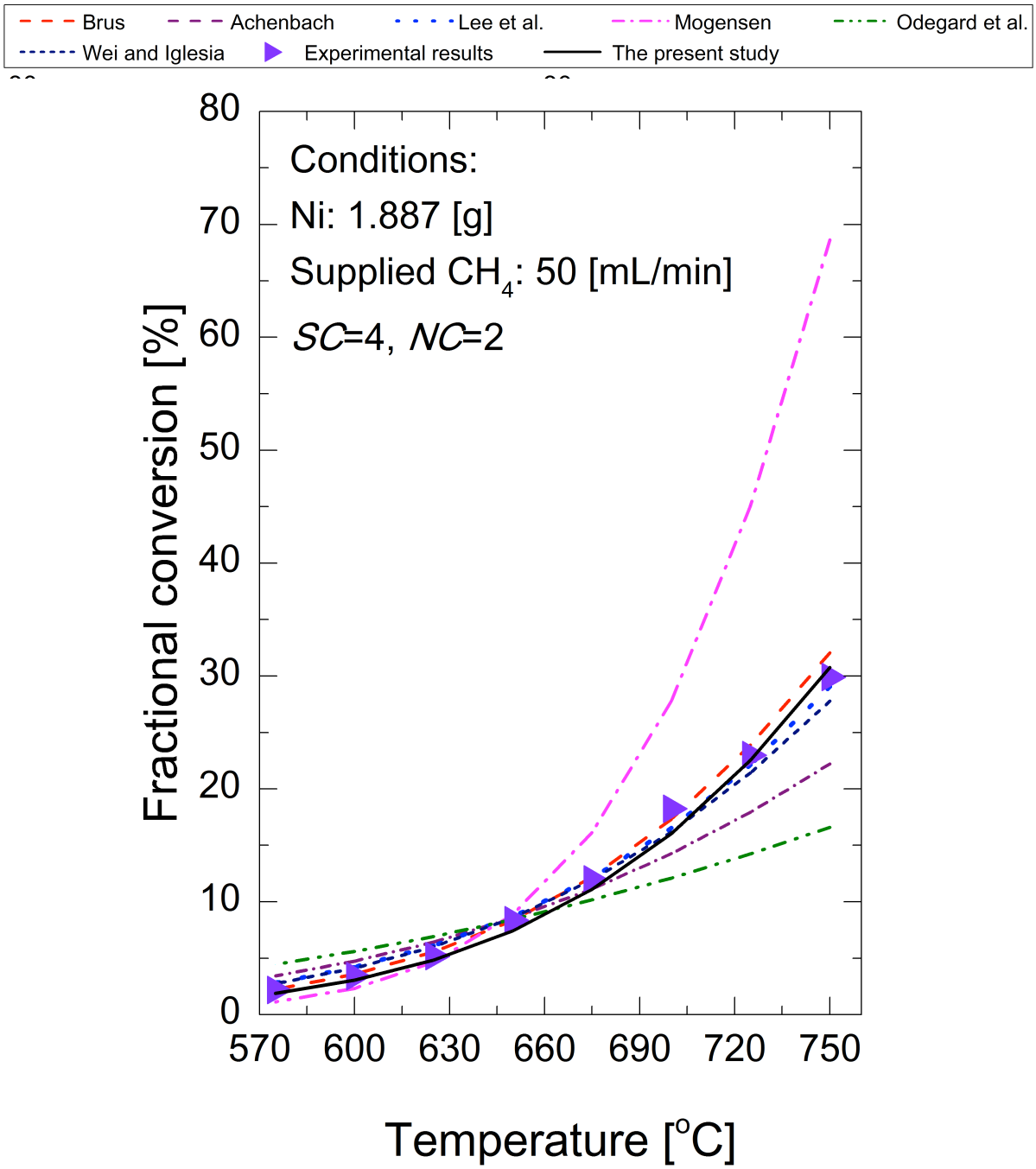

Figure 7.2 The comparison of the obtained fractional conversion with the ones obtained from the proposed reaction kinetics in the published literature [32,81,116,147,148,153] in the conditions of $SC = 4$, $NC = 2$

8 Validation of the various mathematical models by GLS

An application of the Generalized Least Squares algorithm to the methane/steam reforming process was presented in Chapter 6. As it was introduced, the constraint equation set describing the physical phenomena, is implemented directly in the GLS numerical algorithm and determines the quality of the modelling. One of the features of the GLS method is the possibility of providing an objective mathematical evaluation and quantification of the proposed numerical model. In the present chapter, this feature of the GLS method will be applied to judge the quality of the proposed models for the methane/steam reforming process.

8.1 Proposed mathematical models for methane/steam reforming process

To implement a general algorithm and apply the GLS method, the mathematical model describing the chemical process has to be decided. The proposed numerical analyses include various sets of equations to present an increase in the security of the final result with an increasing number of constraints. All the considered models are summarized in Fig. 8.1, and they are consisted with the equations presented in Section 6.2 (Eqs. (6.1)-(6.7)). Each of the models includes 52 measurement points defined by the various flow rates of methane, *SC* and *NC* ratios. At every measurement point, 10 variables were measured. Then, the constraints defined in the model were applied to every measurement point. The number of variables and total number of equations in the proposed models are presented in Fig. 8.1.

In the analysis, 8 black-box tests for various models describing the methane/steam reforming process were conducted. Here, the detailed construction of constraint sets for every test are given. Test 1 includes only one type of equation - the general reaction rate equation governing the process (Eq (6.1)). Tests 2-4 add one additional type of equations: the water-gas-shift equation (Eq (6.2)), the Arrhenius equation (Eq (6.3)) and the balances of the elements (Eq (6.4)-(6.7)) for Tests 2, 3 and 4 respectively. It should be noted that the balance of the elements, in fact, defines 4 various constraint equations. Models in both Tests 6 and 7 are

built with 3 different types of equations (see Table 5) and the model in Test 8 consists of all of the postulated constraints. It should be noted that Test 8 is based on the same equation set as the one proposed in Chapter 6.

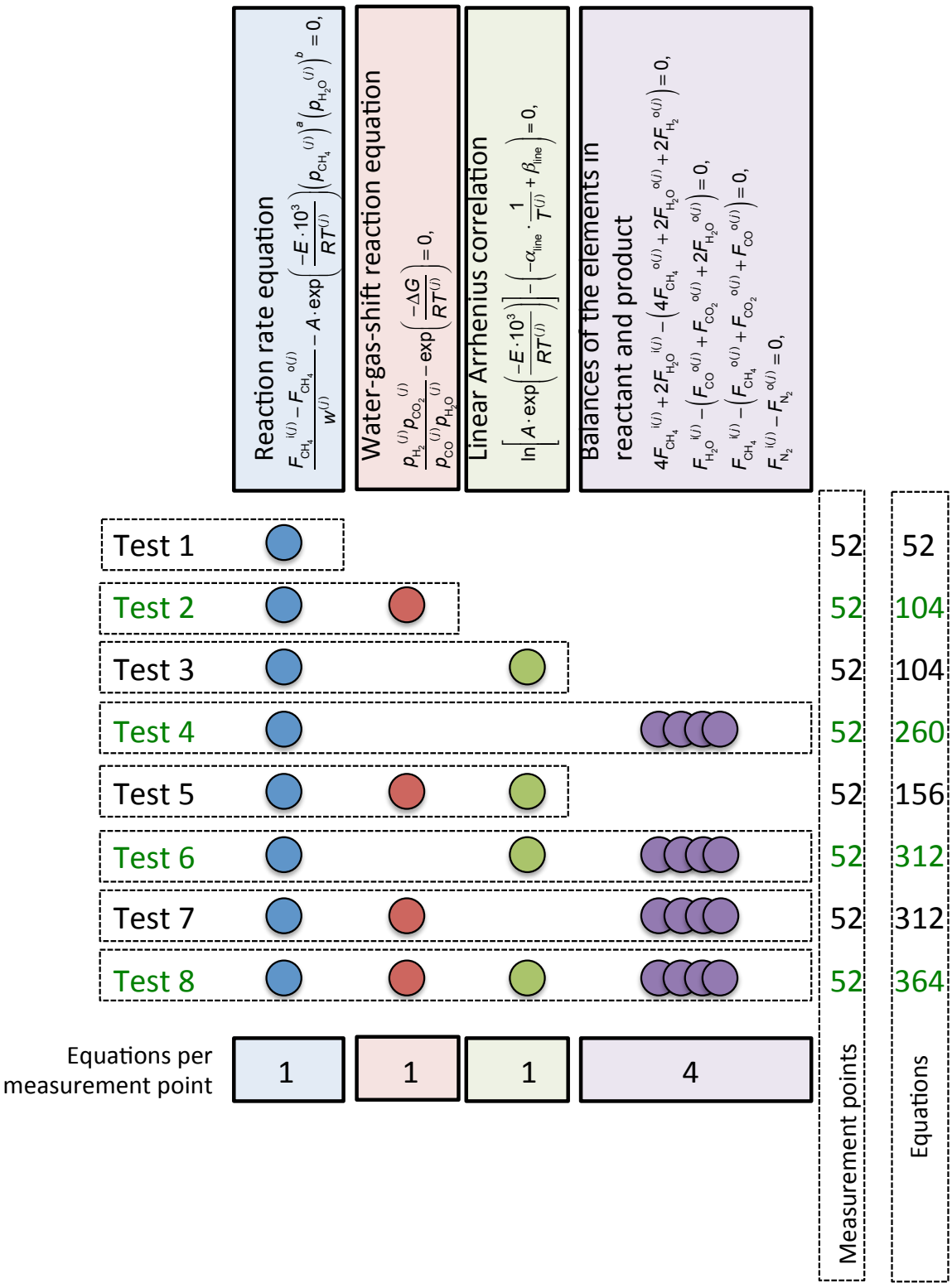

Figure 8.1 Conducted tests and the number of variables and equations included in the each model

The general construction of vector **x** with measured and unknown variables and covariance matrix $\mathbf{C_V}$ were introduced in Chapter 6. Here, the analogical construction is used. Calculations are conducted for the unsintered NiO/YSZ (60:40vol.%) catalyst material provided by the AGC SEIMI CHEMICAL CO. LTD.

8.2 Results of validation of the models

The results after the application of the GLS algorithm with the postulated various sets of constraints equations are summarized in Table 8.1. The calculated values of the most important unknowns describing the reaction order coefficients in respect to methane and steam partial pressure, activation energy and pre-exponential factor that were given are characterized by the *a posteriori* uncertainties. In all the cases, the same initial values of the parameter and their uncertainties were assumed – the values were chosen on the basis of preliminary computations incorporating the stoichiometry of reaction, described in Section 6.5. Note that the values of the activation energy and Arrhenius constant were scaled down in the numerical calculation respectively by the factor 10^{-4} and 10^{-2}, however it does not influence final results. The decrease of *a posteriori* uncertainty of the final result can be observed in comparison with *a priori* error in all the analyzed cases.

Table 8.1 Results of the analysis with the GLS algorithm: parameters *a, b, A* and *E* with their uncertainties for tests with a different number of equations in the model (the values of parameters directly applied in the GLS algorithm)

	a [-]		b [-]		$A\times10^{-2}$ [mol g^{-1} s^{-1} atm$^{-(a+b)}$]		$E\times10^{-4}$ [J mol^{-1}]	
Initial	**0.97**	**±0.97**	**-0.08**	**±0.08**	**26.58**	**±26.58**	**11.72**	**±11.72**
Test 1	0.96	±0.94	-0.08	±0.08	26.60	±26.51	12.30	±2.19
Test 2	0.52	±0.87	-0.09	±0.08	28.79	±26.49	14.64	±1.80
Test 3	0.97	±0.93	-0.08	±0.08	26.55	±26.25	12.27	±2.15
Test 4	0.88	±0.06	0.08	±0.04	39.29	±11.93	12.16	±0.29
Test 5	0.55	±0.86	-0.09	±0.08	28.36	±26.23	14.57	±1.78
Test 6	0.88	±0.06	0.08	±0.04	37.91	±11.25	12.13	±0.28
Test 7	0.90	±0.06	0.05	±0.04	42.48	±11.21	12.29	±0.27
Test 8	0.89	±0.05	0.05	±0.04	41.22	±10.53	12.25	±0.26

On the basis of the results presented in Table 8.1, the final versions of the reaction rate equation obtained in the conducted tests can be presented:

$$\text{Test 1: } R_{st} = w_{cat} \cdot r = w_{cat} \cdot 1.745 \times 10^{-3} \cdot \exp\left(\frac{-123 \times 10^3}{RT}\right)\left(p_{\mathrm{CH_4}}\right)^{0.96}\left(p_{\mathrm{H_2O}}\right)^{-0.08} \tag{8.1}$$

$$\text{Test 2: } R_{st} = w_{cat} \cdot r = w_{cat} \cdot 0.338 \cdot \exp\left(\frac{-146 \times 10^3}{RT}\right)\left(p_{\mathrm{CH_4}}\right)^{0.52}\left(p_{\mathrm{H_2O}}\right)^{-0.09} \tag{8.2}$$

$$\text{Test 3: } R_{st} = w_{cat} \cdot r = w_{cat} \cdot 1.552 \times 10^{-3} \cdot \exp\left(\frac{-123 \times 10^3}{RT}\right)\left(p_{\mathrm{CH_4}}\right)^{0.97}\left(p_{\mathrm{H_2O}}\right)^{-0.08} \tag{8.3}$$

$$\text{Test 4: } R_{st} = w_{cat} \cdot r = w_{cat} \cdot 1.025 \times 10^{-3} \cdot \exp\left(\frac{-122 \times 10^3}{RT}\right)\left(p_{\mathrm{CH_4}}\right)^{0.88}\left(p_{\mathrm{H_2O}}\right)^{0.08} \tag{8.4}$$

$$\text{Test 5: } R_{st} = w_{cat} \cdot r = w_{cat} \cdot 0.235 \cdot \exp\left(\frac{-146 \times 10^3}{RT}\right)\left(p_{\mathrm{CH_4}}\right)^{0.55}\left(p_{\mathrm{H_2O}}\right)^{-0.09} \tag{8.5}$$

$$\text{Test 6: } R_{st} = w_{cat} \cdot r = w_{cat} \cdot 0.989 \times 10^{-3} \cdot \exp\left(\frac{-121 \times 10^3}{RT}\right)\left(p_{\mathrm{CH_4}}\right)^{0.88}\left(p_{\mathrm{H_2O}}\right)^{0.08} \tag{8.6}$$

$$\text{Test 7: } R_{st} = w_{cat} \cdot r = w_{cat} \cdot 1.243 \times 10^{-3} \cdot \exp\left(\frac{-123 \times 10^3}{RT}\right)\left(p_{\mathrm{CH_4}}\right)^{0.9}\left(p_{\mathrm{H_2O}}\right)^{0.05} \tag{8.7}$$

$$\text{Test 8: } R_{st} = w_{cat} \cdot r = w_{cat} \cdot 1.354 \times 10^{-3} \cdot \exp\left(\frac{-123 \times 10^3}{RT}\right)\left(p_{\mathrm{CH_4}}\right)^{0.89}\left(p_{\mathrm{H_2O}}\right)^{0.05} \tag{8.8}$$

where, w_{cat} stands for the weight of a catalyst [g] and p indicates the partial pressure [Pa].

Figure 8.2 presents changes in the uncertainty of the reaction orders with respect to the partial pressure of methane and steam, and the changes in uncertainty of the most important remained unknowns of the model is shows in Fig. 8.3; the activation energy and the Arrhenius constant were shown. It can be noticed that, in general, the uncertainty of the parameters decreases with increasing number of equation in the process model. Although, there is a significant difference in the type of constraints and their influence on the solution; the highest effect on the security of the final results has the balance of the elements. The tests containing the elemental balances are: Test 4, Test 6, Test 7 and Test 8. The significant decrease of

uncertainties characterizing all variables *a*, *b*, *A* and *E* is clearly noticeable in those tests (see Figs. 8.2 and 8.3).

To illustrate the process of decreasing the volume of the covariance matrix $\mathbf{C_{VB}}$ was calculated after the data reconciliation process, the results of all the tests were plotted in Fig. 8.4. The three-dimensional graph presents the correlation of the nominal values and uncertainties of the reaction orders and activation energy calculated in each test. As only limited number of parameters could be presented in a 3-D correlation graph, those variables were chosen on the basis of the criteria described in Chapter 7. The excluded pre-exponential factor is the most dependent variable on the structure of used material and the other one is more universal. The volume of the covariance matrix $\mathbf{C_{VB}}$ constitutes the measure of the quality of the obtained solutions as it was introduced in Section 2.6. The covariance ellipsoid is defined by the central point, which is the vector of values of variables after co-ordination (here the values of the reaction orders and activation energy) and by semi axes, which are equal to the uncertainties of respective variables. The tests characterized by the smaller volume of the covariance ellipsoid (and equivalently the smaller sum of the diagonal elements in covariance matrix) better describes the considered problem. To explain this idea, the two-dimensional projection over the axis defining reaction order in respect to methane and activation energy was presented in Fig. 8.3.

No significant difference can be noticed in the results of Test 1 and Test 3, as it is shown in Figs. 8.4 and 8.5. Those tests have different constraint equation sets: Test 3 contains the reaction rate equation and the linear Arrhenius correlation, while Test 1 includes only the reaction rate equation. Similar dependency is observed for Test 2 and Test 5: no significant difference in results, and constraint equations sets are varied only by the inclusion of the Arrhenius equation. Therefore, it can be concluded that the linear Arrhenius correlation does not influence significantly the quality of the description of the methane/steam reforming process.

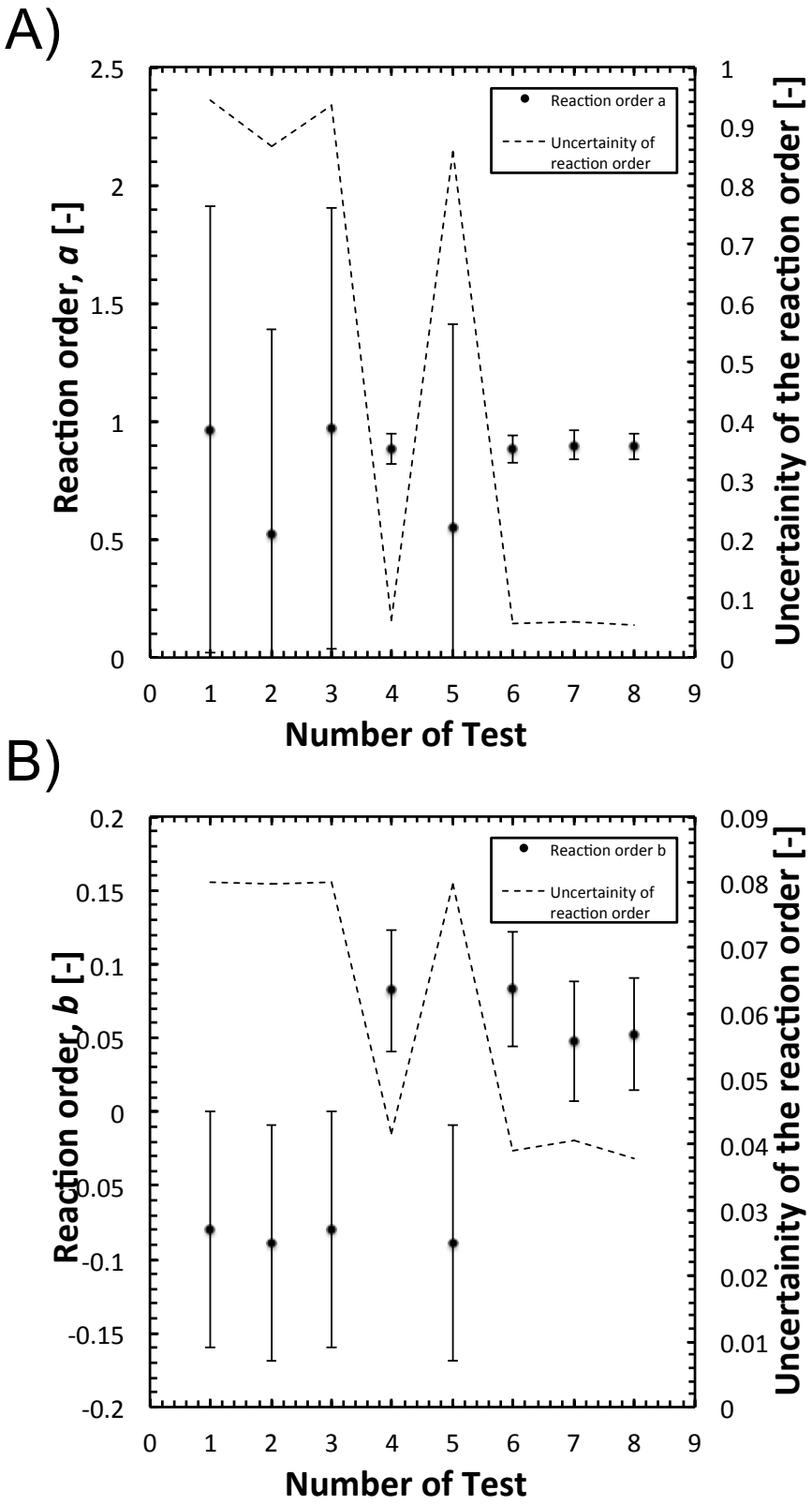

Figure 8.2 Results of the analyzed tests presenting the obtained values of the parameters and their uncertainties: A) reaction order *a* and B) reaction order *b*

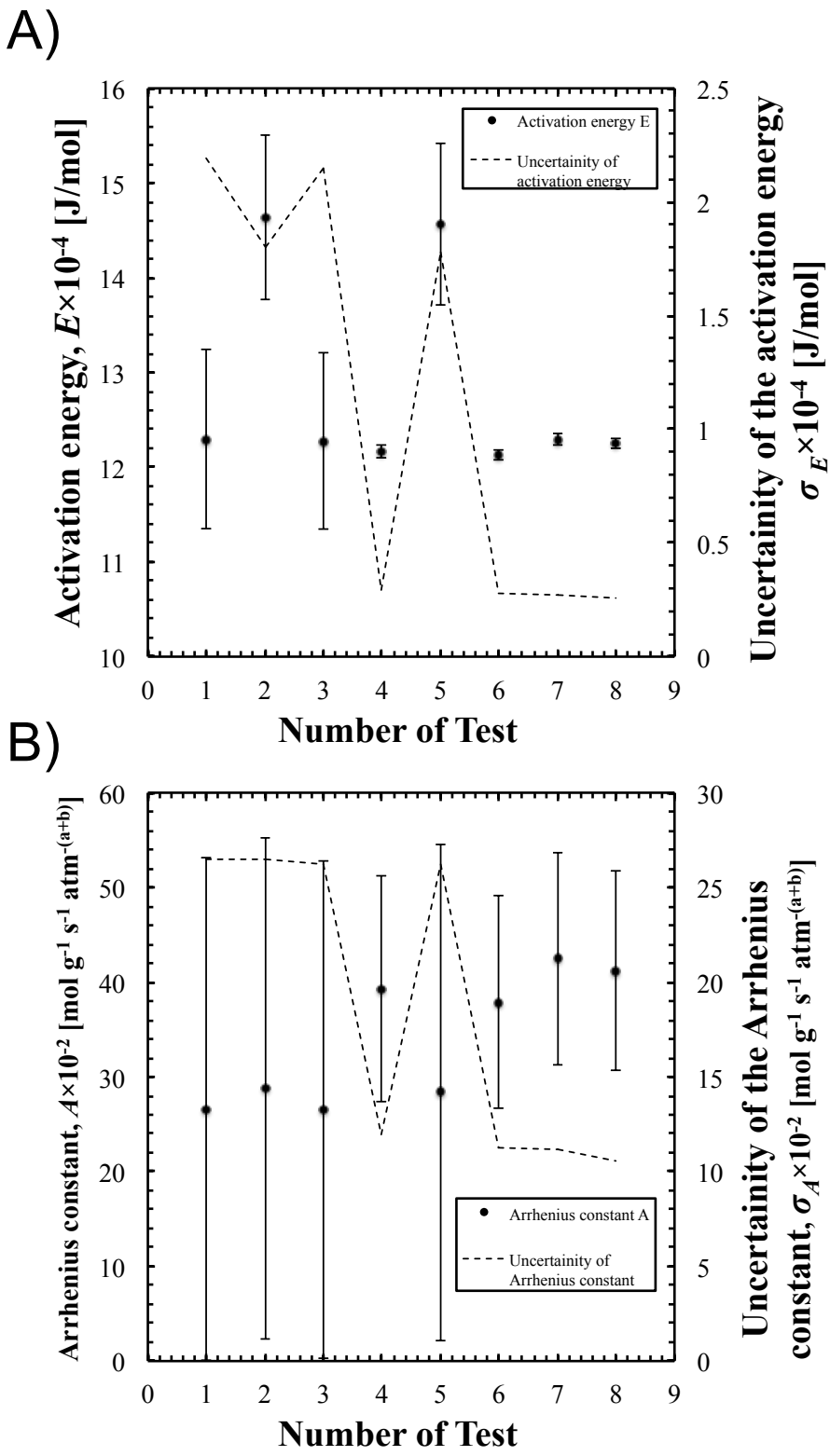

Figure 8.3 Results of the analyzed tests presenting the obtained values of the parameters and their uncertainties: A) activation energy and B) Arrhenius constant

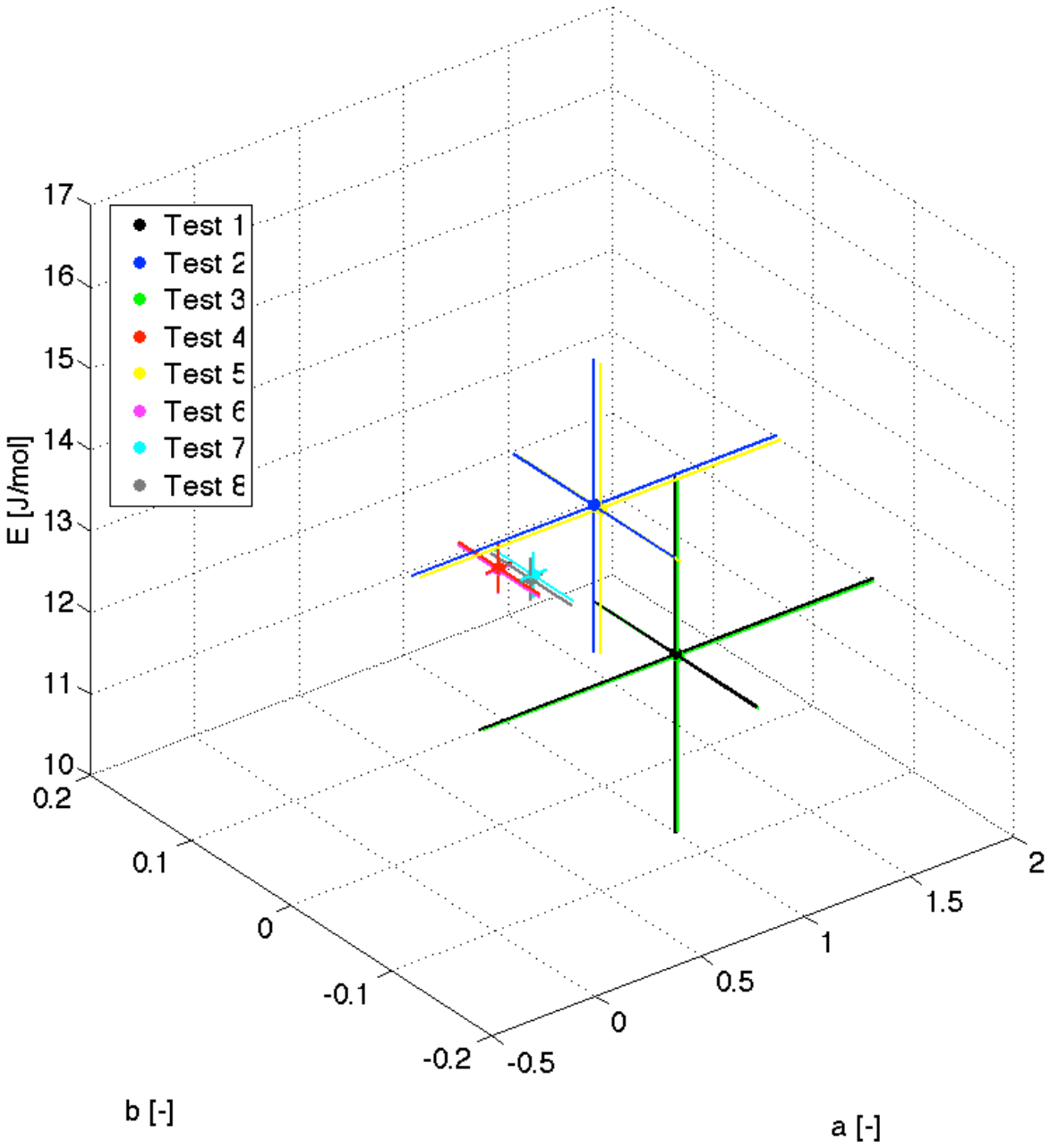

Figure 8.4 Results of the analyzed tests presenting the obtained values of the parameters and their uncertainties for the parameters of the reaction orders and the activation energy

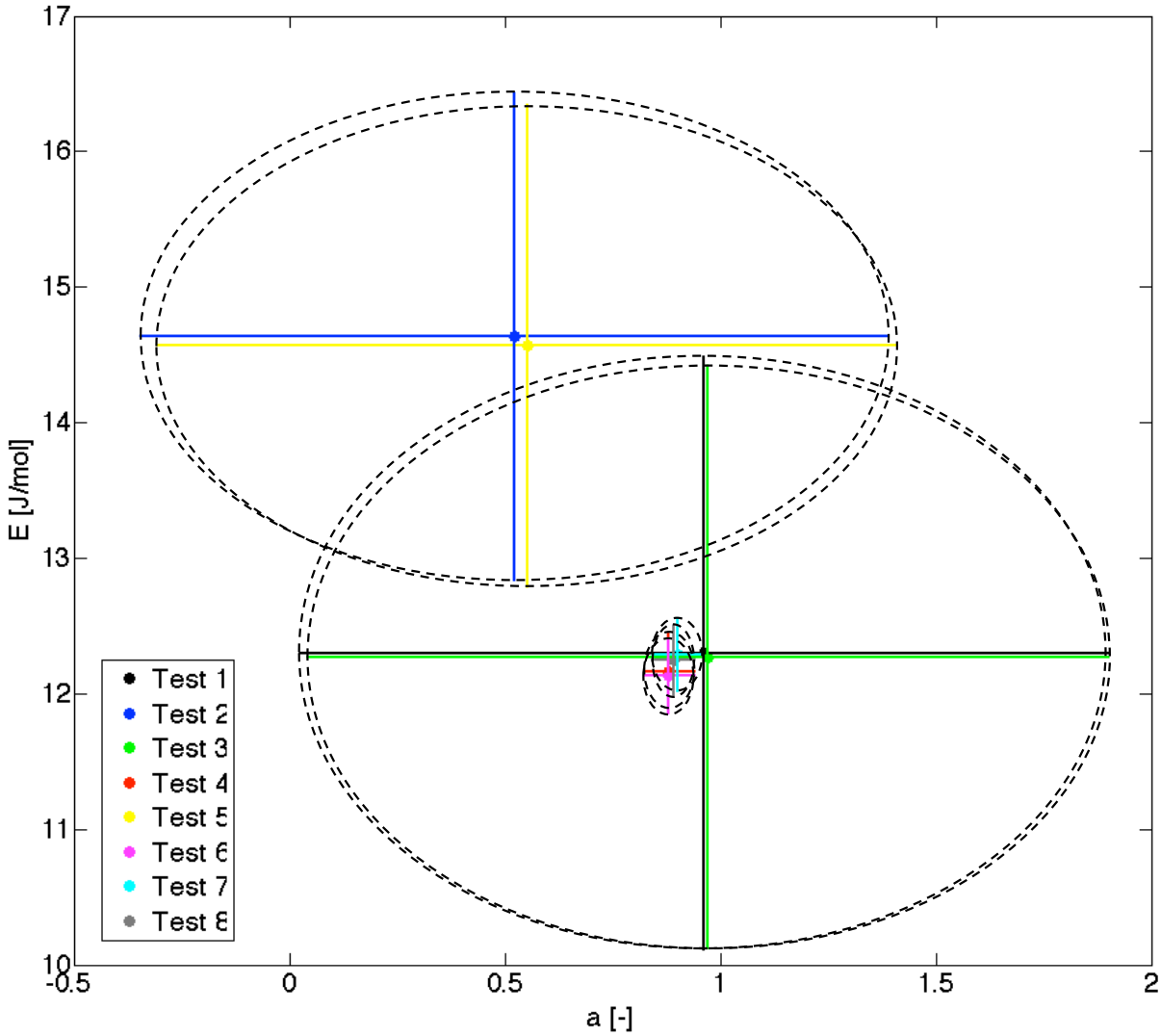

Figure 8.5 Decrease in the volume of the covariance matrix in the projection over the axis defining reaction order with respect to methane and activation energy

The effect of the equations, defining the balance of elements to the volume of the covariance ellipsoid to be decreased in Tests 4, 6, 7 and 8, is clear as shown in 3D and 2D projections in Figs. 8.4 and 8.5. Those deliberations are generalized in Figs. 8.6 and 8.7 showing the averaged decrease of the uncertainty in each model for the most important parameters and the sum of the diagonal elements of the covariance matrix assembled with the measurements and unknowns. The large increase found on the security of the measured and unknown variables in all the cases where the balances of elements were included. The smallest uncertainty of the final result was obtained in Test 8 and Eq 8.8 expresses the kinetic of the process.

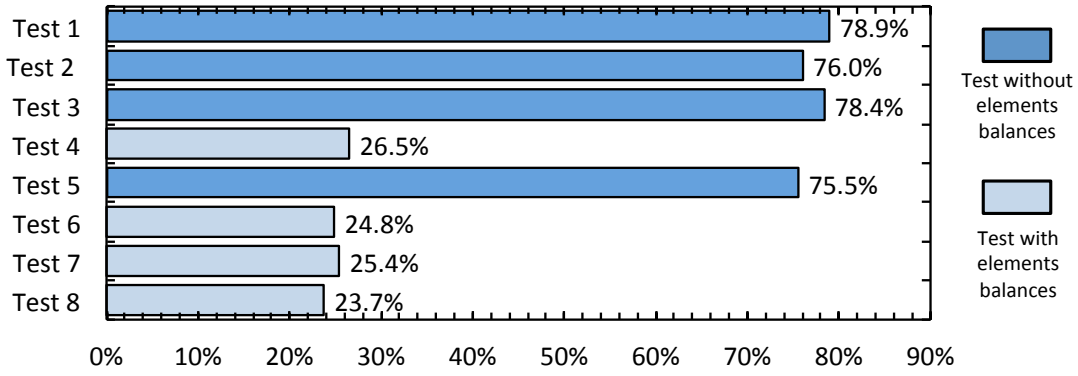

Figure 8.6 Results of the analyzed Tests: a decrease in the final average uncertainty of the compared with initial uncertainty of the unknown parameters of *a, b, A* and *E*

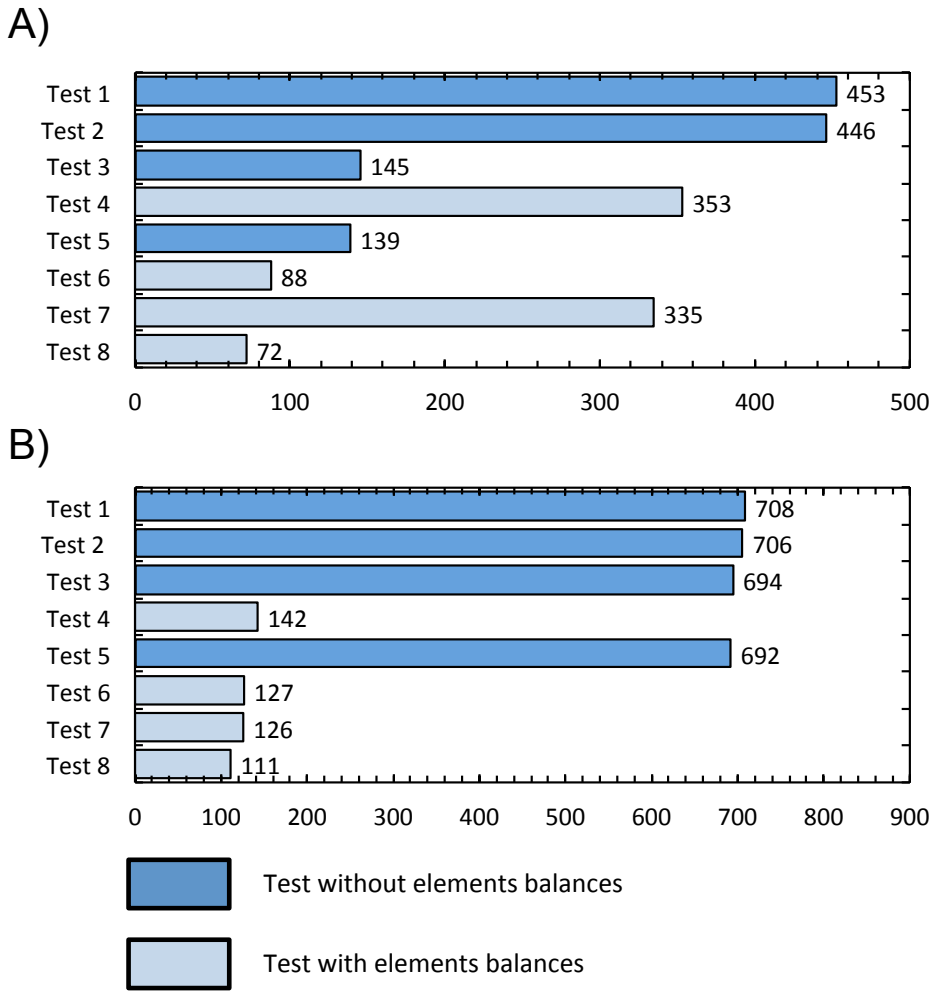

Figure 8.7 Results of the analyzed Tests: sum of diagonal elements of the covariance matrix $\mathbf{C_{VB}}$ after the application of the GLS algorithm for: A) measurements and B) unknowns: *a, b, A* and *E*

9 Conclusions

This dissertation describes techniques and models designed for experimental and numerical studies of the methane/steam reforming process over a nickel catalyst. The primeval focus is on the issues relevant for the incorporating internal reformer into Solid Oxide Fuel Cells system fuelled with hydrocarbon fuel. The lack of uniform depiction, discrepancies between proposed reaction kinetics and the significant influence of the incorporated reforming model in the simulation of the SOFC systems justify the urgent necessity for the systematization of descriptions and a reliable strategy for evaluation the methane/steam reforming kinetic.

9.1 General remarks

In the scope of thesis the following topics were concerned and discussed.

Mathematical algorithms and models

Chapters 2 and 3 of the thesis introduced the mathematical methods, modelling techniques and numerical algorithms proposed for the designation of the methane/steam reforming process. The described theoretical bases were introduced to prepared numerical codes and analysis presented in the subsequent chapters. In particular, Chapter 2 summarizes the mathematical deliberation of the Generalized Least Squares Method and the potential benefits of its incorporation into the determination of the kinetic of the highly nonlinear chemical process. The classical methods of deriving methane/steam reforming kinetic were introduced in Section 3.1. The succeeding sections introduce the mathematical basis of standard and modified approaches to determine the parameters in the power law expression describing methane/steam reforming. Further, the modified approach was generalized in order to conduct calculations simultaneously for all results measured at different temperatures. The last Section 3.8 describes a method of simulation of the composition of the outlet gas composition from determined input conditions. All of the presented algorithms were implemented numerically in C language and MATLAB package and used in the analysis.

Experimental studies

The experimental studies, conducted as part of this dissertation are described in Chapter 4 and supplementary data concerning the experimental setup and prepared catalysts are given in Appendices A and B, respectively. The experimental part of the research was divided into two primal sections. Firstly, the methodology of preparation catalytic materials for methane/steam the reforming process was designed. The different types of powders (Ni/NiO) and dispersion agents were tested; furthermore parameters such as sintering curve, binder agent, mixing and crushing time were adjusted to follow the laboratory and industrial processes of preparing the SOFC anodes. Then, the prepared catalytic materials were tested experimentally in the plug-flow reactors. The studies were conducted on the crushed catalyst in order to avoid the influence of mass transfer in the porous material, which can disturb the results of investigation focused on catalytic properties. The experimental conditions relevant for the proposed numerical algorithms were designed with respect to the specific requirements of each mathematical technique introduced in Chapter 3. Additionally, the correlation between the Gas Space Hourly Velocity and the predicted conversion rate of methane were delivered and discussed in the context of delivering the correct kinetic equation.

Classical analysis of methane steam reforming – comparison of approach

Chapter 5 is divided into two parts. Firstly, the classical approaches to modelling and investigating the methane/steam reforming process were applied to the experimental studies on nickel cermet catalyst with volumetric composition of Ni equalled 60%. The standard and modified methods popularly adopted in the literature were compared. An improvement in the modified method for the simultaneous calculation was proposed: the appropriate reaction order was selected in terms of giving the smallest sum of the relative standard deviation found in the reaction constant for all of the temperatures simultaneously. The influence of the experimental data set for every calculated algorithm was discussed. Finally the activation energy and pre-exponential factor were derived from the Arrhenius plot. The proposed equation was used to simulate the reforming process and compare numerical and experimental results. The influence of the temperature and steam-to-carbon ratio for the outlet gas composition and the conversion rate of methane were discussed. Good agreement was found for the results characterized by the conversion rates lower than 60%. In this context, the change in the experimental conditions and the increase of Gas Space Hourly Velocity are justified in order to derive the proper kinetic equation.

The updated experimental conditions were applied to the analyses in the second part of Chapter 5. The influence of the volumetric composition of nickel cermet catalyst was experimentally investigated. The reaction order rates for various catalytic material were provided and compared with Mogensen and Iwai' research findings, who investigated SOFC dedicated materials. The results were found to be convergent and independent on the volumetric composition in terms of reaction orders.

Application of Generalized Least Squares Algorithm

The Generalized Least Squares (GLS) method is known as a data reconciliation methodology. The reconciled data are more precise in general than the corresponding set of measurements. By the application of the GLS algorithm, the mass and energy balances as well as the physical constraints describing the measurement system are closed and the model is coherent. The application of the GLS method results in an improvement in the quality of the obtained solution by decreasing the uncertainties of the model. In Chapter 6 a novel approach to evaluate the reaction kinetics of the methane/steam reforming process by adopting an Orthogonal Least Squares method was introduced. The advantages of such an approach enables a more general analysis of the problem and provides more precise information about obtained results, which includes their uncertainty. The Generalized Least Square (GLS) method was applied to the calculation of the empirical parameters of the methane/steam reforming reaction on a Ni/YSZ SOFC anode cermet catalyst: the pre-exponential factor of A, the activation energy E, the reaction orders with respect to CH_4 and H_2O, a and b, and therefore to the estimation of the reaction rate and the methane conversion rate of the steam reforming process.

The application of the GLS algorithm is divided into three main phases: the experimental investigation of the methane/steam reforming process over a fine powder catalyst of NiO/YSZ, the numerical analysis of collected data which aimed to find the initial approximations of empirical parameters describing the process, and finally the definition and application of the operators of the GLS algorithm.

In Chapter 6 all elements of the GLS algorithm were precisely defined. The introduced mathematical model has been based only on the fundamental physical equations describing the chemical process, and it can be noted that it does not contain any additional assumptions in accordance with the precise stoichiometry of the occurring reactions. This property

provides for greater versatility of the proposed methodology in comparison with approaches used in the previous studies. The experimental measurements and process unknowns were introduced to the variables vector **x.** In the standard approach to the calculation of the reforming reaction kinetic, different series of experimental measurements are used to calculate the reaction rates and different experimental conditions are required to determine the activation energy and Arrhenius constant. On the other hand, one of the requirements in the proposed GLS model is that all of the experimental results are subjected to all of the model equations, and they have to fulfil all the constraints imposed on the problem. Then, because of the large redundancy in the model definition, an increase in the security of the final solution is observed; it is significant especially when the measurements are influenced by process variability and experimental inaccuracies.

It was proven that the proposed GLS method not only allows for obtaining the most probable values of the estimated parameters but also makes possible the *a posteriori* evaluation of the errors of the directly measured variables and unknown parameters. It was demonstrated that the GLS method is useful in securing higher accuracy of measured data and decreasing the value of the residuum of the constraint equations. The present results primarily proved an applicability of the GLS methodology into the investigation of a chemical reaction process for deriving its reaction kinetics.

Critical Comparison with literature data

A critical comparison of the obtained results with the literature data and discussion on the possible reasons for the essential discrepancies between various studies are presented in Chapter 7. The considerations were focused on the literature studies on methane/steam reforming over nickel cermet catalyst. The multiplicity of the derived modelling equations was listed. The chosen equations were later compared with the results derived in Chapter 6. In order to give a meaningful comparison, the unification of pre-exponential factors had to be conducted, as this parameter is most fragile for individual properties of material and many authors do not provide enough information to identify the investigated catalyst unambiguously. The highest correlation between experimental data and a modelling equation was obtained for the model derived by the GLS algorithm in Chapter 6.

Validation of models for reforming process

The GLS method has the potential to provide objective criteria for the formal evaluation and falsification of different mathematical models of the methane reforming process. The studies in Chapter 8 particularly focused on the importance of the mathematical expressions, of the physical phenomena occurring in the chemical reforming system. The analysis was conducted in the light of improving the precise quantification of uncertainties found in the evaluation of the chemical reaction process and providing a reliable reaction rate equation. The analysis of the volume of covariance ellipsoid provides information about the importance and influence of separated constraints on the final results. The various models of the reforming process analysed in Chapter 8 proved a significant decrease in the uncertainty of the model with increased numbers of modelling equation. The increased security was observed for both: measurements and unknown variables. It was pointed out, that not all constraints are equally valuable, from the point of view of increasing security of the model: the balances of the elements in the system had a critical influence, while the linear Arrhenius correlation slightly changed the result and volume of the covariance ellipsoid. The variations in the volume of the covariance ellipsoid were explained in intuitive projections on three and two-dimensional variable spaces.

9.2 Suggestions for future work

The presented research for methane/steam reforming process attempted to clarify, classify and compare the different experimental and numerical approaches developed over years of studies in the field. The proposed comprehensive description with respect to the simultaneous numerical-experimental methodology in the form of the Generalized Least Squares method introduces novel quality and reliability into studies on highly nonlinear catalytic reactions.

The recommendation for the future work can be given as a research topics related to the presented investigations:

Incorporating GLS method for methane/steam reforming over various catalysts and analysis of different catalytic reactions. The proposed algorithm of GLS can be easily adapted to the mathematical modelling of the fuel reforming process for different catalysts and experimental conditions. Also, the various constraint models can be easily implemented, as they do not change the structure of the numerical algorithm but only insert an additional procedure. The

proposed approach can clarify the divergence between the published contradictory results about the reaction kinetics' parameters. The application of the GLS method can provide a great benchmark in the evaluation of the chemical process and qualify the level of mathematical modelling of reaction processes.

Applying of the GLS algorithm for design of the most favourable experimental conditions. It is postulated, that the complex interactive computational-experimental approach can be applied in order to design the minimal experimental set, which secures highest accuracy of the final solution. By the analysis of the changes in the covariance matrix after the co-ordination process by GLS algorithm, it is possible to evaluate influence of the included data for the uncertainties characterizing the final solution. Therefore, the GLS algorithm can be further used to identify the influence of the experimental data set and experimental uncertainties of the measuring devices for the quality of model. With this knowledge, it is possible to design the minimal experimental data set, resulting in the assumed quality of the model

Evaluating the influence of the applied model for the behaviour of the reformer and SOFC. The presented research can be applied for the sensitivity analysis of the influence of the applied methane/steam reforming model for the behaviour of reforming reactor or SOFC unit with internal reforming. This type of study would be very valuable in order to define the acceptable uncertainty of the reforming reaction model, which does not signify influence the security of the system modelling. On the basis of this information, the experimentation for the various catalysts can be planned to achieve the expected security level with the minimal number of the experimental measurements.

Studying the methane/steam reforming with respect to the micro-model. In the microstructure models of the methane/steam reforming it is important to derive the reaction rate with the respect to the catalyst surface area. The presented research was conducted on the Nickel based catalysts in the form of the fine powder. This excludes the influence of the porosity and microstructure of material, as it was assumed that reforming reaction occurs in the whole volume of the catalyst. However in the case of internal direct reforming for SOFC, the microstructure model including the 3D structure of material, mass and heat transfer phenomena, as well as chemical and electrochemical reactions is necessary. These issues should be further experimentally and numerically investigated.

References

[1] British Petroleum. BP Statistical Review of World Energy. 2015.

[2] Rostrup-Nielsen T. Manufacture of hydrogen. Catalysis Today 106;293–6;2005.

[3] York APE, Xiao T, Green MLH, Claridge JB. Methane oxyforming for synthesis gas production. Catalysis Reviews 49;511–60;2007.

[4] Kolb G. Fuel processing for fuel cells. Weinheim: Wiley-VCH Verlag GmbH & Co. KGaA; 2008.

[5] Bhat, Shrikant A, Sadhukhan J. Modeling and simulation of the polymeric nanocapsule formation process. AIChE Journal 55;408–22;2009.

[6] Wang X, Gorte RJ. A study of steam reforming of hydrocarbon fuels on Pd/ceria. Applied Catalysis A: General 224;209–18;2002.

[7] Laosiripojana N, Sangtongkitcharoen W, Assabumrungrat S. Catalytic steam reforming of ethane and propane over CeO_2-doped Ni/Al_2O_3 at SOFC temperature: Improvement of resistance toward carbon formation by the redox property of doping CeO_2. Fuel 85;323–32;2006.

[8] Schädel BT, Duisberg M, Deutschmann O. Steam reforming of methane, ethane, propane, butane, and natural gas over a rhodium-based catalyst. Catalysis Today 142;42–51;2009.

[9] Huang X, Reimert R. Kinetics of steam reforming of ethane on Ni/YSZ (yttria-stabilised zirconia) catalyst. Fuel 106;380–7;2013.

[10] Veranitisagul C, Koonsaeng N, Laosiripojana N, Laobuthee A. Preparation of gadolinia doped ceria via metal complex decomposition method: Its application as catalyst for the steam reforming of ethane. Journal of Industrial and Engineering Chemistry 18;898–903;2012.

[11] Hardiman KM, Ying TT, Adesina A a., Kennedy EM, Dlugogorski BZ. Performance of a Co-Ni catalyst for propane reforming under low steam-to-carbon ratios. Chemical Engineering Journal 102;119–30;2004.

[12] Li Y, Wang X, Xie C, Song C. Influence of ceria and nickel addition to alumina-supported Rh catalyst for propane steam reforming at low temperatures. Applied Catalysis A: General 357;213–22;2009.

[13] Hou T, Yu B, Zhang S, Zhang J, Wang D, Xu T, et al. Hydrogen production from propane steam reforming over $Ir/Ce_{0.75}Zr_{0.25}O_2$ catalyst. Applied Catalysis B: Environmental 168-169;524–30;2015.

[14] Jeong H, Kang M. Hydrogen production from butane steam reforming over Ni/Ag loaded $MgAl_2O_4$ catalyst. Applied Catalysis B: Environmental 95;446–55;2010.

[15] Avci AK, Trimm DL, Aksoylu a. E, Önsan ZI. Hydrogen production by steam reforming of n-butane over supported Ni and Pt-Ni catalysts. Applied Catalysis A: General 258;235–40;2004.

[16] Braga LB, Silveira JL, Da Silva ME, Tuna CE, Machin EB, Pedroso DT. Hydrogen production by biogas steam reforming: A technical, economic and ecological analysis. Renewable and Sustainable Energy Reviews 28;166–73;2013.

[17] Mortensen PM, Dybkjær I. Industrial scale experience on steam reforming of CO_2-rich gas. Applied Catalysis A: General 495;141–51;2015.

[18] Constantinou D a., Fierro JLG, Efstathiou AM. The phenol steam reforming reaction towards H_2 production on natural calcite. Applied Catalysis B: Environmental 90;347–59;2009.

[19] Basile a., Tereschenko GF, Orekhova N V., Ermilova MM, Gallucci F, Iulianelli a. An experimental investigation on methanol steam reforming with oxygen addition in a flat Pd-Ag membrane reactor. International Journal of Hydrogen Energy 31;1615–22;2006.

[20] Yong ST, Ooi CW, Chai SP, Wu XS. Review of methanol reforming-Cu-based catalysts, surface reaction mechanisms, and reaction schemes. International Journal of Hydrogen Energy 38;9541–52;2013.

[21] Sá S, Silva H, Brandão L, Sousa JM, Mendes A. Catalysts for methanol steam reforming-A review. Applied Catalysis B: Environmental 99;43–57;2010.

[22] Iulianelli a., Ribeirinha P, Mendes a., Basile a. Methanol steam reforming for hydrogen generation via conventional and membrane reactors: A review. Renewable and Sustainable Energy Reviews 29;355–68;2014.

[23] Haryanto a, Fernando S, Murali N, Adhikari S. Current status of hydrogen production techniques by steam reforming of ethanol: A review. Energy & Fuels 19;2098–106;2005.

[24] Hou T, Zhang S, Chen Y, Wang D, Cai W. Hydrogen production from ethanol reforming: Catalysts and reaction mechanism. Renewable and Sustainable Energy Reviews 44;132–48;2015.

[25] Ni M, Leung DYC, Leung MKH. A review on reforming bio-ethanol for hydrogen production. International Journal of Hydrogen Energy 32;3238–47;2007.

[26] Xu X, Li P, Shen Y. Small-scale reforming of diesel and jet fuels to make hydrogen and syngas for fuel cells: A review. Applied Energy 108;202–17;2013.

[27] Dou B, Song Y, Wang C, Chen H, Xu Y. Hydrogen production from catalytic steam reforming of biodiesel byproduct glycerol: Issues and challenges. Renewable and Sustainable Energy Reviews 30;950–60;2014.

[28] Silva JM, Soria M a., Madeira LM. Challenges and strategies for optimization of glycerol steam reforming process. Renewable and Sustainable Energy Reviews 42;1187–213;2015.

[29] Trane R, Dahl S, Skjøth-Rasmussen MS, Jensen a. D. Catalytic steam reforming of bio-oil. International Journal of Hydrogen Energy 37;6447–72;2012.

[30] Angeli SD, Monteleone G, Giaconia A, Lemonidou A a. State-of-the-art catalysts for CH4 steam reforming at low temperature. International Journal of Hydrogen Energy 39;1979–97;2014.

[31] LeValley TL, Richard AR, Fan M. The progress in water gas shift and steam reforming hydrogen production technologies – A review. International Journal of Hydrogen Energy 39;16983–7000;2014.

[32] Wei J, Iglesia E. Isotopic and kinetic assessment of the mechanism of reactions of CH_4 with CO_2 or H_2O to form synthesis gas and carbon on nickel catalysts. Journal of Catalysis 224;370–83;2004.

[33] Saunders JE, Davy MH. High-temperature vibrational Raman spectroscopy of gaseous species for solid-oxide fuel cell research. International Journal of Hydrogen Energy 37;3403–14;2012.

[34] Saunders JE a., Davy MH. In-situ studies of gas phase composition and anode surface temperature through a model DIR-SOFC steam–methane reformer at 973.15 K. International Journal of Hydrogen Energy 38;13762–73;2013.

[35] Mbodji M, Commenge JM, Falk L. Preliminary design and simulation of a microstructured reactor for production of synthesis gas by steam methane reforming. Chemical Engineering Research and Design 92;1728–39;2013.

[36] Bodrov IM, Apel'baum LO, Temkin IM. KInetics of the reaction between methane and water vapour over nickel surface. Kinetika I Kataliz 5;696–705;1964.

[37] Xu J, Froment GF. Methane steam reforming, methanation and water-gas shift: I. Intrinsic kinetics. AIChE Journal 35;88–96;1989.

[38] Peters R, Dahl R, Kluttgen U, Palm C, Stolten D. Internal reforming of methane in solid oxide fuel cell systems. Journal of Power Sources 106;238–44;2002.

[39] Mogensen D, Grunwaldt J-D, Hendriksen PV, Dam-Johansen K, Nielsen JU. Internal steam reforming in solid oxide fuel cells: Status and opportunities of kinetic studies and their impact on modelling. Journal of Power Sources 196;25–38;2011.

[40] Berman a., Karn RK, Epstein M. Kinetics of steam reforming of methane on Ru/Al_2O_3 catalyst promoted with Mn oxides. Applied Catalysis A: General 282;73–83;2005.

[41] Richardson JT, Garrait M, Hung JK. Carbon dioxide reforming with Rh and Pt-Re catalysts dispersed on ceramic foam supports. Applied Catalysis A: General 255;69–82;2003.

[42] Gaddalla AM, Sommer ME. Carbon dioxide reforming of methane on nickel catalysts. Chemical Engineering Science 44;2825–9;1989.

[43] Perera JSH., Couves JW, Sankar G, Thomas JM. The catalytic activity of Ru and Ir supported on Eu_2O_3 for the reaction, $CO_2+CH_4=2H_2+2CO$: a viable solar-thermal energy system. Catalysis Letters 11;219–25;1991.

[44] Sodesawa T, Dobashi A, Nozaki F. Catalytic reaction of methane with carbon dioxide. Reaction Kinetics and Catalysis Letters 12;107–11;1979.

[45] Yamazaki O, Nozaki T, Omata K, Fujimoto K. Reduction of Carbon Dioxide by Methane with Ni-on-MgO-CaO Containing Catalysts. Chemistry Letters 1953–4;1992.

[46] Gadalla AM, Sommer ME. Synthesis and characterization of catalysts in the system Al_2O_3-MgO-NiO-Ni for methane reforming with CO_2. Journal of the American Society Ceramic Society 72;683–7;1989.

[47] Gadalla AM, Bower B. The role of catalyst support on the activity of nickel for reforming methane with CO_2. Chemical Engineering Science 43;3049–62;1988.

[48] Guerrero-Ruiz A, Rodriguez-Ramos I, Sepualveda-Escribano A. Effect of the basic function in Co, MgO/C catalysts on the selective oxidation of methane by carbon dioxide. Journal of the Chemical Society, Chemical Communications 487;1993.

[49] Rostrup-Nielsen JR, Hansen J-HB. CO_2 reforming of methane over transition metals. Journal of Catalysis 144;38–49;1993.

[50] Kim GJ, Cho DS, Kim KH, Kim JH. The reaction of CO_2 with CH_4 to synthesize H_2 and CO over nickel-loaded Y-zeolites. Catalysis Letters 28;41–52;1994.

[51] Quincoces CE, Vargas SP De, Grange P, Gonza MG. Role of Mo in CO_2 reforming of CH_4 over Mo promoted Ni/A_2O_3 catalysts. Materials Letters 56;698–704;2002.

[52] Wang S, Lu GQM. Effects of promoters on catalytic activity and carbon deposition of Ni/g -Al_2O_3 catalysts in CO_2 reforming of CH_4. Journal of Chemical Technology and Biotechnology 595;589–95;2000.

[53] Bradford MCJ, Vannice MA. Catalytic reforming of methane with carbon dioxide over nickel catalysts II. Reaction kinetics. Applied Catalysis A: General 142;97–122;1996.

[54] Olsbye U, Wurzel T, Mleczko L. Kinetic and Reaction Engineering Studies of Dry Reforming of Methane over a Ni/La/Al_2O_3 Catalyst. Industrial & Engineering Chemistry Research 36;5180–8;1997.

[55] Osaki T, Horiuchi T, Suzuki K, Mori T. Catalyst performance of MoS_2 and WS_2 for the CO_2-reforming of CH_4 Suppression of carbon deposition. Applied Catalysis A: General 155;229–38;1997.

[56] Zhang Z, Verykios XE. Mechanistic aspects of carbon dioxide reforming of methane to synthesis gas over Ni catalysts. Catalysis Letters 38;175–9;1996.

[57] Bodrov IM, Apel'baum LO. No Title. Kinetika I Kataliz 8;379;1967.

[58] Nishino T, Szmyd JS. Numerical Analysis of a Cell-Based Indirect Internal Reforming Tubular SOFC Operating With Biogas. ASME Journal of Fuel Cell Science and Technology 7;051004–1 – 0510004–8;2010.

[59] Brus G, Komatsu Y, Kimijima S, Szmyd JS. An analysis of biogas reforming process on Ni/YSZ and Ni/SDC catalysts. International Journal of Thermodynamics 15;43–51;2012.

[60] Brus G, Nowak R, Szmyd JS, Komatsu Y, Kimijima S. An experimental and theoretical approach for the carbon deposition problem during steam reforming of model biogas. Journal of Theoretical and Applied Mechanics 53;2015.

[61] Valentini A, Carreño NLV, Probst LFD, Lisboa-Filho PN, Schreiner WH, Leite ER, et al. Role of vanadium in Ni:Al_2O_3 catalysts for carbon dioxide reforming of methane. Applied Catalysis A: General 255;211–20;2003.

[62] Appari S, Janardhanan VM, Bauri R, Jayanti S, Deutschmann O. A detailed kinetic model for biogas steam reforming on Ni and catalyst deactivation due to sulfur poisoning. Applied Catalysis A: General 471;118–25;2014.

[63] Li L, Howard C, King DL, Gerber M, Dagle R, Stevens D. Regeneration of sulfur deactivated Ni-based biomass syngas cleaning catalysts. Industrial and Engineering Chemistry Research 49;10144–8;2010.

[64] Bartholomew CH, Weatherbee GD, Jarvi GA. Sulfur Poisoning of Nickel Methanation catalysts I. In situ deactivation by H_2S of nickel and nickel bimetallics. Journal of Catalysis 60;257–69;1979.

[65] Tsang SC, Claridge JB, Green MLH. Recent advances in the conversion of methane to synthesis gas. Catalysis Today 23;3–15;1995.

[66] Enger BC, Lødeng R, Holmen A. A review of catalytic partial oxidation of methane to synthesis gas with emphasis on reaction mechanisms over transition metal catalysts. Applied Catalysis A: General 346;1–27;2008.

[67] York A, Xiao T, Green M. Brief overview of the partial oxidation of methane to synthesis gas. Topics in Catalysis 22;345–58;2003.

[68] Zhu Q, Zhao X, Deng Y. Advances in the Partial Oxidation of Methane to Synthesis Gas. Journal of Natural Gas Chemistry 13;191–203;2004.

[69] Slagtern Å, Swaan HM, Olsbye U, Dahl IM, Mirodatos C. Catalytic partial oxidation of methane over Ni-, Co- and Fe-based catalysts. Catalysis Today 46;107–15;1998.

[70] Prettre M, Eichner C, Perrin M. The catalytic oxidation of methane to carbon monoxide and hydrogen. Transactions of Faraday Society 42;335–9;1945.

[71] Hickman D a, Schmidt LD. Steps in CH_4 Oxidation on Pt and Rh Surfaces - High-Temperature Reactor Simulations. Aiche Journal 39;1164–77;1993.

[72] Hickman DA, Haupfear EA, Schmidt LD. Synthesis gas formation by direct oxidation of methane over Rh monoliths. Catalysis Letters 17;223–37;1993.

[73] Hickman DA, Schmidt LD. The role of boundary layer mass transfer in partial oxidation selectivity. Journal of Catalysis 136;300–8;1992.

[74] Hickman DA, Schmidt LD. Production of syngas by direct catalytic oxidation of methane. Science 259;343–6;1993.

[75] Hickman DA, Schmidt LD. Synthesis Gas Formation by Direct Oxidation of Methane over Pt Monoliths. Journal of Catalysis 138;267–82;1992.

[76] Eguchi K, Kojo H, Takeguchi T, Kikuchi R, Sasaki K. Fuel flexibility in power generation by solid oxide fuel cells. Solid State Ionics 153;411–6;2002.

[77] Williams M, Strakey J, Surdoval W, Wilson L. Solid oxide fuel cell technology development in the U.S. Solid State Ionics 177;2039–44;2006.

[78] Singhal S. Solid oxide fuel cells for stationary, mobile, and military applications. Solid State Ionics 152-153;405–10;2002.

[79] Xia C. Electrolytes. In: Fergus J, Hui R, Li X, Wilkinson DP, Zhang J, editors. Solid Oxide Fuel Cells: Materials Properties and Performance, Boca Raton: CRC Press; 2009, p. 1–73.

[80] Shri Prakash B, Senthil Kumar S, Aruna ST. Properties and development of Ni/YSZ as an anode material in solid oxide fuel cell: A review. Renewable and Sustainable Energy Reviews 36;149–79;2014.

[81] Mogensen D. Methane steam reforming kinetics over Ni-YSZ anode materials for solid oxide fuel cells. Technical University of Denmark, 2011.

[82] Kyobayashi Y, Ando Y, Nishiura M, Tomida K, Kishizawa H, Matake N. Next-Generation SOFC-Combined Power Generation System (High Efficiency Hybrid Power Generation System). Mitsubishi Heavy Industries Technical Review 50;42–6;2013.

[83] Hennessy D. " Solid Oxide Fuel Cell Diesel Auxiliary Power Unit Demonstration ." 2012.

[84] Dominovas Energy, Delphi to develop SOFC manufacturing. Fuel Cells Bulletin 2014;11;2014.

[85] Wincewicz K, Cooper J. Taxonomies of SOFC material and manufacturing alternatives. Journal of Power Sources 140;280–96;2005.

[86] Aguiar P, Brett DJL, Brandon NP. Feasibility study and techno-economic analysis of an SOFC/battery hybrid system for vehicle applications. Journal of Power Sources 171;186–97;2007.

[87] Patakangas J, Ma Y, Jing Y, Lund P. Review and analysis of characterization methods and ionic conductivities for low-temperature solid oxide fuel cells (LT-SOFC). Journal of Power Sources 263;315–31;2014.

[88] Ding J, Liu J, Yin G. Fabrication and characterization of low-temperature SOFC stack based on GDC electrolyte membrane. Journal of Membrane Science 371;219–25;2011.

[89] Ormerod RM. Fuels and Fuel Processing. In: Singhal S, Kendall K, editors. High Temperature Solid Oxide Fuel Cell Fundamentals, Design and Applications, Tokyo, Japan: 2003, p. 333.

[90] Ormerod RM. Solid oxide fuel cells. Chemical Society Reviews 32;17–28;2003.

[91] Clarke SH, Dicks AL, Pointon K, Smith T a., Swann A. Catalytic aspects of the steam reforming of hydrocarbons in internal reforming fuel cells. Catalysis Today 38;411–23;1997.

[92] Rostrup-Nielsen JR, Christiansen LJ. Internal steam reforming in fuel cells and alkali poisoning. Applied Catalysis A, General 126;381–90;1995.

[93] Finnerty CM, Coe NJ, Cunningham RH, Ormerod RM. Carbon formation on and deactivation of nickel-based/zirconia anodes in solid oxide fuel cells running on methane. Catalysis Today 46;137–45;1998.

[94] Brus G. An analysis of transport phenomena in an internal indirect reforming type solid oxide fuel cell. Ph. D. Thesis in AGH University of Science and Technology, Poland, 2011.

[95] Simwonis D, Tietz F, Stover D. Nickel coarsening in annealed Ni/8YSZ anode substrates for solid oxide fuel cells. Solid State Ionics 132;241–51;2000.

[96] Klein J-M, Bultel Y, Georges S, Pons M. Modeling of a SOFC fuelled by methane: From direct internal reforming to gradual internal reforming. Chemical Engineering Science 62;1636–49;2007.

[97] Costamagna P, Selimovic A, Del Borghi M, Agnew G. Electrochemical model of the integrated planar solid oxide fuel cell (IP-SOFC). Chemical Engineering Journal 102;61–9;2004.

[98] Haberman B a., Young JB. Three-dimensional simulation of chemically reacting gas flows in the porous support structure of an integrated-planar solid oxide fuel cell. International Journal of Heat and Mass Transfer 47;3617–29;2004.

[99] Hosseini S, Ahmed K, Tadé MO. CFD model of a methane fuelled single cell SOFC stack for analysing the combined effects of macro/micro structural parameters. Journal of Power Sources 234;180–96;2013.

[100] Nagel FP, Schildhauer TJ, Biollaz SM a, Stucki S. Charge, mass and heat transfer interactions in solid oxide fuel cells operated with different fuel gases-A sensitivity analysis. Journal of Power Sources 184;129–42;2008.

[101] Obara S. Dynamic-characteristics analysis of an independent microgrid consisting of a SOFC triple combined cycle power generation system and large-scale photovoltaics. Applied Energy 141;19–31;2015.

[102] Santin M, Traverso A, Magistri L, Massardo A. Thermoeconomic analysis of SOFC-GT hybrid systems fed by liquid fuels. Energy 35;1077–83;2010.

[103] Komatsu Y, Kimijima S, Szmyd JS. Performance analysis for the part-load operation of a solid oxide fuel cell-micro gas turbine hybrid system. Energy 35;982–8;2010.

[104] Chan SH, Ding OL. Simulation of a solid oxide fuel cell power system fed by methane. International Journal of Hydrogen Energy 30;167–79;2005.

[105] Nehter P. Two-dimensional transient model of a cascaded micro-tubular solid oxide fuel cell fed with methane. Journal of Power Sources 157;325–34;2006.

[106] Selimovic A, Palsson J. Networked solid oxide fuel cell stacks combined with a gas turbine cycle. Journal of Power Sources 106;76–82;2002.

[107] Palsson J, Selimovic A, Sjunnesson L. Combined solid oxide fuel cell and gas turbine systems for efficient power and heat generation. Journal of Power Sources 86;442–8;2000.

[108] Riensche E, Stimming U, Unverzagt G. Optimization of a 200 kW SOFC cogeneration power plant Part I: Variation of process parameters. Journal of Power Sources 73;251–6;1998.

[109] Riensche E, Stimming U, Unverzagt G. Optimization of a 200 kW SOFC cogeneration power plant Part II: variation of the flowsheet. Journal of Power Sources 73;251–6;1998.

[110] Lehnert W, Meusinger J, Thom F. Modelling of gas transport phenomena in SOFC anodes 0–6;2000.

[111] Sunde S. Simulations of composite electrodes in fuel cells. Journal of Electroceramics 5;153–82;2000.

[112] Selimovic A, Kemm M, Torisson T, Assadi M. Steady state and transient thermal stress analysis in planar solid oxide fuel cells. Journal of Power Sources 145;463–9;2005.

[113] Yakabe H, Ogiwara T, Hishinuma M, Yasuda I. 3-D model calculation for planar SOFC. Journal of Power Sources 102;16–25;2001.

[114] Nikooyeh K, Jeje AA, Hill JM. 3D modeling of anode-supported planar SOFC with internal reforming of methane 171;601–9;2007.

[115] Komatsu Y, Kimijima S, Szmyd JS. Numerical analysis on dynamic behavior of solid oxide fuel cell with power output control scheme. Journal of Power Sources 223;232–45;2013.

[116] Achenbach E. Three-dimensional and time-dependent simulation of a planar solid oxide fuel cell stack. Journal of Power Sources 49;333–48;1994.

[117] Costamagna P, Arato E, Bonino GB, Calabria R. Partial oxidation of CH4 in Solid Oxide Fuel Cells: simulation model of the electrochemical reactor and experimental validation. Chemical Engineering Science 51;3013–8;1996.

[118] Pfafferodt M, Heidebrecht P, Stelter M, Sundmacher K. Model-based prediction of suitable operating range of a SOFC for an Auxiliary Power Unit. Journal of Power Sources 149;53–62;2005.

[119] Sidwell RW, Coors WG. Large limits of electrical efficiency in hydrocarbon fueled SOFCs. Journal of Power Sources 143;166–72;2005.

[120] Chan SH, Ho HK, Tian Y. Multi-level modeling of SOFC-gas turbine hybrid system. International Journal of Hydrogen Energy 28;889–900;2003.

[121] Apfel H, Rzepka M, Tu H, Stimming U. Thermal start-up behaviour and thermal management of SOFC's. Journal of Power Sources 154;370–8;2006.

[122] Demin a, Alderucci V, Ielo I, Fadeev G, Maggio G, Giordano N, et al. Thermodynamic analysis of methane fueled solid oxide fuel cell system. International Journal of Hydrogen Energy 17;451–8;1992.

[123] Achenbach E, Riensche E. Metahne/steam reforming kinetics for solid oxide fuel cell. Journal of Power Sources 52;283–8;1994.

[124] Drescher I, Lehnert W, Meusinger J. Structural properties of SOFC anodes and reactivity. Electrochimica Acta 43;3059–68;1998.

[125] Ahmed K, Foger K. Kinetics of internal steam reforming of methane on Ni/YSZ-based anodes for solid oxide fuel cells. Catalysis Today 63;479–87;2000.

[126] Leinfelder R. Reaktionskinetische Untersuchungen zur Methan-Dampf-Reformierung und Shift-Reaktion an Anoden oxidkeramischer Brennstoffzellen,. Erlangen-Nürnberg, Germany: Universität Erlangen-Nürnberg; 2004.

[127] Drescher I. Kinetik der Methan-Dampf-Reformierung. Jülich, Germany: Forschungszentrum Jülich; 1999.

[128] Hecht ES, Gupta GK, Zhu H, Dean AM, Kee RJ, Maier L, et al. Methane reforming kinetics within a Ni–YSZ SOFC anode support. Applied Catalysis A: General 295;40–51;2005.

[129] Brus G, Miyawaki K, Iwai H, Saito M, Yoshida H. Tortuosity of an SOFC anode estimated from saturation currents and a mass transport model in comparison with a real micro-structure. Solid State Ionics 265;13–21;2014.

[130] Li W, Shi Y, Luo Y, Cai N. Theoretical modeling of air electrode operating in SOFC mode and SOEC mode: The effects of microstructure and thickness. International Journal of Hydrogen Energy 39;13738–50;2014.

[131] Nishino T, Iwai H, Suzuki K. Comprehensive numerical modeling and analysis of a cell-based indirect internal reforming tubular SOFC. ASME Journal of Fuel Cell Science and Technology 3;33–44;2006.

[132] Janardhanan VM, Deutschmann O. CFD analysis of a solid oxide fuel cell with internal reforming: Coupled interactions of transport, heterogeneous catalysis and electrochemical processes. Journal of Power Sources 162;1192–202;2006.

[133] Campanari S, Iora P. Comparison of finite volume SOFC models for the simulation of a planar cell geometry. Fuel Cells 5;34–51;2005.

[134] Al-Masri a., Peksen M, Blum L, Stolten D. A 3D CFD model for predicting the temperature distribution in a full scale APU SOFC short stack under transient operating conditions. Applied Energy 135;539–47;2014.

[135] Schluckner C, Subotić V, Lawlor V, Hochenauer C. Three-dimensional numerical and experimental investigation of an industrial-sized SOFC fueled by diesel reformat – Part I: Creation of a base model for further carbon deposition modeling. International Journal of Hydrogen Energy 39;19102–18;2014.

[136] Bove R, Lunghi P, Sammes NM. SOFC mathematic model for systems simulations. Part one: From a micro-detailed to macro-black-box model. International Journal of Hydrogen Energy 30;181–7;2005.

[137] Bove R, Lunghi P, Sammes NM. SOFC mathematic model for systems simulations - Part 2: Definition of an analytical model. International Journal of Hydrogen Energy 30;189–200;2005.

[138] Petersen TF, Houbak N, Elmegaard B. A zero-dimensional model of a 2nd generation planar SOFC using calibrated parameters. International Journal of Thermodynamics 9;161–9;2006.

[139] De Lorenzo G, Fragiacomo P. Energy analysis of an SOFC system fed by syngas. Energy Conversion and Management 93;175–86;2015.

[140] Greco a., Sorce a., Littwin R, Costamagna P, Magistri L. Reformer faults in SOFC systems: Experimental and modeling analysis, and simulated fault maps. International Journal of Hydrogen Energy 39;21700–13;2014.

[141] Sucipta M, Kimijima S, Suzuki K. Performance analysis of the SOFC-MGT hybrid system with gasified biomass fuel. Journal of Power Sources 174;124–35;2007.

[142] Klein J-M, Georges S, Bultel Y. Modeling of a SOFC Fueled by Methane:Anode Barrier to Allow Gradual Internal Reforming Without Coking. Journal of The Electrochemical Society 155;B333;2008.

[143] Gemmen RS, Trembly J. On the mechanisms and behavior of coal syngas transport and reaction within the anode of a solid oxide fuel cell. Journal of Power Sources 161;1084–95;2006.

[144] Ni M, Leung DYC, Leung MKH. Modeling of methane fed solid oxide fuel cells: Comparison between proton conducting electrolyte and oxygen ion conducting electrolyte. Journal of Power Sources 183;133–42;2008.

[145] Ni M, Leung DYC, Leung MKH. Importance of pressure gradient in solid oxide fuel cell electrodes for modeling study. Journal of Power Sources 183;668–73;2008.

[146] Nagata S, Momma A, Kato T, Kasuga Y. Numerical analysis of output characteristics of tubular SOFC with internal reformer. Journal of Power Sources 101;60–71;2001.

[147] Odegard R, Johnsen E, Karoliusen H. Methane reforming on Ni/zirconia SOFC anodes. In: Dokiya M, Yamamoto O, Tagawa H, Singhal SC, editors. Proceedings of 4th International Symposium on Solid Oxide Fuel Cells (SOFC-IV), Yokohama, Japan: ECS; 1995, p. 810–9.

[148] Brus G. Experimental and numerical studies on chemically reacting gas flow in the porous structure of a solid oxide fuel cells internal fuel reformer. International Journal of Hydrogen Energy 37;17225–34;2012.

[149] Olaf Deutschmann group (Karlsruhe Institute of Technology). DETCHEM Mechanisms 2006.

[150] King D, Strohm J, Wang X, Roh H, Wang C, Chin Y, et al. Effect of nickel microstructure on methane steam-reforming activity of Ni–YSZ cermet anode catalyst. Journal of Catalysis 258;356–65;2008.

[151] Iwai H, Ueda M, Takahashi T, Saito M, Yoshida H. Evaluation of steam methane reforming on SOFC porous anode considering its microstructure. Proceedings of the 8th International Symposium on Heat Transfer (ISHT-8), Beijing: 2012, p. ISHT – 8–06 – 1, 1–8.

[152] Timmermann H, Fouquet D, Weber A, Ivers-Tiffée E, Hennings U, Reimert R. Internal reforming of methane at Ni/YSZ and Ni/CGO SOFC cermet anodes. Fuel Cells 6;307–13;2006.

[153] Lee AL, Zabransky RF, Huber WJ. Internal reforming development for solid oxide fuel cells. Ind Eng Chem Res 29;766–73;1990.

[154] Wei J, Iglesia E. Structural requirements and reaction pathways in methane activation and chemical conversion catalyzed by rhodium. Journal of Catalysis 225;116–27;2004.

[155] Kuehn DR, Davidson H. Computer Control II. Mathematics of Control. Chemical Engineering Progress 57;44–7;1961.

[156] Dutka J. Robert Adrain and the Method of Least Squares. Archive for History of Exact Sciences 41;171–84;1990.

[157] Legendre A-M. Nouvelles méthodes pour la détermination des orbites des comètes. Paris: F. Didot; 1805.

[158] Adrain R. Research concerning the probabilities of the errors which happen in making observations, The Analyst; or Mathematical Museum 1;93–109;1808.

[159] Gauss CF. Theoria motus corporum coelestium in sectionibus conicis solem ambientium. Hamburg: Friedrich Perthes and I.H. Besser; 1809.

[160] Plackett RL. Studies in the History of Probability and Statistics. XXIX: The Discovery of the Method of Least Squares. Biometrika 59;239–51;2014.

[161] Stigler S. Gauss and the invention of Least Squares. The Annals of Statistics 9;465–74;1981.

[162] Celmins A. The method of Gauss in 1799. Statistical Science 13;123–35;1998.

[163] Hulse R a. The discovery of the binary pulsar. Reviews of Modern Physics 66;699–710;1994.

[164] Taylor J. Binary Pulsars and Relativistic Gravity. Reviews of Modern Physics 66;711–9;1994.

[165] Crowe CM. Data reconciliation - progress and challenges. Journal of Process Control 6;89–98;1996.

[166] Reilly PM, Carpani RE. Application of statistical theory of adjustment to material balances. 13th Canadian Chemical Engineering Conference, Montreal: 1963.

[167] Swenker AG. Ausgleichung von Meßergebnissen in der chemischen Industrie. Acta IMEKO: Berichte Der III. Internationalen Konferenz Für Messtechnik und Gerätebau, 1964, p. 29–48.

[168] Szargut J. Application of the Least Squares Method in Energy Engineering. Wroclaw, Poland: Ossolineum Press; 1989.

[169] Kolenda Z, Allman J. Energy balances with additional data. Bull De l'Academie Pol De Sci 22;6–10;1974.

[170] Kolenda Z, Szmyd J. Coordinated material and energy balances of the flash smelting process. Archives of Metallurgy and Materials 3;3–20;1985.

[171] Szargut J, Kolenda Z, Taramin K. Coordination of material and energy balances as a basis of combustion process optimization. Energy Research 5;253–61;1981.

[172] Kolenda Z, Szmyd J, Slupek S, Baez L. Numerical modelling of heat transfer processes with supplementary data. The Canadian Journal of Chemical Engineering 61;627–34;1983.

[173] Szmyd J, Suzuki K, Kolenda Z, Humphrey J. A study of thermo-fluid phenomena with uncertainties by making use of interactive computational-experimental methodology. JSME International Journal, Series II 35;599–607;1992.

[174] Kolenda Z, Szmyd J, Dziedziniewicz K. Evaluation of carbon dioxide standards emissivity using the least squares method. Archives of Metallurgy and Materials 32;587–611;1987.

[175] Kolenda Z, Donizak J, Bocardo J. Least-Squares adjustment of mathematical model of heat and mass transfer processes during solidification of binary alloys. Metallurgical and Materials Transactions B 30B;505–13;1999.

[176] Kolenda Z, Zembura Z, Donizak J, Zembura M. An application of unified least squares method to the mathematical modelling of autocatalytic reactions. Journal of Electroanalytical Chemistry 382;1–15;1995.

[177] Skorek J. Zastosowanie metod stochastycznych i spektralnych do rozwiązywania granicznych zagadnień odwrotnych przewodzenia ciepła. Gliwice: Politechnika Śląska; 1994.

[178] Skorek J. Applying the least squares adjustment technique for solving inverse heat conduction problems. In: Taylor C, editor. Proceedings of the 8th Conference on Numerical Methods in Laminar and Turbulent Flow, Swansea, U.K: Pinerdage Press; 1993, p. 189–98.

[179] Szmyd JS, Suzuki K, Kolenda Z, Hagiwara Y. An application of interactive computational-experimental methodology to optimization of the position of the probe in conduction heat transfer processes. Proceedings of the International Symposium on Heat and Mass Transfer, 1994, p. 147–52.

[180] Sciazko A, Komatsu Y, Kimijima S, Kolenda Z, Szmyd JS. An application of the Generalized Least Squares method to the analysis of the heat transfer process with supplementary data. IHTC 15, the 15 International Heat Transfer Conference : August 10–15, 2014, Kyoto : proceedings, 2014, p. 1–15 IHTC15–9920.

[181] Bendig M, Roesser G, Marechal F. Enhanced Data Reconciliation. Proceedings of the 27th International Conference on Effciency, Cost, Optimization, Simulationa dn Environmental Impact on Energy System (ECOS2014), Turku: 2014, p. 2102–18.

[182] Singhmaneeskulchai P, Angsutorn N, Siemanond K. Dynamic data reconciliation in a hot-oil heat exchanger for validating energy consumption. Chemical Engineering Transactions 35;493–8;2013.

[183] Sciazko A, Komatsu Y, Brus G, Kimijima S, Szmyd JS. An application of generalized least squares method to an analysis of methane/steam reforming process on a Ni/YSZ catalyst. ECS Transactions 57;2987–96;2013.

[184] Sciazko A, Komatsu Y, Brus G, Kimijima S, Szmyd JS. A novel approach to the experimental study on methane/steam reforming kinetics using the Orthogonal Least Squares method. Journal of Power Sources 262;245–54;2014.

[185] Sciazko A, Komatsu Y, Brus G, Kimijima S, Szmyd JS. A novel approach to improve the mathematical modelling of the internal reforming process for solid oxide fuel cells using the orthogonal least squares method. International Journal of Hydrogen Energy 39;16372–89;2014.

[186] Romagnoli J, M. S. Data Processing and Reconciliation for Chemical Process Operations. San Diego, California: Academic Press; 2000.

[187] Mikhail EMKM, Ackermann FE. Observations and least squares. New York: T.Y. Cronwell Comp.; 1976.

[188] Kolenda Z, Styrylska T, Donizaki J, Guzik A. Numerical and experimental mathematical modelling of heat and mass transfer processes using unified least squares method. Energy Conversion and Management 39;1763–72;1998.

[189] Brandt S. Statistical and computational methods in data analysis. Amsterdam: North-Holland Publishing Company; 1970.

[190] Szargut J, Kolenda Z. Theory of co-ordination of material and energy balances in metallurgical chemical processes. Archives of Metallurgy and Materials XIII;153–69;1968.

[191] Xu J, Froment GF. Methane steam reforming: II. diffusional limitations and reactor simulation. AIChE Journal 35;97–103;1989.

[192] Suzuki K, Iwai H, Nishino T. Electrochemical and thermo-fluid modeling of a tubular solid oxide fuel cell with accompanying indirect internal fuel reforming. In: Sunden B, Faghri M, editors. Transport Phenomena in Fuel Cells, Southampton, Boston: WIT Press; 2005, p. 83–133.

[193] Bebelis S, Zeritis A, Tiropani C, Neophytides SG. Intrinsic kinetics of the internal steam reforming of CH_4 over a Ni−YSZ−cermet catalyst−electrode. Industrial & Engineering Chemistry Research 39;4920–7;2000.

[194] Blaylock DW, Teppei Ogura, William HG, Gregory JOB. Computational investigation of thermochemistry and kinetics of steam methane reforming on Ni(111) under realistic conditions. Journal of Physical Chemistry C 113;4898–908;2009.

[195] Jones G, Jakobsen JG, Shim SS, Kleis J, Andersson MP, Rossmeisl J, et al. First principles calculations and experimental insight into methane steam reforming over transition metal catalysts. Journal of Catalysis 259;147–60;2008.

[196] Wei J, Iglesia E. Reaction Pathways and Site Requirements for the Activation and Chemical Conversion of Methane on Ru - Based Catalysts. J Phys Chem C 108;7253–62;2004.

[197] Wei J, Iglesia E. Isotopic and kinetic assessment of the mechanism of methane reforming and decomposition reactions on supported iridium catalysts. Physical Chemistry Chemical Physics 6;3754–9;2004.

[198] Brus G, Szmyd JS. Numerical modelling of radiative heat transfer in an internal indirect reforming-type SOFC. Journal of Power Sources 181;8–16;2008.

[199] Vannice MA. Kinetic of catalytic reactions. New York: Springer; 2005.

[200] Itoh N, Yu W. Kinetic analysis on low-temperature using a ruthenium steam supported reforming catalyst of methane. Journal of the Japan Institute of Energy 85;307–13;2006.

[201] ARRHENIUS S. Selected Readings in Chemical Kinetics. Elsevier; 1967.

[202] Ribeiro NFP, Souza MMVM, Neto ORM, Vasconcelos SMR, Schmal M. Investigating the microstructure and catalytic properties of Ni/YSZ cermets as anodes for SOFC applications. Applied Catalysis A: General 353;305–9;2009.

[203] Jiang SP, Chan SH. A review of anode materials development in solid oxide fuel cells. Journal of Materials Science 39;4405–39;2004.

[204] Wang FH, Guo RS, Wei QT, Zhou Y, Li HL, Li SL. Preparation and properties of Ni/YSZ anode by coating precipitation method. Materials Letters 58;3079–83;2004.

[205] AGC SEMI CHEMICAL Co. Ltd. Catalyst analysis sheets. 2009.

[206] Mozdzierz M, Brus G, Sciazko a., Komatsu Y, Kimijima S, Szmyd JS. An attempt to minimize the temperature gradient along a plug-flow methane/steam reforming reactor

by adopting locally controlled heating zones. Journal of Physics: Conference Series 530;012040;2014.

[207] Belyaev VD, Politova TI, Mar'ina OA, Sobyanin VA. Internal steam reforming of methane over Ni-based electrode in solid oxide fuel cells. Applied Catalysis A: General 133;47–57;1995.

[208] Dicks AL, Pointon KD, Siddle A. Intrinsic reaction kinetics of methane steam reforming on a nickel/zirconia anode. Journal of Power Sources 86;523–30;2000.

[209] Akers WW, Camp DP. Kinetics of the methane-steam reaction. AIChE Journal 1;471–5;1955.

[210] Nakagawa N, Sagara H, Kato K. Catalytic activity of Ni-YSZ-CeO_2 anode for the steam reforming of methane in a direct internal-reforming solid oxide fuel cell. Journal of Power Sources 92;1–5;2001.

[211] Yokokawa H, Tu H, Iwanschitz B, Mai A. Fundamental mechanisms limiting solid oxide fuel cell durability. Journal of Power Sources 182;400–12;2008.

[212] Dicks A. Advances in catalysts for internal reforming in high temperature fuel cells. Journal of Power Sources 71;111–22;1998.

Appendix A: Details of the experimental apparatus

Here, the detailed specifications of the experimental equipment are listed (see Table A.1).

Table A. 1 Specification of devices used for building experimental setup

Equipment designation	Model	Producer	Quantity
Containers			
Reformer	R3A03828	OKURA RIKEN	1
Purifier	R3A03830	OKURA RIKEN	1
Vaporizer	R3A03829	OKURA RIKEN	1
Water tank	TK-140	KATO STAINLESS	1
Cooler	R3H02162	OKURA RIKEN	1
Gas-liquid seprator	R3H02271	OKURA RIKEN	1
Heaters			
Vaporizer heater	1M-1-600	SAKAGUCHI E.H	1
Electric furnace	R3H02375	ASAHI RIKA	1
Moisturizing cover			1
Mantle heater			1
Pump			
Tubing pump	NP-KX-110	NIHON SEIMITSU KAGAKU	1
Flow controllers			
Massflow controller	HM1141A08Z011111D141	HEMMI Slide Rule	1
Flow meter	RK1250-15-B-1 4-H2-300ML/MIN-0.1MPa	KOFLOC	1
Flow meter	RK1100-PV-15-A-1 4-N2-300ML/MIN-0.1MPa	KOFLOC	1
Dry gas meter	DC-Da-1C	SHINAGAWA	1
Perssure controllers			
Perssuer gauge	DRM2-S01N G1/4	NISSHIN KEIKI	3
Pressure transmitters	KH15-623-6711003	NAGANO KEIKI	1
Pressure gauge with contact	DBU2E-φI75-G1/4-2MPa-SUS	EBARA KEIKI	1

Appendix A: Details of the experimental apparatus

Valves			
Stop valve	SS-41GS2	Swagelok	5
Stop valve	SS-42GS4	Swagelok	2
Three-way valve	SS-41GXS1	Swagelok	1
Three-way valve	SS-41GXS2	Swagelok	1
Pressure deducting valve	RD4-254	HEMMI Slide Rule	3
Clack valve	SS-2C-1	Swagelok	3
Clack valve	SS-2C-25	Swagelok	1
Safety valve	SS-RL3S4	Swagelok	1
Electromagnetic valve	AB31-01-1-E00B-AC100V	CKD	2
Electromagnetic valve	AB42-02-3-E00B-AC100V	CKD	1
Other apparatuses			
Electronic balance	GF-3000	A&D	1
Thermocouple	S6A-K16-C-U-350-KXG-100	ICHIKAWA METAL	1
Thermocouple	S6A-K32-C-U-150-KXG-100	ICHIKAWA METAL	1
Thermocouple	S6A-K16-C-U-200-KXG-100	ICHIKAWA METAL	1
Thermocouple	S6A-K10-C-U-400-KXG-100	ICHIKAWA METAL	1
Gauges			
Thermoregulator indicator	UT150-VN/AL	Yokogawa Electric	3
SSR	G3NA-210B DC5～24V	OMRON	3
Temperature indicator	UT130-RN	Yokogawa Electric	1
Massflow indicator	DM1501A	HEMMI Slide Rule	1
Massflow adjuster	DP1001A	HEMMI Slide Rule	
Massflow 1ch power source	PU1501A	HEMMI Slide Rule	6
Pressure indicator	SD16-890-1300	SHIMADEN	1
Gas meter indicator	SUP	SHIMADEN	1
H2 gas alarm	GP-571A-A5	RIKEN KEIKI	1
CO gas alarm	FU-3C	FUSORIKA	1
Seismoscope	D7H-A1	OMRON	1
Peripherals			
Gas chromatograph	GC390B	GL Sciences	1
Methanizer	MT221	GL Sciences	1
Humidistant	DP281	GL Sciences	1
Control timer	RT730	GL Sciences	1
Date logger	8422-50	HIOKI	1
Ciruculatory cooling	LTC-1200N	AS ONE	1

Appendix B: Properties of investigated catalysts

B.1 SEM images of catalyst powders

The prepared catalyst materials were investigated by the Scanning Electron Microscopy (SEM) method. The industrial catalysts of NiO/YSZ (60:40vol.%) and NiO/SDC (60:40vol.%), from AGC SEIMI CHEMICAL CO. LTD., are presented in Fig. B.1. In Figs. B.2 and B.3, the laboratory-scale catalysts of NiO/YSZ (60:40vol.%) and Ni/YSZ (in various compositions of 70:30vol.%, 60:40vol.%, 50:50vol.%, 40:60vol.% and 30:70vol.%) are presented. Essentially, all the presented catalysts are in the form of NiO/YSZ after the sintering process and before the reduction process. However, there is a difference among them depending on the fact that whether a NiO/YSZ mixture was prepared with Ni powder or NiO powder before the sintering process. Note that to clearly distinguish them, the term "NiO/YSZ" and "Ni/YSZ" was used here whenever the actual form of the catalyst is.

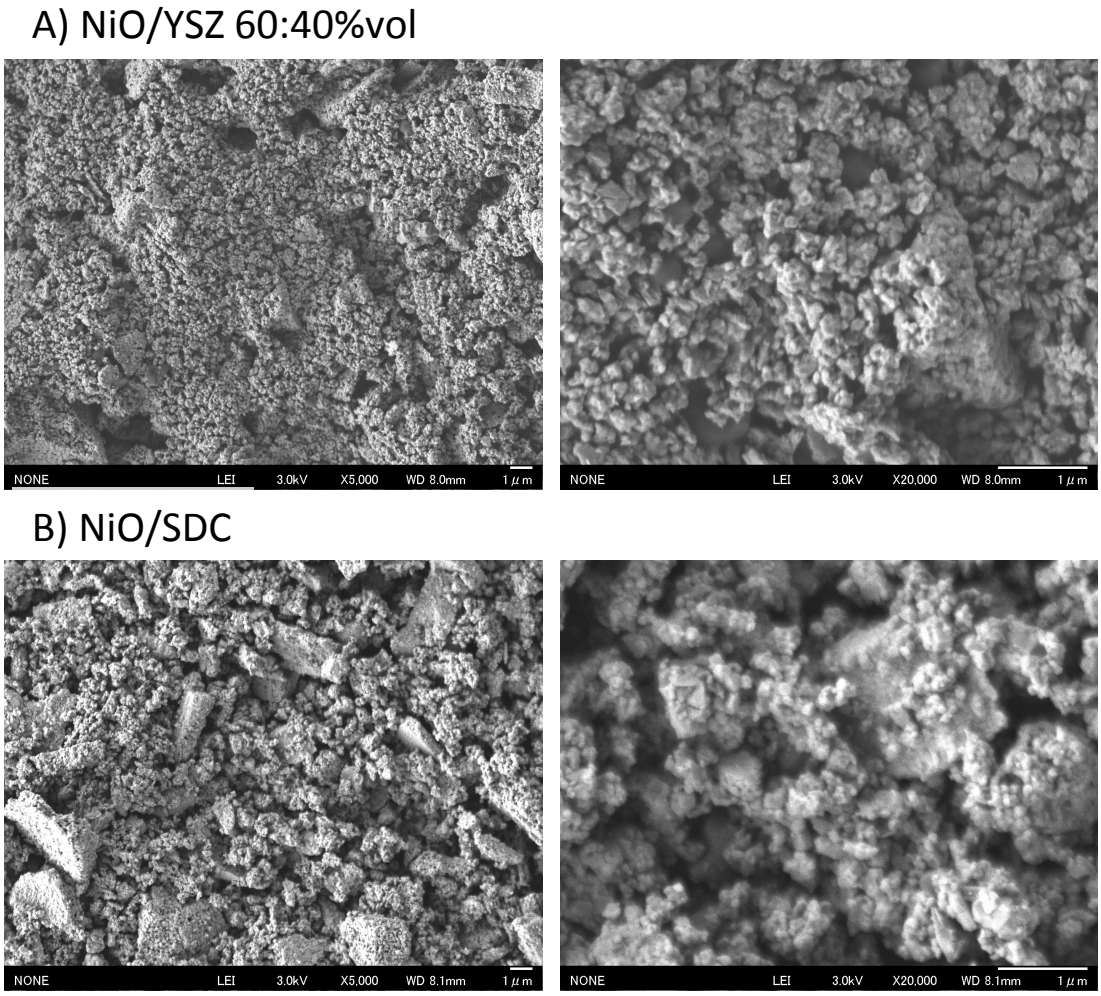

Figure B. 1 SEM images of the catalyst powders from AGC SEIIMI CHEMICAL CO. LTD.,: A) NiO/YSZ (60:40vol.%) and B) NiO/SDC (60:40vol.%)

A) NiO/YSZ 60:40%vol

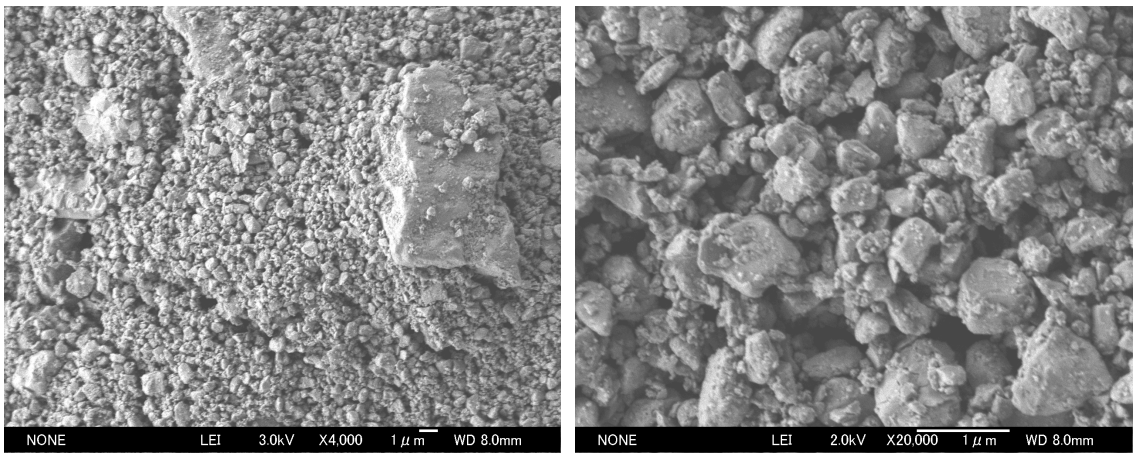

B) Ni/YSZ 70:30%vol

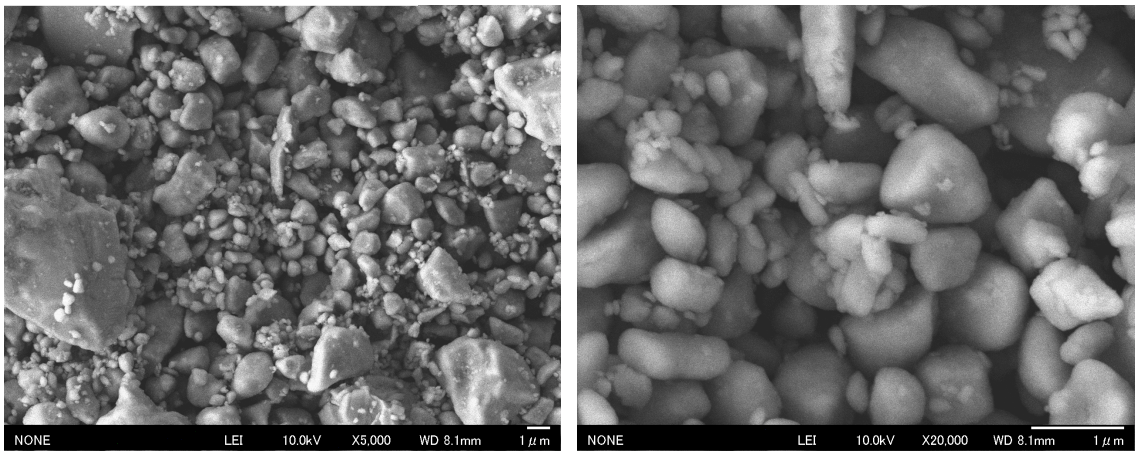

C) Ni/YSZ 60:40%vol

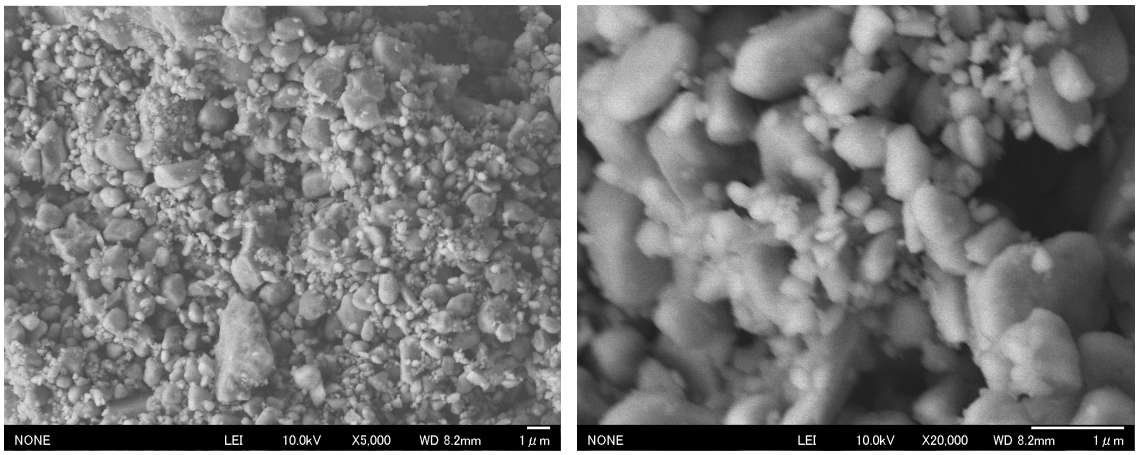

Figure B. 2 SEM images of the mechanically-crushed catalyst powders, prepared with acetone dispersant, before conducting the experiment: A) NiO/YSZ (60:40vol.%), B) Ni/YSZ (70:30vol.%), and C) Ni/YSZ (60:40vol.%)

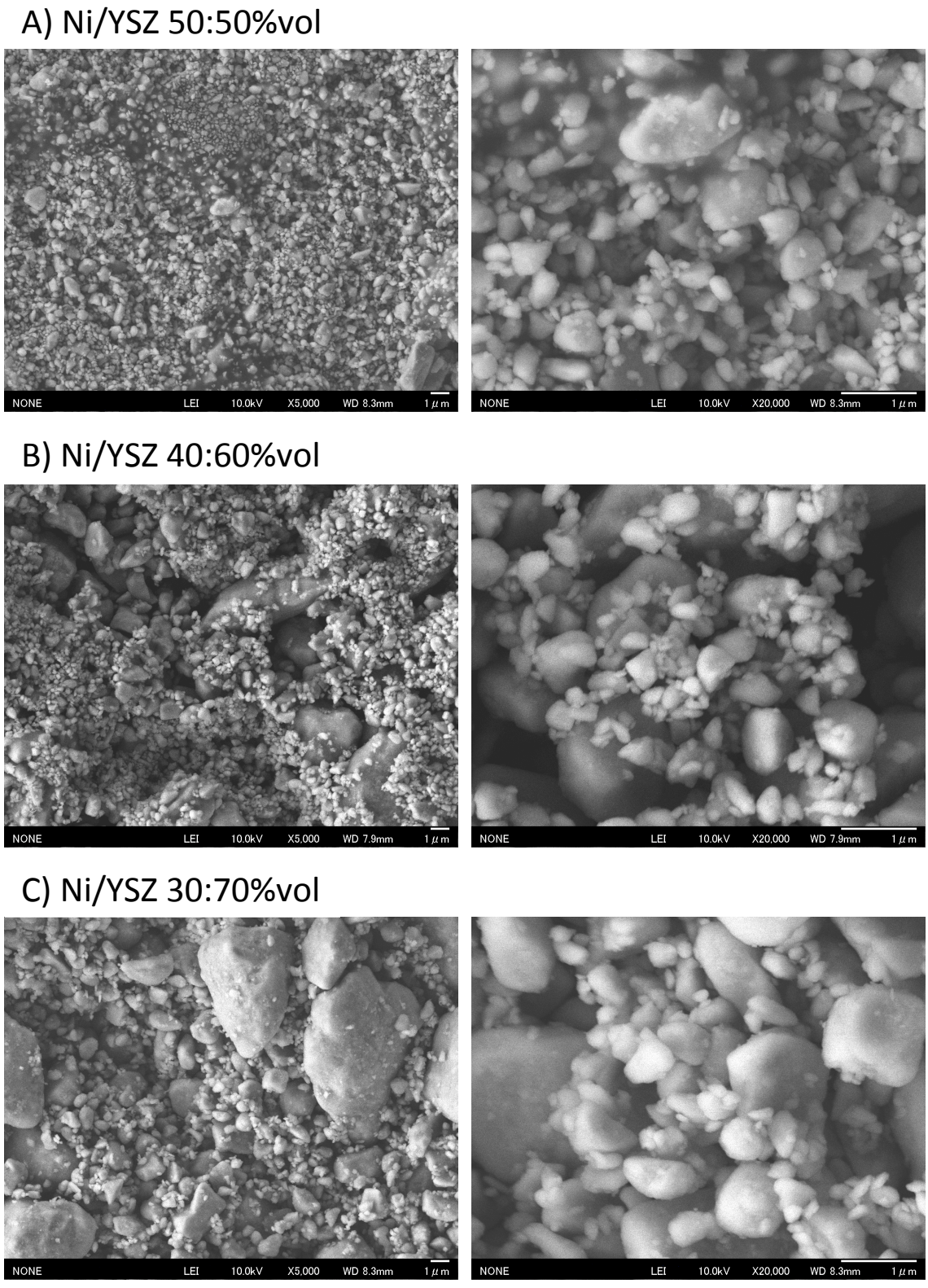

Figure B. 3 SEM images of the mechanically-crushed catalyst powders prepared with acetone dispersant, before conducting the experiment:, A) Ni/YSZ (50:50vol.%), B) Ni/YSZ (40:60vol.%) and C) Ni/YSZ (30:70vol.%)

It can be noticed that even though all of the catalysts were prepared with the same procedure and all of them were crushed mechanically for 48h, in general with a decreasing volumetric share of Nickel, the size of the catalyst particles increases. It is resulted from the increased share of YSZ, which is hard ceramic material.

On the other hand, when compare NiO/YSZ (60:40vol.%) catalyst before conducting the methane/steam experiment in Fig. B.2.A to the same catalytic material after experimentation in Fig. B.4.A, a significant decrease in the grains size can be observed. The same can be observed for the Ni/YSZ catalyst at a ratio of 60:40vol.% in Fig. B.2. C and Fig. B.4 B. This is explained by the first stage of the experimentation, which is the reduction process of nickel oxide in hydrogen flow. It is also influential in the case of Ni/YSZ catalyst, because nickel at high sintering temperatures is subjected to the oxidation process.

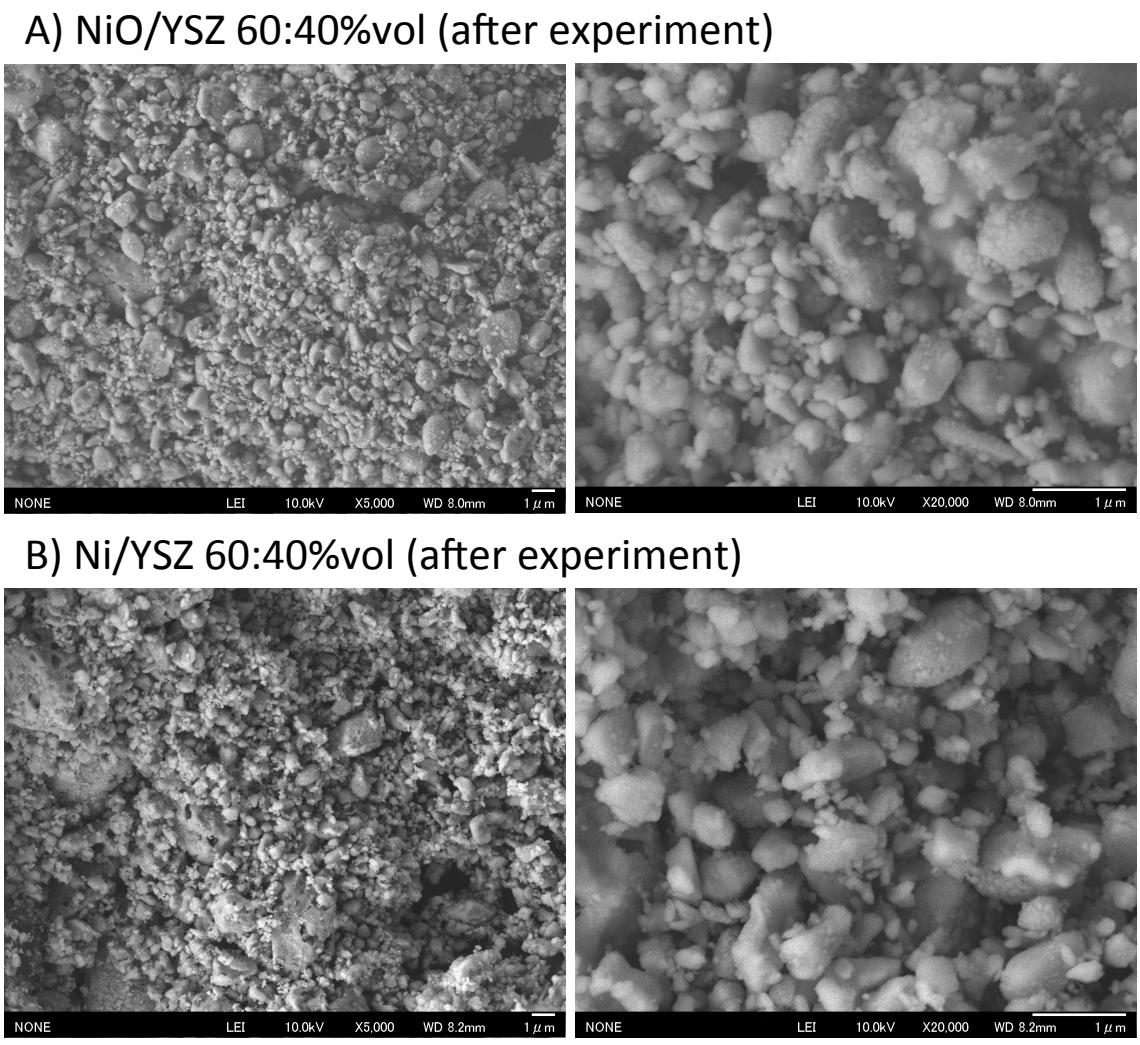

Figure B. 4 SEM images of catalyst powders prepared with acetone dispersant, mechanically crushed, after conducting experiment: A) Ni/YSZ (60:40vol.%) and B) NiO/YSZ (60:40vol.%)

B.2 Measurement of particle size

The assessment of the average particle size was conducted by the Free-Fall Type Dry Measurement (SHIMADZU SALD-DS3) for the laboratory prepared catalysts: NiO/YSZ (60:40vol.%) and Ni/YSZ (in various composition ratios of 70:30vol.%, 60:40vol.%, 50:50vol.%, 40:60vol.% and 30:70vol.%). The results of the measurement are summarized in Table B.1 by giving the mode, median, average value and standard deviation of the particle diameter in the each investigated catalyst material. Each measurement was conducted three times and high reputability of the results can be observed. The individual probability density function and the cumulative probability function are presented in Fig. B.5.

Table B. 1 Results of the Free-Fall Type Dry Measurement for laboratory prepared catalysts

Catalyst	Test	Median diameter [µm]	Mode diameter [µm]	Average diameter [µm]	Standard deviation [µm]
NiO/YSZ 60:40%vol	1	0.638	0.504	0.978	0.466
	2	0.646	0.504	1.134	0.545
	3	0.63	0.628	0.829	0.39
Ni/YSZ 70:30%vol	1	0.783	0.404	0.901	0.320
	2	0.798	0.404	0.915	0.321
	3	0.850	0.404	0.974	0.338
Ni/YSZ 60:40%vol	1	0.667	0.628	0.737	0.263
	2	0.774	0.628	0.836	0.296
	3	0.643	0.628	0.699	0.239
Ni/YSZ 50:50%vol	1	0.800	0.404	0.932	0.342
	2	0.854	0.404	0.995	0.350
	3	0.777	0.404	0.925	0.340
Ni/YSZ 40:60%vol	1	0.918	0.404	1.043	0.368
	2	0.915	0.404	1.032	0.365
	3	0.909	0.404	1.064	0.379
Ni/YSZ 30:70%vol	1	1.265	0.404	1.325	0.447
	2	1.181	0.404	1.291	0.430
	3	1.290	0.404	1.326	0.446

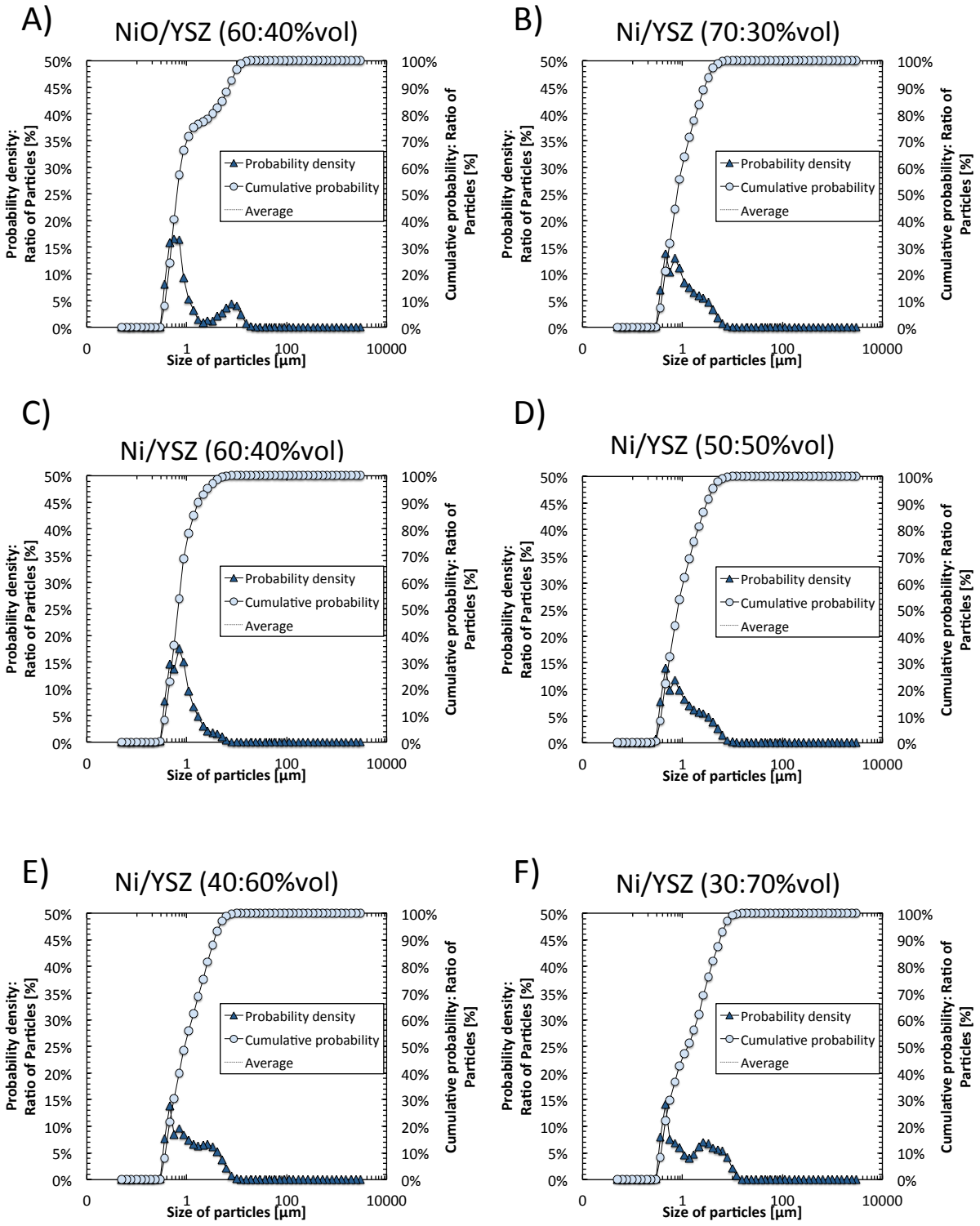

Figure B. 5 Size of particles - probability density function and cumulative probability function for catalysts: A) NiO/YSZ at the ratio of 60:40vol.%, B) Ni/YSZ at the ratio of 70:30vol.%, C) Ni/YSZ at the ratio of 60:40vol.%, D) Ni/YSZ at the ratio of 50:50vol.%, E) Ni/YSZ at the ratio of 40:60vol.% and F) Ni/YSZ at the ratio of 30:70vol.%

A comparison of the average particle size and particle medians for the laboratory prepared catalytic materials are presented in Fig. B.6. The observation from Appendix B.1 is proven with a decreasing share of nickel, the particles increased their size. An increasing amount of ceramic compound decreases the grindability of the final material.

As is seen in Fig. B.6A, the NiO/YSZ (at the composition ratio of 60:40vol.%) catalyst is characterized by the smallest reputability of the measured result – it can be explained by the probability density function (in Fig. B.5A) which is a composition of two normal distributions.

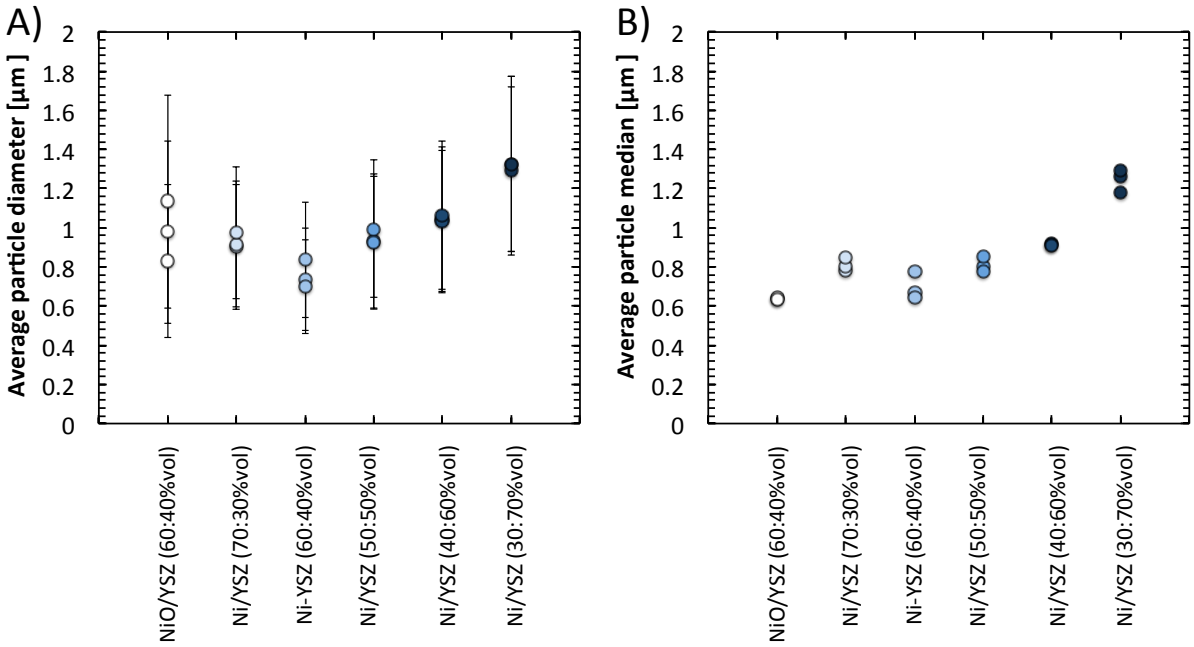

F**igure B. 6** A) Average size of particles and B) Median of the size of the particles for laboratory prepared catalysts

Appendix C: Derivation of methane steam kinetic using the basic methodologies

This appendix presents detailed results of the numerical investigations, which were not included in the main discussion of this dissertation. The presented studies were conducted for the NiO/YSZ catalyst at the ration of 60:40vol.% prepared with ethanol dispersant.

Section C.1 presents the results of the application of the standard method. Figures C.1 and C.2 presents the results of the investigation of the reaction kinetic by the standard method. The presented results include experimentation at the reaction temperatures of 550 ^{o}C (A and E), 575 ^{o}C (B and F), 650 ^{o}C (C and G) and 700 ^{o}C (D and H).

The increasing deviation of the partial pressure with the increasing temperature of the conducted experiment can be observed in Fig. C.2. The errors are bigger in the case of the partial pressure of steam, what can be caused by both factors: the increased conversion of methane which changes the final partial pressures and the instability of the catalyst and nickel coursing phenomena occurring at the higher test temperature.

Section C.2 focuses on the analysis conducted by the application of the modified method. Firstly, Fig. C.3 presents the results of the modified method with applied measurements conducted in modified experimental conditions (Series 3 in Table 4.5). Approximations are given for measurements at temperatures of A) 500 ^{o}C B) 525 ^{o}C C) 550 ^{o}C D) 575 ^{o}C E) 625 ^{o}C F) 650 ^{o}C G) 675 ^{o}C and H) 700 ^{o}C. Next, the analysed results of the measurements in standard experimental conditions (Series 1 and 2 in Table 4.5) are presented in Figs. C.4 and C.5. Figures C.4 and C.5 include analysis in temperatures 550^{o}C, 575^{o}C and 650^{o}C.

C.1 Results of the standard method

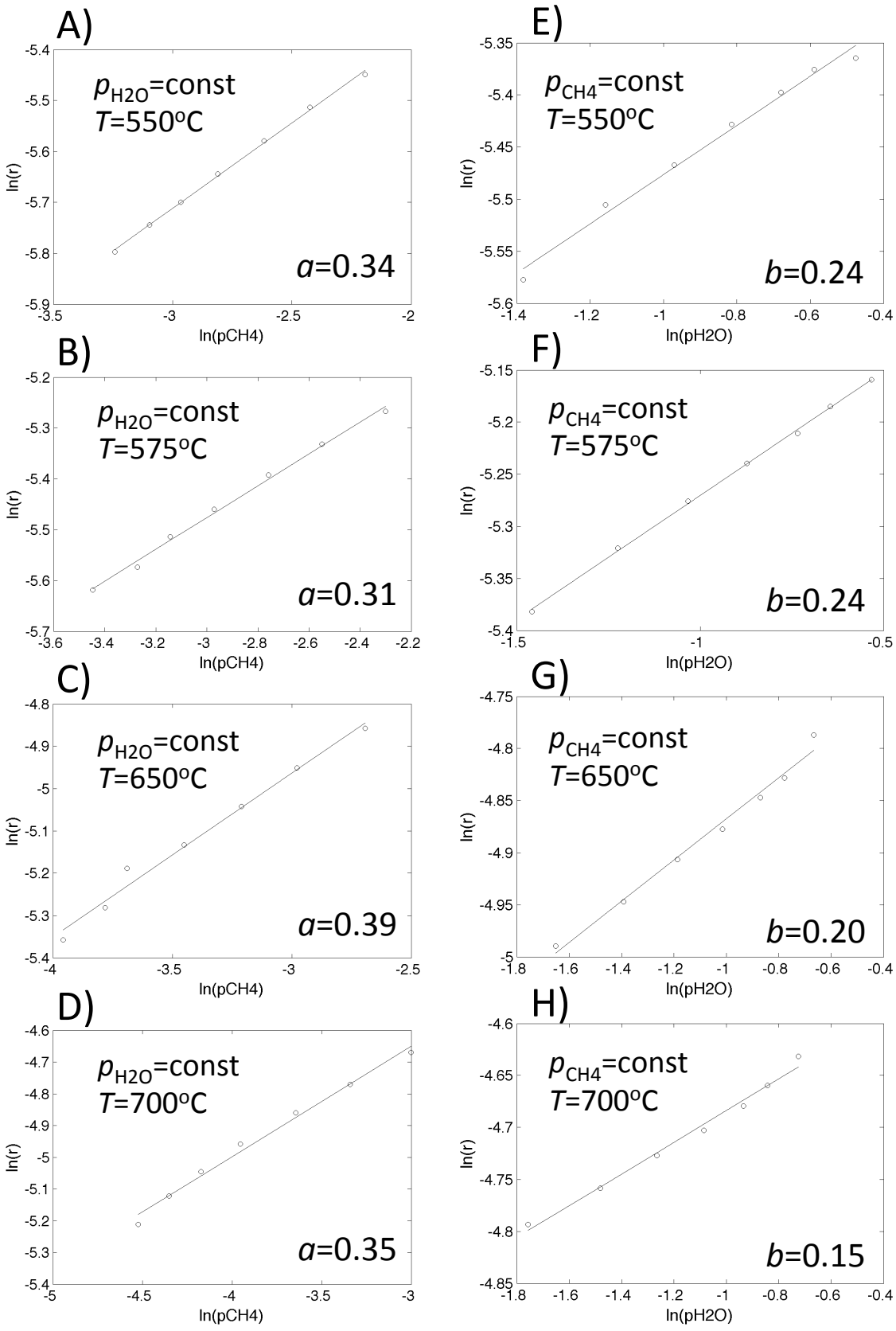

Figure C. 1 Approximation of the reaction orders by the standard approach A)-D) parameter *a* and E)-H) parameter *b* in temperature 550°C (A, E), 575°C (B, F), 650°C (C, G) and 700°C (D, H)

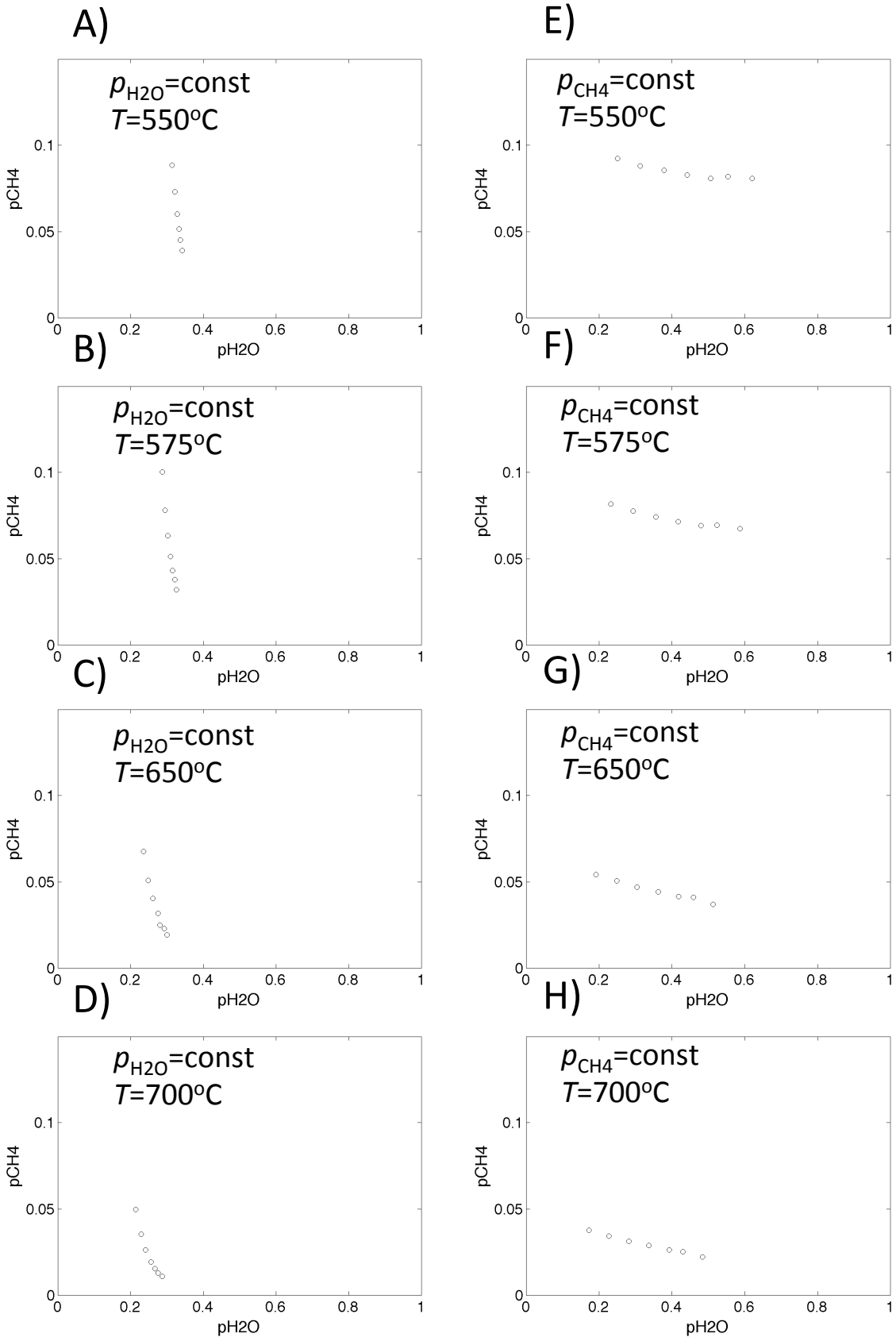

Figure C. 2 Correlation between partial pressures of methane and water at temperatures 550°C (A and E), 575°C (B and F), 650°C (C and G) and 700°C (D and H) for measurements A)-D) at the constant flow rate of steam and E)-H) at the constant flow rate of methane

C.2 Results of the modified method

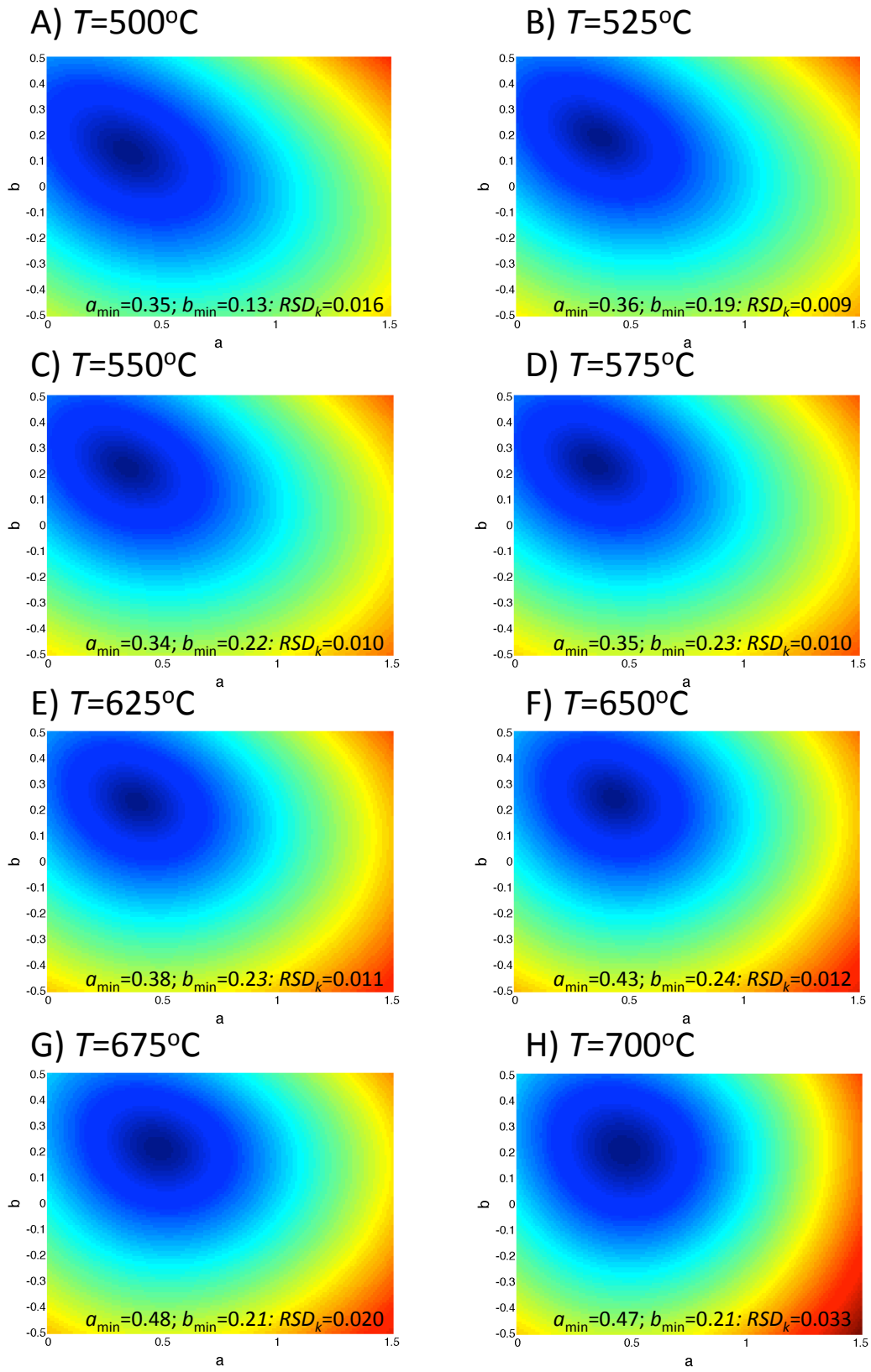

Figure C. 3 Approximation of the reactions orders using the modified approach with modified experimental data at temperatures A) 500 °C B) 525 °C C) 550 °C D) 575 °C E) 625 °C F) 650 °C G) 675 °C and H) 700 °C

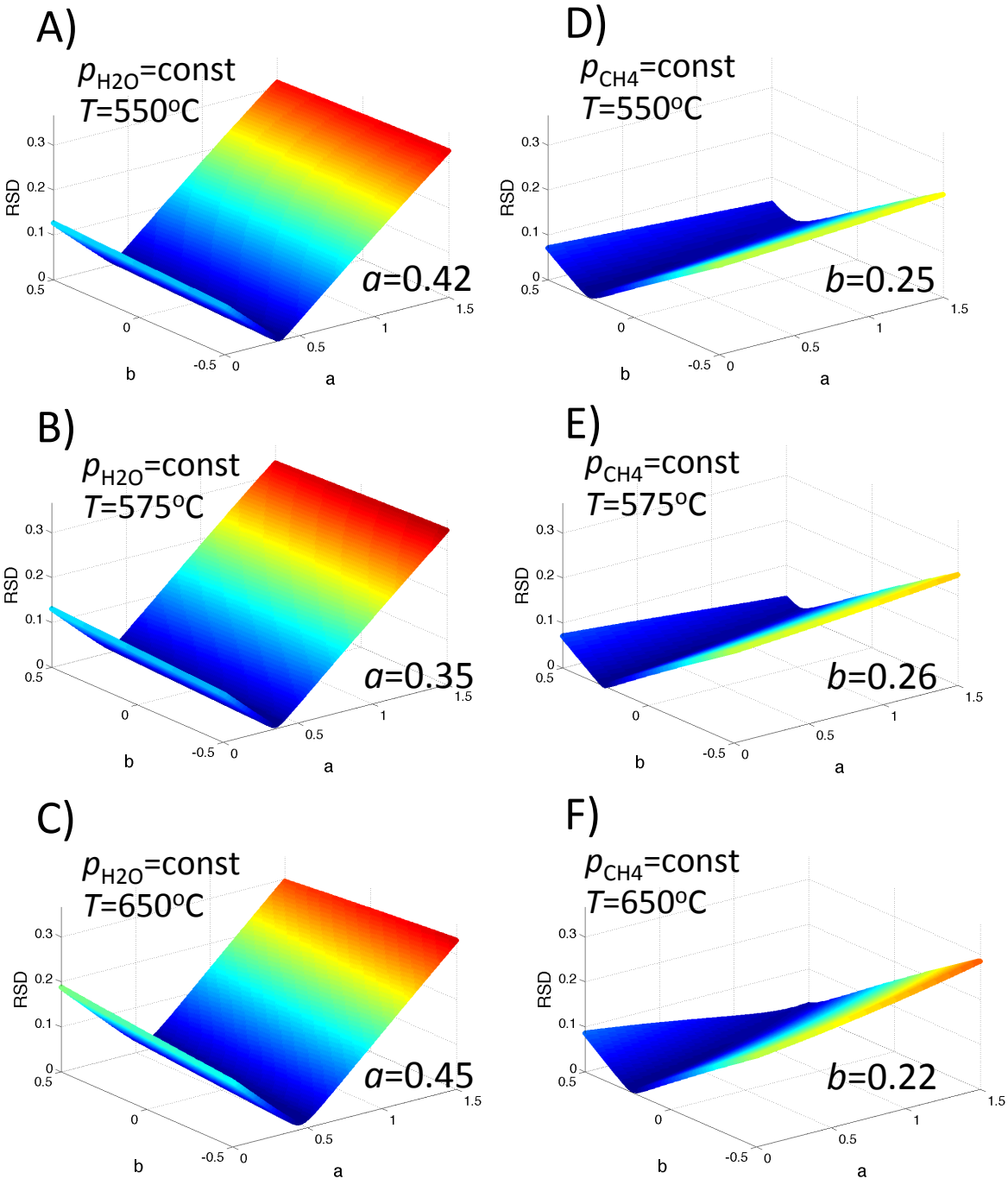

Figure C. 4 Approximation of reaction orders using the modified approach with standard experimental data at a constant flow rate of steam (A-C) and at a constant flow rate of methane (D-F) for the analysis in temperature 550°C (A and D), 575°C (B and E) and 650°C (C and F),

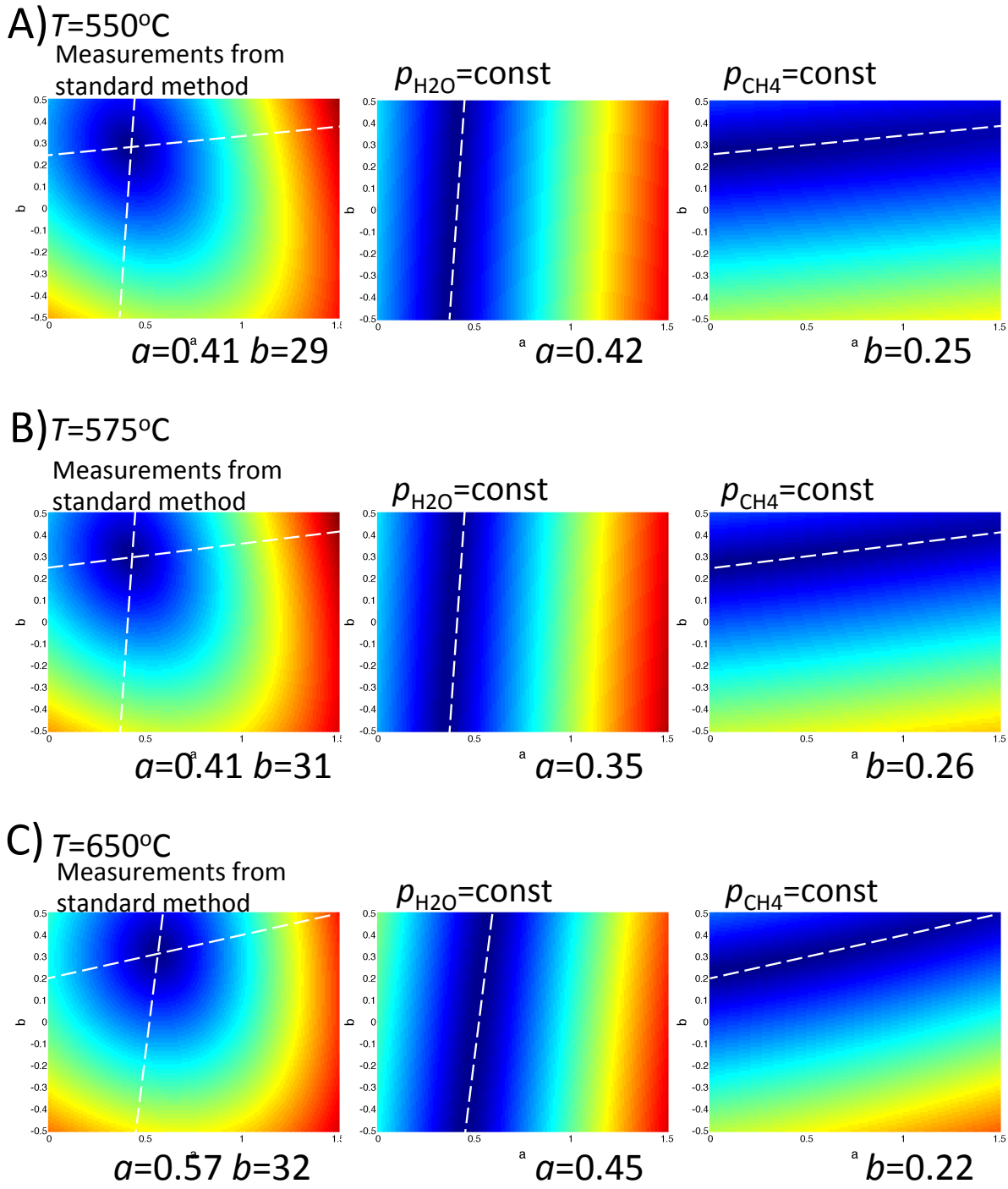

Figure C. 5 Influence of the unstable partial pressure of methane for the approximation of reaction orders by the modified approach with standard experimental data at temperatures A) 550°C B) 575°C and C) 650°C